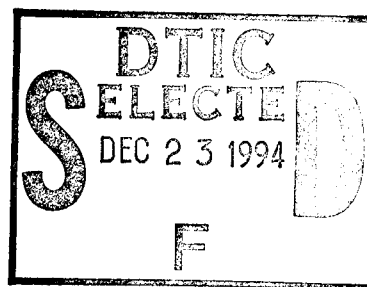


PL-TR-94-2222

DEVELOPMENT OF SUPERCONDUCTING TECHNOLOGY FOR INERTIAL GUIDANCE, GRAVITY SURVEY, AND FUNDAMENTAL GRAVITY EXPERIMENTS

**Ho Jung Paik
Edgar R. Canavan
Benjamin Bachrach
Hans J. Haucke**

**Department of Physics
University of Maryland,
College Park, Maryland 20742**



1 August 1994

**Final Report
30 September 1987 - 31 December 1993**

Approved for public release; distribution unlimited.




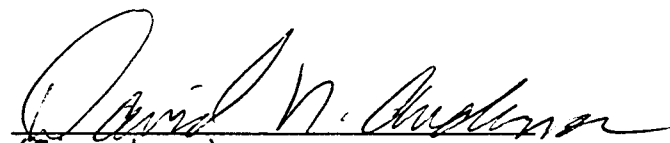
**PHILLIPS LABORATORY
Directorate of Geophysics
AIR FORCE MATERIEL COMMAND
HANSCOM AIR FORCE BASE, MA 01731-3010**

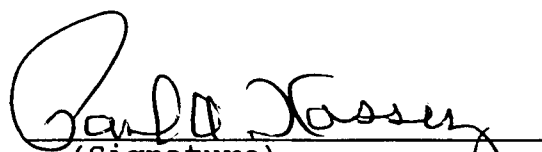
19941219 072

DTIC QUALITY ASSURANCE 1

"This technical report has been reviewed and is approved for publication"


(Signature)
JAMES C. BATTIS
Contract Manager


(Signature)
DAVID N. ANDERSON
Branch Chief


(Signature)
PAUL A. KOSSEY
Deputy Division Director

This report has been reviewed by the ESC Public Affairs Office (PA) and is releasable to the National Technical Information Service (NTIS).

Qualified Requestors may obtain additional copies from the Defense Technical Information Center (DTIC). All others should apply to the National Technical Information Service (NTIS).

If your address has changed, if you wish to be removed from the mailing list, or if the addressee is no longer employed by your organization, please notify PL/TSI, 29 Randolph Road, Hanscom AFB, MA 01731-3010. This will assist us in maintaining a current mailing list.

Do not return copies of this report unless contract obligations or notices on a specific document requires that it be returned.

REPORT DOCUMENTATION PAGE			Form Approved OMB No. 0704-0188	
<small>Public reporting burden for this collection of information is estimated to average 1 hour per response, including the time for reviewing instructions, searching existing data sources, gathering and maintaining the data needed, and completing and reviewing the collection of information. Send comments regarding this burden estimate or any other aspect of this collection of information, including suggestions for reducing this burden, to Washington Headquarters Services, Directorate for Information Operations and Reports, 1215 Jefferson Davis Highway, Suite 1204, Arlington, VA 22202-4302 and to the Office of Management and Budget, Paperwork Reduction Project (0704-0188), Washington, DC 20503.</small>				
1. AGENCY USE ONLY (Leave blank)	2. REPORT DATE 1 August 1994	3. REPORT TYPE AND DATES COVERED Final (30 Sep 1987-31 Dec 1993)		
4. TITLE AND SUBTITLE Development of Superconducting Technology for Inertial Guidance, Gravity Survey and Fundamental Gravity Experiments		5. FUNDING NUMBERS PE 62101F PR 7600 TA 06 WU BP		
6. AUTHOR(S) Ho Jung Paik Edgar R. Canavan Benjamin Bachrach		Contract F19628-87-K-0053		
7. PERFORMING ORGANIZATION NAME(S) AND ADDRESS(ES) University of Maryland Department of Physics College Park, Maryland 20742-4111		8. PERFORMING ORGANIZATION REPORT NUMBER		
9. SPONSORING/MONITORING AGENCY NAME(S) AND ADDRESS(ES) Phillips Laboratory 29 Randolph Road Hanscom AFB, MA 01731-3010 Contract Manager: James Battis/GPEG		10. SPONSORING/MONITORING AGENCY REPORT NUMBER PL-TR-94-2222		
11. SUPPLEMENTARY NOTES				
12a. DISTRIBUTION/AVAILABILITY STATEMENT Approved for public release; Distribution unlimited			12b. DISTRIBUTION CODE	
13. ABSTRACT (Maximum 200 words) The principles and test results of the superconducting inertial instruments, developed under Air Force contract F19628-87-K-0053, are reported. An improved model of Superconducting Six-axis Accelerometer (SSA-1b) was constructed and operated in both open- and closed-loop (force rebalance) mode. The device has intrinsic noise levels of $10^{-11} \text{ ms}^{-2} \text{ Hz}^{-\frac{1}{2}}$ and $10^{-9} \text{ rad s}^{-2} \text{ hz}^{-\frac{1}{2}}$ for the linear and angular acceleration, respectively, and has an open-loop bandwidth of 10 Hz. An ac-driven Superconducting Gravity Gradiometer (SAGG), capable of withstanding hostile moving-base environments, has also been tested under the contract. A three-axis Superconducting Gravity Gradiometer (SGG-11b), developed with NASA support, was used to carry out a precision laboratory test of the gravitational inverse square law under the Air Force contract.				
14. SUBJECT TERMS Accelerometer Inertial guidance Navigator			15. NUMBER OF PAGES 168	
Geodesy Gravity survey Superconductivity			16. PRICE CODE	
17. SECURITY CLASSIFICATION OF REPORT Unclassified	18. SECURITY CLASSIFICATION OF THIS PAGE Unclassified	19. SECURITY CLASSIFICATION OF ABSTRACT Unclassified	20. LIMITATION OF ABSTRACT SAR	

Table of Contents

1. Introduction	1
2. Superconducting Six-axis Accelerometer	4
2.1. Introduction	4
2.1.1. Motivation: Applications	4
2.1.2. Principle of operation	5
2.2. Development History	8
2.2.1. Model I	8
2.2.2. Model II	9
2.2.3. Model Ib	10
2.3. Mechanical Elements	12
2.3.1. SSA Sensor package	12
2.3.2. Materials considerations	13
2.3.3. Ancillary hardware	15
2.4. Levitation and Proof Mass Dynamics	17
2.4.1. Dynamics of Model II	17
2.4.2. Dynamics of Model I and Ib	23
2.5. Displacement Sensing	29
2.5.1. Model Ib: design	29
2.5.2. Model Ib: open loop measurements	37
2.6. Control of the SSA-Ib	43
2.6.1. Transfer functions of the SSA-Ib	44
2.6.2. Closed loop operation	46
2.6.3. Simulation results	51
2.7. Noise Analysis	55
2.7.1. Linearized noise model of SSA-Ib	56
2.7.2. Noise comparison between open and closed loop operation: Low frequency	59
2.7.3. Noise comparison between open and closed loop operation: Wide-band	64
2.8. Controller Implementation	74

2.8.1. Controller structure and transfer functions	74
2.9. Preliminary Testing of the SSA-Ib	94
2.9.1. SQUID saturation	94
2.9.2. Controller saturation and unmodeled dynamics	95
2.10. Future enhancements	98
3. AC Gradiometer	101
3.1. Introduction	101
3.2. Principles of Operation	102
3.3. Mechanical and Electrical Construction	108
3.3.1. Electronics	108
3.3.2. Software	109
3.3.3. Suspension	109
3.4. Noise and Error Sources	110
3.4.1. SQUID noise	110
3.4.2. External vibration	111
3.4.3. Bridge unbalance effects	111
3.4.4. Drive current back action	112
3.4.5. Temperature fluctuations	112
3.4.6. Microphonics	113
3.5. Gradiometer Performance Assessment	114
4. Precision Tests of gravity	117
5. References	120
6. List of Publications Resulting from this Contract	122
7. List of Related Contracts	123
8. Contributing Personnel	124
9. Appendices	125

Accession For	
NTIS GRA&I	J
DTIC TAB	
Unannounced	
Justification	
By	
DIRT	
A-1	

Development of Superconducting Technology for Inertial Guidance, Gravity Survey, and Fundamental Gravity Experiments

1. INTRODUCTION

The Einstein Equivalence Principle states that a local measurement can not distinguish gravity from acceleration. Thus, one must measure the difference between at least two distinct points to separate the effect of gravity. However, gravity is a weak force. In precision laboratory experiments, the variation in gravity with the motion of even a large gravity source is small compared to the natural and man-made accelerations experienced on the floor of a building. In gravity survey, the change in gravity due to geological-scale mass fluctuations is small compared to the accelerations experienced in moving vehicle. Thus, differential measurements always involve subtracting two large acceleration signals to recover a small gravity signal. This requires very stable and very high resolution acceleration measurements. Inertial navigation is also limited by the resolution and stability of accelerometers. It is limited as well by the Equivalence Principle: In order to navigate precisely, one must be able to distinguish local gravity from acceleration with respect to the inertial frame. This can be done either by using an instrument that measures the local gravity in real time, or by knowing the local gravity *a priori* from a gravity survey.

A fundamental limit on the resolution of accelerometers is imposed by the Fluctuation-Dissipation Theorem of statistical mechanics: Any dissipation in a system causes random fluctuations in the variables describing its state. The fluctuations are commonly known as Johnson noise in electrical systems and Brownian motion in mechanical systems. Their amplitude is proportional to the square root of temperature. From a technical standpoint, it is relatively straightforward to reduce the temperature by approximately two orders of magnitude by using liquid helium, the substance with the lowest boiling

point (4.2 K). With this reduction in temperature, one could expect to reduce the inherent noise by one order of magnitude. However, through judicious use of the low temperature properties of materials, the reduction in noise can be much greater. Many dissipation mechanisms are thermally activated, and are consequently frozen out at these temperatures. In low frequency electrical systems, the use of superconducting materials can effectively eliminate dissipation altogether. Furthermore, some of the more subtle properties of superconductors have been used to create the Superconducting Quantum Interference Device (SQUID), which can be used as an extremely low noise, low impedance, high gain magnetic flux-to-voltage converter. SQUIDs with energy resolution close to the Heisenberg uncertainty ($\Delta E \Delta t \leq h/2\pi$) limit have been demonstrated.

Reducing the temperature also facilitates the attainment of high stability. In mechanical elements, temperature coefficients of mechanical properties are typically much smaller at 4.2 K. For example, the thermal coefficient of expansion for most materials is three to four orders of magnitude lower than at room temperature. Furthermore, mechanical creep, which is a result of thermally activated processes, is almost entirely frozen out. In electrical systems, one can take advantage of the fact that the flux trapped in a closed superconducting loop is perfectly constant. For example, a superconducting mass may be levitated above a superconducting loop by trapping an appropriately large flux in the loop. The effective spring constant of the system is determined only by the geometry of the system and the flux, and hence is quite stable. (The temperature variation of the penetration depth, the effective depth to which flux penetrates into a superconductor, will affect the geometry, giving the spring constant some temperature dependence). One can also use the stability of flux trapped in superconducting circuits to create a highly stable displacement sensor.

Thus, cryogenic instruments have the potential for greatly improving our ability to measure inertial acceleration and gravity. This will better our knowledge of density fluctuations in the earth's crust, through improved gravity mapping, and our knowledge of

gravity itself, through improved precision tests of the laws of gravity. Indeed, the most sensitive gravity gradiometer is currently the superconducting gravity gradiometer (SGG) developed at the University of Maryland. It has performed the most precise test of the inverse square law of gravity at laboratory length scales (~ 1 m).

This report covers work on three aspects of superconducting inertial technology funded by the USAF/PL under this contract. The first is the Superconducting Six-axis Accelerometer (SSA). This instrument has a single, fully magnetically levitated proof mass. Six superconducting ac inductance bridges are configured to measure the relative displacement of the proof mass in all six degrees of freedom. The SSA can potentially provide acceleration measurements in all six degrees of freedom with several orders of magnitude lower noise than conventional instruments with a relatively compact sensor (~ 10 cm, excluding dewar vessel). The second aspect covered is the development of the Superconducting AC Gravity Gradiometer (SAGG). This device is similar to a single axis of the Superconducting Gravity Gradiometer (SGG) developed with NASA funding, except that it uses a superconducting ac bridge to sense the gravity gradient. This technique has certain advantages, particularly for applications in which the gradiometer must be moved, such as in gravity survey. The final aspect is the precision test of the inverse square law of gravity, which was performed using the SGG. Although NASA funded the development of the SGG, this contract funded the fundamental gravity experiment performed with the instrument.

2. SUPERCONDUCTING SIX-AXIS ACCELEROMETER

2.1 Introduction

2.1.1 Motivation: Applications

The initial impetus for the invention of the Superconducting Six-Axis Accelerometer (SSA) came from the requirements of the Superconducting Gravity Gradiometer (SGG). The SGG consists of six single-axis accelerometers mounted on a precision cube, with the sensitive axes normal to the face of the cube. By using sensing circuits that measure the differential displacement between pairs of proof masses on opposite sides of the cube, the device measures the gravity gradient along three orthogonal axes. With proper tuning, each sensing circuit can be made to reject the acceleration of the device along that axis. However, limitations on the precision with which the device can be fabricated give rise to non-parallelism and non-collinearity between the sensitive axes of accelerometer pairs. Imperfect parallelism causes sensitivity of each gradiometer axis to accelerations along the other two axes. Imperfect collinearity causes sensitivity to angular accelerations about the other two axes (Chan and Paik, 1987). Thus, the acceleration of the gradiometer platform in all six degrees of freedom need to be known so that these errors can be removed. The compact, symmetrical design of the SSA arose from the desire to fit it inside the mounting cube of the SGG, in such a way that the center of mass of the SSA proof mass coincided with the center of mass of the SGG. In this way, the SSA measures the necessary components of the acceleration directly.

For many applications of the gradiometer, nonlinearity in the sensitivity to acceleration may make the removal of these error terms difficult. In these cases, it is desirable to stabilize the platform using the information from the SSA. For this reason, the SSA uses a displacement sensing scheme somewhat different from the SGG. The key component in both sensing circuits is a SQUID, which is inherently a flux-to-voltage converter in

which the voltage is a periodic function of flux. Commercial versions use feedback to linearize the response. However, if the signal exceeds the slew rate of the feedback electronics, they can temporarily "lose lock", and re-lock onto a different cycle, causing a step in the output. Such a step is problematical when it occurs in a platform feedback loop. Theoretically, it could be removed through digital processing, but that has not yet been demonstrated. The SSA uses an ac sensing scheme in which the signal from the SQUID is demodulated, so steps in the dc level appear only as pulses in the output.

Because of its suitability as a readout device for six-axis platform control, the SSA has other potential applications where extremely quiet platforms are required. For example, the seismic noise on even the quietest passively-stabilized platforms exceeds the instrument noise of state-of-the-art conventional accelerometers. In order to be able to measure the instrument noise of these devices, one must stabilize the platform using accelerometers with lower noise than the devices under test. Another example is the stabilized platforms that will support the end masses in laser interferometer gravitational wave antennas such as LIGO (Robertson, 1991). The SSA could also be used as a sensitive inertial navigation system, which, when combined with a GPS receiver, could be used for gravity survey. Because the SSA gives acceleration in all six degrees of freedom, it appears feasible to extract the full gravity vector from the data. A paper giving a briefer, more intuitive description of the SSA and covering some of its applications is included as Appendix A.

2.1.2 Principle of operation

The key component of SSA is its proof mass, shown in Figure 1. It may be thought of as three orthogonal, intersecting square slabs of niobium (Nb). The proof mass fits into a housing with the same shape and slightly larger dimensions, so that when the proof mass is centered in the housing there is a ~ 0.3 mm gap between the two on all sides. On each inner surface of the housing (except the narrow cruciform ones), there are

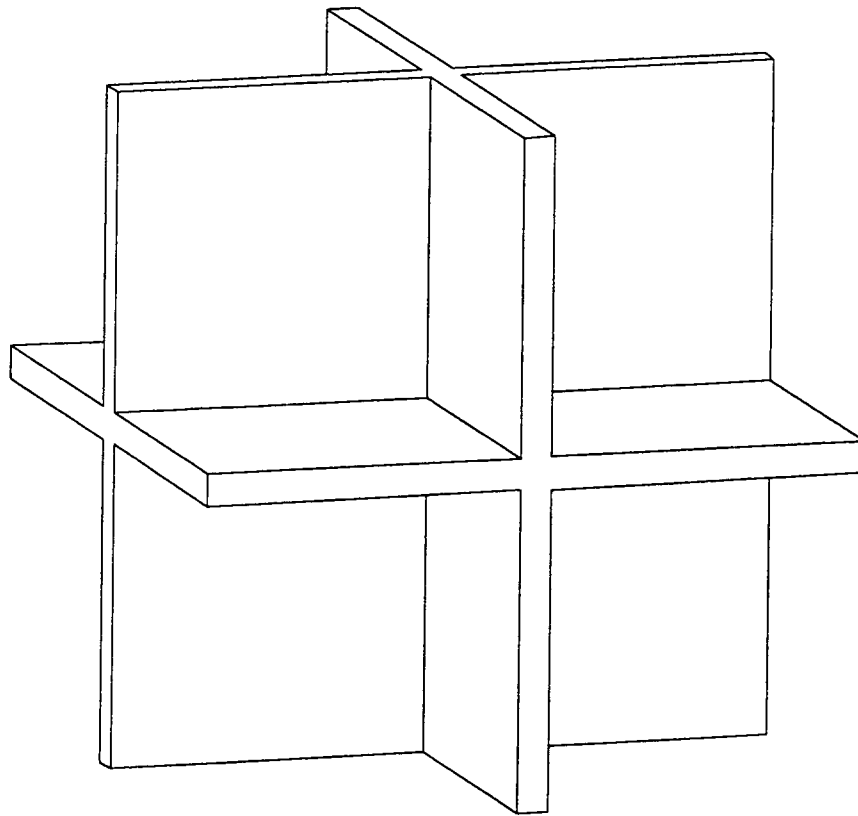


Figure 1: SSA proof mass. It consists of 3 orthogonal square slabs of niobium, 50.20 mm (1.976 in) on a side and 2.40 mm (0.094 in) thick. It is fabricated as a composite structure of four interlocking pieces.

one or two flat, spiral superconducting coils. The superconducting proof mass excludes all flux, confining the field to the gap. Consequently, the inductance of each coil is a function of the gap. Twenty-four of these coils are connected to form six four-coil inductance bridges. A transformer couples the signal from a sinusoidal current source across one diagonal of the bridge, and the input coil of a SQUID sensor is connected across the other diagonal. The inductance bridges are arranged so that, if the proof mass is centered, the inductances of the coils are equal (ignoring geometrical imperfections) and the bridges are all "balanced" — no oscillator current passes through the SQUID. If the proof mass is displaced in one degree of freedom, the mismatch in the inductors of the corresponding bridge circuit causes part of the oscillator current to pass through its SQUID. The output

of the SQUID is demodulated with a lock-in amplifier to produce a voltage proportional to the displacement of the proof mass.

Flux is excluded from the interior of superconductors because a field impinging on the body induces surface currents which screen the interior. The surface currents repel the currents that induced the field. Hence, by storing persistent current through coils below the proof mass, we can levitate it against gravity. By storing additional currents, we can also generate a torque on it. In versions of the device with two coils per face, the additional 24 coils are connected to form 6 circuits, each of which provides force (or torque) in a separate degree of freedom. In the version with only one coil per face, dc currents are stored through the proper arms of the sensing circuit to provide the levitation force. In both cases, each circuit also contains a transformer, through which a feedback current can be applied. A feedback controller uses the bridge output signal to generate the current necessary to center the proof mass.

2.2 Development History

2.2.1 Model I

The first version of the SSA was constructed under the previous contract (Paik et al., 1989). It had two coils on each interior surface. The 48 coils were connected to form 6 sensing and 6 levitation circuits. The coil forms were designed so that the sensing coils were slightly closer to the proof mass than the levitation coils. This provides some improvement in performance, because moving the levitation coils away from the proof mass reduces the effective spring constant, while moving the sensing coils closer improves the displacement sensitivity. Unfortunately, having two planes substantially complicated fabrication. Because of difficulties in trying to produce the coils with pure niobium wire, they were eventually wound with stronger niobium-titanium alloy wire. However, alloy superconductors are Type II, meaning they do not exhibit complete flux exclusion. Some flux creep, which can cause low frequency noise, is expected. The coil forms for this model were machined from Ti6Al4V, a standard titanium alloy. Perhaps because of some unusual heat treatment, the particular batch used for the coil forms had an anomalously high superconducting transition temperature, slightly greater than the bath temperature. Because a coil on a superconducting form produces almost no levitation field, the device had the mildly annoying feature that it required a heater and a temperature controller. For economy, the first version used only a single SQUID coupled to all 6 levitation circuits in series. Different circuits were driven at different frequencies. However, the drive frequencies must be separated by more than twice the desired accelerometer bandwidth, so the highest frequency must be more than twelve times that bandwidth above the lowest. Unfortunately, commercially available SQUIDs are slow rate limited above approximately 100 Hz. The maximum tolerable signal amplitude drops rapidly with frequency above this. In addition, having all the circuits connected together allowed resonances that were difficult to disentangle.

In spite of these difficulties, Model I ran successfully, demonstrating levitation and sensing in all six degrees of freedom. Many of the essential results of these tests have been reported previously. However, substantial additional testing was performed. The transfer function matrix, including in-line (diagonal) and cross coupling (off-diagonal) terms, was measured and found to match the calculated transfer function matrix quite well. A set of simple single-input, single-output (SISO) PID (proportional, integral, differential) controllers was built and tested, and closed-loop transfer functions were measured for individual axes. From the analysis of the transfer function matrix, a theoretical design of a more sophisticated controller was developed. This multiple-input, multiple-output controller (MIMO) would strongly suppress the cross-terms in the closed-loop transfer function matrix, as well as increasing the bandwidth and the damping of the in-line terms.

2.2.2 Model II

At the start of the period, the primary goal of the SSA project was the development of a device suitable for six-axis platform control on the Superconducting Gravity Gradiometer Mission (SGGM). In the SGGM, a satellite containing an advanced SGG was to be placed in a low Earth orbit to map the gravity field of the entire globe with high accuracy (~ 2 mgal) and fine spatial resolution (50 - 100 km). For space missions, high reliability and high sensitivity are the major concerns. It was realized that the number of coils could be reduced by a factor of two, and the number of connections by almost as much, if additional heat switches were added to the sensing circuit to allow dc levitation current to be stored in the proper path. Also, since this scheme used only one coil per coil form face, the entire area could be used for sensing, which increases the sensitivity. Although the high currents needed in a terrestrial laboratory test would produce additional error terms in this device, in orbit, where much smaller currents would be required, these would not be as significant.

Modeling of the proof mass dynamics indicated that the open loop transfer function matrix is similar to that of the first version, except that an additional set of off-diagonal elements appear. Although these terms are somewhat larger than the other off-diagonal terms, further calculation indicated that a modification of the control design would suppress them sufficiently in the closed-loop transfer functions.

In constructing the second version of the device, we incorporated some of the improvements suggested by tests of the previous version. The coil forms were machined from TiZr alloy, which was measured to have a T_c well below the operating temperature of the device. Separate SQUIDs were used for each sensing circuit. In order to avoid the possibility of drifts caused by flux creep, it was decided that the coils would be made from pure niobium. However, in spite of significant work to improve the quality, wire breakage continued to hamper progress. Finally, we invented a new type of wire, with a NbTi core and a Nb cladding. Since currents travel on the surface of a superconductor, the electrical properties are determined by the cladding, but the mechanical properties of this composite wire should be dominated by the strong NbTi core.

2.2.3 Model Ib

At this point, the immediate goals of the SGG program had shifted to the demonstration of airborne gravity survey. In aerial survey the amplitude of platform motion is quite large, and the need for a sensitive motion sensor is even more pressing. However, in this application, where large currents are needed to cancel the one g_E field, the accelerometer scheme with separate levitation and sensing circuits has important advantages. For example, when large levitation currents are used, large sensing currents are needed to achieve high coupling. With large ac currents, low frequency amplitude noise, which couples through coil mismatch, becomes a significant problem. The effect is much smaller with separate levitation and sensing circuits. Since we were about to rewind the coils with

the new composite wire, we decided to rewind them with separate levitation and sensing coils.

The latest version of the SSA, in addition to the new composite wire, had several other enhancements. The feedback transformers were redesigned to reduce the resonance frequency of the translational axes. The relative polarity of the levitation and sensing coils on each face was measured and the circuits were wired in such a way as to cancel the effect of mutual inductance. A more compact design for the connection box was produced. On the translational circuits, Quantum Design rf SQUIDs were replaced by BTI rf SQUIDs, which showed greater immunity to rf interference in the SGG. A set of more stable voltage-to-current converters were produced for exciting the bridge. After some additional improvement in the theoretical design, a very stable, low-noise analog implementation of the controller design was built.

2.3 Mechanical Elements

2.3.1 SSA Sensor package

The components of the present SSA sensor are shown in Figure 2. The overall size is determined by the precision mounting cube, 101.60 mm (4.000 in) on a side, which is identical to the one used in the SGG. Six identical niobium pieces, which fit into holes

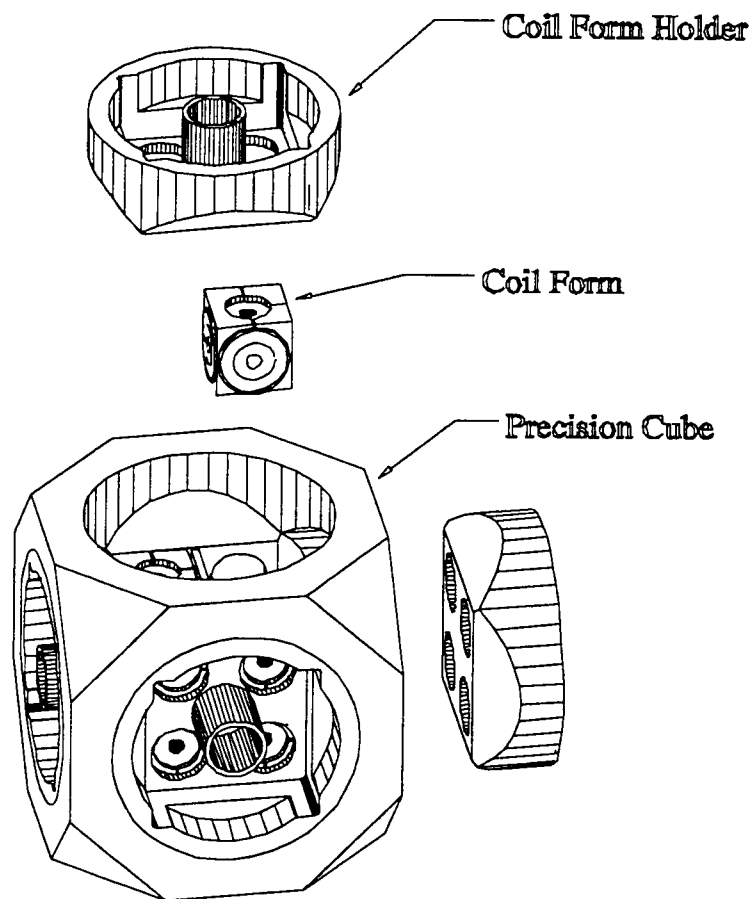


Figure 2: Components of the SSA sensor, shown partially disassembled. The precision cube is 101.60 mm (4.000 in) on a side. A niobium coil form holder fits into the hole on each face of the precision cube. They form a cubical cavity 50.80 mm (2.000 in) on a side. The cubical coil forms fit into the eight corners of this cavity. They in turn form a cavity in the shape of the proof mass, but 0.6 mm (0.024 in) larger in all dimensions. There are single layer spiral coils on all interior faces of the coil forms.

bored in the center of each face of the mounting cube, create the cubical enclosure, 50.8 mm (2.000 in) on a side, that houses the coil forms and the proof mass. The eight coil forms fit into the corners of enclosure, forming a cavity that fits around the proof mass with a ~ 0.3 mm (0.012 in) gap. Two flat, spiral, single layer coils are wound concentrically on each interior face of the proof mass. The inner coil is used for displacement sensing and the outer coil is used for levitation. Four interlocking plates 2.36 mm (0.093 in) thick form the proof mass, which sits at the center of the device.

2.3.2 Materials considerations

In almost any sophisticated device, proper operation depends critically on the proper choice of materials. The precision mounting cube must be stiff, to minimize deflection under the weight of the gradiometer accelerometers. It is also useful that it be hard, so that it can easily be ground to give the high degree of parallelism and orthogonality required to minimize errors in the gradiometer. For this reason, it is made of Ti6Al4V, a standard aerospace alloy. The coil forms are also of titanium alloy because of the unusually high resistivity of titanium alloys. Because the ac displacement sensing scheme of the SSA requires its input to be continuously connected to external electronics, it was feared that the rf noise coupled through these connections would interfere with the operation of the very rf-sensitive SQUIDs. For this reason, the coil forms of the SSA are metal rather than ceramic, as is used in the SGG. However, a very resistive metal is needed so that the dissipation is low at the bridge drive frequency. Titanium alloys are among the most resistive of common structural metals. The thermal contraction of titanium alloy is also well matched to that of niobium. As mentioned in Section 2.2.2, the original Ti6Al4V alloy was replaced by Ti36Zr, which has a lower superconducting transition temperature.

Most other elements of the SSA sensor, including the enclosure walls, the proof mass, the junction boxes, and the wires that make up the circuits, are of niobium. Niobium is used because it is the material with the highest first critical field, H_{c1} , the maximum

field at which magnetic flux is completely excluded from the interior. Complete flux exclusion is used in the walls and the junction boxes to provide shielding at low frequencies, in the proof mass to allow stable levitation, and in the circuits to allow truly persistent currents. Both the yield strength and the ultimate strength of niobium increase substantially with decreasing temperature, but unfortunately, the yield strength rises more rapidly, so at some temperature, the metal will break before yielding. This is not a problem in the large structural elements of the SSA, but some of the fine wires suffer stress during cool down and will break if they are in the brittle state while cooling. The ductile-to-brittle transition temperature of niobium is strongly dependent on the concentration of interstitial impurities such as hydrogen and oxygen. Problems with wire breakage on the SSA and SGG have been traced to a change in the manufacturer's fabrication process in which they introduced an air anneal. Proper control of the fabrication greatly ameliorated this problem. To eliminate it entirely, a new type of wire was invented, as mentioned in Section 2.2.2, consisting of a NbTi core surrounded by a pure niobium cladding. Although there was no physical reason why the wire itself would not give the expected properties, it was not known whether good spot welds could be made with it. However, test welds with this wire exhibited higher critical currents (maximum superconducting current) than with either NbTi or pure Nb wire.

Several important improvements were made in the fabrication of the superconducting coils. In order improve adhesion and eliminate shorts to ground, the coil forms are now cleaned and etched using a process developed by the aerospace industry, and coated with an epoxy specifically developed for strong adhesion at cryogenic temperatures. After machining the layer to the correct height, the coils are wound on it. Both coils are wound in the same plane, as in the SGG; this greatly simplifies fabrication. Many additional improvements in the coil winding process have been made, so that the uniformity and matching of the coils are now limited by fluctuations in the diameter of the wire, a factor that is apparently difficult for the manufacturer to control with greater accuracy.

2.3.3 Ancillary hardware

A cryostat like the one shown schematically in Figure 3, provides the necessary environment for the operation of the SSA. The sensor is suspended in a vacuum can immersed in liquid helium. The vacuum isolates the SSA from thermal and acoustic noise associated with the boiling helium. Without gas in the gap, the damping of the proof mass motion is small enough that the associated Brownian motion noise is negligible compared

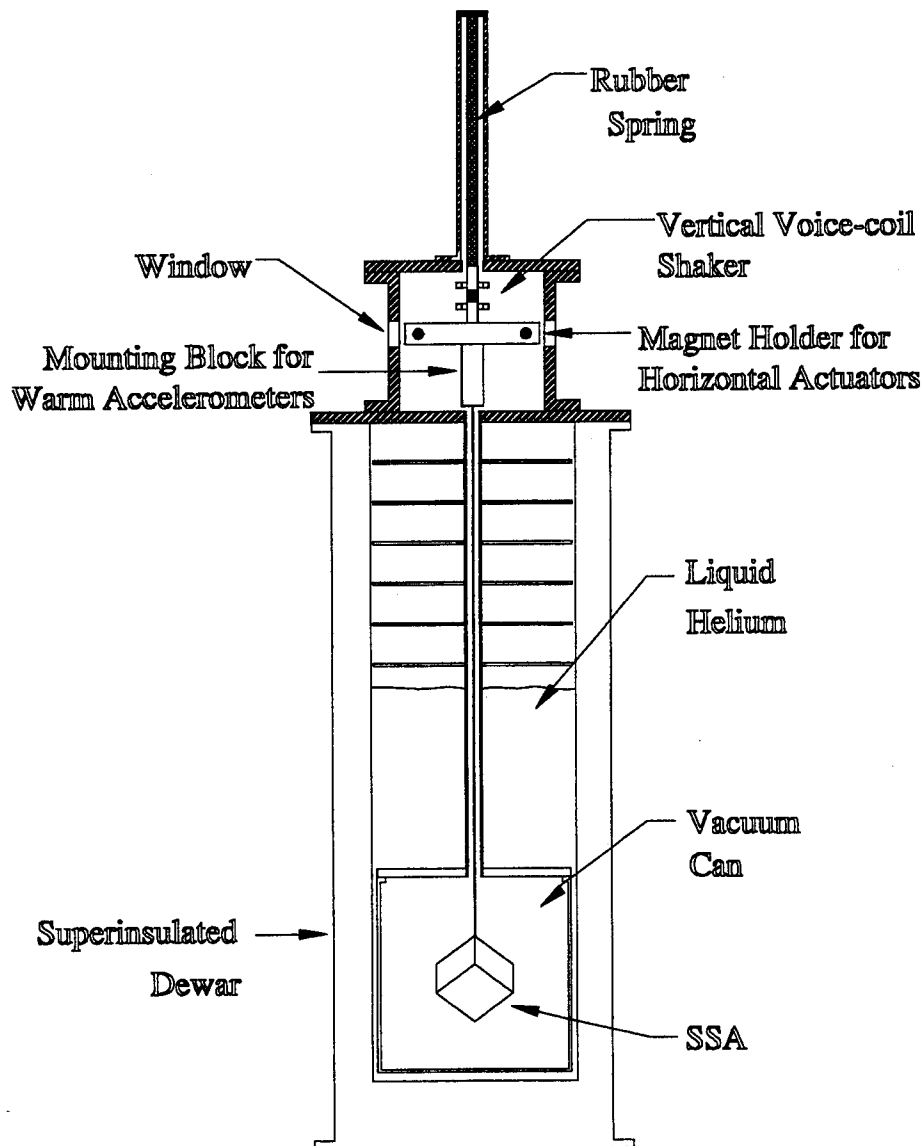


Figure 3: Schematic diagram of the SSA in its cryostat.

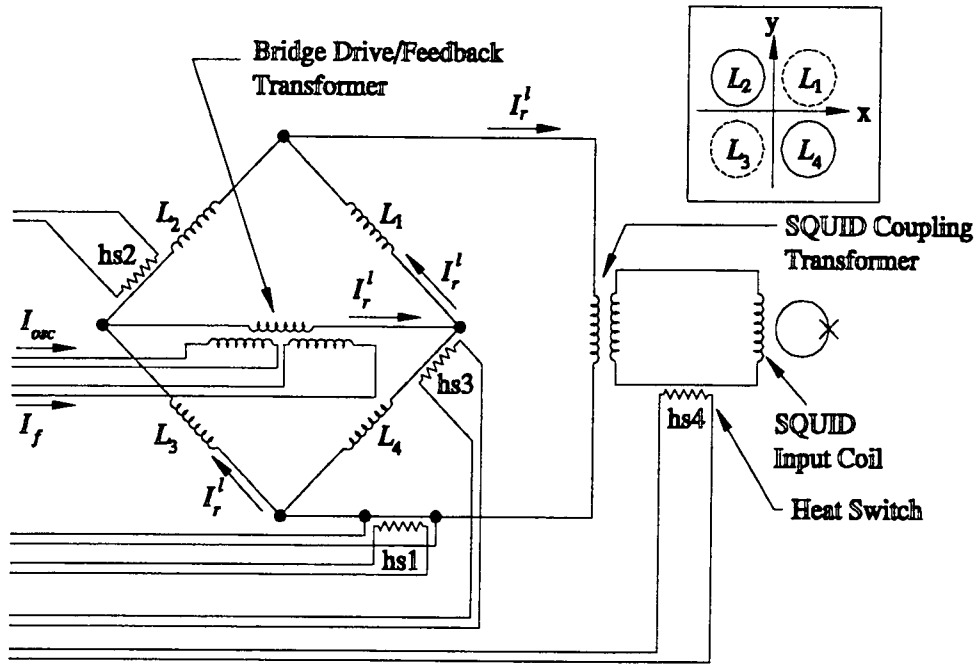
to the SQUID amplifier noise. The SSA is suspended by a long, stiff rod attached to a long rubber spring, which provides isolation, above its resonance frequency of 1.8 Hz, from the seismic noise of the laboratory floor. The presence of strong peaks in the seismic noise spectrum, particularly near the proof mass resonance frequency, would limit the achievable sensitivity if there were no seismic isolation. A set of three standard room temperature accelerometers (Sundstrand QA-900) mounted orthogonally in a block between the rubber spring and the suspension rod allow an approximate calibration of the device. Also attached to this block is a horizontal aluminum cross with permanent magnets mounted on the end of each of the four arms. The cross member and accelerometer mounting block are suspended from the rubber spring by an aluminum shaft that holds a fifth permanent magnet. A pair of Helmholtz coils is centered around each magnet, and fixed to the dewar. Each magnet and coil set form a voice-coil actuator. With the five actuators, the block can be shaken vertically, rotated about the vertical axis, and, well below the pendulum frequency, translated in the two horizontal directions.

2.4 Levitation and Proof Mass Dynamics

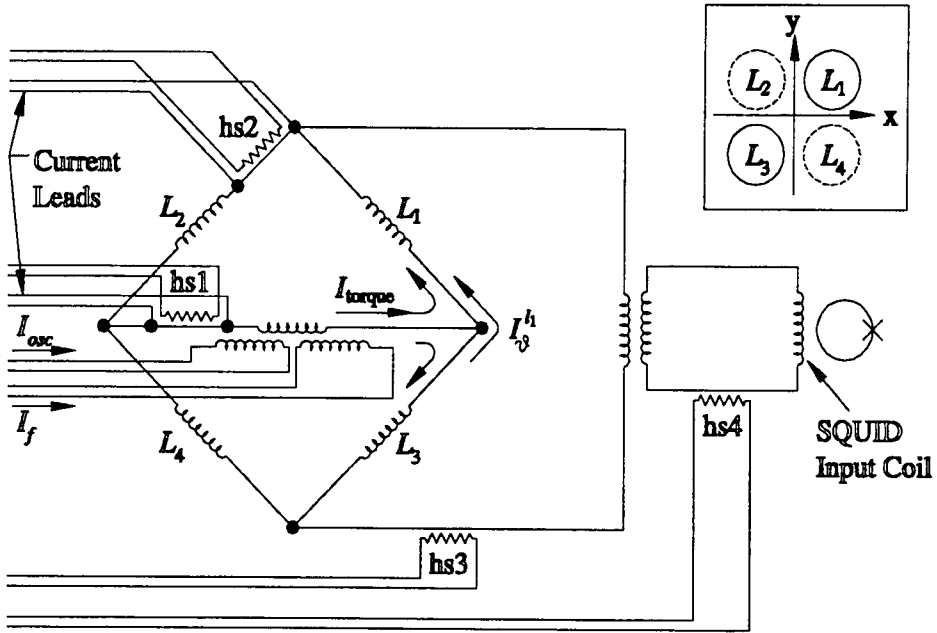
2.4.1 Dynamics of Model II

Although the Model II SSA uses the same mechanical components as the Model I and Ib, and a displacement sensing circuit almost identical to that of Model Ib, its levitation scheme, and thus the dynamics of the proof mass, are different. Figures 4a and b show the sensing/levitation circuits for the translational and rotational degrees of freedom, respectively. The circuits are identical except for the placement of heat switches and for the relative location of the coils. The small inset in Figure 4a shows the location of the coils in the z translational circuit. The two coils on the upper ($+z$) side of the proof mass, L_2 and L_4 , are represented by solid circles, and the two coils on the lower ($-z$) side of the proof mass, L_1 and L_3 , are represented by dashed circles. The subscripts correspond to the number of the quadrant in the xy plane. To levitate the proof mass, current is applied through the current leads while heat switches 2, 3, and 4 are held open to prevent current from flowing through the upper coils and the SQUID input coil. Then heat switch 1 is momentarily held open to force the current to flow along the desired path. After heat switch 1 cools, the current source is removed and the power to the other heat switches is turned off. As the figure shows, the feedback current, I_f , adds to the levitation current through the same transformer that couples the sensing current into the bridge. The transformer has separate primaries for the sensing and feedback currents because different turns ratios are required. This scheme also avoids the need for precisely adding two quite different signals with warm electronics.

Applying a torque with the rotational circuit is slightly more complicated. We must first hold open heat switches 1, 3 and 4 in Figure 4b and store the current $I_0^{I_1}$ using heat switch 2 and the associated current leads. This is a bias current which produces no dc force on the proof mass because an equal current flows through all four coils. Holding open heat switches 3 and 4 while storing current with heat switch 1 and the associated



a) Translational



b) Rotational

Figure 4: Sensing/levitation circuit for the Model II SSA. $hs1, \dots, hs4$ denote the four heat switches and L_1, \dots, L_4 denote the four sensing/levitation coils. The inset in each figure shows the relative location of the coils in the xy plane. Dashed circles represent coils below the proof mass, and solid circles represent coils above it.

current leads then produces a torquing current, I_{torque} . If the currents have the senses shown in the figure, I_{torque} adds to I_{θ}^1 through coils L_1 and L_2 and subtracts from it through coils L_3 and L_4 . By considering the relative positions of the coils shown in the inset of the figure, it can be seen that increasing the current through coils L_1 and L_2 increases the torque in the right-handed sense about the y axis, while increasing the current through coils L_3 and L_4 increases the torque in the left-handed sense. Thus, I_{torque} as shown in the figure produces a net torque about the y axis in the right-handed sense. As with the translational circuit, the feedback current and sensing current couple to the circuit through the same transformer.

From these circuits we can extract the proof mass dynamics. The linearized equations of motion of a proof mass inside a housing were derived in Parke (1990). The equations may be written

$$\ddot{\mathbf{r}} + \frac{\nabla_r V}{\mathbf{m}} = \begin{pmatrix} \mathbf{a} \\ \boldsymbol{\alpha} \end{pmatrix}, \quad (2-1)$$

where the 3-vectors \mathbf{a} and $\boldsymbol{\alpha}$ are given by

$$\begin{aligned} \mathbf{a} &= -\ddot{\mathbf{r}}^H - 2\boldsymbol{\omega}^H \times \dot{\mathbf{r}}^P - \dot{\boldsymbol{\omega}}^H \times \mathbf{r}^P - \boldsymbol{\omega}^H \times (\boldsymbol{\omega}^H \times \mathbf{r}^P) - \nabla\phi, \\ \boldsymbol{\alpha} &= -\dot{\boldsymbol{\omega}}^H - \frac{1}{2}\boldsymbol{\omega}^H \times \dot{\boldsymbol{\theta}}^P + \dot{\boldsymbol{\omega}}^H \times \boldsymbol{\theta}^P, \end{aligned} \quad (2-2)$$

and where

- \mathbf{r}^H = the position of the housing with respect to the origin of the inertial reference frame,
- \mathbf{r}^P = the position of the proof mass with respect to the housing,
- $\boldsymbol{\omega}^H$ = the angular velocity of the housing with respect to inertial reference frame,
- $\boldsymbol{\omega}^P$ = the angular velocity of the proof mass with respect to the housing,
- $\boldsymbol{\theta}^P$ = the angular position of the proof mass with respect to the housing (It is related to the rotation matrix \mathbf{R}^P through $\mathbf{R}^P = e^{\boldsymbol{\theta}^P \cdot \mathbf{J}}$, where \mathbf{J} is generator of the antisymmetric matrix.),

$\mathbf{m} = \{ m, m, m, J, J, J \}^T$, where m is the mass of the proof mass and J is its moment of inertia (It is assumed that the principal axes of the proof mass coincide with the axes of the proof mass frame of reference, and that the body is symmetric, so all three diagonal components of the moment of inertia tensor are equal.),

$\mathbf{r} = \begin{pmatrix} \mathbf{r}^P \\ \boldsymbol{\theta}^P \end{pmatrix}$, a 6-vector describing the position and orientation of the proof mass with respect to the housing,

V = the potential energy internal to the accelerometer.

Note that the division symbol in Eq. (2-1) represents term-by-term division (i.e. $\mathbf{c} = \mathbf{a} / \mathbf{b}$ implies $c_i = a_i / b_i$.) In the SSA, V is electromagnetic potential energy due to the current flowing within the device. Because the circuits in the Model II SSA are different from those of the Model I SSA, V will be different.

Calculation of the potential V , though tedious, is conceptually simple. For the sake of brevity, we will ignore the effect of the sensing current, which would appear only as an additional term in the expression for the resonance frequency. In reality, technical considerations constrain the sensing currents to values low enough that they have no significant effects on the dynamics. Solving the circuit equations (current conservation into nodes, flux conservation through loops) gives a set of equations for the current in each branch, I_i , in terms of the inductances, L_i , and the initial currents and inductances, L_{0i} and I_{0i} , respectively, when the proof mass is centered in the housing. Here $i \in \{1, 2, 3, 4, \text{tran}, \text{SQUID}\}$, where L_1, \dots, L_4 are as shown in Figure 4, L_{tran} is the secondary inductance of the bridge drive/feedback transformer, and L_{SQUID} is the effective inductance of the SQUID input coil, as reflected through the matching transformer. The potential energy due to the currents in the circuit is then simply $\sum_{i=1}^6 L_i I_i$. The inductances of the sensing/levitation coils are a function of proof mass position. This functional dependence is approximated as an expansion about the centered inductance:

$$L = L_0 + \lambda x - \frac{\gamma}{2} x^2 - \frac{\beta}{2} \theta^2, \quad (2-3)$$

where λ , γ , and β are coefficients. The displacement of the center of the coil, x , in the coordinate system of the proof mass, is related to the proof mass position and orientation by

$$\mathbf{x} = (\mathbf{R}^P)^{-1} (\mathbf{x}'_0 - \mathbf{r}^P). \quad (2-4)$$

Here \mathbf{x}'_0 is the position of the coil in the housing reference frame. Substituting Eq. (2-3) into the expression for the potential energy of each circuit, then substituting the proper components of \mathbf{x} (from Eq. (2-4)) and θ^P into the result, and summing over all the circuits yields a rather lengthy expression for V in terms of the proof mass position and orientation. Performing a Taylor expansion of this to second order gives an expression of the form

$$V = v_0 + \mathbf{r} \cdot \mathbf{v}_1 + \mathbf{r} \cdot \mathbf{V}_2 \cdot \mathbf{r}, \quad (2-5)$$

where v_0 is a scalar, \mathbf{v}_1 is a 6-vector, and \mathbf{V}_2 is a 6×6 matrix.

The expression for the potential, Eq. (2-5), can then be substituted in the equations of motion, Eq. (2-1). After some rearrangement, this gives

$$\ddot{\mathbf{r}} + \boldsymbol{\Omega} \cdot \mathbf{r} = \begin{pmatrix} \mathbf{a} \\ \boldsymbol{\alpha} \end{pmatrix} - \mathbf{v}_1 \quad (2-6)$$

This is just a somewhat generalized form of the equation for a harmonic oscillator. The vector \mathbf{v}_1 gives a set of constant forces: $\mathbf{v}_1 = \{ f_{DC}, f_{DC}, f_{DC}, 0, 0, 0 \}^T$, where $f_{DC} = \Lambda(I_r^l)^2$. The translational levitation current, I_r^l , is chosen so that f_{DC} cancels the component of the gravity vector along each axis. (Here, f_{DC} is taken to be equal for all three axes, but in reality they will differ because of imperfect alignment of the SSA with respect to vertical.) In contrast to the Model I, in the Model II f_{DC} is independent of the bias current in the rotational circuits, because equal currents flow through the upper and lower coils in the rotational circuits when the proof mass is centered.

The matrix Ω can be written in terms of four blocks:

$$\Omega = \begin{pmatrix} \omega_r^2 \mathbf{I} & \frac{f_{DC}}{m} \mathbf{S} \\ -\frac{f_{DC}}{J} \mathbf{S} & (\omega_\theta^2 + \zeta) \mathbf{I} - \zeta \mathbf{1} \end{pmatrix}, \quad (2-7)$$

where

\mathbf{I} = 3×3 identity matrix,

$\mathbf{1}$ = 3×3 ones matrix,

$\mathbf{S} = \begin{pmatrix} 0 & -1 & 1 \\ 1 & 0 & -1 \\ -1 & 1 & 0 \end{pmatrix}$ is the unit anti-symmetric matrix,

$$\zeta = \frac{c^2}{J} \left(\frac{\Lambda^2}{L_0} + \gamma \right) (I_r^l)^2,$$

d = the proof mass - coil gap.

The origin of the housing coordinate system is fixed at the geometrical center of the SSA, and the planes formed by the axes are parallel to the coils. In this coordinate system, one of the coordinates of a coil center has magnitude equal to d plus half the proof mass thickness. The magnitude of the other two coordinates is c . The proof mass resonance frequencies in the translational and rotational degrees of freedom, ω_r and ω_θ respectively are given by

$$\omega_r^2 = \frac{1}{m} \left[\left(\frac{\Lambda^2(2L_0 + L_5 + L_6)}{(L_0 + L_5)(L_0 + L_6)} + \gamma \right) (I_r^l)^2 + \left(\frac{\Lambda^2}{L_0} + \frac{\gamma}{2} \right) (I_\theta^l)^2 \right], \quad (2-8)$$

$$\omega_\theta^2 = \frac{1}{J} \left[2 \left(\frac{c^2 \Lambda^2}{L_0} + d\Lambda + c^2 \gamma + \beta \right) (I_r^l)^2 + \left(\frac{c^2 \Lambda^2}{(L_0 + L_5)} + d\Lambda + c^2 \gamma + \beta \right) (I_\theta^l)^2 \right]. \quad (2-9)$$

Although computing the equations of motion is significantly more difficult for Model II than for Model I, the results are very similar. The most important difference is the appearance of the term ζ in the Ω matrix((Eq. 2-7). The presence of these off-

diagonal elements indicates an additional cross-coupling between rotational degrees of freedom.

The analysis presented above does not include the effect of the feedback current. If we add the feedback currents into the initial current through the transformer secondary, we get, after dropping all terms that are second order in \mathbf{r} or \mathbf{I}_f , an additional term in Eq. (2-6) of the form $\mathbf{K} \cdot \mathbf{I}_f$, where \mathbf{I}_f is the vector of feedback currents and \mathbf{K} is a diagonal matrix:

$$\mathbf{K} = \begin{pmatrix} k_r \mathbf{I} & \mathbf{0} \\ \mathbf{0} & k_\theta \mathbf{I} \end{pmatrix}, \quad (2-10)$$

where

$$k_r = \frac{4\Lambda_L \rho_r^f I_r^l}{m},$$

$$k_\theta = \frac{2c\Lambda_L \rho_\theta^f J_\theta^l}{J}.$$

Here, ρ_r^f and ρ_θ^f are the turns ratios of the translational and rotational feedback transformers, respectively.

2.4.2 Dynamics of Model I and Ib

One of the major benefits of operating the SSA in space is that the levitation currents can be greatly reduced, thereby reducing the resonance frequency, and greatly enhancing the sensitivity. For terrestrial operation, it is helpful to minimize the resonance frequency within the constraints of the design. For an SSA with separate sensing and levitation circuits, the resonance frequency in a translational degree of freedom is (Paik et al., 1989)

$$\omega_r^2 = \frac{4}{m} \left(\frac{4\Lambda^2}{4L_0 + L_{fb}} + \frac{\gamma}{2} \right) (I_r^l)^2, \quad (2-11)$$

where we have ignored the effect of the relatively small sensing currents and the rotational bias current. Note that we can reduce ω_r by making the secondary inductance of the feedback transformer, L_{fb} , larger, until the first term in Eq. (2-11) is small compared to the second. The design of the latest version of the SSA takes advantage of this fact: L_{fb} is chosen so that the first term is approximately one sixth the second.

To understand other factors that affect the resonance frequency, it is helpful to examine the simple case given by $\lim_{L_{fb} \rightarrow \infty} \omega_r^2$. The translational levitation current, I_r^l , is fixed by the requirement that the dc force that it generates exactly cancels the component of the proof mass weight along the sensitive axis, $mg_E \cos \phi$. Normally, the SSA is in "umbrella" orientation, such that $\cos \phi = 1/\sqrt{3}$ for all three axes. The force balance can be written as

$$f_{DC} = 2\Lambda(I_r^l)^2 = \frac{mg_E}{\sqrt{3}}. \quad (2-12)$$

Setting the first term to zero and substituting Eq. (2-12) gives an expression for the minimum resonance frequency in the limit of very large L_{fb} :

$$\omega_r^2 = \frac{g_E \gamma}{\sqrt{3} \Lambda}. \quad (2-13)$$

Equation (2-13) has the form of the pendulum frequency equation, with an effective pendulum length of $\xi = \Lambda/\gamma$. Thus, to reduce the resonance frequency further, ξ must be maximized. One way is increase the gap, d , because ξ increases monotonically with d . However, displacement sensitivity decreases with increasing gap. Furthermore, because the coils are arranged on the surfaces of a cube, increasing d (while keeping the coil diameter fixed) reduces the distance between the edges of coils on different faces of the cube. This distance must be large compared to d to keep the inductive coupling between circuits small.

Given the constraints on dimensions, the only other obvious way of decreasing ω , is by changing the coil shape. The effect of shape can be explored in a limited way using a simple model: If the proof mass is represented by an infinite superconducting plane, and the turns of the coil are represented by circular current rings in a parallel plane a distance d away, then the force between them is equal to the force between the current rings and a set of image rings in a plane a distance d on the other side of the superconducting plane. This model does not take into account the finite thickness of the wire, and the redistribution of current along its surface, but these effects are only important when the gap is smaller than about twice the wire diameter. The model also does not include the effect of the enclosure walls, which confine the field to a cubical cavity. However, if d is small compared to the minimum distance between the walls and the outermost turn of the coil, the model should be reasonably accurate. Inclusion of the effect of the walls would require finite element analysis software. Under the assumptions of the simple model, Λ is twice the force between the current rings and their images, divided by the current squared. Summing the equation for the force between coaxial rings (Smythe, 1989) over all the rings and image rings, we obtain

$$\Lambda = \sum_i \sum_j 2\mu_0 d \sqrt{\frac{m}{r_i r_j}} \left[-K(m) + \frac{E(m)(m-2)}{2(m-1)} \right]. \quad (2-14)$$

Differentiating with respect to d yields

$$\gamma = \sum_i \sum_j \frac{\mu_0 m}{(m-1)r_i^2 r_j^2 \sqrt{\frac{m}{r_i r_j}}} \{ [(m-1)(m-2)r_i r_j - 2m(m^2 - m + 1)d^2] E(m) \\ + (m-1)[2(1-m)r_i r_j + m(m-2)d^2] K(m) \}, \quad (2-15)$$

where

$$m = \frac{4r_i r_j}{(r_i + r_j)^2 + (2d)^2}$$

and $K(m)$ and $E(m)$ are the complete elliptic integrals of the first and second kinds, respectively. The r_i and r_j are the radii of the current rings and their images, respectively.

Equations (2-13), (2-14), and (2-15) can be used to calculate the minimum resonance frequency as a function of d for different coil cross sections.

Figure 5 shows the results of such a calculation for three different coil shapes: a single-layer flat coil, a single-layer solenoid, and a coil with a square cross-section (i.e., having equal numbers of turns in the radial and axial directions.) In all cases, the number of turns and the outside diameter were the same. As can be seen from the figure, these very different coil shapes give values of ξ that differ by at most a factor of two, suggesting that ξ is not a sensitive function of coil geometry. A more thorough study would be needed to confirm this for the general case, but these results for easily manufacturable shapes are sufficient to conclude that there is little to be gained from changing the shape of the

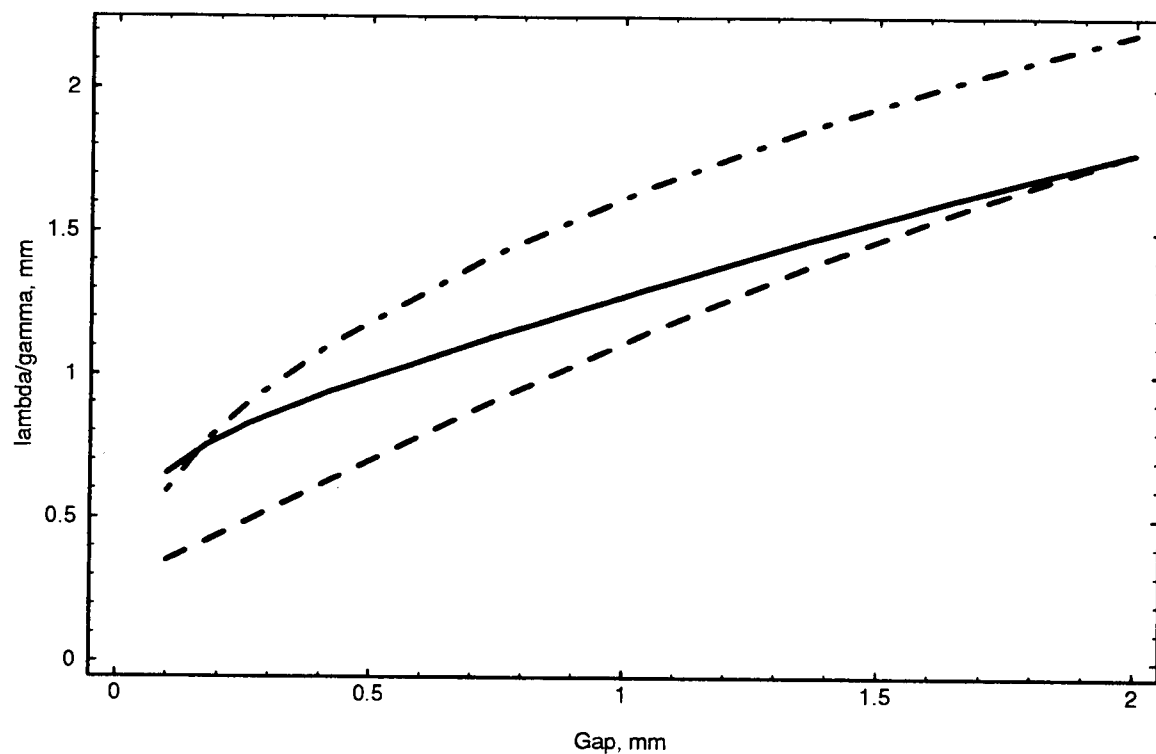


Figure 5. Effect of coil shape on minimum resonance frequency.

Solid line: single-layer flat coil.

Dashed line: square cross-section coil.

Dash-dot line: single-layer cylindrical coil.

levitation coils. For this reason, the levitation coils on the most recent version of the SSA are single-layer spirals.

A comparison of the calculated and measured resonance frequencies and levitation currents would provide a good check of the accuracy of our model. However, as discussed in Section 2.7, because of imperfect mating of the pieces making up the enclosure walls, the gap, d , differs from the design value and from axis to axis. Furthermore, d is difficult to measure accurately. Therefore, it is better to perform a consistency check. Using the measured values of I_r^l and I_θ^l , we first calculate the value of d for each axis by solving the force balance equation,

$$2\Lambda(d) \left[(I_r^l)^2 - (I_\theta^l)^2 \right] = \frac{mg_E}{\sqrt{3}} \quad (2-16)$$

for d (with $\Lambda(d)$ given by Eq. (2-14), using a numerical root finding scheme. Substituting these values into Eq. (2-15) and Eq. (2-11) then gives the predicted values of the resonance frequencies. Table 1 shows the results of these computations for the most recent version of the SSA, and a comparison with the measured values.

On average, the measured resonance frequencies are less than 6% above the predicted values, primarily because the model does not take into account the fact that the

	r_x	r_y	r_z
I_r^l (measured), A	4.9351	5.5640	5.4414
I_θ^l (measured), A	0.0000	2.1240	2.0000
d , μm	357	455	416
$\omega/2\pi$ (calculated), Hz	12.21	15.94	16.05
$\omega/2\pi$ (measured), Hz	13.31	16.84	16.31

Table 1. Values of the gap inferred from a particular configuration of currents in the translational circuits, and the resulting resonance frequencies.

field is confined by the walls of the enclosure. The scatter in the ratio $\omega_{\text{measured}}/\omega_{\text{calculated}}$ is most likely due to imperfections in the alignment of the SSA with vertical, as well as mismatch between the inductance parameters of sets of coils caused by the variation of the wire diameter.

2.5 Displacement Sensing

2.5.1 Model Ib: design

In designing the sensing circuits for the most recent SSA, a number of considerations were taken into account, and several changes were made to the original design. A schematic diagram of the sensing circuit is shown in Figure 6. A comparison of this circuit with that of the sensing circuit of the original SSA shows two obvious changes. First, the bridge circuit of each axis now has its own SQUID. By reducing the coupling between channels, it is hoped that the spacing between bridge modulation frequencies can be reduced, or that the same frequency can be used by more than one bridge, thus decreasing the maximum modulation frequency. As mentioned in Section 2.2.1, the dynamic range of the SQUIDs presently used decreases with frequency, so decreasing the maximum modulation frequency improves the dynamic range of the corresponding axes. The second change to the circuit is that the current drive of the new circuits is nonresonant; the capacitor across the primary of the bridge drive transformer has been removed. The resonant bridge drive provided some additional gain in the drive current. However, the gain was strongly frequency dependent and difficult to calculate accurately. In addition,

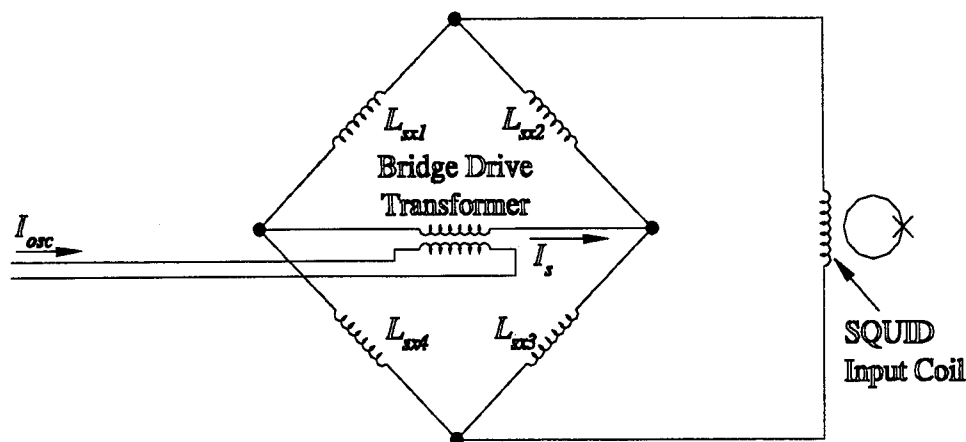


Figure 6: Model Ib sensing circuit. The orientation of the coils in the translational and rotational circuits are as shown in the insets of Figure 4a and b, respectively.

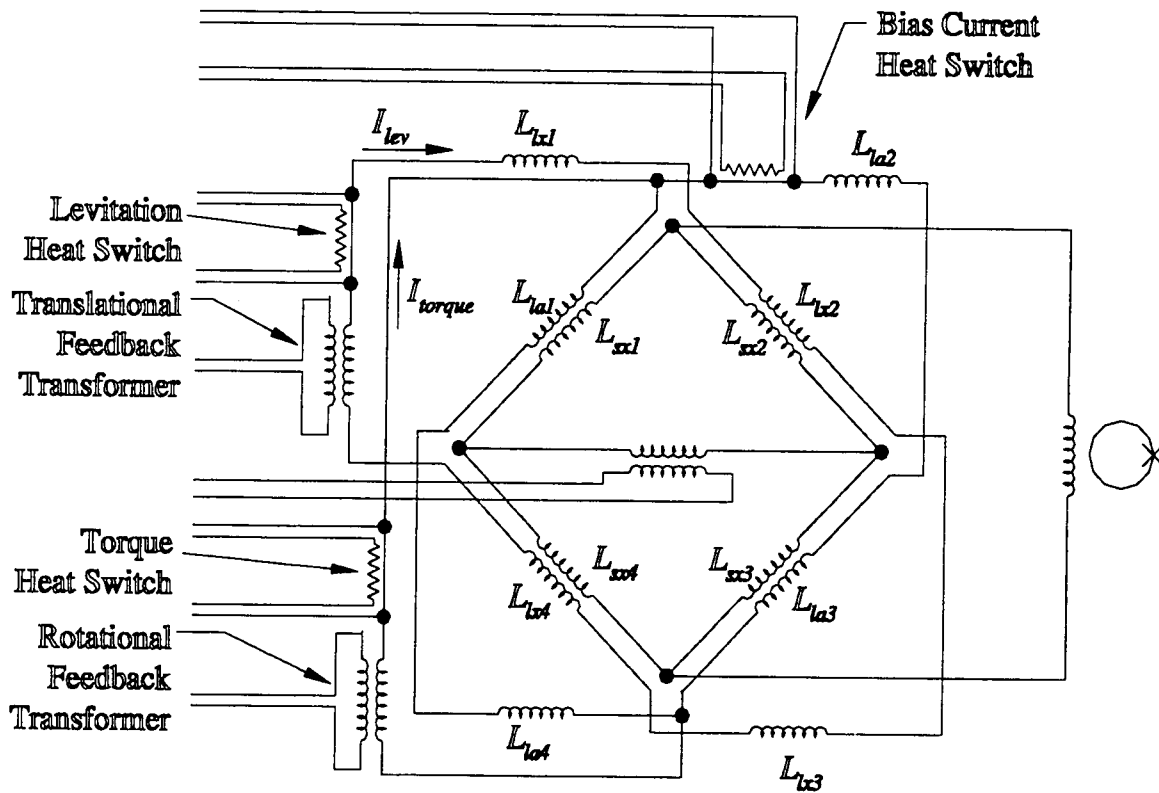


Figure 7: Translational sensing circuit for the Model Ib SSA, including coupling to levitation circuits.

achieving a large drive current is not a problem — other factors limit the amount of drive current to less than the maximum amplitude of a voltage-to-current converter. Furthermore, the nonresonant circuit is more flexible, easier to operate, and easier to analyze because the amplitude and phase of the drive current are weakly dependent on frequency over the range of frequencies normally used. The remaining frequency dependence comes from the resistance of the core of the bridge drive transformer.

Figure 6 shows an ideal circuit. Because the sensing and levitation coils are in close proximity, there is some mutual inductance between them. Figure 7 shows the circuit including the effect of the mutual inductance. The coupling between the sensing and levitation circuits has two effects. First, when persistent currents are stored in the levitation circuit, they will induce some dc current in the sensing circuit, which will be

modulated by the motion of the proof masses with respect to the sensing coils. Second, changes in the levitation current due to motion of the proof mass with respect to the levitation coils will induce corresponding currents in the sensing circuit. Both effects produce a low frequency signal at the SQUID, particularly near the resonance frequencies of the proof mass motion. The first effect can be removed by putting heat switches in each branch of the sensing circuit, so that the dc current can be purged. However, this does not eliminate the second coupling mechanism. In addition, heat switches add parasitic inductance, worsening the inherent misbalance of the bridge. If the low frequency signal is small enough that it does not overload the SQUID, it can be removed in the lock-in amplifier with a high pass filter. Such a filter, though, will add phase shift, which can cause difficulty for the controller.

The mutual inductance between the levitation and sensing coils can be calculated in the same way as Λ and γ (Eq. (2-14) and (2-15)), by modeling the coils as sets of concentric current rings and the proof mass as an infinite superconducting plane. Again, this configuration is equivalent to a set of rings and their mirror images. The image rings are in a plane parallel to, and a distance $2d$ from, the plane of the coils. In this case, however, there are two coplanar sets of rings. Summing the expression for the mutual inductance between 2 coaxial rings (Smythe, 1989) over all the levitation rings and their images for each sensing ring, and taking into account the negative sense of the image currents gives the total mutual inductance between the coils,

$$M = \sum_i \sum_j 2\mu_0 \left\{ \sqrt{\frac{r_{s,i} r_{l,j}}{m(0)}} \left[\left(1 - \frac{m(0)}{2} \right) K(m(0)) - E(m(0)) \right] - \sqrt{\frac{r_{s,i} r_{l,j}}{m(2d)}} \left[\left(1 - \frac{m(2d)}{2} \right) K(m(2d)) - E(m(2d)) \right] \right\}, \quad (2-17)$$

where

$$m(z) = \frac{4r_{s,i} r_{l,j}}{(r_{s,i} + r_{l,j})^2 + z^2},$$

and z is the separation of the two planes of the two rings. The summation over i runs over all the turns of the sensing coil and the summation over j runs over all the turns of the levitation coil. Written in terms of the coupling constant, $k = M/\sqrt{L_s L_l}$, and using the values of d from Table 1 in Eq. (2-17) yields $k = 0.087, 0.096$, and 0.104 , for the r_x, r_y , and r_z axis, respectively. The SGG also has coil forms with two coils, but these coils are separated by a small "dummy" coil. Making the width of the dummy coil several times the coil-proof mass gap reduces this coupling by more than an order of magnitude. However, the ratio of the gap to the coil form radius is several times smaller for the SSA, so an equivalent dummy coil would take up a much larger fraction of the available surface area. Because of this and the substantial additional cost of the more complex design, this concept was not used in the present version of the SSA.

There is another way of removing the coupling to the levitation circuit: By keeping track of the polarity of the mutual inductance between the two coils on each face, one can assemble the levitation circuits so that for each pair of coils that are coupled to a sensing circuit, the polarities have opposite senses. In this way, the induced currents cancel, to the degree that the mutual inductances match. This scheme works simply for the coupling to the levitation circuit. In the rotational levitation circuit, the bias current through each coil is the same, so its effect will cancel. The torquing current, though, has opposite polarity in the two branches of the circuit, and so its coupling to the sensing circuit will not cancel. Fortunately, the dc torquing current are small compared to the levitation and bias currents. (If the SSA were dimensionally perfect and the coils were perfectly matched, then no dc torquing currents would be needed.) In recent tests, this coupling caused a signal at the proof mass resonance on the order of $20 \mu\text{A}$. For the BTI SQUIDs, this is a substantial fraction of the maximum low frequency amplitude, so good isolation at the proof mass resonance frequency is necessary to avoid saturating the SQUID.

Most of the design parameters of the SSA are set by the geometry of the proof mass. One free parameter is the outer diameter of the sensing coils (which is also the inner diameter of the levitation coils). This parameter can be set to minimize the sensing current

needed to achieve optimum coupling. The accelerometer reaches optimum coupling when the sensing current is raised to the point at which the spring constant, k_s , due to the sensing current, I_s , (the current through the secondary of the bridge drive transformer) equals the spring constant due to the levitation current, k_l :

$$k_s = k_l. \quad (2-18)$$

Increasing the sensing current beyond this point reduces the overall sensitivity because the response of the proof mass to acceleration declines faster with I_s than the displacement sensitivity increases. The translational spring constant due to levitation current is implied by Eq. (2-11). The levitation current is determined by the force balance condition, Eq. (2-12). Eliminating the levitation current, we obtain

$$k_l = \left(\frac{8\Lambda_l^2}{4L_0 + L_{fb}} + \gamma_l \right) \frac{mg_E}{\sqrt{3} \Lambda_l}. \quad (2-19)$$

The spring constant due to the sensing current can be obtained by summing the forces on the proof mass applied by the current in each sensing coil:

$$F_s = \sum_i \frac{-\text{sgn}_i(\Lambda_i - \gamma_i x_i)}{2} I_i^2, \quad (2-20)$$

where sgn_i is +1 if the coil is above the proof mass (if the component of the coil position normal to the plane of the coil is positive) and -1 if it is below. Solving the circuit equations (conservation of current at nodes, voltages around loops sum to zero) provides the current, I_i , through each coil i in terms of the inductances in the circuits and the currents I_{osc} through the primaries of the bridge drive transformers. Upon substituting Eq. (2-3) for the coil inductances, Eq. (2-4) for x_i in terms of the proof mass position and orientation, \mathbf{r} , yields a set of expressions for I_i as functions of \mathbf{r} . The results can be simplified if we express them as a function of the current through the transformer secondary, I_s . When the proof mass is centered ($\mathbf{r} = 0$),

$$I_s = \frac{L_{dr}}{L_{dr} + L_s} M I_{osc}. \quad (2-21)$$

L_{dr} is the inductances of the transformer secondary, L_s is the inductance of a sensing coil when the proof mass is centered, and M is the mutual inductance of the transformer. Substituting the expressions for I_l and Eq. (2-21) into Eq. (2-20), and taking the derivative with respect to one of the axes, we obtain an expression for the spring constant as a function of position and orientation. When the proof mass is centered ($\mathbf{r} = 0$), the expression for a translational spring constant simplifies to

$$k_s = \left(\frac{\Lambda_s^2}{L_{SQUID} + L_s} + \frac{\gamma_s}{2} \right) I_{s,r}^2 + \frac{\gamma_s}{2} I_{s,\theta}^2. \quad (2-22)$$

Assuming, for simplicity, that the sensing current in the angular circuits, $I_{s,\theta}$, has the same amplitude and phase as the sensing current in the translational circuits, $I_{s,r}$, substituting Eq. (2-19) and Eq. (2-22) into Eq. (2-18), and solving for the r.m.s. amplitude of I_s , we obtain

$$\langle I_{s,opt} \rangle = \sqrt{\frac{(L_{SQUID} + L_s) [8\Lambda_l^2 + \gamma_l(4L_0 + L_{fb})] mg_E}{(4L_0 + L_{fb}) [\Lambda_s^2 + \gamma_s(L_{SQUID} + L_s)] \sqrt{3} \Lambda_l}}. \quad (2-23)$$

It is important that $I_{s,opt}$ not be too large, for the fundamental reason that the field due to this current must not exceed the first critical field (to avoid a sharp increase in dissipation), as well as for the practical reason that it becomes more difficult to build a stable ac current source as the currents become much larger than 1 A. Note that, except for the proof mass weight, all the variables in Eq. (2-23) are purely functions of geometry. All the important dimensions are fixed by fundamental or practical considerations except the outer radius of the sensing coil, r_s , which is also the inner radius of the levitation coil. To see how $I_{s,opt}$ depends on the partition of the coil form area between levitation and sensing coils, we plot it as a function of this radius. Figure 8 shows this plot, with r_s ranging from the inner to the outer radius of the coil form. Note that there is a minimum at $r = 8.5$ mm, although there is relatively little change in $I_{s,opt}$ over the range $r_s = 6$ to 10 mm. The actual sensing coil outer radius, 6.32 mm, was chosen to be somewhat smaller than the radius at the minimum to reduce the required levitation current (which increases with increasing r_s .)

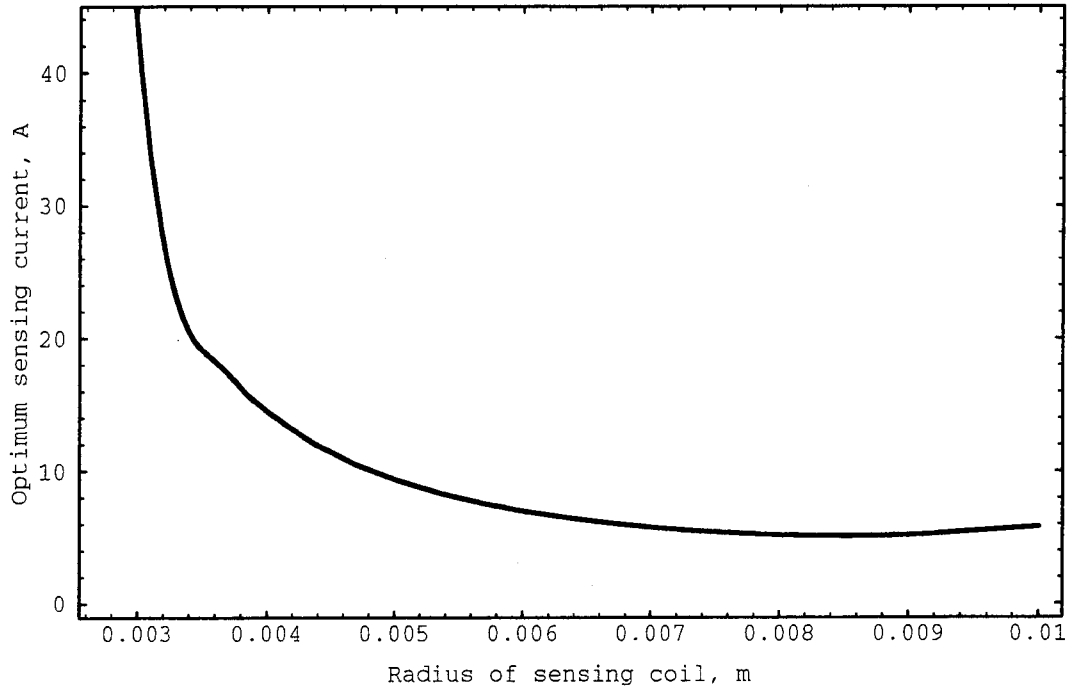


Figure 8. The optimum sensing current, the current that produces optimum coupling, as a function of the outer radius of the sensing coil.

The full expression for the force on the proof mass due to the sensing currents, F_s , from which we obtained Eq. (2-22) is rather lengthy, but reduces to zero when the proof mass is centered. However, this is only true under the assumption that the parameters L_s , Λ_s , and γ_s are equal for all the coils. In the real SSA, the wire-wound coils show significant variations in their dimensions, particularly the outer radius. For Λ and γ , the predominant error is in the diameter of the wire, which varies along its length because of limitations in the drawing and coating processes used by the manufacturer. Because of this, the outer radius varies by approximately $\pm 0.5\%$ from coil to coil. The parameter Λ can be approximated

$$\Lambda \approx \pi \mu_0 (r_{\text{outer}}^2 - r_{\text{inner}}^2) \left(\frac{N}{r_{\text{outer}} - r_{\text{inner}}} \right)^2. \quad (2-24)$$

The number of turns, N , and the inner radius, r_{inner} , can be controlled with good accuracy. From Eq. (2-24) we obtain

$$\frac{d\Lambda}{\Lambda} = \left(\frac{2r_{\text{inner}}r_{\text{outer}}}{r_{\text{outer}}^2 - r_{\text{inner}}^2} \right) \frac{dr_{\text{outer}}}{r_{\text{outer}}}. \quad (2-25)$$

For the Model Ib sensing coils, the value of the coefficient is 0.9, so the relative error in Λ is $\pm 0.5\%$. There is no equivalent simple expression for γ . Computations using Eq. (2-15) and Eq. (2-14) show that the coefficient relating the fractional error in γ to the fractional error in r_{outer} is about four times greater than for Λ .

Because of these variations in the coil diameter, the sensing current will apply a force to the proof mass. We can estimate its magnitude by considering the simple case of a proof mass confined to motion in one degree of freedom, with the coils on the lower side of the mass having Λ larger by a factor $1 + \epsilon$ than those on the upper. Dropping the quadratic terms, and approximating the inductance at $x = 0$ by $L_s \approx \Lambda d$, the inductances become

$$\begin{aligned} L_{\text{lower}} &= \Lambda(d+x) (1 + \epsilon), \text{ and} \\ L_{\text{upper}} &= \Lambda(d-x). \end{aligned} \quad (2-26)$$

As above, we solve the circuit equations to get expressions for the current through each branch of the circuit. Setting the expression for the current through the SQUID input coil to zero, substituting Eq. (2-26), and solving for x gives the displacement at which the bridge is balanced:

$$x = \frac{\epsilon d}{2 + \epsilon} \quad (2-27)$$

Again, we substitute the expressions for the current, as well as Eq. (2-21), into Eq. (2-20), to obtain the force as a function of position. Using Eq. (2-27) and performing a Taylor expansion, we find the force when the bridge is balanced:

$$F_s = \frac{\epsilon \Lambda}{4} I_s^2 + O[\epsilon^2]. \quad (2-28)$$

The current I_s is sinusoidal, $I_s = I_{s,0} \cos(\omega_{osc} t)$, so assuming that it has no dc offset, the force will be applied at dc and $2\omega_{osc}$. The proof mass displacement in response to the force at $2\omega_{osc}$ is small because $\omega_{osc} \gg \omega_0$, the resonance frequency, but the force at dc appears as an acceleration $\langle F_s \rangle / m$.

Hence, any fluctuations in the amplitude of the bridge drive current will appear as acceleration noise. We can make an estimate of the magnitude of this noise. A small change in the current, δI_s , will produce a change in acceleration of

$$\delta a = \frac{\epsilon \Lambda}{2m} I_s^2 \left(\frac{\delta I_s}{I_s} \right). \quad (2-29)$$

Using $\epsilon = 1\%$ and the value for I_s at optimum coupling for the SSA-Ib, the coefficient of the relative current error becomes $\sim 10^{-2} \text{ m/s}^2$. The critical components of the current source can have temperature coefficients as low as 10 ppm/K. If these elements can be controlled so that the temperature noise does not exceed $10^{-2} \text{ K/Hz}^{1/2}$, the equivalent acceleration noise should be of the order of $10^{-9} \text{ m/s}^2 \text{ Hz}^{1/2}$. At frequencies of order 0.1 Hz and higher, temperature fluctuations in the critical components will be smaller, so acceleration noise will be lower. This noise source has not been observed in preliminary tests of SSA because I_s was limited by other considerations to a value well below the value at optimum coupling.

2.5.2 Model Ib: open loop measurements

Ideally, the noise of the instrument is dominated by that of the SQUID amplifier. However, below the proof mass resonance frequency, ω_p , the SQUID noise is not detectable below the seismic noise experienced by the platform. However, above ω_p , the displacement of the proof mass to an acceleration of given amplitude drops off as ω_p^{-2} , so the white noise level becomes visible at several times ω_p , depending on the drive current. Initial tests indicate that the measured power spectral density of the SQUID output is white

in this region and it meets the manufacturers specifications ($1 \mu\text{V}/\text{Hz}^{1/2}$ at the output, $10^{-11} \text{ A}/\text{Hz}^{1/2}$ referred to the SQUID input) with currents into the oscillator drive transformer primary up to the maximum amplitude of the voltage-to-current converters, $45 \text{ mA}_{\text{rms}}$. Well below the proof mass resonance frequency, the signal at the SQUID input coil is related to acceleration by

$$\langle I_{SQ} \rangle = \langle I_{osc} \rangle \left(\frac{M}{L_{dr} + L_s} \frac{\Lambda_s}{L_{SQ} + L_s} \right) A, \quad (2-30)$$

where $A = a_{r_i}$ for translational acceleration and $A = c\alpha_{\theta_i}$ for rotational acceleration, and $i \in x, y, z$. In preliminary tests, the factor in parentheses matches the calculated values to within the error on the knowledge of the parameters ($\sim 3\%$). For $\langle I_{osc} \rangle = 45 \text{ mA}$ and SQUID noise of $10^{-11} \text{ A}/\text{Hz}^{1/2}$, this coefficient gives a power spectral density of acceleration noise of $9 \times 10^{-11} g_E/\text{Hz}^{1/2}$ for translational circuits and $7 \times 10^{-8} \text{ rad/s}^2 \text{ Hz}^{1/2}$ for rotational circuits. (These numbers vary slightly with modulation frequency and the configuration of levitation currents.) This represents an improvement by a factor of four and two for the translational and rotational circuits, respectively, over noise of the Model I SSA with the same drive current amplitude.

One advantage of the ac displacement sensing scheme is that it is not limited by the $1/f$ noise of the SQUID, because the signal is modulated to a frequency well above the transition to the white noise regime. However, at low frequencies, there are many other mechanisms that can possibly contribute to random fluctuations in the accelerometer output. Nonlinearity in the levitation force and the displacement sensing, and other nonlinear effects, such as the motion of wires in response to the sensing currents, may contribute to down-conversion of noise. Another nonlinear process, slip-stick motion of the wires, may contribute to drift when the suspended accelerometer moves with respect to the vacuum can. The fluctuation of the accelerometer temperature may couple to the acceleration output through the temperature dependence of the superconducting penetration depth. Finally, temperature fluctuation in the dewar, especially the rubber suspension spring, can cause

a change in the position and orientation of the accelerometer. Changes in position can couple to tilt through asymmetries in the suspension. A change in the tilt angle changes the component of gravitational acceleration along the sensitive axes. This last effect is not a problem with the accelerometer, but with the test rig.

Most of these mechanisms that generate low frequency noise will affect all six channels approximately equally. However, at low frequencies ($\omega \ll 1$), variation in the angle of the housing with respect to vertical will affect the translational acceleration much more strongly, because it modulates the full field of the Earth: $\delta\alpha = g_E \sin\theta \delta\theta = (8.00 \text{ m/s}^2) \delta\theta$, whereas it affects the angular acceleration only through the small factor ω^2 : $\delta\alpha = \omega^2 \delta\theta$. Fluctuations in the temperature of the accelerometer body will also affect the translational channels more strongly than the angular. The effect of the penetration depth variation acts through the levitation circuits, for which all coils are on one side of the proof mass. For a simple circuit consisting only of the levitation coils in series, the proof mass moves so that the effective spacing between itself and the coils, which equals the gap minus twice the penetration depth, remains constant. (In the actual circuit, the change in the secondary inductance of the feedback transformer must be taken into account.) However, torque is created by a difference in the levitation force on the two sides of the torque axis. Therefore, if the initial angular displacement is close to zero (so that a small dc torquing current is needed), a uniform temperature change will not create a torque (though modulation of the secondary inductance of the feedback transformer will modulate the torquing current.) The displacement sensing circuits are, to first order, unaffected by a change in the penetration depth, because a uniform change in the gaps above and below the proof mass does not alter the bridge balance.

Figure 9 shows the power spectral density of the outputs of one linear and one angular acceleration channel below 1 Hz. The amplitude of the bridge drive current is the same for both channels. The signals are referred to current through the SQUID input coil. Thus, the relative amplitude of the signals shows the relative degree of bridge misbalance.

The top and bottom traces are signals from translational and rotational circuits, respectively. In this frequency range, the seismic noise is generally quite low. Below the microseism peak, which can be seen in the translational signal near 200 mHz, it drops rapidly, reaching a minimum of several times $10^{-10} \text{ m/s}^2 \text{ Hz}^{1/2}$ near 10 mHz. Therefore, the translational signal below 100 mHz does not appear to be related to the seismic motion of the floor. However, except for temperature, errors internal to the accelerometer should be the same for the two channels. The noise on the rotational channel is within a factor of two of the SQUID amplifier noise ($10^{-11} \text{ A/Hz}^{1/2}$) down to $\sim 40 \text{ mHz}$, and then rises with a power law dependence of less than $1/f$. Fluctuation in temperature of the SSA is too small to

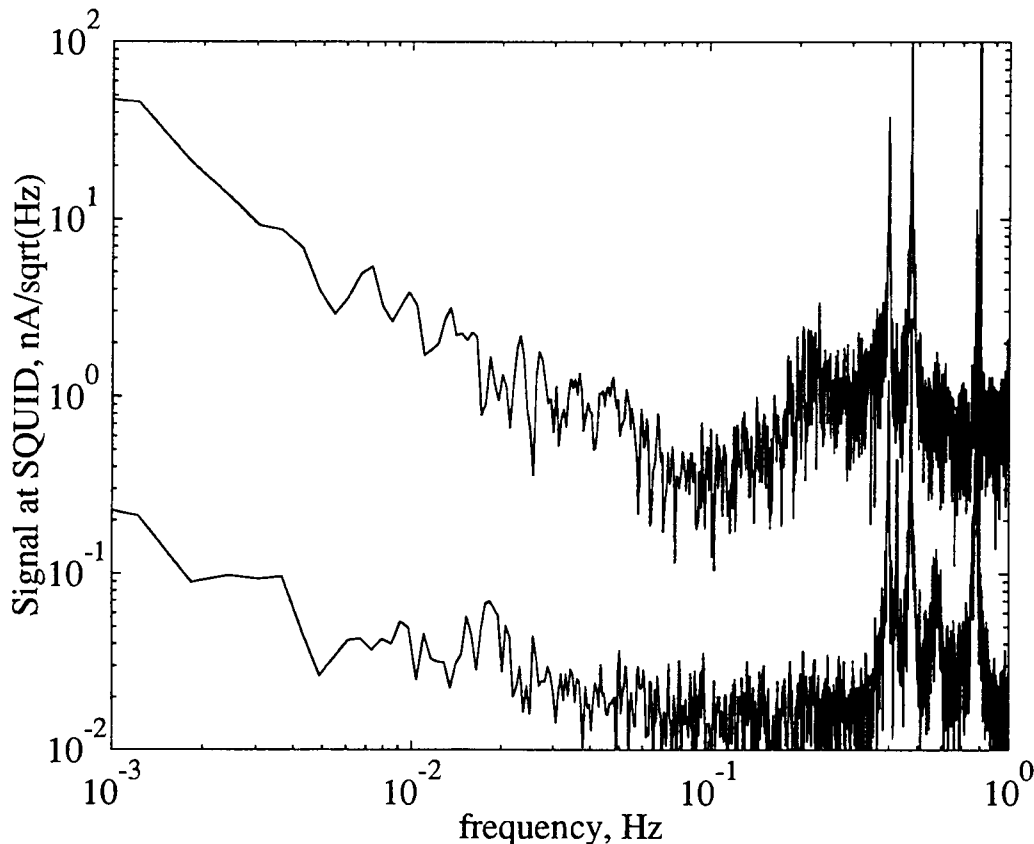


Figure 9. Power spectral densities of a translational and a rotational channel at low frequencies. The upper curve represents translational acceleration along the y axis. The lower curve represents angular acceleration about the x axis. The signal has been referred back to current through the SQUID input coil. Typical SQUID noise is $\sim 10^{-11} \text{ A/Hz}^{1/2}$. Both channels have the same bridge drive amplitude.

account for the excess noise on the translational signal, which has approximately a $1/f$ frequency dependence, and is most likely due to the variation of the orientation of the device with respect to vertical.

The maximum drive current, and thus the maximum sensitivity, is limited in the SSA-Ib by the resistive component of the bridge misbalance signal. The inductances of the sensing coils are functions of the gap, and by adjusting the position of the proof mass, the inductances can be adjusted to balance the bridge. However, the arms of the bridge can also have resistance, due, for example, to coupling to the resistive coil forms. The resistive component of coil impedance will not be a sensitive function of gap, and so mismatch in the resistive component of the bridge arms can not be removed by adjusting the gap. The inductive component of bridge misbalance causes a current through the SQUID input coil that is in phase with the sensing current, I_s . The resistive component causes an I_{SQ} 90° out of phase with I_s . Figure 10 shows the in- and out-of-phase components of the demodulated SQUID output with several different currents stored in the corresponding levitation circuit. The output voltages have been converted to the degree of bridge balance (I_{SQ}/I_s) by dividing by the SQUID current-to-voltage gain and the sensing current, I_s (obtained with Eq. (2-21)). The lock-in measures phase with respect to the oscillator, which includes a constant phase shift, predominantly from the resistive core of the bridge drive transformer. This phase angle has been removed. With the resolution of the current source used for adjusting the levitation current, the in-phase component of the bridge balance can be adjusted to a few parts in 10^5 . When operated in closed loop, the balance improves by more than an order of magnitude. The out-of-phase component of the bridge balance varied from 1×10^{-5} to 4×10^{-5} . Therefore, especially in closed-loop operation, the misbalance signal at the oscillator frequency is due primarily to the out-of-phase component. At 1 kHz, the slew rate limit of the BTI SQUID controller restricts the maximum current through the input coil to less than $2.0 \mu A$, so for a bridge balance of 4×10^{-5} , the maximum I_s is 0.5 A, which is less than the current required for optimum coupling.

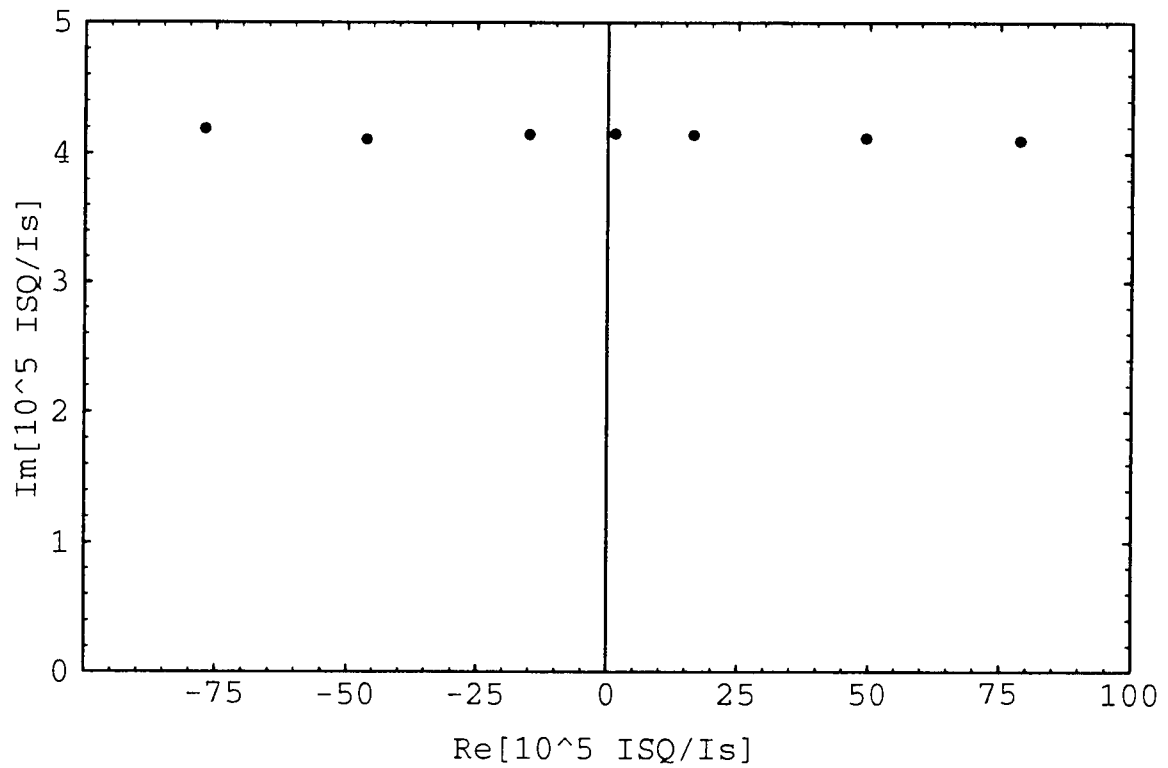


Figure 10. The degree of balance of the r_z sensing bridge on the complex plane during a current storing sequence. The bridge balance is the current through the SQUID input coil divided by the current through the secondary of the bridge drive transformer. The horizontal axis is the signal in phase with the oscillator and the vertical axis is the out-of-phase signal. The different points represent the balance with different currents stored in the r_z levitation circuit.

2.6 Control of the SSA-Ib

A six-axis accelerometer measures translational and rotational acceleration in all six degrees of freedom. The desired outputs of the instrument are six signals, each proportional to the acceleration of the device along one of the measured axes, and independent of the accelerations along the other axes. Hence, the instrument should ideally have a diagonal transfer function matrix. However, analysis of the linearized model of the system reveals that in open loop operation, the SSA-Ib does not have a diagonal transfer function. In fact, due to the weak damping of the modes of the SSA-Ib, it does not even have a diagonally dominant transfer function. These lightly damped modes also complicate the design of a precompensator to provide diagonal dominance to the open loop system. The goal of the control aspect of the project is to design an easily implementable compensator that will provide a diagonal (or almost diagonal) closed loop transfer function matrix, while also improving the linearity and bandwidth of the instrument. By taking advantage of the particular structure of the open loop transfer function, it is possible to develop a relatively simple controller which fulfills these requirements. The controller consists of two main components: a decoupling component, and a set of single-input, single-output (SISO) controllers which provides the required bandwidth and improves the linearity of the SSA-Ib. Using this approach, we reduce a multi-input, multi-output (MIMO) design problem to six independent SISO design problems.

The stability and stability robustness of the proposed controller have been analyzed in Bachrach *et al.* (1990a). The stability of the closed loop system is analyzed using Rosenbrock's Inverse Nyquist Array (INA) method (Rosenbrock, 1969), and a very simple set of conditions for the stability of the closed loop system are obtained. The stability robustness of the closed loop system is studied using a singular values decomposition approach (Doyle and Stein, 1981). In this report we will summarize these results. For a more detailed treatment of these topics, refer to Bachrach *et*

al. (1990a), included in Appendix B.

2.6.1 Transfer functions of the SSA-Ib

The equations of motion of the SSA-I or SSA-Ib are derived as outlined in Section 2.4 (or for a more detailed analysis, see Parke (1990)). Taking the Laplace transform of the linearized equations of motion of the SSA-Ib, we can obtain the relations between the proof mass displacements, the external accelerations and the feedback currents. These relations can be written in matrix form. Define

$$\bar{r}(s) \equiv \begin{bmatrix} r_x \\ r_y \\ r_z \\ \theta_x \\ \theta_y \\ \theta_z \end{bmatrix}, \quad \bar{I}_f(s) \equiv \begin{bmatrix} I_{r_{xf}} \\ I_{r_{yf}} \\ I_{r_{zf}} \\ I_{\theta_{xf}} \\ I_{\theta_{yf}} \\ I_{\theta_{zf}} \end{bmatrix}, \quad \bar{a}^E(s) \equiv \begin{bmatrix} a_x^e + \frac{f_{DC}}{m} \frac{1}{s} \\ a_y^e + \frac{f_{DC}}{m} \frac{1}{s} \\ a_z^e + \frac{f_{DC}}{m} \frac{1}{s} \\ \alpha_x^e \\ \alpha_y^e \\ \alpha_z^e \end{bmatrix}, \quad (2-30)$$

where $\bar{r}(s)$ denotes the position of the proof mass with respect to the housing, $\bar{I}_f(s)$ denotes the feedback currents and $\bar{a}^E(s)$ denotes the external accelerations, including gravitational force (the dependence of the vector elements on s has been omitted for brevity). Further, define the matrices:

$$\Psi(s) \equiv \begin{bmatrix} T_{r_x}(s) & 0 & 0 & 0 & -f_m & f_m \\ 0 & T_{r_y}(s) & 0 & f_m & 0 & -f_m \\ 0 & 0 & T_{r_z}(s) & -f_m & f_m & 0 \\ 0 & f_I & -f_I & T_{\theta_x}(s) & 0 & 0 \\ -f_I & 0 & f_I & 0 & T_{\theta_y}(s) & 0 \\ f_I & -f_I & 0 & 0 & 0 & T_{\theta_z}(s) \end{bmatrix}, \quad (2-31)$$

$$K = \text{diag}\{k_{r_x}, k_{r_y}, k_{r_z}, -k_{\theta_x}, -k_{\theta_y}, -k_{\theta_z}\},$$

where

$$\begin{aligned} T_i(s) &= s^2 + \frac{\omega_i}{Q_i}s + \omega_i^2, \quad i = r_x, \dots, \theta_z, \\ k_{r_i} &= \frac{4\Lambda_L \rho_{r_i}^f I_r^l}{m}, \quad k_{\theta_i} = \frac{2c\Lambda_L \rho_{\theta_i}^f I_\theta^l}{I}, \quad i = x, y, z, \\ f_I &= \frac{f_{DC}}{I}, \quad f_m = \frac{f_{DC}}{m}. \end{aligned} \quad (2-32)$$

We add the second term in $T_i(s)$ to account for damping. It assumes that the damping force is linear with velocity. With these definitions, the equations of motion of the proof mass become

$$\Psi(s)\bar{r}(s) = K\bar{I}_f(s) + \bar{a}^E(s). \quad (2-33)$$

It is not hard to interpret the meaning of the matrices $\Psi(s)$ and K . $\Psi(s)$ relates the position of the proof mass with respect to the casing to the external accelerations (including gravity). K relates the applied feedback current to equivalent feedback accelerations. Inverting Eq. (2-33), we obtain an expression for the position of the proof mass as a function of the external acceleration and feedback currents:

$$\bar{r}(s) = \Psi^{-1}(s)K \left[\bar{I}_f(s) + K^{-1}\bar{a}^E(s) \right]. \quad (2-34)$$

Finally, since the signals measurable to the controller are the output voltages of the sensing circuits, we need to relate the position of the proof mass to the output voltages. This relation is modeled by the diagonal matrix $\Xi(s)$ (sensing mechanism), the displacement-to-voltage transfer function

$$\bar{V}_{out} = \Xi(s)\bar{r}(s), \quad \Xi(s) = \text{diag}\{\sigma_{r_x}, \dots, \sigma_{\theta_z}\}f(s), \quad (2-35)$$

where $f(s)$ is the low pass filter (LPF) transfer function of the lock-in amplifiers, and σ_i is the gain produced by the sensing mechanism, for the i -th axis. Equation (2-34) becomes

$$\bar{V}_{out}(s) = \underbrace{\Xi(s)\Psi^{-1}(s)K}_{G(s)} \left[\bar{I}_f(s) + K^{-1}\bar{a}^E(s) \right]. \quad (2-36)$$

where we have introduced the definition $G(s) \equiv \Xi(s)\Psi^{-1}(s)K$.

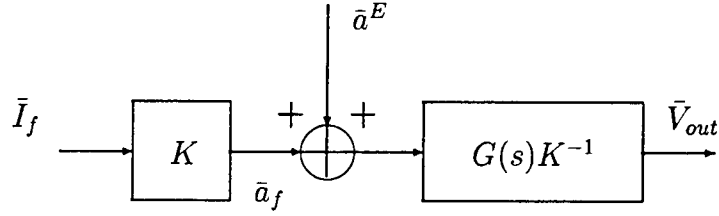


Figure 11: SSA-Ib in open loop operation

The linearized model of the SSA-Ib is shown in Figure 11. Under the assumption of perfect geometry (perfect symmetry), the parameters of the three translational degrees of freedom are the same, as are the parameters of the three rotational degrees of freedom. We will use this model in the design of the SSA-Ib controller.

2.6.2 Closed loop operation

In Bachrach *et al.* (1990b) it was shown that in order to improve the linearity of the SSA-Ib, it is necessary to minimize the displacements and displacement velocities of the proof mass. This can be achieved by adding a feedback controller, thus operating the instrument as a null detector (Figure 12). The second important requirement is for the closed loop transfer function to be diagonal, or at least diagonally dominant.

Figure 12 shows the main components of a conventional feedback controller design. The block $F(s)$ corresponds to the dynamics of the controller, while the block \mathcal{U} corresponds to a MIMO, diagonal, voltage-controlled-current-source (VCCS) defined as

$$\mathcal{U} = \text{diag} \{ \mathcal{U}_{r_x}, \dots, \mathcal{U}_{\theta_z} \}. \quad (2-37)$$

This stage is added since for the linearized model of the SSA-Ib, the force on the proof mass is proportional to the current added to the feedback circuit (levitation coils). The transfer function between acceleration input \bar{a}^E and controller output voltage

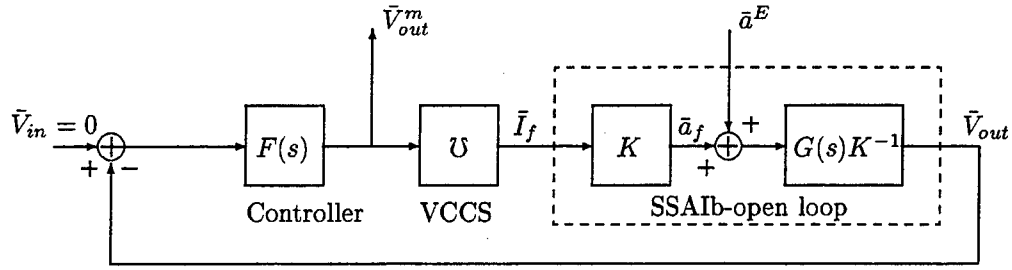


Figure 12: The SSA-Ib in closed loop operation

\bar{V}_{out}^m is

$$\bar{V}_{out}^m(s) = -[I + F(s)G(s)U]^{-1} F(s)G(s)K^{-1}\bar{a}^E, \quad (2-38)$$

or

$$\bar{V}_{out}^m(s) = -U^{-1}[(U F(s)G(s))^{-1} + I]^{-1} K^{-1}\bar{a}^E. \quad (2-39)$$

Mathematically, this transfer function could be made perfectly diagonal simply by choosing $F(s)$ in the following way (remember U is diagonal):

$$F(s) = U^{-1}\Lambda(s)G^{-1}(s), \quad (2-40)$$

where $\Lambda(s)$ is a diagonal transfer function which could be designed to produce a desirable closed loop transfer function. This scheme, however, is based on the assumption that one could construct a controller $F(s)$ such that $F(s)G(s) = U^{-1}\Lambda(s)$, or in other words that we can construct an inverse of $G(s)$. In practice, this is very difficult to achieve in a reliable manner over a wide frequency range, mainly because of plant uncertainties. In the SSA-Ib, realizing such an $F(s)$ would be especially difficult because the modes of the SSA-Ib are very lightly damped (Q_{θ_i} as high as 1500), making the product $F(s)G(s)$ particularly sensitive to model uncertainties. Also, the construction of such controller would require the implementation of 36 complex transfer functions. The proposed decoupling controller will require only the implementation of 18 transfer functions, out of which 12 have only one pole and one zero, while the remaining 6 are also relatively simple.

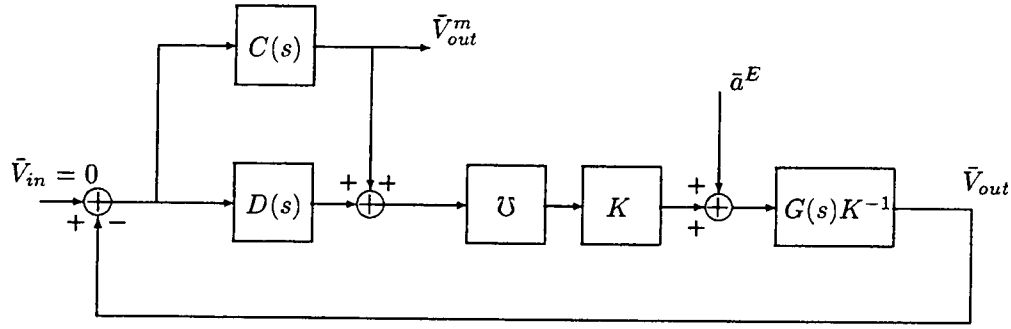


Figure 13: Complete solution

Since attaining a perfect diagonalizing controller according to Eq. (2-40) is not feasible, we could place a weaker assumption on $F(s)$, requiring only that it produces a diagonally dominant $F(s)G(s)$. The stability and robustness of the resulting closed loop system could then be analyzed using Rosenbrock's Inverse Nyquist Array (INA) (Rosenbrock, 1969) method. For the SSA-Ib, however, finding a relatively simple $F(s)$ which would ensure diagonal dominance of $F(s)G(s)$ proves particularly difficult because of the high values of Q_{r_i} and Q_{θ_i} .

The Controller

Equation (2-39) does not immediately suggest any other choices of $F(s)$. Let us consider the configuration shown in Figure 13. In this configuration the purpose of the component $D(s)$ is to decouple the system, while the component $C(s)$ provides the necessary feedback to produce the desired bandwidth and response to the overall system. We will denote by $D_0(s)$ an ideal decoupling $D(s)$, which for now we assume to be realizable. The closed loop transfer function of the new configuration will be (assuming, for the moment that $D(s) = D_0(s)$)

$$\bar{V}_{out}^m = -C(s) \left[G^{-1}(s) + UC(s) + UD_0(s) \right]^{-1} K^{-1} \bar{a}^E. \quad (2-41)$$

One can see from Eq. (2-41) that the closed loop transfer function can be made diagonal by choosing $D_0(s)$ such that

$$[D_0(s)]_{ij} = -[\mathcal{U}^{-1}G^{-1}(s)]_{ij} (1 - \delta_{ij}); \quad i, j = 1, \dots, 6, \quad (2-42)$$

where

$$\delta_{ij} = \begin{cases} 1 & \text{if } i = j, \\ 0 & \text{if } i \neq j, \end{cases} \quad (2-43)$$

and

$$C(s) = \text{diag} \{c_{r_x}(s), \dots, c_{\theta_z}(s)\}. \quad (2-44)$$

Thus, $D_0(s)$ cancels the non-diagonal elements of $G^{-1}(s)$. Assuming such cancellation to be possible, the transfer function thus obtained is diagonal. Based on the definition of $G(s)$, it is convenient to rewrite $C(s)$ and $D_0(s)$ in terms of the matrices K , $\Xi(s)$, $\Psi(s)$ and \mathcal{U} . Thus, we write $C(s)$ and $D_0(s)$ as follows:

$$C(s) = \mathcal{U}^{-1}K^{-1}\Phi(s)\Xi^{-1}(s), \quad (2-45)$$

where

$$\Phi(s) = \text{diag} \{\phi_{r_x}(s), \dots, \phi_{\theta_z}(s)\}, \quad (2-46)$$

and we write $D_0(s)$ as

$$D_0(s) = \mathcal{U}^{-1}K^{-1}\hat{\Psi}(s)\Xi^{-1}(s), \quad (2-47)$$

where

$$[\hat{\Psi}(s)]_{ij} = -[\Psi(s)]_{ij} (1 - \delta_{ij}); \quad i, j = 1, \dots, 6. \quad (2-48)$$

With these definitions, it is possible to rewrite the closed loop transfer function in the following manner:

$$\bar{V}_{out}^m = -\mathcal{U}^{-1}K^{-1}\Phi(s) [\Psi(s) + \hat{\Psi}(s) + \Phi(s)]^{-1} \bar{a}^E. \quad (2-49)$$

Expression (2-49) does not provide any new information, but it emphasizes the simplicity of the proposed scheme, since the only parameters left to be designed are the diagonal elements of the matrix $\Phi(s)$ (all non-diagonal elements are 0), corresponding

to the $C(s)$ component of the controller. Moreover, the problem of designing $\Phi(s)$ is in fact equivalent to six independent SISO design problems.

So, under the assumption that $D_0(s)$ can be implemented to cancel the non-diagonal elements of $G^{-1}(s)$, $C(s)$ can be designed as six independent SISO controllers, transforming our MIMO design problem into six independent SISO design problems. In the present case, however, $D_0(s)$ as defined in Eq. (2-47) is not realizable since the non-diagonal terms of $G^{-1}(s)$ are not realizable. Thus, a crucial question for the design is: How accurately do the elements of $D_0(s)$ have to approximate the non-diagonal elements of $G^{-1}(s)$? A realizable transfer function can be made to fit well at low frequencies, but it diverges from the ideal function at high frequencies, since the non-diagonal terms of $G^{-1}(s)$ are not *proper*¹. In Bachrach *et al.* (1990a) it was proved using Rosenbrock's INA method, that the cancellation of the non-diagonal elements need not be perfect; it is sufficient for the stability of the closed loop system that $G^{-1}(s) + UD(s) + UC(s)$ (where $D(s)$ is an implementable version of $D_0(s)$) be diagonally dominant. Fortunately, the diagonal terms of $G^{-1}(s)$ for the SSA-Ib are of higher order than the non-diagonal terms, so that at high frequencies $G^{-1}(s)$ is naturally diagonally dominant. Thus, $D(s)$ needs to be an accurate approximation of the non-diagonal terms of G^{-1} only over a limited frequency range. Moreover, this analysis reveals that the closed loop will remain stable even if any or all the elements of $D(s)$ are zero. Thus, this is also a possible implementation of the controller, although, as can be expected, the decoupling performance of the controller deteriorates. For the SSA-Ib, a relatively simple implementation of $D_0(s)$ will satisfy all the stability and performance requirements.

¹A transfer function is proper (strictly proper) if the number of poles is equal to (strictly smaller than) the number of zeros.

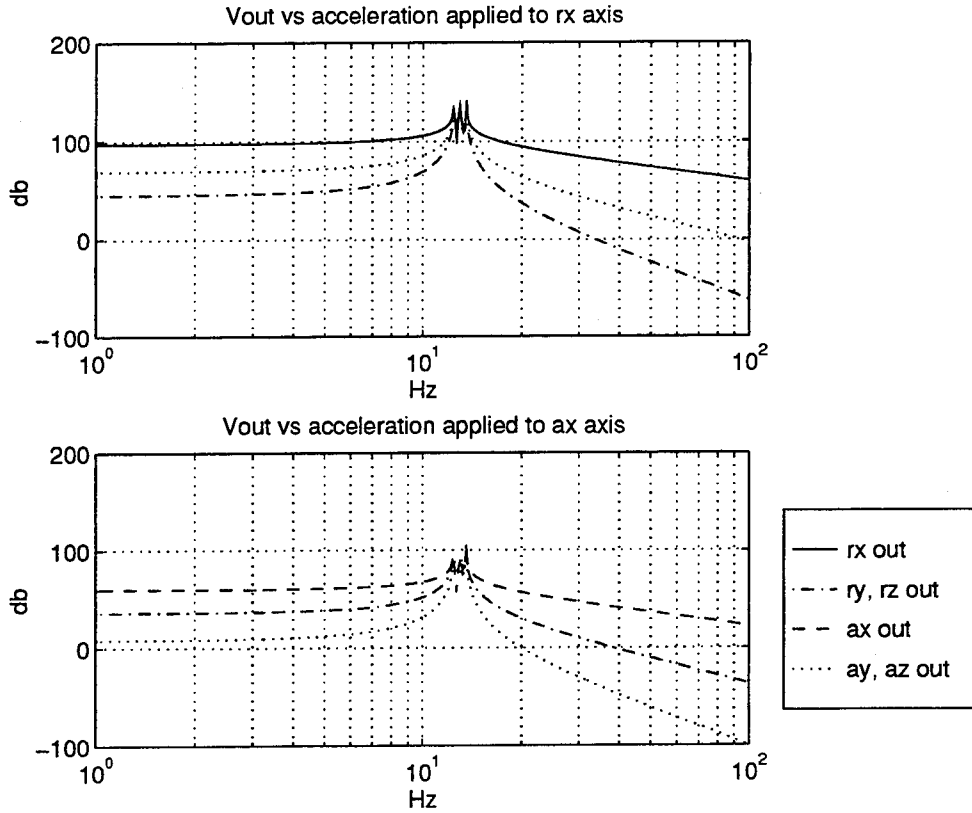


Figure 14: Open loop transfer functions between acceleration and \bar{V}_{out}

2.6.3 Simulation results

The transfer function obtained through the linearization of the dynamic equations of the SSA-Ib can easily be simulated and compared to the measured equations. For SSA-I, we obtained a very good match between the measured and the modeled transfer functions (Bachrach, 1990b). For SSA-Ib, the open loop transfer functions have been simulated, and the resulting transfer functions for a translational (r_x) and a rotational (θ_x) input are shown in Figure 14². As can be seen, the open loop transfer function is not diagonal, nor is it diagonally dominant.

Figure 15 shows the closed loop transfer functions for the translational and

²For all the figures included in this document, the terms “ri” and “ai” refer to r_i and θ_i .

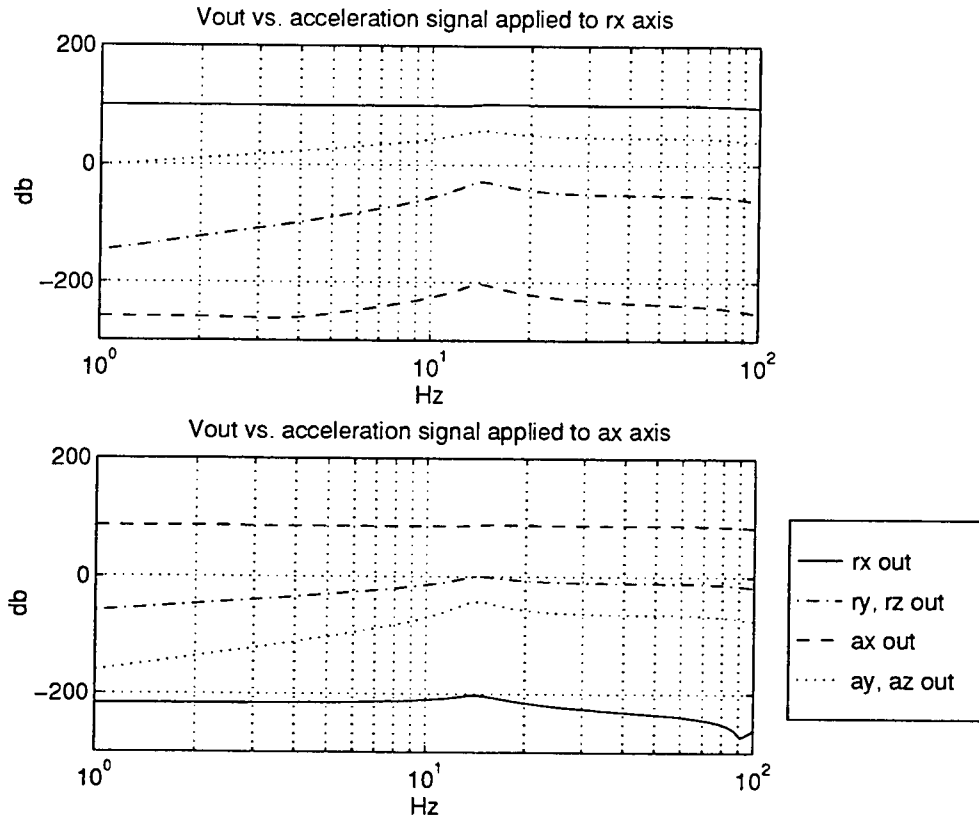


Figure 15: Closed loop transfer functions between acceleration and \bar{V}_{out}

rotational input. Clearly, a considerable improvement in the decoupling has been achieved. For the translational degrees of freedom we achieve a rejection of about 50 dB with respect to the closest transfer function, while for the rotational degrees of freedom the rejection reaches about 100 dB. In order to improve the linearity of the instrument, integrators were included in the components of $C(s)$ to minimize the displacement of the proof mass in the low frequency region. By minimizing the displacement of the proof mass we improve the linearity of the instrument. The robustness of the closed loop system was analyzed in Bachrach *et al.* (1990a), and it was shown that input or output multiplicative perturbations (which can be considered as magnitude errors) of about $\pm 80\%$ at the worst possible frequency could be tolerated without causing the closed loop system to become unstable. In Bachrach *et al.* (1990a) it was also proved that even if one or all terms of $D(s)$ were disconnected, the closed

loop system cannot become unstable. Notice finally that in closed loop operation, the degree of rejection (or decoupling) improves as the frequency decreases, while for the open loop system the coupling is constant below the resonance frequency of the plant.

Equation (2-49) shows that the overall gain of the closed loop system depends on the gain of the VCCS. The gains of the VCCS were fixed so that the maximum desirable acceleration applied to a given axis (10^{-5} m/s² for translational degrees of freedom, 5×10^{-5} rad/s² for rotational degrees of freedom) produces a 10 V output signal (\bar{V}_{out}^m) for the corresponding channel.

Once these gains are set, and a set of nominal parameters are chosen for the sensing mechanism, the gains of the controller components can be calculated (the zeros and poles of the controller are independent of these gains, see Eqs. (2-45) and (2-47)). The controller transfer functions shown in Table 2 correspond to a given set of nominal parameters for the sensing mechanisms. This set is included in Appendix C, and will be used for all simulations thereafter. For a more detailed discussion of the controller, see Section 2.8.

Controller transfer functions	
VCCS	
$v_i \ (i = r_x, r_y, r_z)$	$v_i \ i = r_x, \dots, \theta_z.$ -46.095 $\mu\text{A/V}$
$v_i \ (i = \theta_x, \theta_y, \theta_z)$	-92.476 $\mu\text{A/V}$
Diagonal controller	
$g_i \ (i = r_x, \dot{r}_y, r_z)$	$c_i(s) = g_i \frac{(1+\frac{s}{z_1})(z_i^2+z_i/Qs+s^2)}{s(1+\frac{s}{p_1})(1+\frac{s}{p_2})(1+\frac{s}{p_3})}, \ i = r_x, \dots, \theta_z.$ -0.073
$g_i \ (i = \theta_x, \theta_y, \theta_z)$	-1.084
$z_i \ (i = r_x, r_y, r_z)$	84.5 rad/s
$z_i \ (i = \theta_x, \theta_y, \theta_z)$	85.3 rad/s
z_1	753.9 rad/s
p_1	1068.1 rad/s
p_2	1256.6 rad/s
p_3	7539.8 rad/s
Q	4
Off-diagonal controller	
$g_j \ (j = fm)$	$d_j(s) = g_j \frac{(1+\frac{s}{z_1})}{(1+\frac{s}{p_1})}, \ j = fm, fi.$ -0.086
$g_j \ (j = fi)$	-0.836
z_1	785.4 rad/s
p_1	7853.9 rad/s

Table 2: Controller transfer functions

2.7 Noise Analysis

The SSA-Ib is designed to be an extremely sensitive measurement device. Hence, one of the most important aspects of its design are noise limitations. This section is devoted to the analysis of the open loop and closed loop performance of the instrument with noise-generating components.

We will compare the performance of the SSA-Ib in both open and closed loop operation in two ways. First, we study the effect of noise on stationary, very low-frequency, single-axis accelerations. This analysis will be carried out algebraically, and will be helpful to understand how the parameters of the different components of the sensing mechanism affect the smallest detectable acceleration with and without the use of a feedback controller. A second approach will be based on the fact that the controller implementation is available for measurement, and the power spectral density of the noise sources considered in the first analysis can be measured. Having these data available, their effect can be estimated in terms of the measured output and, more significantly, in terms of *equivalent acceleration noise*. We can thus accurately evaluate the smallest measurable signal for the particular implementation of the controller, and for the nominal parameters of the SSA-Ib over any frequency range.

For both of these analyses we make two fundamental assumptions. We assume all noise signals to be white, mutually uncorrelated, and uncorrelated with the acceleration signals being measured. Also, we will not include the effect of Brownian motion noise (see Paik *et al.* (1989) or Parke (1990)), since it is indistinguishable from acceleration signals, and will be unaffected by the addition of a feedback controller.

2.7.1 Linearized noise model of SSA-Ib

The first step in the study of the noise performance of the SSA-Ib will be to obtain a linearized model of the overall system including noise. Figure 16 shows the detection mechanism for the i -th axis of the SSA-Ib, where two input signals (i_A^n and v_A^n) have been added. These signals represent the input-current noise (i_A^n) and output-voltage noise (v_A^n) of the SQUID amplifier. A detailed noise model of the SQUID can be found in Hollenhorst (1979) or Hollenhorst and Giffard (1980). Based on this model and experimental measurements, it has been determined that the SQUID noise is dominated by the input-current noise, and we therefore neglect v_A^n . Clearly, i_A^n contributes to the output of the lock-in amplifier (V_{out}^i) in a non-linear way. In this section we obtain a linearized noise model of the SSA-Ib.

In order to obtain the noise spectral density at the lock-in amplifier output due to the SQUID noise, we will first compute the autocorrelation function of the voltage signal $V_4^i(t)$ after demodulation³. According to Figure 16, we find that the voltage after demodulation is

$$V_4^i(t) = A \left[i^p(t) I_s^i \lambda_s^i \cos(\omega_i^s t + \varphi) + i_A^n(t) \right] \cos(\omega_i^s t + \varphi), \quad (2-50)$$

where φ is a random variable uniformly distributed over the interval 0 to 2π , and we assume that the phase shift between the source signal and the demodulation signal (ϕ_i in Figure 16) has been properly adjusted so that the detection is synchronized.

We denote the autocorrelation function of signal j as K_j . We can write the autocorrelation function of the signal after demodulation as

$$K_{V_4^i}(t, s) = E_\varphi \left\{ [i^p(t) I_s^i \lambda_s^i \cos(\omega_i^s t + \varphi) + i_A^n(t)] A \cos(\omega_i^s t + \varphi) \right. \\ \left. [i^p(s) I_s^i \lambda_s^i \cos(\omega_i^s s + \varphi) + i_A^n(s)] A \cos(\omega_i^s s + \varphi) \right\}, \quad (2-51)$$

³The lock-in amplifiers do not use a sinusoidal wave in the demodulation stage, but a square wave. We consider only the first harmonic, since all others will not affect the noise performance.

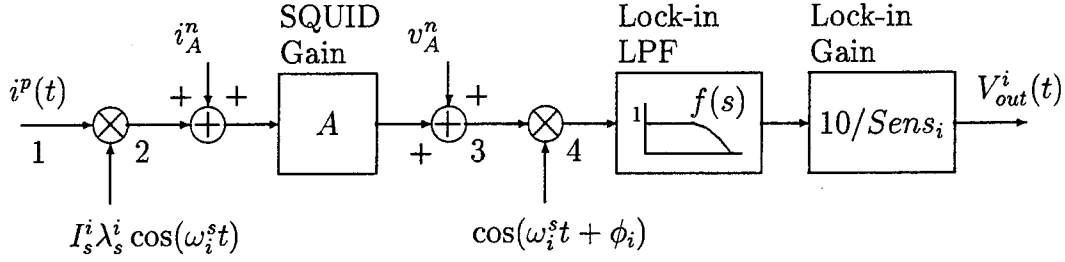


Figure 16: Sensing mechanism including noise sources, $i = r_x, \dots, \theta_z$.

where $E_\varphi\{f(\varphi)\}$ denotes the expected value of $f(\varphi)$ for some given probability distribution of φ . Since i_A^n is uncorrelated with the displacement signal i^p , we obtain⁴

$$K_{V_4^i}(t, s) = (I_s^i \lambda_s^i A)^2 K_{i^p}(t, s) E_\varphi [\cos^2(\omega_i^s t + \varphi) \cos^2(\omega_i^s s + \varphi)] \\ + A^2 K_{i_A^n}(t, s) E_\varphi [\cos(\omega_i^s t + \varphi) \cos(\omega_i^s s + \varphi)]. \quad (2-52)$$

By the fact that φ is a random variable uniformly distributed over the interval 0 to 2π , it can be shown that

$$E_\varphi [\cos^2(\omega_i^s t + \varphi) \cos^2(\omega_i^s s + \varphi)] = \frac{1 + \cos(2\omega_i^s(t-s))}{4}, \\ E_\varphi [\cos(\omega_i^s t + \varphi) \cos(\omega_i^s s + \varphi)] = \frac{\cos(\omega_i^s(t-s))}{2}. \quad (2-53)$$

Hence, assuming i_A^n to be white, and i^p to be stationary, we can rewrite the autocorrelation function as

$$K_{V_4^i}(\tau) = (I_s^i \lambda_s^i A)^2 K_{i^p}(\tau) \frac{1 + \cos(2\omega_i^s(\tau))}{4} + A^2 K_{i_A^n}(\tau) \frac{\cos(\omega_i^s(\tau))}{2}, \quad (2-54)$$

where $\tau = t - s$. The Fourier transform of Eq. (2-54) gives

$$S_{V_4^i}(\omega) = \frac{(I_s^i \lambda_s^i A)^2}{4} \left[S_{i^p}^i(\omega) + \frac{S_{i^p}^i(\omega - 2\omega_i^s) + S_{i^p}^i(\omega + 2\omega_i^s)}{2} \right] + \frac{A^2}{2} S_{i_A^n}^i, \quad (2-55)$$

where we denote $S_j^i(\omega)$ = spectral density of signal j for the i -th degree of freedom, and where we have used the fact that $S_{i_A^n}^i$ is frequency independent. Finally, the low pass filter will (approximately) remove the second order harmonic terms $S_{i^p}^i(\omega - 2\omega_i^s)$

⁴Regretfully, the letter i is used both in i^p (denoting position of the proof mass) and in i_A^n (denoting the SQUID current noise).

and $S_{ip}^i(\omega + 2\omega_i^s)$. Including the low pass filter transfer function, $f(s)$, and the gain of the output stage of the lock-in amplifiers, $10/Sens_i$, we obtain

$$S_{V_{out}}^i(\omega) = \left[\frac{(I_s^i \lambda_s^i A)^2}{4} S_{ip}^i(\omega) + \frac{1}{2} A^2 S_{i_A}^n \right] \left(\frac{10}{Sens_i} \right)^2 |f(j\omega)|^2. \quad (2-56)$$

Based on Eq. (2-56), and noting that

$$\sigma_i = I_s^i \lambda_s^i \frac{A}{2} \frac{10}{Sens_i}, \quad (2-57)$$

the equivalent output of the i -th sensing circuit can be written as

$$V_{out}^i(s) = \left[\sigma_i i^p(s) + \frac{10}{Sens_i} \frac{A}{\sqrt{2}} i_A^n(s) \right] f(s), \quad i = r_x, \dots, \theta_z. \quad (2-58)$$

Hence, we modify our model of the SSA-Ib in open loop operation (Eq. (2-36)) to include the equivalent SQUID noise as follows:

$$\bar{V}_{out}(s) = G(s) \left[\bar{I}_f(s) + K^{-1} \bar{a}^E(s) \right] + \bar{v}_{A_e}^n(s), \quad (2-59)$$

where

$$\bar{v}_{A_e}^n(s) = \left[\frac{10}{Sens_{r_x}} \frac{10}{Sens_{r_y}} \frac{10}{Sens_{r_z}} \frac{10}{Sens_{a_x}} \frac{10}{Sens_{a_y}} \frac{10}{Sens_{a_z}} \right]' \frac{A i_A^n(s)}{\sqrt{2}} f(s). \quad (2-60)$$

Figure 17 shows the SSA-Ib in closed loop operation, where we have included the different possible noise signals due to the SQUID and the controller. These signals are

- (1) \bar{v}_C^n : Input referred noise of block $C(s)$ of the controller,
- (2) \bar{v}_D^n : Input referred noise of block $D(s)$ of the controller,
- (3) $\bar{v}_{A_e}^n$: Equivalent SQUID current noise,
- (4) \bar{v}_U^n : Input referred noise of VCCS.

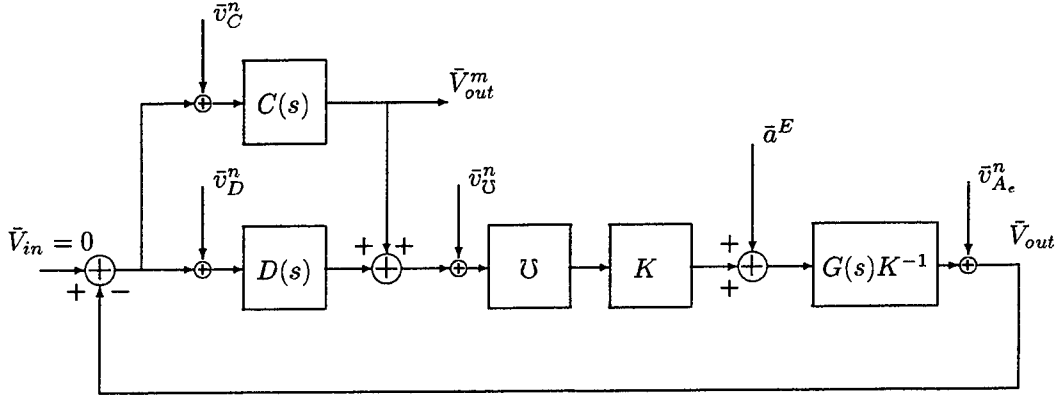


Figure 17: Closed loop system with noise sources

We express \bar{V}_{out}^m as a function of all the input signals. From Figure 17 we obtain the following system of equations:

$$\begin{aligned}\bar{V}_{out}^m &= C(s)(\bar{v}_C^n - \bar{V}_{out}), \\ \bar{V}_{out} &= \bar{v}_{A_e}^n + G(s)K^{-1} \left[\bar{a}^E + K\bar{U}(\bar{v}_U^n + \bar{V}_{out}^m + D(s)(\bar{v}_D^n - \bar{V}_{out})) \right].\end{aligned}\quad (2-61)$$

Solving for \bar{V}_{out}^m , we obtain the following expression for the output:

$$\begin{aligned}\bar{V}_{out}^m &= -C(s)[G^{-1}(s) + \bar{U}C(s) + \bar{U}D(s)]^{-1}G^{-1}(s)\bar{v}_{A_e}^n \\ &\quad -C(s)[G^{-1}(s) + \bar{U}C(s) + \bar{U}D(s)]^{-1}K^{-1}\bar{a}^E \\ &\quad -C(s)[G^{-1}(s) + \bar{U}C(s) + \bar{U}D(s)]^{-1}\bar{U}(\bar{v}_U^n + D(s)\bar{v}_D^n) \\ &\quad +C(s)[G^{-1}(s) + \bar{U}C(s) + \bar{U}D(s)]^{-1}[G^{-1}(s) + \bar{U}D(s)]\bar{v}_C^n.\end{aligned}\quad (2-62)$$

We will use these expressions to evaluate the effect of the feedback loop in the noise performance of the SSA-Ib.

2.7.2 Noise comparison between open and closed loop operation: Low frequency

The purpose of deriving expressions (2-59) and (2-62) is to compare the performance of the SSA-Ib in open and closed loop operation. To make such comparison we study

the response of the system to very low frequency signals ($\omega \ll \omega_i$). Although this is done mainly to simplify the mathematical analysis, the low frequency region also corresponds to the region of interest for the instrument.

The choice of a low frequency signal is mathematically convenient because we can greatly simplify the resulting expressions by taking the limit as $s \rightarrow 0$ of Eq. (2-62). Making the comparison for accelerations along a single axis, though, requires some consideration. As already shown, the open loop transfer function matrix of the SSA-Ib is not diagonally dominant, and although at low frequencies the coupling is small, it is orders of magnitude larger than in closed loop operation. Hence, the output of any of the axis is not only contaminated by the noise sources under consideration, but also by *accelerations* along other axes. In closed loop operation, on the other hand, the closed loop transfer function is almost diagonal at low frequencies (0 - 0.1 Hz). Thus, it is important to note that the conclusions of this comparison are not entirely "fair", since the chosen test signal biases the results in favor of the open loop configuration.

Minimum Detectable Signal in Open Loop Operation

From Eq. (2-59), we find that the response of the SSA-Ib in open loop operation to a low frequency translational acceleration can be approximated by

$$\lim_{s \rightarrow 0} \bar{V}_{out}(s) = \lim_{s \rightarrow 0} \left(\Xi(s) \Psi^{-1}(s) \bar{a}^E(s) + \bar{v}_{A_e}^n(s) \right). \quad (2-63)$$

Substituting Eq. (2-60), and since $\lim_{s \rightarrow 0} f(s) = 1$,

$$\lim_{s \rightarrow 0} \bar{V}_{out}(s) = \Xi(0) \Psi^{-1}(0) \bar{a}^E(0) + \text{diag} \{10/Sens_{r_x}, \dots, 10/Sens_{\theta_z}\} \frac{A}{\sqrt{2}} \bar{i}_A^n, \quad (2-64)$$

where we have made use of the assumption that the SQUID current noise is white, so that the dependency of the spectral density on frequency is omitted. If we consider

the response to acceleration along the x axis, a_x^e ,

$$\lim_{s \rightarrow 0} V_{out}^{r_x}(s) = \frac{\sigma_{r_x}}{\omega_{r_x}^2} \lim_{s \rightarrow 0} a_x^e(s) + \frac{10}{Sens_{r_x}} \frac{A}{\sqrt{2}} i_A^n. \quad (2-65)$$

We assume the signals in question to be uncorrelated, so that we can directly obtain the spectral density of the output at low frequencies:

$$S_V^{r_x}(\omega) = \left(\frac{\sigma_{r_x}}{\omega_{r_x}^2} \right)^2 S_{a_x^e}^{r_x}(\omega) + \left(\frac{10}{Sens_{r_x}} \right)^2 \frac{A^2}{2} S_{i_A^n}. \quad (2-66)$$

A signal will be considered detectable at a given frequency if its spectral density is higher than that of the noise at the same frequency, or mathematically stated, if the first term of Eq. (2-66) is greater than the second. Hence, a low frequency signal will be detectable along the r_x axis if its spectral density is greater than

$$\left(S_{a_{min}^e}^{r_x} \right)_{o.l.} = \frac{\omega_{r_x}^4}{\sigma_{r_x}^2} \left(\frac{10}{Sens_{r_x}} \right)^2 \frac{A^2}{2} S_{i_A^n}. \quad (2-67)$$

In general, for the i -th degree of freedom,

$$\left(S_{a_{min}^e}^i \right)_{o.l.} = \frac{\omega_i^4}{\sigma_i^2} \left(\frac{10}{Sens_i} \right)^2 \frac{A^2}{2} S_{i_A^n}, \quad i = r_x, \dots, \theta_z. \quad (2-68)$$

Minimum Detectable Signal in Closed Loop Operation

We can approximate the closed loop response of the SSA-Ib to a slowly varying signal by taking the limit of Eq. (2-62) as $s \rightarrow 0$. In this way, it is possible to obtain a relatively simple expression for the output of the SSA-Ib (including noise). Further, we assume that $D(s) = D_0(s)$ for the frequencies of interest. For the last term of Eq. (2-62),

$$\begin{aligned} C(s)[G^{-1}(s) + \mathcal{U}C(s) + \mathcal{U}D(s)]^{-1}[G^{-1}(s) + \mathcal{U}D(s)] \\ = \text{diag} \left\{ \frac{c_i(s)(G^{-1}(s))_{ii}}{(G^{-1}(s))_{ii} + \mathcal{U}_i c_i(s)} \right\}. \end{aligned} \quad (2-69)$$

Taking the limit as $s \rightarrow 0$, and since $\lim_{s \rightarrow 0} c_i(s) = \infty$, we obtain

$$\begin{aligned} \lim_{s \rightarrow 0} C(s)[G^{-1}(s) + \mathcal{U}C(s) + \mathcal{U}D(s)]^{-1}[G^{-1}(s) + \mathcal{U}D(s)] \\ = \mathcal{U}^{-1} \text{diag} \{ \omega_i^2 \} \Xi^{-1}(0) K^{-1}. \end{aligned} \quad (2-70)$$

In the first three terms of Eq. (2-62), the limit as $s \rightarrow 0$ for the common factor is

$$\lim_{s \rightarrow 0} C(s)[G^{-1}(s) + \mathcal{U}C(s) + \mathcal{U}D(s)]^{-1} = \mathcal{U}^{-1}. \quad (2-71)$$

Thus,

$$\begin{aligned} \lim_{s \rightarrow 0} \bar{V}_{out}^m(s) &= -\mathcal{U}^{-1}G^{-1}(0)\bar{v}_{A_e}^n - \mathcal{U}^{-1}K^{-1}\bar{a}^E - (\bar{v}_{\mathcal{U}}^n + D(0)\bar{v}_D^n) \\ &\quad + \mathcal{U}^{-1}\text{diag}\{\omega_i^2\}\Xi^{-1}(0)K^{-1}\bar{v}_C^n. \end{aligned} \quad (2-72)$$

Substituting the definitions of $G(s)$ and $D_0(s)$ (since we assume that $D(s) = D_0(s)$ for these frequencies):

$$G(s) = \Xi(s)\Psi^{-1}(s)K, \quad D_0(s) = \mathcal{U}^{-1}K^{-1}\hat{\Psi}(s)\Xi^{-1}(s), \quad (2-73)$$

where $(\hat{\Psi})_{i,j} = (\Psi)_{i,j}(\delta(i,j) - 1)$, we obtain

$$\begin{aligned} \lim_{s \rightarrow 0} \bar{V}_{out}^m(s) &= -\mathcal{U}^{-1}K^{-1}[\Psi(0)\Xi^{-1}(0)\bar{v}_{A_e}^n + \hat{\Psi}(0)\Xi^{-1}(0)\bar{v}_D^n \\ &\quad - \text{diag}\{\omega_i^2\}\Xi^{-1}(0)\bar{v}_C^n + K\mathcal{U}\bar{v}_{\mathcal{U}}^n + \bar{a}^E], \end{aligned} \quad (2-74)$$

where dependencies on s have been omitted from all signals for brevity. After simplifying, we obtain for the r_x degree of freedom

$$\begin{aligned} \lim_{s \rightarrow 0} (\bar{V}_{out}^m(s))_{r_x} &= \frac{1}{\mathcal{U}_{r_x}k_{r_x}} \left[\frac{\omega_{r_x}^2}{\sigma_{r_x}^2} [\bar{v}_C^n - \bar{v}_{A_e}^n]_{r_x} + \frac{f_m}{\sigma_{\theta_y}} [\bar{v}_{A_e}^n - \bar{v}_D^n]_{\theta_y} \right. \\ &\quad \left. + \frac{f_m}{\sigma_{\theta_z}} [\bar{v}_D^n - \bar{v}_{A_e}^n]_{\theta_z} - \bar{a}_{r_x}^E - \mathcal{U}_{r_x}k_{r_x}(\bar{v}_{\mathcal{U}}^n)_{r_x} \right]. \end{aligned} \quad (2-75)$$

Under the assumption that all noise signals are uncorrelated, and uncorrelated with the measured signal, we obtain the noise spectral density:

$$\begin{aligned} S_{V_{out}^m}^{r_x} &= \frac{1}{\mathcal{U}_{r_x}^2 k_{r_x}^2} \left[\frac{\omega_{r_x}^4}{\sigma_{r_x}^2} (S_{\bar{v}_C^n}^{r_x} + S_{\bar{v}_{A_e}^n}^{r_x}) + \frac{f_m^2}{\sigma_{\theta_y}^2} (S_{\bar{v}_{A_e}^n}^{\theta_y} + S_{\bar{v}_D^n}^{\theta_y}) \right. \\ &\quad \left. + \frac{f_m^2}{\sigma_{\theta_z}^2} (S_{\bar{v}_D^n}^{\theta_z} + S_{\bar{v}_{A_e}^n}^{\theta_z}) + S_{\bar{a}^E}^{r_x} + \mathcal{U}_{r_x}^2 k_{r_x}^2 S_{\bar{v}_{\mathcal{U}}^n}^{r_x} \right]. \end{aligned} \quad (2-76)$$

To make Eq. (2-76) more comprehensible we make one more assumption. Since $C(s)$ and $D(s)$ are implemented with similar electronic components (since in both cases we will try to make them as quiet as possible), and since they are also connected to similar sources (the lock-in amplifiers) and loads (the feedback circuits), it

is reasonable to assume that their noise spectral density will be of similar magnitude. Thus, we conclude that $(S_{\bar{v}_C}^{r_x} + S_{\bar{v}_{A_e}}^{r_x})$, $(S_{\bar{v}_{A_e}}^{\theta_y} + S_{\bar{v}_D}^{\theta_y})$ and $(S_{\bar{v}_D}^{\theta_z} + S_{\bar{v}_{A_e}}^{\theta_z})$ should be of similar magnitude. Thus we can approximate Eq. (2-76) by

$$S_{V_{out}}^{r_x} = \frac{1}{v_{r_x}^2 k_{r_x}^2} \left[\left(f_m^2 \left(\frac{1}{\sigma_{\theta_y}^2} + \frac{1}{\sigma_{\theta_z}^2} \right) + \frac{\omega_{r_x}^4}{\sigma_{r_x}^2} \right) (S_{\bar{v}_C}^{r_x} + S_{\bar{v}_{A_e}}^{r_x}) + S_{a_e}^{r_x} + v_{r_x}^2 k_{r_x}^2 S_{\bar{v}_U}^{r_x} \right]. \quad (2-77)$$

Hence, the minimum detectable noise in closed loop operation is

$$(S_{a_{min}}^{r_x})_{c.l.} = \left[f_m^2 \left(\frac{1}{\sigma_{\theta_y}^2} + \frac{1}{\sigma_{\theta_z}^2} \right) + \frac{\omega_{r_x}^4}{\sigma_{r_x}^2} \right] (S_{\bar{v}_C}^{r_x} + S_{\bar{v}_{A_e}}^{r_x}) + v_{r_x}^2 k_{r_x}^2 S_{\bar{v}_U}^{r_x}. \quad (2-78)$$

Under the assumption of symmetry, we can rewrite for any translational degree of freedom

$$(S_{a_{min}}^r)_{c.l.} = \left(f_m^2 \frac{2}{\sigma_\theta^2} + \frac{\omega_r^4}{\sigma_r^2} \right) (S_{\bar{v}_C}^r + S_{\bar{v}_{A_e}}^r) + v_r^2 k_r^2 S_{\bar{v}_U}^r. \quad (2-79)$$

Comparing this result with Eq. (2-68), we find that

$$(S_{a_{min}}^r)_{c.l.} = (S_{a_{min}}^r)_{o.l.} + \left(f_m^2 \frac{2}{\sigma_\theta^2} + \frac{\omega_r^4}{\sigma_r^2} \right) S_{\bar{v}_C}^r + \left(f_m^2 \frac{2}{\sigma_\theta^2} \right) S_{\bar{v}_{A_e}}^r + v_r^2 k_r^2 S_{\bar{v}_U}^r. \quad (2-80)$$

Equation (2-80) allows us to make a comparison between the closed loop and open loop noise performance of the SSA-Ib. Based on this result, we conclude that:

- (1) The addition of a feedback controller can only worsen the noise performance of the SSA-Ib for the frequency range in question.
- (2) The effect of the controller noise ($S_{\bar{v}_C}^r$) can be reduced by increasing σ_r and σ_θ .
- (3) The effect of the SQUID noise ($S_{\bar{v}_{A_e}}^r$) can be reduced both in open and closed loop operation by increasing σ_i (the gain of the sensing circuits). It is important, though, to increase σ_i by maximizing the sensing currents I_s^i instead of increasing the gain of the lock-in amplifiers (i.e., instead of taking $Sens_i$ small), since the SQUID noise is also amplified by the lock-in amplifier gain (see Eq. (2-58)).
- (4) Increasing σ_i does not reduce the noise caused by the VCCS. Hence, for the satisfactory closed loop performance of the SSA-Ib, it is critical to design the

corresponding circuits as noiseless as possible. This will be taken into consideration in the Section 2.8.

We must keep in mind though that, as previously explained, this comparison is not entirely fair since it does not take into consideration the difference in coupling between the different axes of the SSA-Ib in open and closed loop operation. Hence, although conclusions 2, 3 and 4 will always be valid, conclusion 1 depends for its correctness on the signal being considered. An even more important consideration is that the comparison just made assumes that the parameters of the sensing mechanism are the same for open and closed loop operation. It is reasonable to assume that it will be possible to apply higher sensing currents I_s^i in closed loop operation than in open loop, since the proof mass will be much better balanced. This was in fact verified in SSA-I (the first prototype). Hence, it is possible that the *overall* noise level will be lower in closed loop operation than in open loop operation. Again, it is for this reason that great care was taken in the design of the VCCS, since it is the only noise source which we cannot attenuate by increasing the sensing currents.

2.7.3 Noise comparison between open and closed loop operation: Wide-band

In the previous section we examined the low frequency region in order to obtain relatively simple expressions which help us study the influence of the different instrument gains on the noise signals at the measured output⁵. Also, we determined the minimum measurable acceleration for the SSA-Ib in open and closed loop operation. From a different point of view, we can also interpret the results of the previous section as having obtained the *equivalent acceleration noise* due to the different noise sources

⁵Notice that once the controller is operational, the measurement output of the system is no longer the output of the lock-in amplifiers, but the voltage output of the controller.

both in open and closed loop operation. In this section we will take this approach, but we no longer limit the analysis to the low frequency region. The price we pay for this extension is that we will obtain results corresponding to a given controller implementation and a given configuration of the SSA-Ib, i.e., the nominal configuration in which it will be operated in closed loop.

Once the different measurement parameters of the SSA-Ib and the parameters of the controller are chosen, it is possible to obtain the transfer function between the different noise inputs and the measurement output over any desired frequency range. Moreover, once the hardware implementation is built, it is possible to accurately measure the contribution of each noise source, and obtain estimates of their contribution to the overall noise at the measured output. Finally, we can refer this noise contribution to equivalent acceleration noise, and thus obtain wide-band estimates of the lowest measurable acceleration.

This analysis complements the low frequency analysis shown in the previous section. As it was concluded that the controller will inevitably increase the noise level of the instrument, it is important to determine how significant this effect will be, and what happens at higher frequencies. The present analysis will allow us to determine whether the proposed closed loop configuration significantly affects the performance of the instrument in closed loop operation. As before, we assume that all the signals are stationary, uncorrelated, and uncorrelated to each other.

Modeled noise-to-output transfer functions

In order to estimate the contribution of the different noise sources on the measured output, a MATLAB program was written which calculates the different transfer functions between the noise sources and the measured controller output (\bar{V}_{out}^m). The results of these simulations follow. The parameters used in this simulation are the same as

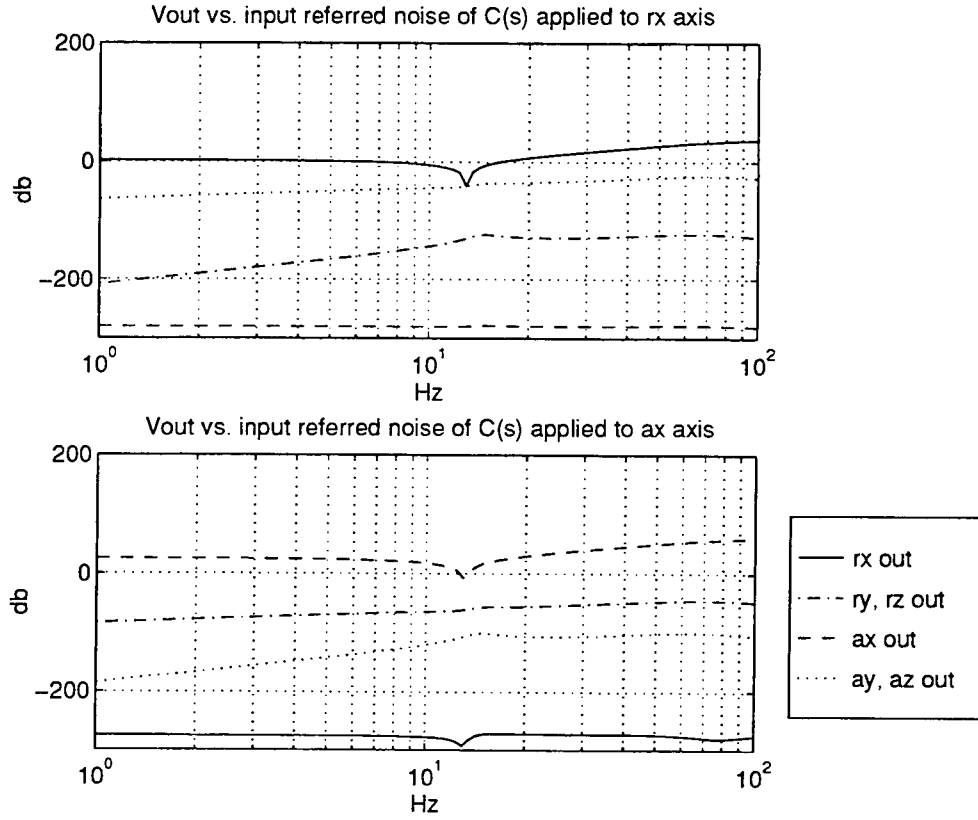


Figure 18: \bar{v}_C^n to \bar{V}_{out}^m transfer function

the ones used in the design of the controller. A complete set of these parameters can be found in Appendix B.

The top plot of Figure 18 shows the transfer functions between the measured outputs of the different degrees of freedom, and a noise signal applied to the r_x degree of freedom input of \bar{v}_C^n . Similarly, the bottom plot of Figure 18 corresponds to a signal applied to the θ_x input of \bar{v}_C^n . The same calculation was performed for all the noise sources in consideration. For example, Figure 19 corresponds to \bar{v}_C^n , and Figure 20 corresponds to the SQUID current noise \bar{i}_A^n (the relationship between the equivalent SQUID noise $\bar{v}_{A_e}^n$ and the SQUID current noise is given by Eq. (2-60)).

It is important to remember that these transfer functions correspond to a particular set of nominal parameters (i.e., gains of the sensing mechanism). Equations

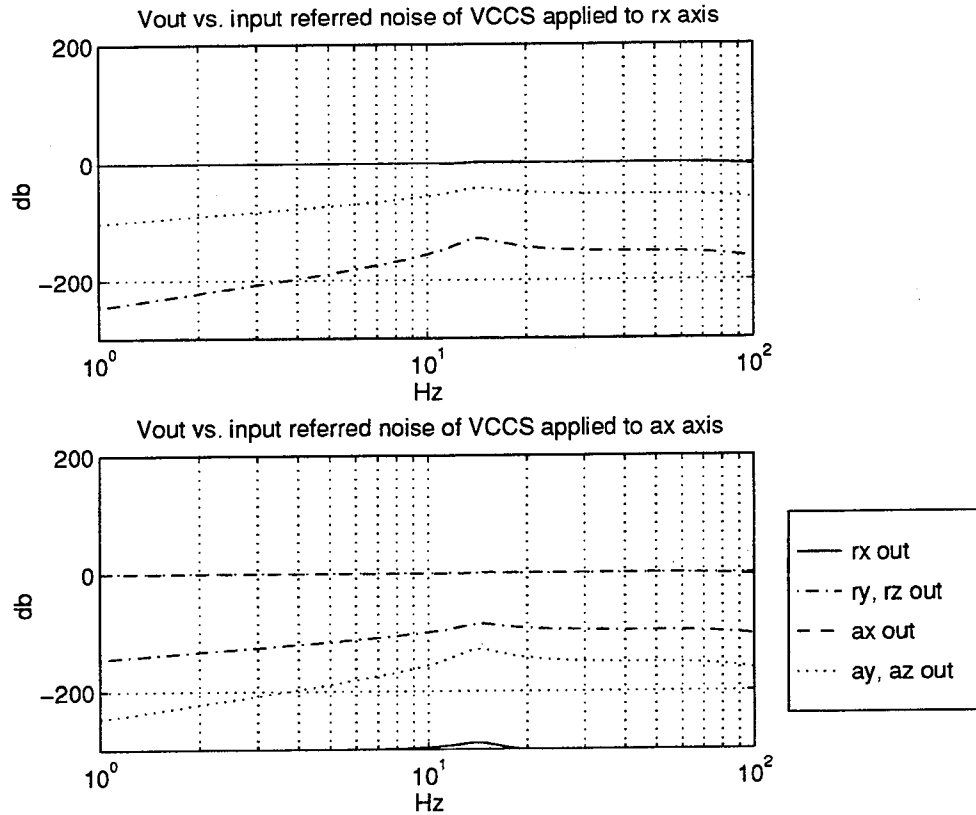


Figure 19: \bar{v}_U^n to \bar{V}_{out}^m transfer function

tion (2-74) is a good guide to understanding the relationship between these nominal parameters and the resulting transfer functions. For example, the gain of the transfer functions corresponding to \bar{v}_C^n (Figure 18) can be decreased by increasing the gains of the sensing circuits (σ_i), but the gains of the transfer functions corresponding to \bar{v}_U^n (Figure 19) cannot be modified by varying the parameters of the sensing mechanism (see Eq. (2-74)). As already mentioned, it is for this reason that special care was taken in the design and implementation of the VCCS.

Modeled equivalent acceleration noise

After completing the controller hardware we measured the power spectral density of the noise signals \bar{v}_C^n , \bar{v}_D^n and \bar{v}_U^n shown in Figure 17. As for the SQUID input current

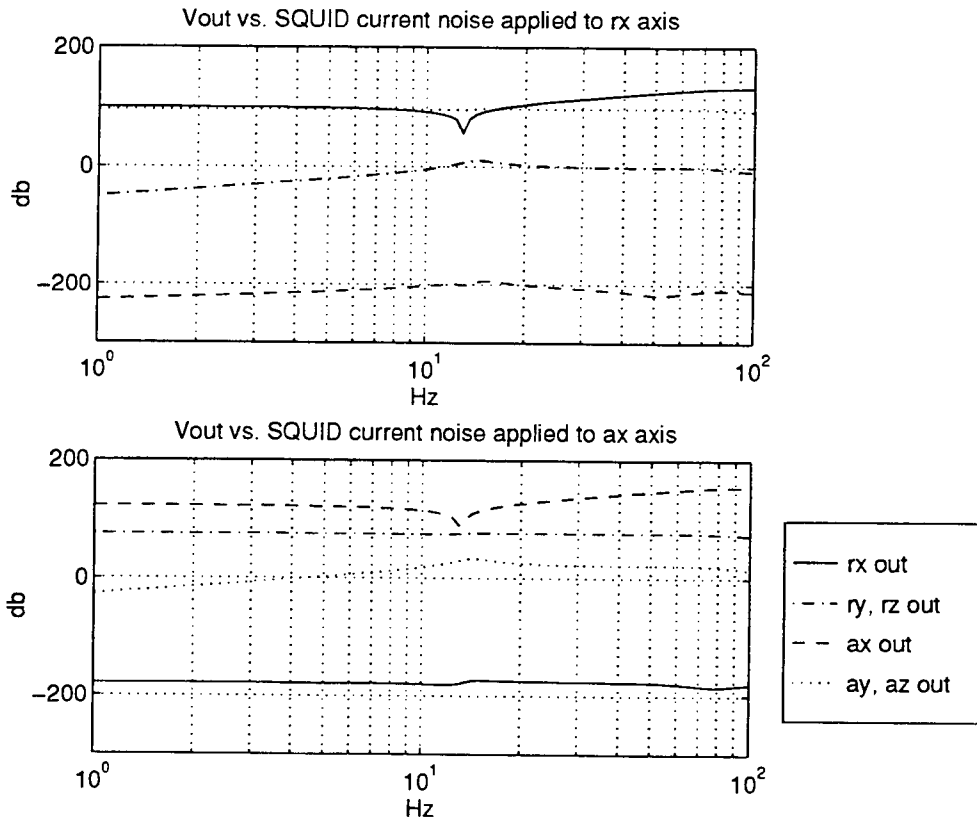


Figure 20: \bar{i}_A^n to \bar{V}_{out}^m transfer function

noise, we assume a noise spectral density of $10^{-11} \text{ A}/\sqrt{\text{Hz}}$. These measurements, together with the calculated transfer functions, were used to obtain the spectral density at the measured output (\bar{V}_{out}^m) due to the different noise sources. However, in order to make a comparison between open and closed loop operation of the SSA-Ib, all these noise signals were translated into equivalent acceleration noise, i.e., the equivalent noise signal at the acceleration input which would produce the given noise signal at the measured output, either the output of the lock-in amplifiers in open loop operation, or the voltage output of the controller in closed loop operation.

Figure 21 shows the equivalent acceleration noise produced by the measured input referred noise of the components of $C(s)$. In this calculation, we assume that all six channels of $C(s)$ are noisy, and that all the channels have the same input referred

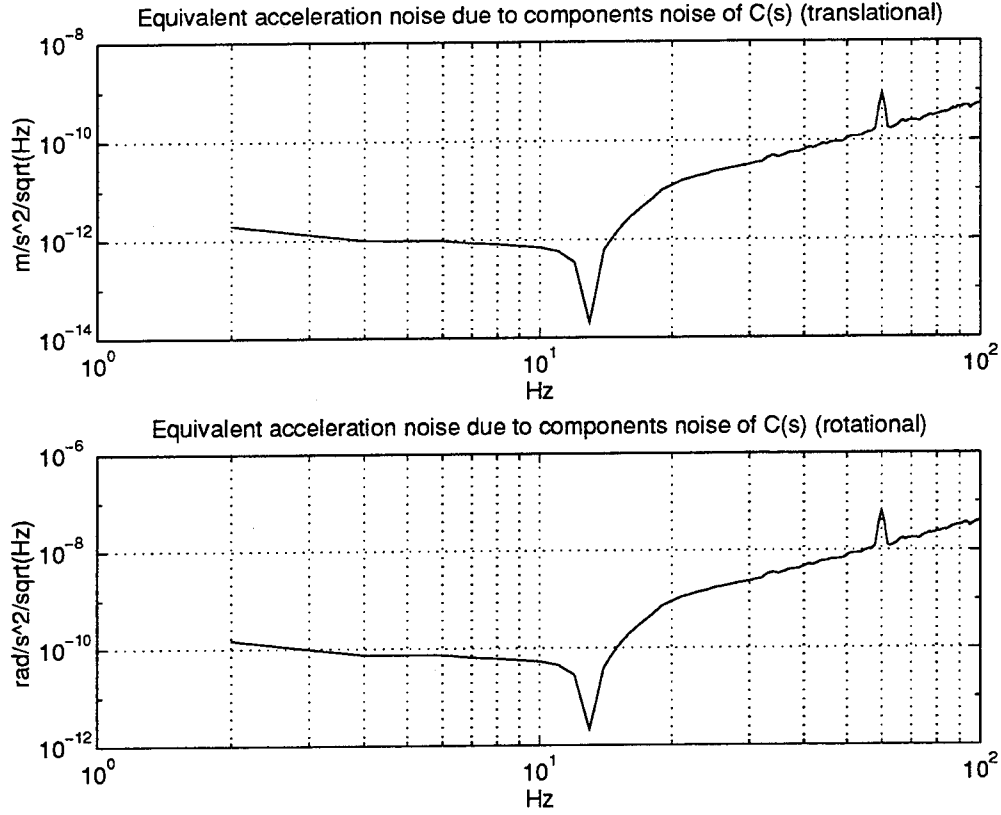


Figure 21: Equivalent acceleration noise spectral density due to \bar{v}_C^n

noise. Thus, due to the symmetry of the system, we get the same noise level for all outputs corresponding to translational degrees of freedom, and the same noise levels for all outputs corresponding to rotational degrees of freedom. Hence, each plot in Figure 21 corresponds to three overlapping traces. Similarly, Figure 22 shows the equivalent noise acceleration due to $D(s)$, Figure 23 corresponds to the noise due to the VCCS, and Figure 24 corresponds to the noise due to the SQUID in closed loop operation.

Most interesting is to compare the overall equivalent acceleration noise in closed and open loop operation. Figure 25 shows the contribution of the SQUID both in open and closed operation, and the overall contribution of the controller. As expected, the contribution of the SQUID in open and closed loop operation is almost

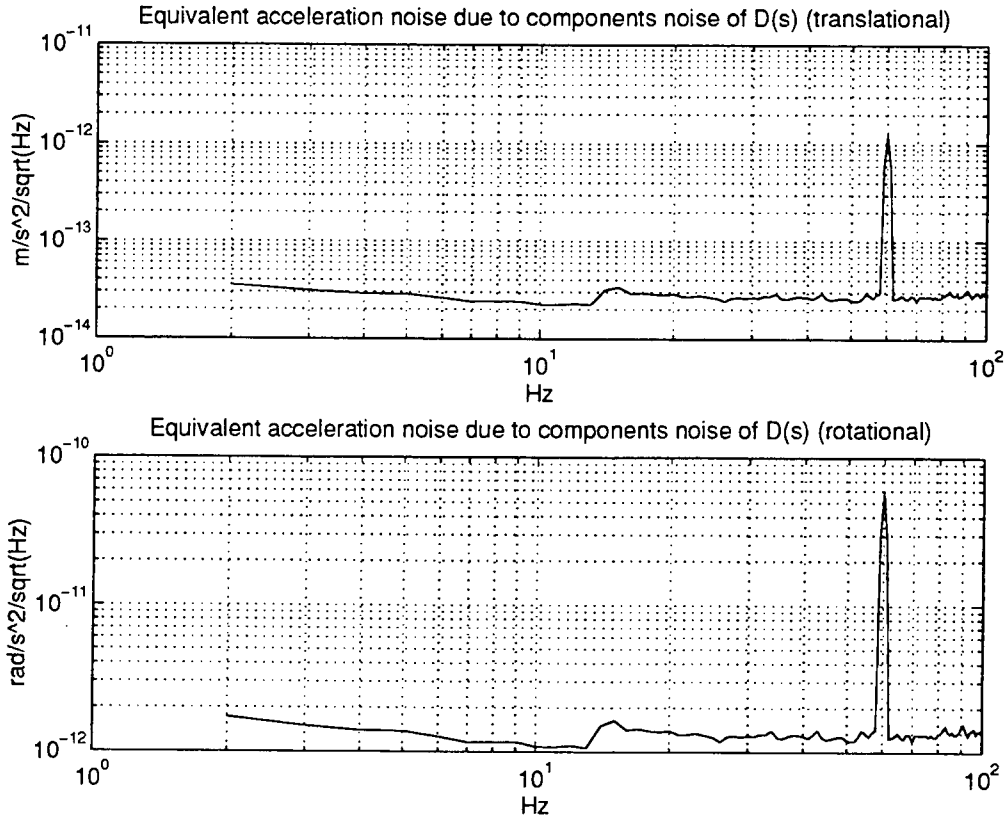


Figure 22: Equivalent acceleration noise spectral density due to \bar{v}_D^n

identical. Especially significant is the fact that the contribution of the controller is significantly lower than that of the SQUID at frequencies below the resonance ($\omega < \omega_i$). In other words, the noise performance of the SSA-Ib is almost the same in open and closed loop operation over the frequency region of interest, and currently the noise limitation is imposed by the SQUID, not the controller implementation. Hence, although the controller does add noise to instrument, the contribution is neglectable below the resonance frequency of the plant, and the performance loss is thus minimal. It is important to keep in mind though, that these conclusions are valid for the nominal parameters, and that the comparison was made assuming that the same parameters were used in open and closed loop operation. As already mentioned, it is reasonable to expect that it will be possible to use higher sensing

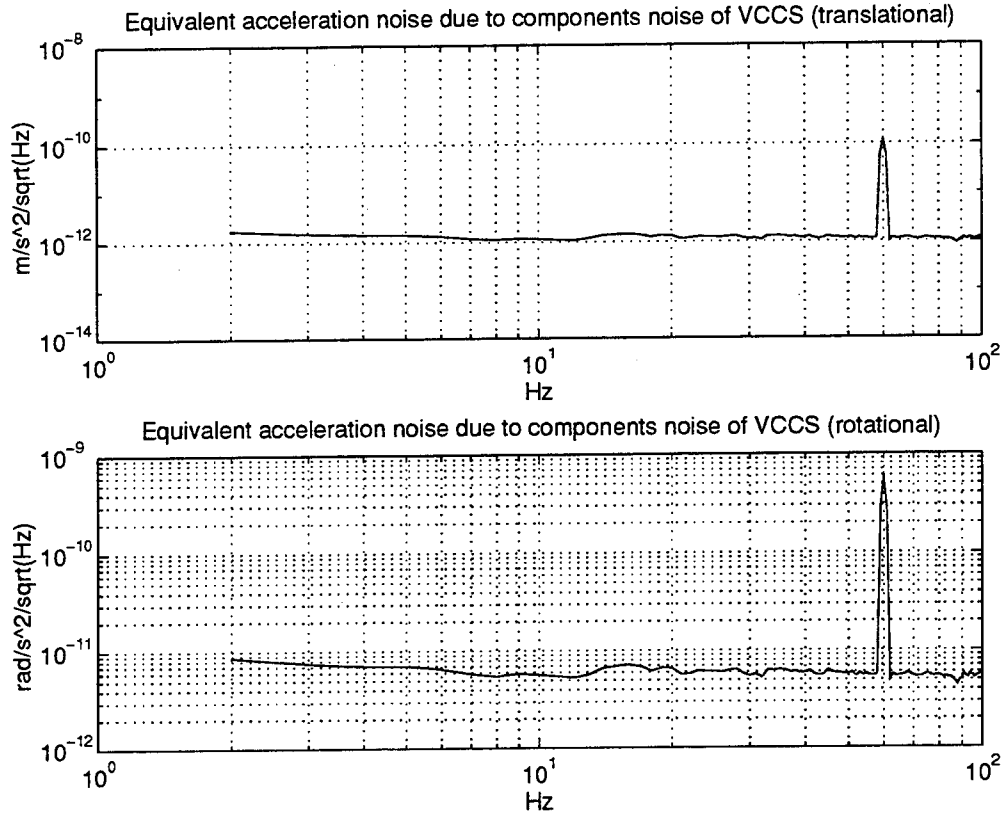


Figure 23: Equivalent acceleration noise spectral density due to \bar{v}_G^n

currents in closed loop operation since the balance of the proof mass will be much better. This was in fact our experience with SSA-I, the first experimental prototype of the six axis accelerometer. Based on this observation, and in the results of the preceding analysis, it is entirely possible that the noise performance of the SSA-Ib could in fact improve with the addition of feedback control. The most significant result of this section is then that:

- (1) The equivalent acceleration noise due to the SQUID is almost the same in open and closed loop operation.
- (2) The overall equivalent acceleration noise in closed loop operation is dominated by the SQUID noise for all frequencies below the SSA-Ib resonance.

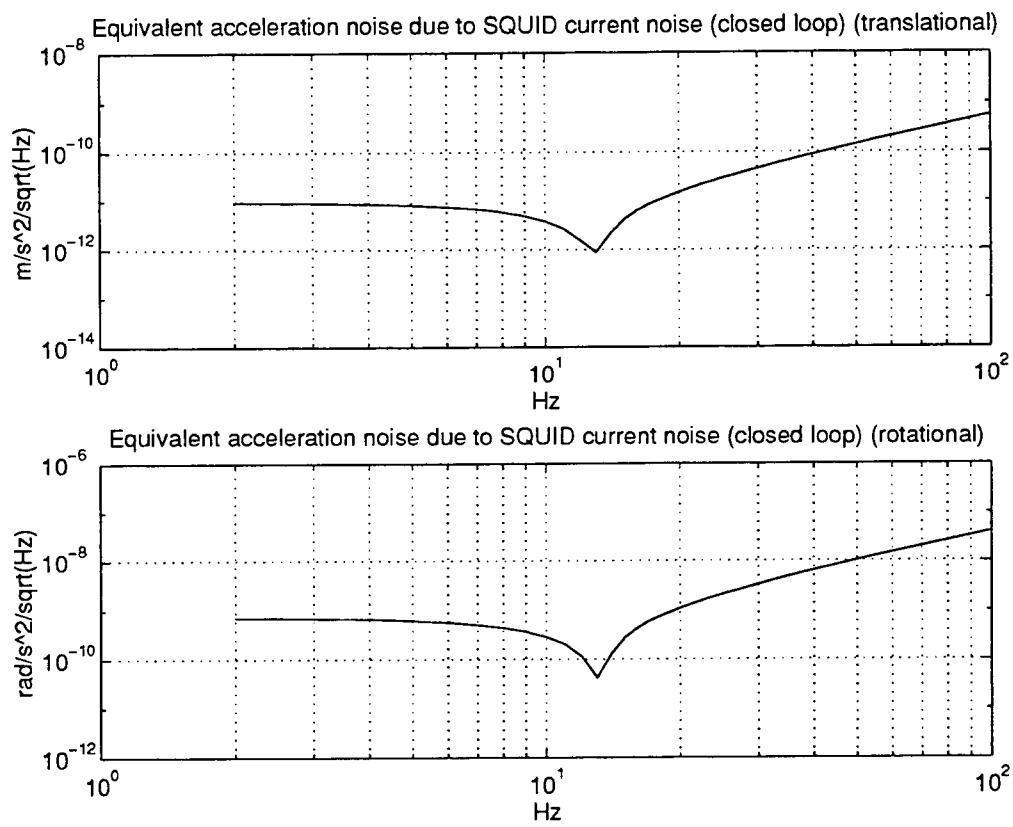
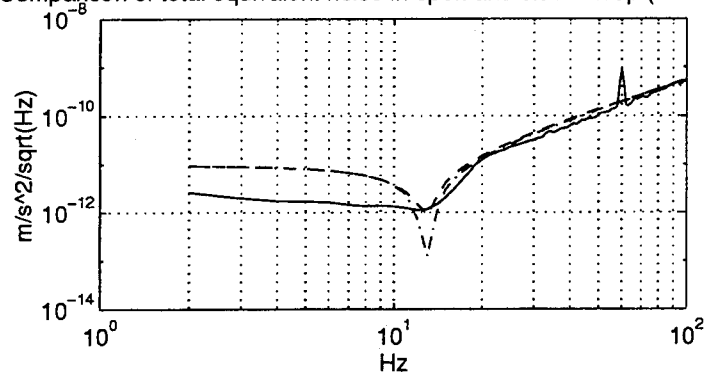


Figure 24: Equivalent acceleration noise spectral density due to \bar{i}_a^n

Comparison of total equivalent noise in open and closed loop (translational)



Comparison of total equivalent noise in open and closed loop (rotational)

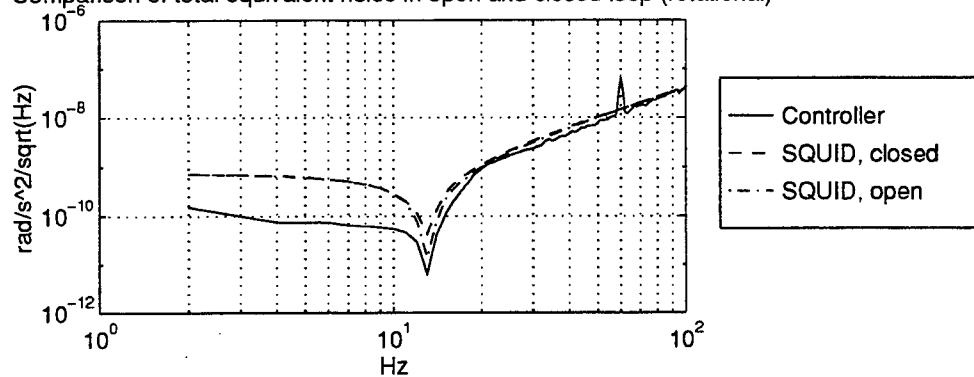


Figure 25: Comparison of equivalent acceleration noise spectral density of open loop and closed loop systems

2.8 Controller Implementation

In the design of a controller for the SSA-Ib, both an analog and a digital implementation were considered. However, although digital controllers offer great advantages in flexibility, technical considerations led to the choice of an analog implementation. One important constraint is the sensitivity of the SQUID to rf interference. Because of its inherent rf clock noise, it is desirable in general to avoid having digital circuits attached to the sensitive superconducting circuitry. More importantly, the use of a digital controller would have required to sacrifice one of the most significant advantages of the SQUID sensing circuit, its large dynamic range. Generally, digital controllers are 16 bit devices, which would limit the resolution of the inputs and outputs to ± 1 part in 32K. Averaging techniques and expensive components can stretch this limit by a few more bits, but that still does not match the dynamic range of the SQUID.

Table 3 shows the parameters used as nominal operating conditions for the SSA-Ib. The complete set of nominal operating parameters used in the design of the controller is included in Appendix C. While the controller design is based on these values, there is significant flexibility built into the system, and it is capable of performing even if any of these parameters changes. For example, the open loop gain of each individual feedback channel can be adjusted, if it becomes necessary either due to uncertainty in the SSA-Ib dynamics or changes in the gains of the instruments used to sense the position of the proof mass.

2.8.1 Controller structure and transfer functions

The structure of the controller is shown in Figure 26. It consists of a total of 12 independent cards, out of which 6 are input cards and 6 are output cards, with

Nominal parameters used in controller design		
Maximum measurable acceleration		
Translational		10^{-4} m/s^2
Rotational		$5 \times 10^{-4} \text{ rad/s}^2$
SQUID gain		$10^4 \text{ V/A (scale 3)}$
VCCS (sensing current drive) gain		1 A/V
Lock In amplifier		
Vosc.		100 mV (rms)
Gain (Sens.)		$10 (1 \text{ V})$
Levitation Currents		
Translational		4.88554 A
Rotational		0.48855 A

Table 3: simulation parameters

a total of 12 inputs and 12 outputs: 6 voltage inputs (V_i^{in}) which receive signals corresponding to the position of the proof mass (these signals are produced by the the lock-in amplifiers), 6 noise inputs (V_i^n) for diagnostic and tuning purposes, 6 voltage outputs (V_i^{out}) which correspond to the accelerations being measured, and 6 current outputs (I_i^{out}) which feed currents to the levitation circuits of the SSA-Ib. In Figure 26, the dashed rectangle corresponds to an input card and each dotted rectangle corresponds to an output card. This structure was chosen for its modularity, which simplifies the design, implementation and debugging of the circuitry. In the following sections we provide detailed explanations of the considerations involved in the design of each of these cards, and more specifically, of each sub-circuit within each card.

The main technical challenge for an analog implementation is to deliver the required dynamic range. For this reason, great care was taken in optimizing the dynamic range of the overall controller, and maintaining the noise produced by it to a

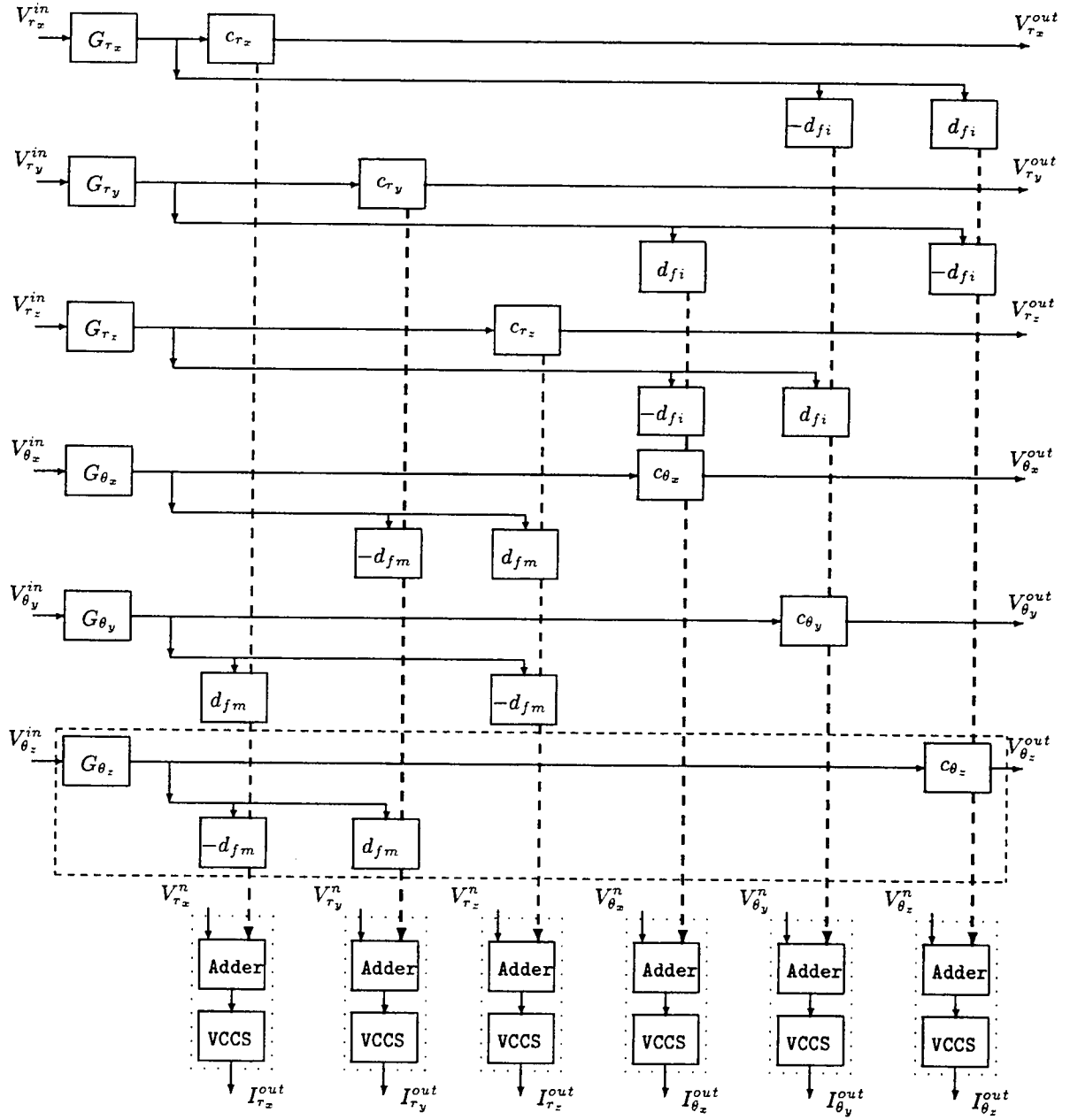


Figure 26: Structure of controller implementation

minimum. In order to optimize the dynamic range of the overall instrument, the gain of the VCCS in the output stage of the controller was chosen so that for the maximum possible signal at the input of the VCCS (10 V), a feedback current corresponding to the maximum measurable acceleration would be produced. The maximum acceleration was chosen based on the knowledge of the acceleration environment of the platform obtained from previous tests. Once this gain is chosen, all the other gains of the transfer functions are set.

As will be pointed out in the description of the circuitry of the output card, extreme care was taken in making the VCCS stage and the adder stage in the output card of each channel as gain-stable as possible. The reason for this requirement is the following. Due to the topology of the closed loop, any variation in the gain between the output voltage (V^{out} , see the controller diagram) and the acceleration input will appear as a variation of the gain of the closed loop system. Thus, the gain between these two points must be extremely stable. Special care was taken both in the circuit configuration and the components used to achieve the best possible gain-stability for this section of the output card. This can also be seen in Eq. (2-49), where the gain of the closed loop transfer function is proportional to the gain of the VCCS.

All the circuits of the controller were implemented with three similar operational amplifiers: OP27, OP227 and OP177. All these operational amplifiers have very low voltage noise, voltage offset, and voltage offset temperature drift. A few subtle differences motivated choosing among them in different sections of the circuit.

The OP27 was chosen as the building block of the controller because of its excellent noise and stability characteristics. The OP227 is simply a dual OP27 and was used in some critical parts of the circuit where good matching between the operational amplifiers was desired. The OP177 has a lower voltage offset, bias current and offset current than the OP27, but has higher voltage noise and lower slew rate. It is better matched to higher input impedances, where the effect of a bias current and

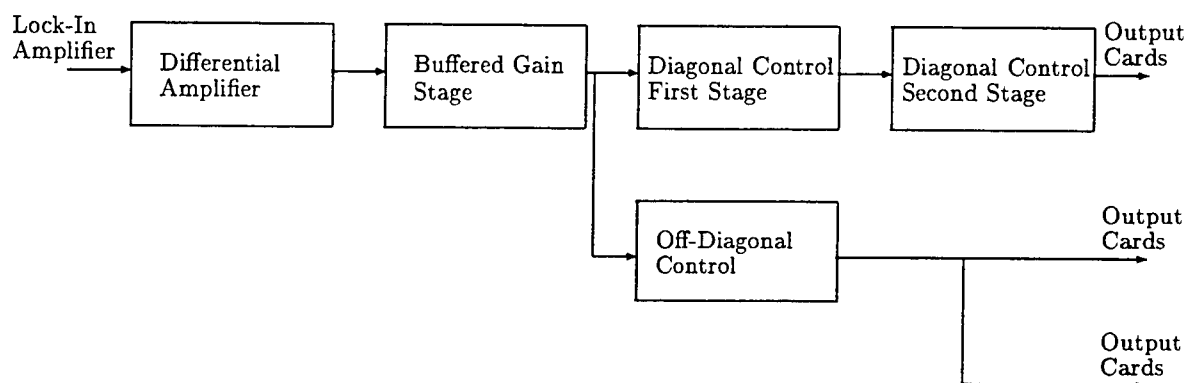


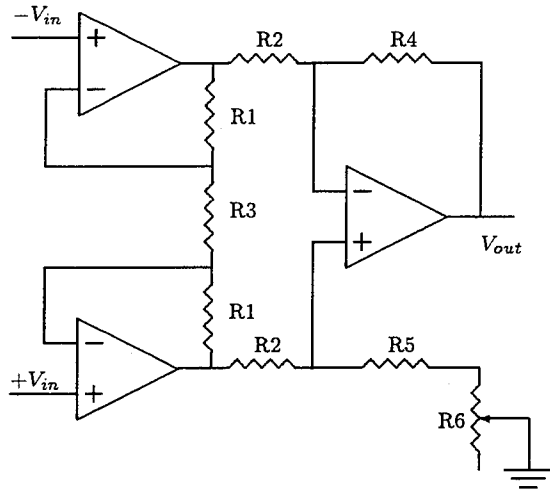
Figure 27: Input card schematic

bias current drift is more important, and where low voltage noise is less important. Care was taken to check that its lower slew rate did not introduce distortion. It was used in some sections of the circuit where it was desired to avoid the need for a resistor between the positive leg of the operational amplifier and ground, and where its higher voltage noise and lower slew rate did not adversely affect the performance of the circuit.

Input Card

Figure 27 shows a block diagram of the input card. Its main components are:

- (1) Differential amplifier: Receives a signal proportional to the position of the proof mass from the lock-in amplifier. Its high CMRR reduces interference and problems associated with different ground potentials between the instruments.
- (2) Buffered gain: Controls the overall gain for the corresponding axes, and acts as a buffer between the differential amplifier and the following stages.
- (3) Diagonal control first stage: Implements part of the diagonal transfer function of the controller (integrator, 120 Hz zero, 1200 Hz pole).



	Trans.	Rot.
Gain	1.35	21
R1	4.99 kΩ	4.99 kΩ
R2	2.0 kΩ	2.0 kΩ
R3	28 kΩ	0.5 kΩ
R4	2.0 kΩ	2.0 kΩ
R5	1.96 kΩ	1.96 kΩ
R6	0.2 kΩ	0.2 kΩ

Figure 28: Schematic diagram of differential amplifier stage

- (4) Diagonal control second stage: Implements part of the diagonal transfer function of the controller (complex conjugate zeros, 200 Hz pole and 170 Hz pole).
- (5) Off-diagonal stage: Implements part of the off-diagonal transfer function of the controller.

Differential amplifier

The circuit transfer function is given by (see Figure 28)

$$G_{diff} = \frac{R4}{R2} \frac{(R3 + 2R1)}{R3} (V_{in+} - V_{in-}).$$

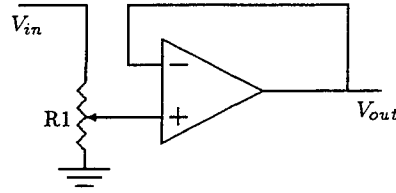
The differential amplifier is part of the block G_i , $i = r_x, \dots, \theta_z$ in Figure 26. Made with one OP227 and one OP27, it is a standard implementation of a differential amplifier. This stage of the circuit receives the signal from the lock-in amplifier corresponding to the position of the proof mass. Its high common mode rejection ratio reduces radiated interference received by cables and eliminates problems associated with different ground potentials in different instruments.

Design Parameters: The gain of the differential amplifier was chosen to obtain

the maximum possible dynamic range. Hence, an input signal of maximum possible amplitude would result in an output signal of 10 V (which is the maximum nominal voltage for this circuit). In order to calculate the maximum possible input signal for this stage, a simulation program was written in MATLAB which produces the magnitude of the output of each stage of the controller (and in this case, of the lock-in amplifier) as a function of frequency, assuming that the maximum tolerable acceleration is experienced at all frequencies. This program was used to calculate the gains of each stage of the controller in an optimal way.

For this stage, the maximum input signal takes place at the resonance frequency of the corresponding axes. The calculated gain assumes a maximum measurable acceleration of 10^{-4} m/s^2 for the translational degrees of freedom and $5 \times 10^{-4} \text{ rad/s}^2$ for the rotational degrees of freedom (see Table 3). As a result, the desired gains are 1.33 for the translational degrees of freedom, and 19.72 for the rotational degrees of freedom. The implemented gains were chosen slightly higher than the modeled gains (1.35 for the translational degrees of freedom and 21 for the rotational degrees of freedom) because we can always decrease the overall gain of the stage with the help of the following stage (buffered gain stage) but we cannot increase it.

In order to obtain the best possible common mode rejection ratio, an OP227 was used in the first stage of the differential amplifier. The OP227 has the advantage of operating as a pair of matched OP27's. DC offset adjustment and common mode rejection tuning were implemented according to the manufacturer's recommendations. This minimizes voltage noise, without unnecessarily loading the OP's. The DC offset network was chosen to adjust voltage offsets at one of the OP227's over a range of $\pm 56 \text{ } \mu\text{V}$. As suggested by the manufacturer, two $4.99 \text{ k}\Omega$ and a variable $0.2 \text{ k}\Omega$ resistors were used. Common mode rejection and DC offset potentiometers are not accessible when all the circuit boards are installed in the box, and must be adjusted beforehand.



	Trans.	Rot.
R1	5.0 kΩ	5.0 kΩ

Figure 29: Schematic diagram of buffered gain control stage

Buffered gain

The buffered gain is part of the block G_i , $i = r_x, \dots, \theta_z$ in Figure 26. This stage is both a gain control stage and a buffer stage to guarantee that enough current is available to drive the following stages without loading the differential amplifier stage. It is implemented as a simple buffered voltage divider with a single OP27 (see Figure 29). It controls the overall gain of the controller for a given input card, so that if changes in the gain of the sensing instrumentation are necessary, the open loop gain can be maintained by adjusting only the buffered gain stage of the corresponding input card.

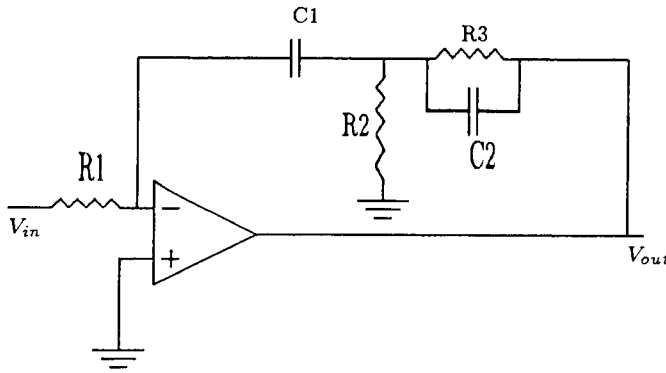
Design Parameters: The value of the potentiometer, $R1 = 5 \text{ k}\Omega$, was chosen so as not to draw too much current from the previous stage, while maintaining the voltage noise due to this resistor low. The potentiometer is mounted in the upper edge of the card, so it can be adjusted even when the cards are installed in the box. Notice that by implementing this stage in this fashion, it is possible to vary the gain down to zero, or in other words, completely cancel any chosen input.

Diagonal control first stage

The circuit transfer function is given by (see Figure 30)

$$c_{i_1}(s) = \frac{1}{R1 \frac{C1C2}{C1+C2}} \frac{(s + \frac{R2+R3}{(C1+C2)R2R3})}{s(s + \frac{1}{C2R3})}, \quad i = r_z, \dots, \theta_z.$$

The diagonal controller had to be divided into two stages for its implementa-



	Trans.	Rot.
R1	14.5 k Ω	14.5 k Ω
R2	13.0 k Ω	13.0 k Ω
R3	1.3 k Ω	1.3 k Ω
C1	1 μ f	1 μ f
C2	0.1 μ f	0.1 μ f

Figure 30: Schematic diagram of first diagonal control stage

tion. The following is a description of the first of these stages. This stage is part of the block c_i , $i = r_x, \dots, \theta_z$ (see Figure 26). This section of the controller input card implements the following transfer function:

$$c_{i1}(s) = g_{i1} \frac{(1 + \frac{s}{z_1})}{s(s + \frac{s}{p_3})}, \quad i = r_x, \dots, \theta_z.$$

This implementation was achieved with a single OP177. The OP177 was chosen over the OP27 because its very low bias current eliminates the need for a resistor between the positive leg and ground to match the source resistances of the two inputs. In addition, the Johnson noise of the source resistance (approximately $R1 = 14.5 \text{ k}\Omega$) produces approximately $15 \text{ nV}/\sqrt{\text{Hz}}$ which is greater than the voltage noise of the OP177 ($10 \text{ nV}/\sqrt{\text{Hz}}$) and much greater than the voltage noise of the OP27 ($3 \text{ nV}/\sqrt{\text{Hz}}$), so there is no advantage in using the low noise OP27.

Design Parameters: Most of the values of this stage were chosen to obtain the required pole (at 1200 Hz) and zero (at 120 Hz) using standard component values. The only free parameter left was $R1$, the resistance at the input of this stage (which determines the overall gain of the stage, g_{i1}). As with all other stages, the main consideration in choosing the gain of this stage was to maximize the dynamic range. Hence, as with the differential amplifier stage, the gain of this stage was chosen so that at the maximum input signal to this stage, the output signal would have the maximum possible amplitude. Since both the differential amplifier and the buffered

gain stage have flat transfer functions, the maximum input signal shows up at the same frequency as at the input of the differential amplifier, i.e., at the resonance frequency of the corresponding axes. Also, since the same consideration was used for the differential amplifier, the amplitude of the input signal at this frequency will be 10 V (assuming the buffered gain stage is set to its maximum gain, 1). Hence, the gain of this stage was chosen to be 1 at the resonance frequency of the corresponding axes, which corresponds to $R1 = 14.5 \text{ k}\Omega$.

Diagonal control second stage

The circuit transfer function is given by (see Figure 31)

$$c_{i_2}(s) = \frac{R4}{R3} \frac{s^2 + (\frac{1}{R1C1} - \frac{R3}{R8R2C1})s + \frac{R3}{R7R6R2C1C2}}{s^2 + (\frac{1}{R1C1})s + \frac{R4}{R5R7R2C1C2}}, \quad i = r_x, \dots, \theta_z.$$

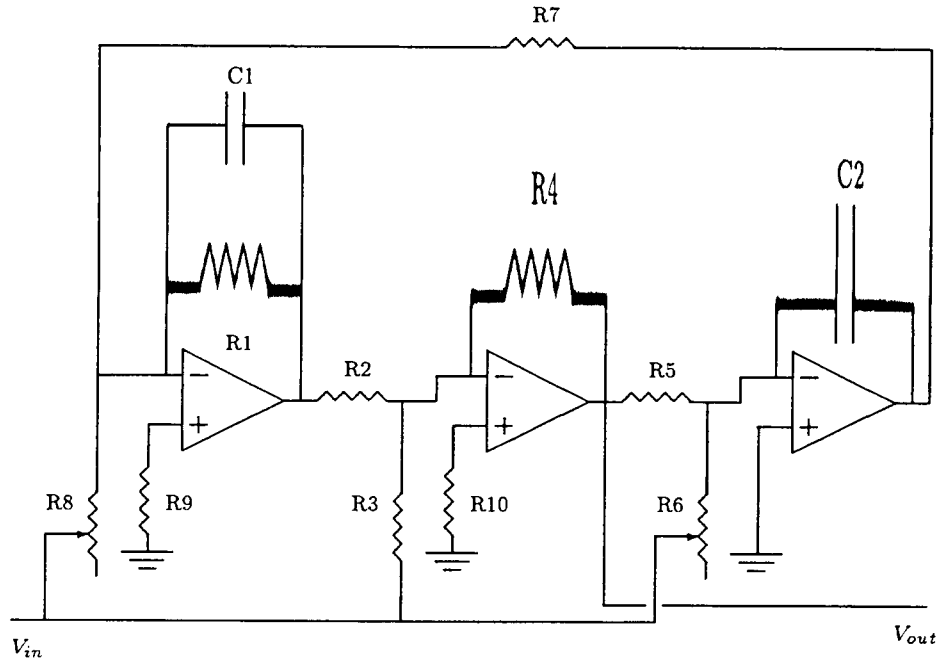
The second stage of the diagonal controller implements the following transfer function:

$$c_{i_2}(s) = g_{i_2} \frac{(z_s^2 + z_s/Qs + s^2)}{(1 + \frac{s}{p_1})(1 + \frac{s}{p_2})}, \quad i = r_x, \dots, \theta_z.$$

This stage is part of the block c_i , $i = r_x, \dots, \theta_z$ (see Figure 26).

Design Parameters: This circuit was chosen because it allows the frequency and quality of the complex zeros to be tuned independently, each with a single potentiometer. An admissible set of components was chosen to implement the desired poles and the pair of tunable complex conjugate zeros. The variable resistor R6 (see Figure 31) controls the frequency, while R8 controls the damping of the complex conjugate pair of zeros. The designed and implemented values are:

	12 Hz	21 Hz	implemented low	implemented high
R8	4.301 k Ω	4.328 k Ω	4.26 k Ω	4.36 k Ω
R6	87.24 k Ω	28.49 k Ω	114 k Ω	14 k Ω



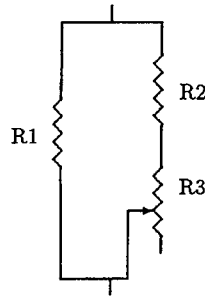
	Trans.	Rot.		Trans.	Rot.
R1	4.32 k Ω	4.32 k Ω	R7	20 k Ω	20 k Ω
R2	1.0 k Ω	1.0 k Ω	R8	4.26-4.36 k Ω	4.26-4.36 k Ω
R3	1.0 k Ω	1.0 k Ω	R9	1.96 k Ω	1.96 k Ω
R4	100 k Ω	100 k Ω	R10	0.5 k Ω	0.5 k Ω
R5	39.2 k Ω	39.2 k Ω	C1	0.1 μ f	0.1 μ f
R6	14-114 k Ω	14-114 k Ω	C2	1 μ f	1 μ f

Figure 31: Schematic diagram of second stage of diagonal control stage

The values of these resistors were chosen to enable the tuning of this stage to resonance frequencies between 12 and 21 Hz, while maintaining the resonance damping at 4, according to the controller design.

To improve resolution, R8 was implemented as shown in Figure 32. These values allow the controller to be tunable for resonance frequencies between 10.5 and 30 Hz. All other values were chosen as close as possible to their designed values.

This stage was implemented with two OP27's and one OP177. The effective source impedance of the rightmost OP in Figure 31 is relatively high. Therefore, an OP177 is better matched, and is used instead of an OP27. The potentiometers



	Trans.	Rot.
R1	6.23 kΩ	6.23 kΩ
R2	13.5 kΩ	13.5 kΩ
R3	1.0 kΩ	1.0 kΩ

Figure 32: Detail of R8

which control both the frequency and quality of the complex zeros are mounted in the upper edge of the card, so that they can both be adjusted even when all the cards are installed in the box.

Off-diagonal filter

The circuit transfer function is given by (see Figure 33)

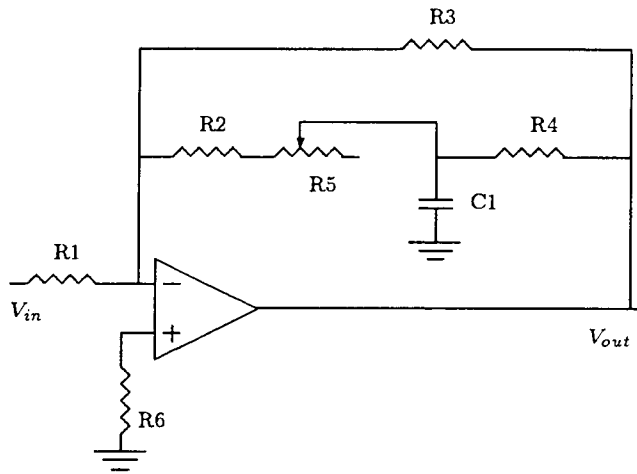
$$d_{i_2} = \frac{R3}{R1} \frac{\left(s + \frac{R2+R4+R5}{C1R4(R2+R5)}\right)}{\left(s + \frac{R2+R4+R5+R3}{C1R4(R2+R5)}\right)}, \quad i = fi, fm.$$

This section of the controller input card implements the following transfer functions:

$$d_i = g_{i_1} \frac{(s + 785.398)}{(s + 7853.98)}, \quad i = fi, fm.$$

This stage is part of the blocks d_{fi} and the blocks d_{fm} in Figure 26. It is implemented with a single OP27. This stage includes a zero at 125 Hz (to “cancel” the pole introduced at the output filter of the lock-in pole amplifier) and a pole at 1250 Hz.

Design Parameters: Once an admissible set of components was chosen to implement the desired transfer function, the only parameter left was the gain of this stage. The gain of this stage was chosen so as to avoid saturation, while maintaining the output signal relatively large, although not necessarily maximal. This stage was



	Trans.	Rot.
R1	5.49 k Ω	78.4 k Ω
R2	2.49 k Ω	2.49 k Ω
R3	46.4 k Ω	46.4 k Ω
R4	2.49 k Ω	2.49 k Ω
R5	0.5 k Ω	0.5 k Ω
R6	2.49 k Ω	2.49 k Ω
C1	1.0 μ f	1.0 μ f

Figure 33: Schematic diagram of off-diagonal controller stage

not optimized for dynamic range because the optimal gain would have required the use of relatively large resistors at the adder stage of the output cards, which would have increased the noise level of the instrument. The potentiometer controlling the frequency of the zero (nominally at 125 Hz) is located at the upper edge of the circuit card, and thus accessible when all the cards are installed in the controller box.

Output Card

Figure 34 shows a block diagram of the output card. Its main components are:

- (1) Buffered independent gain stages: Provides independent gain control of each for the signals received from the input cards (diagonal and off-diagonal signals). This also allows to completely cancel any specific signal. These stages also act as buffers to avoid loading the input cards unnecessarily.
- (2) Diagonal output gain stage: Provides the correct scaling so that the output voltage is easily related to the measured acceleration. It also provides part of the gain required for the diagonal feedback loops.

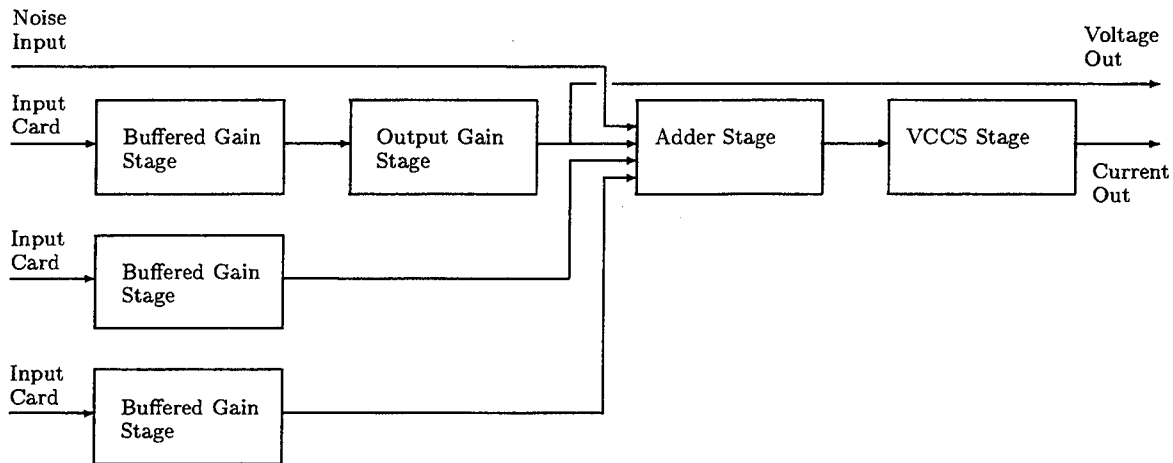


Figure 34: Output card schematic

- (3) Adder stage: Produces a weighted sum of the signals received from the input cards, and from a noise input used for diagnostic purposes. It also allows for sign changes in these signals, if necessary (except for the noise signal).
- (4) Voltage controlled current source (VCCS): Converts the voltage signal into a current signal to be applied to the feedback coils of the SSA-Ib.

Independent gain stages

Each of these variable gain stages are implemented as buffered voltage dividers (see Figure 35). Their purpose is to provide independent control of the gain corresponding to the diagonal and off-diagonal components of the control signal before they are added. Also, these stages act as buffers to avoid loading the input cards unnecessarily. Each of these stages are implemented with a single OP27.

Design Parameters: As in the input card, the only parameter to be chosen is the resistance $R1$. As in the case of the input card, a value of $R1 = 5 \text{ k}\Omega$ was chosen.

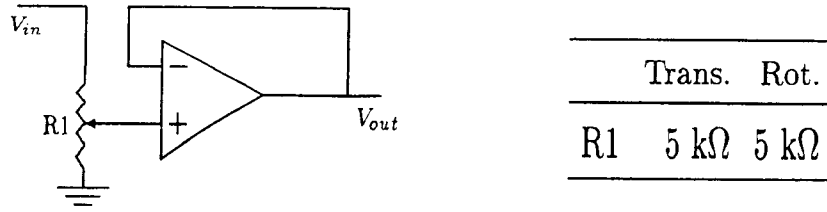


Figure 35: Schematic diagram of independent gain stages

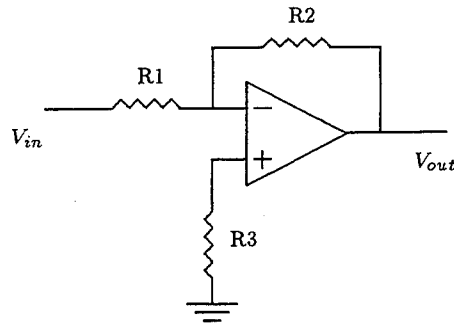
Diagonal output gain stage

This stage (see Figure 36) provides additional gain for the measured acceleration output (V_i^{out}). The gain of this stage was chosen so that a 10 V output signal corresponds to the maximum measurable acceleration for the corresponding axes. In this way, the dynamic range of the circuit is optimized. Also, this stage provides part of the gain required for the diagonal components of the feedback system.

Design Parameters: The only parameter to be chosen for this stage is its gain, and the resistance values to implement it. The gain was fixed by the considerations previously explained, so that for the translational degrees of freedom we obtain a gain of 9.731, and for the rotational degrees of freedom we obtain 9.724. The components were chosen so as to obtain a gain value as close as possible to the required while using standard components (and avoiding the use of large resistance values).

Adder stage

The adder stage produces at its output a weighted sum of the signals at its input. It adds all the required signals to be fed to the feedback coils of the levitation circuit of the corresponding axes of the accelerometer. This adder has been designed to provide the option of changing the sign with which each signal is added (see Figure 37). The adder stage also includes a noise input for diagnostic and tuning purposes. It is implemented with two OP177's.

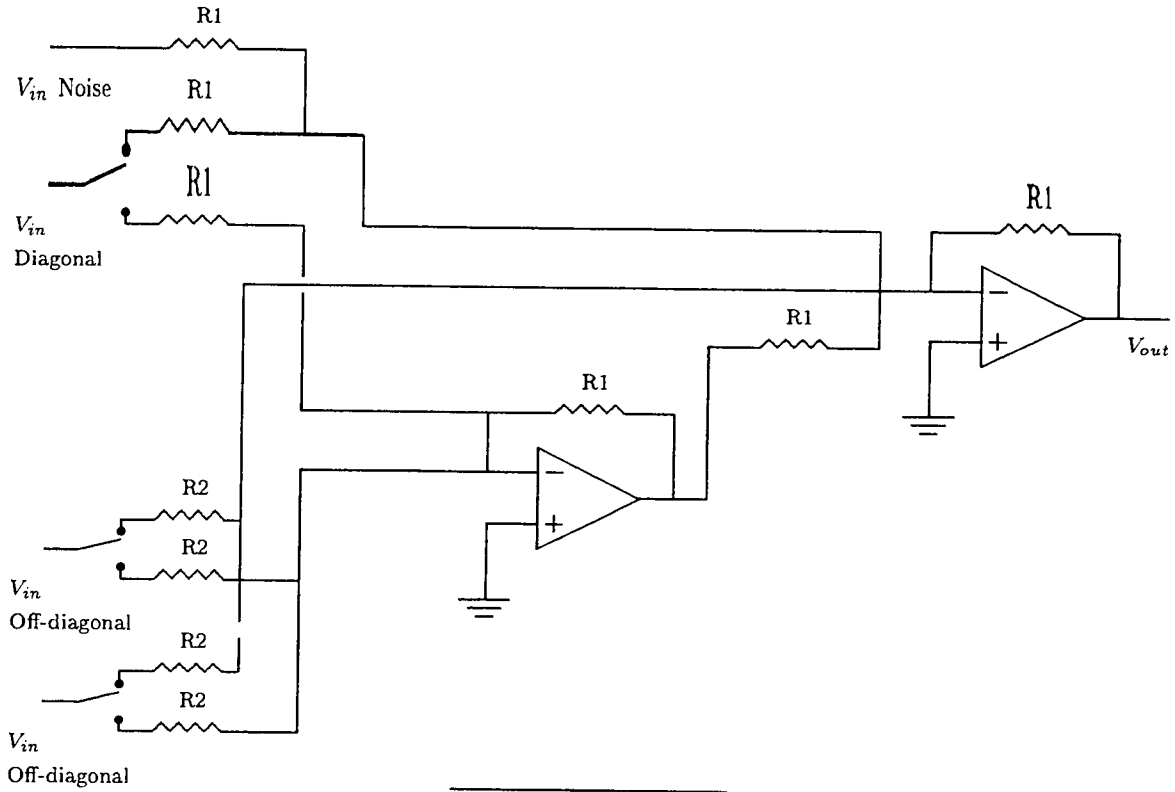


	Trans.	Rot.
gain	9.72	9.72
R1	4.32 k Ω	4.32 k Ω
R2	42 k Ω	42 k Ω
R3	4.32 k Ω	4.32 k Ω

Figure 36: Schematic diagram of diagonal output gain stage

Design Parameters: The resistors which determine the gain of the signal corresponding to the diagonal control term are very accurate and highly stable with respect to temperature variations. The resistor pairs which control the different gains of this stage are physically part of a monolithic resistor network with extremely low differential temperature coefficients. Hence, the resulting gains for each of the channels of this adder stage are extremely stable. All this provisions were taken as a result of an analysis made of the gain stability of the closed loop system. As this analysis reveals, in order to achieve the required gain stability for the overall closed loop system, it is critical that the gain of the controller stages between the measurement point (V_i^{out}) and the current output (I_i^{out}) be as stable as possible. For this reason, the resistors used for this stage and the next stage of the controller (the VCCS) were chosen to have very low temperature coefficients (0.5 - 1.5 ppm for Vishay networks 300144 and 300145, 0.6 ± 1.5 ppm for S102C and ± 2.5 ppm for S102K resistors), and very good absolute accuracy and matching.

The gain of the off-diagonal paths was calculated so as to provide the overall desired off-diagonal gain. As mentioned in the off-diagonal stage of the input card, the choice of gain in this stage and in the input card stage was a compromise between good dynamic range and maintaining the values of the required resistors at the output card relatively low.



	Trans.	Rot.
R1	2 k Ω	2 k Ω
R2	28 k Ω	20 k Ω

Figure 37: Schematic diagram of output stage adder

VCCS: Voltage-to-current converter

The final stage of the controller converts the voltage feedback signal produced by the controller into a current signal. Defining G to be the gain of the differential amplifier in the feedback loop, i.e., $G = (2R5 + R6)/R5$, and assuming $2R7 \gg Zl$ and $GR2 \gg R3$, the voltage-to-current transfer function of this stage is

$$v_i(s) = \frac{R3}{GR1R7} \frac{1}{(sC1R3G + 1)}.$$

As with all previous stages of the controller, the parameters of this stage were chosen so as to optimize the dynamic range of the controller. Also, as mentioned in

the previous section, because the gain of this stage is critical to the gain stability of the controller, great care was taken in using very stable components.

Design Parameters: In order to obtain the best possible gain stability for this stage, great care was taken in the selection of the components used in the implementation. All the resistors for this stage of the controller were chosen to have very low temperature coefficient (0.5 - 1.5 ppm for Vishay networks 300144 and 300145, 0.6 ± 1.5 ppm for S102C and ± 2.5 ppm for S102K resistors), and very good absolute accuracy and matching. Furthermore, all the resistors R4, R8, as well as R5 and R6 are part of resistor networks embedded in single components, having extremely low differential temperature coefficients so that the respective ratios remain constant even if there are severe temperature changes. Similarly, the capacitor C1 was chosen to have the lowest possible temperature coefficient, and relatively high absolute accuracy.

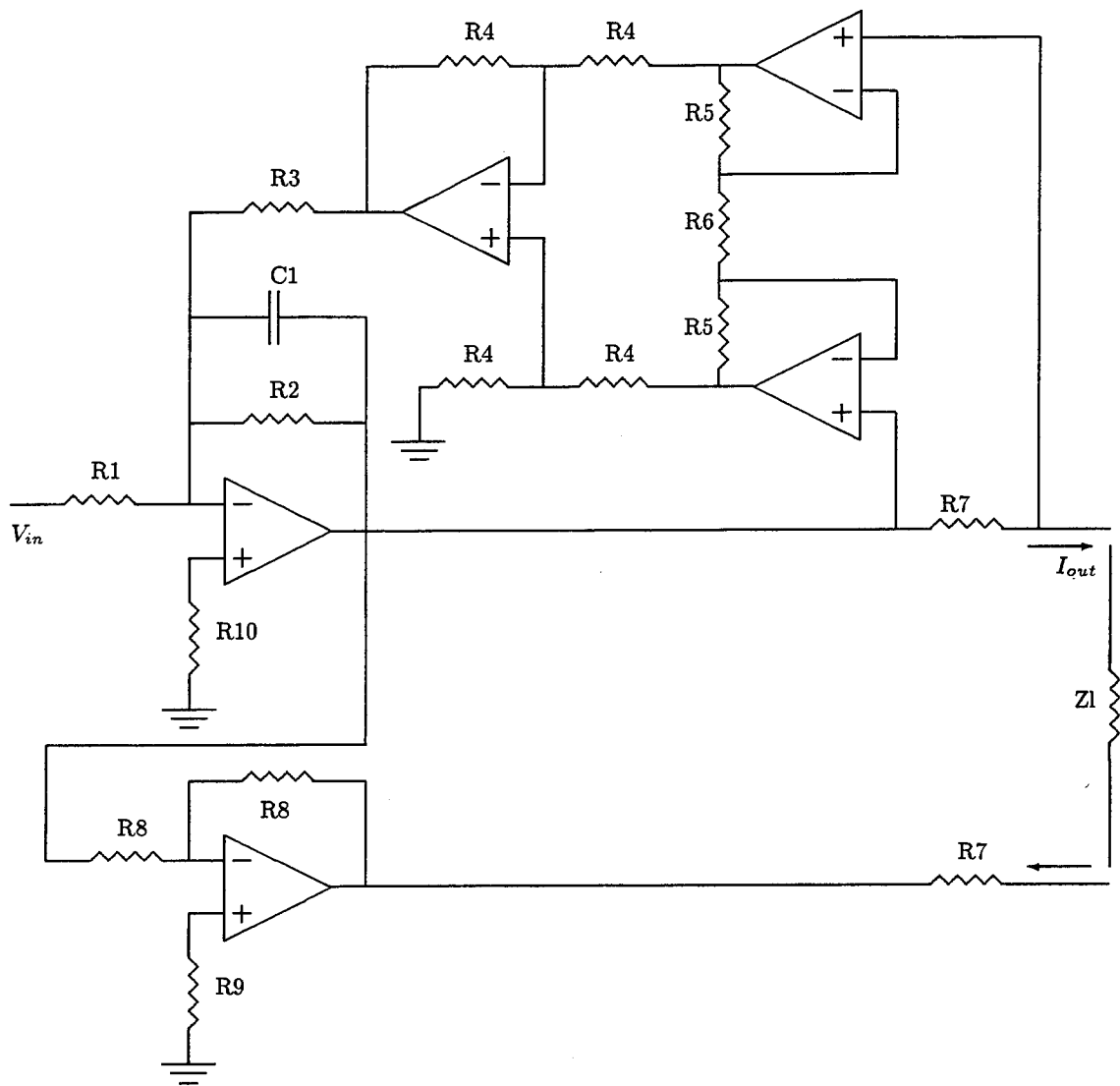
The first parameter to be chosen for this section was the shunt resistor (R7). Because two OP's are used to provide a "push-pull" configuration, the overall compliance of the output stage of this circuit is 20 V. Since the maximum required current is 1 mA, the shunt resistor could not exceed $10\text{ k}\Omega$ (The impedance of the load can be neglected for our application). On the other hand, since it is impossible to implement a differential amplifier of gain 1 (with the given configuration), and in order to improve the common mode rejection of the differential amplifier, it was decided to implement a differential amplifier with gain 2 in the feedback loop. Then, in order to avoid saturation of the output of the differential amplifier for the maximum required current, the value of the shunt resistor was chosen to be $5\text{ k}\Omega$.

Next, the overall gain of the VCCS was designed so that for the maximum possible signal at the input of the VCCS (10 V), a feedback current corresponding to the maximum measurable acceleration would be produced. The desired gains and the implemented ones are shown in Table 4.

	designed gain	implemented gain
Translational	-46.09 $\mu\text{A}/\text{V}$	-46.1 $\mu\text{A}/\text{V}$
Rotational	-92.48 $\mu\text{A}/\text{V}$	-92.6 $\mu\text{A}/\text{V}$

Table 4: Designed and implemented parameters of VCCS

Another consideration was to provide as much bandwidth as possible to the VCCS, so that variations in the capacitor value (which is the least stable component of the circuit, and which determines the VCCS bandwidth) due to temperature changes would not affect the gain of the VCCS for the frequency range of interest, and also so that the dynamics of the VCCS would not affect the performance of the controller. The bandwidth of the VCCS as designed is 14.5 kHz.



	Trans.	Rot.		Trans.	Rot.
Gain	-46.1 $\mu\text{A/V}$	-92.6 $\mu\text{A/V}$	R6	4 k Ω	4 k Ω
R1	2.17 k Ω	1.08 k Ω	R7	5 k Ω	5 k Ω
R2	200 k Ω	200 k Ω	R8	2 k Ω	2 k Ω
R3	3 k Ω	3 k Ω	R9	1 k Ω	1 k Ω
R4	2 k Ω	2 k Ω	R10	1 k Ω	1 k Ω
R5	2 k Ω	2 k Ω	C1	0.1 μf	0.1 μf

Figure 38: Schematic diagram of output VCCS stage

2.9 Preliminary Testing of the SSA-Ib Controller

A complete version of the SSA-Ib feedback controller has been built and tested to verify noise levels, transfer functions, and other performance requirements. The results of these tests show that the controller implementation fulfills all design objectives. Tests of the controller connected to the SSA-Ib have also been performed, and no interaction problems have been found between the two systems. Individual axes of the SSA-Ib have been operated in closed loop, without causing any negative effects on the SQUIDs such as unlocks. Acceleration measurements over relatively long periods of time (on the order of 1 to 3 days) with individual axes of the SSA-Ib operating in closed loop have also been made without any problems. However, the full performance of the feedback configuration has not been achieved due to the problems to be discussed below.

2.9.1 SQUID saturation

Dynamic resistance:

We have observed the presence of out-of-phase signals of larger than expected magnitude at the output of the lock-in amplifiers. Apparently, these signals are caused by dynamic resistance in the sensing coils. The dynamic resistance of the sensing coils produces a current signal at the input of the SQUID which has a frequency equal to the modulation frequency of the lock-in amplifier of the corresponding axes, and is phase shifted by 90° . Moreover, the magnitude of this signal is proportional to the magnitude of the sensing current of the corresponding axes. Since the SQUID is sensitive to both the in-phase and the out-of-phase components of the signals detected by the sensing coils, the presence of an unexpectedly large out-of-phase components limits the magnitude of the current which can be used to drive the sensing circuits.

Sensing/levitation inductive coupling:

A large low frequency signal corresponding to the motion of the proof mass has been detected at the output of the SQUID. This problem arises due to the presence of mutual inductance between the sensing and levitation coils. The coupling between the sensing and levitation coils causes the sensing coils to detect current signals induced by the motion of the proof mass in the levitation coils. These signals appear in the low frequency region (base-band) of the spectrum due to the low frequency dynamics of the proof mass, and are in turn sensed by the SQUID.

As a result of these two effects, the input stage of the SQUID is saturated at lower sensing currents than expected, forcing a decrease in the magnitude of the achievable sensing currents. The main consequence of decreasing the magnitude of the sensing currents is analyzed in Section 2.7 section. Equations (2-68) and (2-79) show that the equivalent acceleration noise due to the SQUID current noise (in both open and closed loop operation) is inversely proportional to the sensing currents. Thus, the presence of dynamic resistance in the sensing coils, and the mutual inductance between the sensing and the levitation coils effectively limit the achievable sensitivity of the instrument.

2.9.2 Controller saturation and unmodeled dynamics

The mutual inductance between the sensing and the levitation coils has an additional detrimental effect. As mentioned earlier, the coupling between these two circuits produces a low frequency noise signal at the input of the lock-in amplifier. After demodulation by the lock-in amplifier, this signal is aliased to high frequencies (more precisely, to the modulation frequency of the lock-in amplifier). Since in the design of the controller large signals were not expected at high frequencies, we have noticed that the controller can be saturated at gains lower than expected.

In order to avoid the problems associated with these high-magnitude high-frequency signals at the input of the controller, it has been necessary to introduce additional filtering of the signal at the output of the lock-in amplifier. This has been done in practice by making use of the high pass filters at the input of the lock-in amplifiers. As a result of these additional filters, and because these filters were not included in the original controller design (unmodeled dynamics), the full performance of the feedback configuration has not been achieved. The reason for not achieving the desired performance is that the presence of unmodeled dynamics makes it impossible to increase the gain of the feedback controller to the required levels.

The problem arising due to the addition of unmodeled dynamics is one of *conditional stability*, which did not appear in the original design. Conditional stability means that the closed loop system can become unstable for some gains between zero and nominal, but not at nominal gains. Thus, it is not the case that the closed loop system is unstable when operating at nominal parameters, but there are intermediate gains at which the system does become unstable. Since the first step to operate the SSA-Ib in closed loop is to gradually increase the gains of the controller up to their nominal values, it is in this process that the instability occurs. The fact that these unexpected filtering poles produce such a drastic effect should not be considered as a design flaw, and indeed is not very surprising. The SSA-Ib has such low damping coefficients (or such high quality factors) at the resonance frequencies that the addition of unexpected poles would have posed a similar problem for any possible design.

In a first attempt to solve this problem without extensive modification of the SSA-Ib, a new MATLAB simulation program which includes these additional poles has already been developed, and testing of possible modifications of the controller has already begun. At this stage, we hope that minor changes to the controller parameters will solve the problem. An alternative approach might require a complete redesign of

the controller. If such need arises, the modular structure of the controller will make it unnecessary to completely redesign the controller implementation.

It should also be mentioned that high gain feedback with a similar (and much more primitive) controller was possible in SSA-I, and high bandwidth closed loop transfer functions were achieved. This experience with SSA-I indicates that it should be possible to achieve the required performance of SSA-Ib. Also, it is worth mentioning that SSA-I used different SQUIDs than those being used in SSA-Ib, and it is possible that the difference in the SQUIDs (dynamic range, for example) contributes to some of the problem encountered.

2.10 Future enhancements

Recent measurements on the SSA suggest several design changes that could overcome obstacles preventing it from fully achieving its inherent sensitivity. The most important obstacle to overcome is the out-of-phase component of the bridge balance. It is believed that this signal is proportional to the misbalance of the resistive component of the ac bridge. The superconducting coils of the bridge have a resistive component to their impedance because they are inductively coupled to the metal coil forms. Better matching between the resistive components may be hard to achieve because it depends on factors that are difficult to control. For example, the coupling to the coil form will depend on the coil-proof mass gap, which will not be matched, even with the inductance bridge in balance, because of imperfect matching of coil form heights and imperfect alignment of the enclosure walls.

One way to greatly reduce the effective coil resistance is by changing the material of the coil form to a dielectric, such as Macor, a machineable glass-ceramic used for the coil forms of the SGG. Although the metal coil forms do provide some attenuation from rf signals coupled through the oscillator leads, the gradiometer described in Section 3, which also uses an ac displacement sensing technique, has recently operated successfully using Macor coil forms. Switching to Macor coil forms was considered early in the SSA program, but was rejected because of high machining costs. However, winding coils on the metal forms without short circuits requires many more steps than winding coils on insulating forms, so that the lower coil winding cost will more than make up for the higher machining cost. Based on experience with the ac gradiometer, we expect that the resistive component of the bridge mismatch will be reduced by at least an order of magnitude, so that it will no longer be an important limitation on the drive current. In this case, the drive current will be limited by the SQUID dynamic range and the level of platform accelerations. On a very quiet platform, drive currents large enough to give optimum coupling should be attainable.

Another problem that complicates the operation of the SSA is the coupling between the levitation and sensing coils. As discussed in Section 2.5.1, this could be greatly reduced by putting a gap between the coils using a small dummy coil. Reducing the available coil area will increase the necessary levitation current somewhat, but the current will still be low enough that the levitating field does not exceed the critical field of niobium. Decreasing the coil-proof mass gap will also reduce the coupling.

Improvement of the dimensional accuracy of the SSA, particularly the parallelism and orthogonality of the coil form and proof mass surfaces, would improve the performance of the SSA. It would better the alignment of the sensitive axis. It would also reduce the torquing and bias currents required to balance the angular acceleration bridges. The present housing design (see Figure 2) is not ideal from the standpoint of precision assembly. The chamfered surfaces on each of the pieces that make up the enclosure walls must accurately mate with four similar surfaces, and the cylindrical surfaces must fit with close tolerance inside the holes of the precision cube. Thus, there are many constraints on the position of each part that must be simultaneously satisfied. A new design for the housing is shown in Figure 39. In this design, four of the enclosure walls are cut out of a single block using wire EDM (electric discharge machining), a process that can usually hold tolerances of $\pm 2.5 \mu\text{m}$. The surfaces that mate with the end caps can also be cut in this way. The only requirements on the end caps are then that they be flat and parallel, requirements that are easily met with standard machining techniques. It is expected that this housing design could reduce the dimensional errors by nearly an order of magnitude, to a few parts in 10^4 . This would require an improved proof mass, which could be obtained by cutting a new mass out of a single block using EDM.

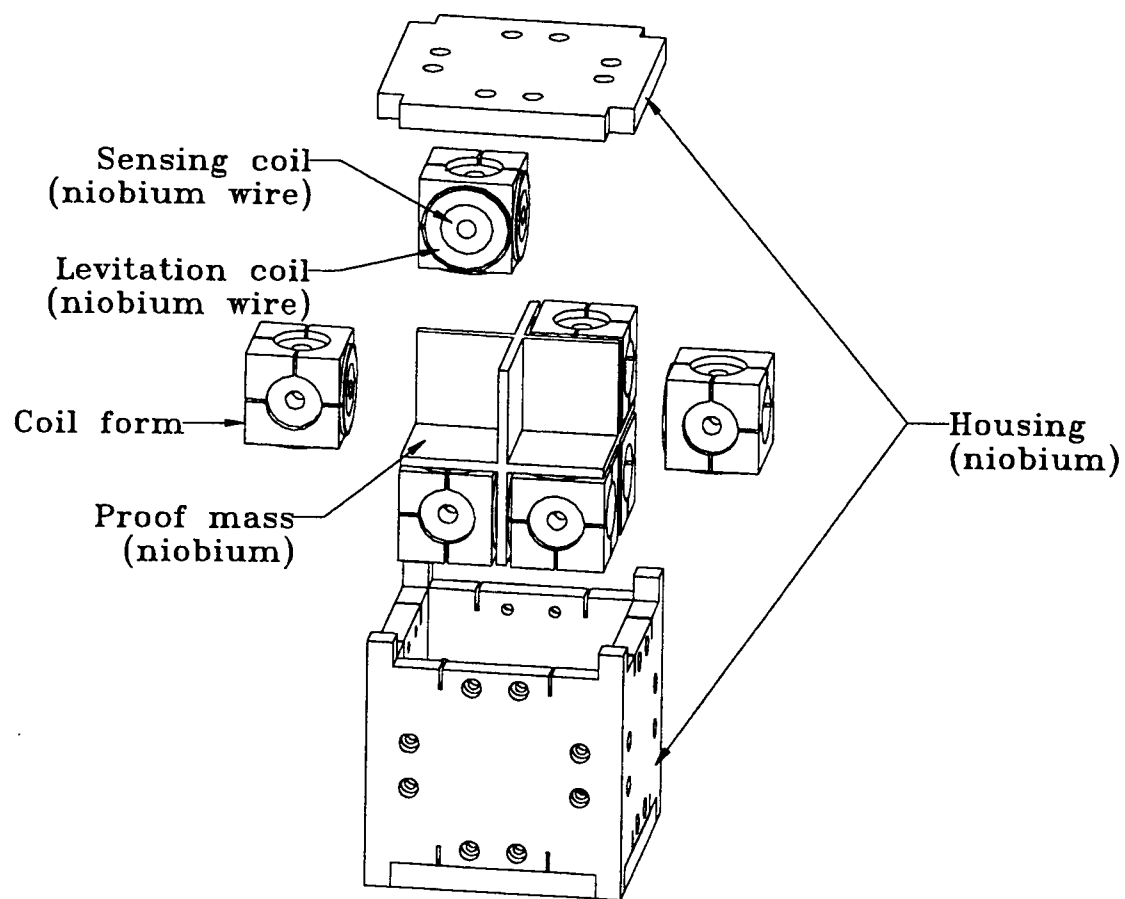


Figure 39. SSA showing improved housing design.

3. AC GRADIOMETER

3.1 Introduction

Development of the Superconducting AC gravity gradiometer (SAGG) was initiated with the intent of producing an instrument suitable for moving base applications. Previous gravity gradiometers developed at the University of Maryland have sensed test mass positions using persistent (dc) currents which are constant in time, provided that the test masses are stationary. In contrast, the SAGG uses sinusoidal (ac) sensing currents.

This provides various advantages and disadvantages relative to the dc gradiometer. Most of the fundamental noise sources are the same for both devices, but limitations on available electronics suggest that the SAGG will have a sensitivity inferior to that of the dc device, except possibly at frequencies far below the $1/f$ knee of the SQUID amplifier. However, the dc devices suffer from step changes in the output (due to SQUID control loop unlocks) which, if not compensated for, give rise to a loss of continuity in the data. This problem makes it difficult to acquire low frequency data. The SAGG uses the same type of amplifier, but because of the modulation of the sensing current, an unlock event only produces a short length of bad data, with continuity before and after the unlock.

A moving base device, contrasted with a fixed gradiometer, is likely to have a less stringent requirement on absolute sensitivity, but is much more subject to large transient electrical and vibrational inputs which can produce unlock events. Possible moving base applications include measurements aboard airplanes, trucks, and elevators. All these situations are considerably more harsh than the laboratory environment. For moving base applications, we can expect acceleration transients of about 0.01 to $1 g_E$ to occur during a measurement interval of perhaps 15 minutes to 3 hours. This compares to a laboratory environment with accelerations of $10^{-7} g_E$ and measurement intervals of about 10 to 100 seconds. Both dc and ac gradiometer designs may ultimately be developed into moving base devices, but at present the SAGG appears to have significant advantages.

3.2 Principles of Operation

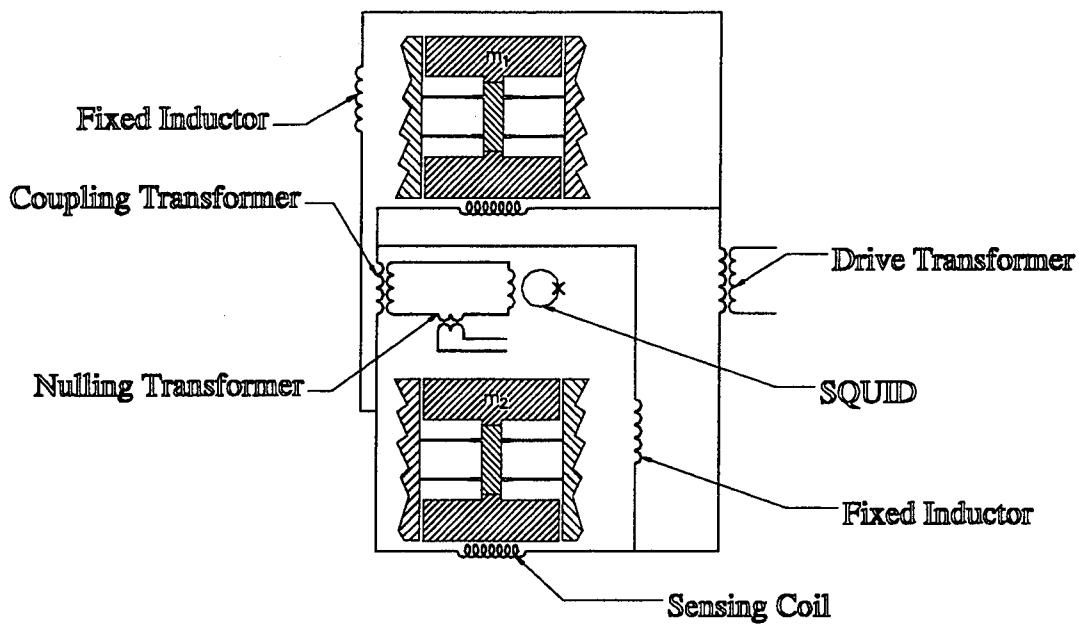
We can for convenience separate the gradiometer into electrical, mechanical, and thermal components. The electrical circuits of the device can be divided into three types: levitation, sensing, and feedback. The circuits are depicted in Figures 40 and 41. Note that the feedback transformers are part of the levitation circuit. Mechanical subsystems include the springs and test masses, and the suspension. Thermal components are the dewar, liquid helium bath, vacuum can, and temperature stabilization features.

An idealized mechanical picture of the gradiometer is as follows: A housing contains two test masses, each connected to the housing by a spring. Each mass-spring element is an accelerometer. The housing is coupled to the Earth by a suspension. If the suspension is very soft, we can model the gradiometer as three masses (the housing and two test masses) connected by two springs. If the springs are collinear and only allow motion along one axis, then the normal modes of this system are the common mode and differential mode. (Because of the non-zero stiffness of the suspension, there are low frequency modes involving the entire gradiometer. These modes are in general a mixture of translations and rotations, which are weakly coupled to the common mode.) The common mode involves both masses being displaced in the same direction, as occurs when an external vibration shakes the housing. The differential mode involves the two masses moving toward or away from each other, as occurs in the case of a gravity gradient. Two readout or sensing circuits exist, one to sense differential mode (DM) gradients, and the other to sense common mode (CM) accelerations.

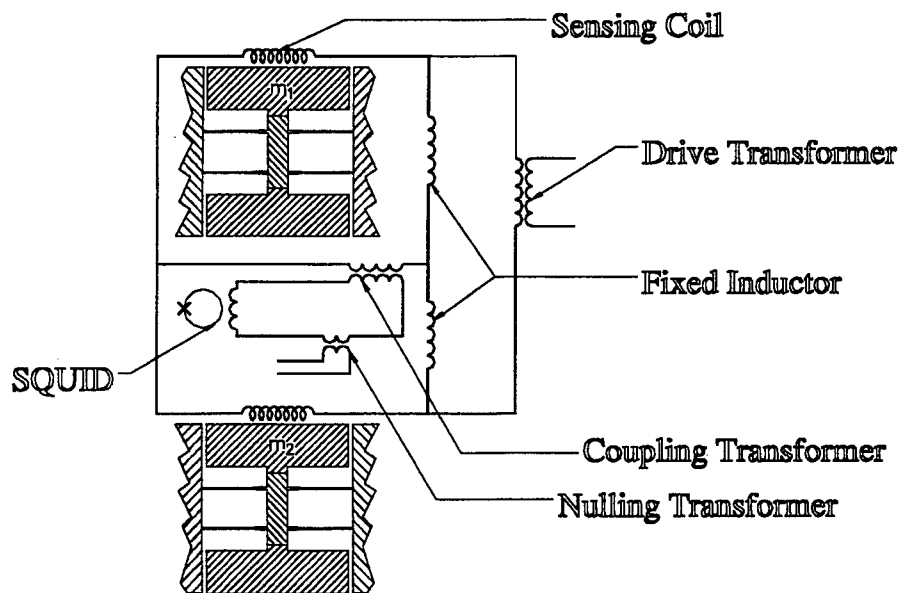
Figure 40 shows the sensing circuits. Both DM and CM circuits use two flat coil inductors as sensing elements together with two fixed inductors, forming a bridge configuration. In the current sheet approximation, the inductance of a flat spiral coil is

$$L = \Lambda d, \tag{3-1}$$

$$\Lambda = \mu_0 AN^2, \tag{3-2}$$



a) Common mode



b) Differential mode

Figure 40. Displacement sensing circuits of the ac gradiometer.

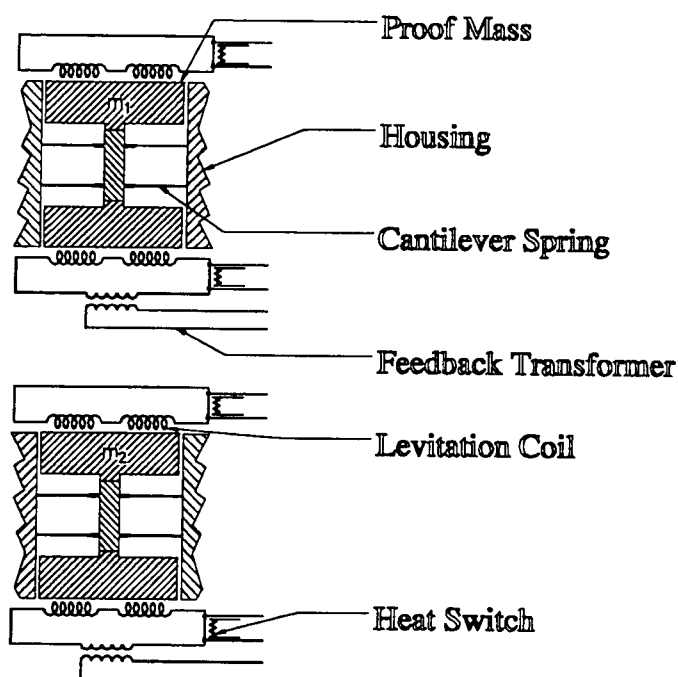


Figure 41. Levitation circuits of the ac gradiometer.

where d is the gap between the coil and the adjacent flat parallel superconducting surface, N is the pitch of the coil, and A the coil area. The sinusoidal excitation current is transformer coupled in from a room temperature current source. When the bridge is unbalanced, current flows through a coupling transformer, which impedance matches the bridge to the SQUID input coil.

The SQUID amplifier produces an output voltage proportional to the input current. Our SQUIDs are commercial devices. Their performance characteristics will be discussed later.

In order to obtain the desired sensitivity to gradients, this type of gradiometer design requires a rather precise balancing of the bridge (of order one part in 10^6). If the bridge is not balanced, then the SQUID will be overloaded (more precisely, the slew rate limit on the SQUID controller feedback loop will be exceeded causing the controller to lose lock). The high degree of balance required is partially a consequence of the large

ratio between the coil-to-test mass gap (0.015 cm) and the smallest detectable displacement ($\sim 10^{-12}$ cm). Coarse bridge balance is achieved by storing currents in the levitation circuits, which repositions the test masses, and thereby changes the inductances of the sensing coils. Fine control is accomplished by sending small steady currents into the feedback transformer primaries. Thus far, we have not attempted to run the gradiometer in a closed loop mode of operation.

This device uses biased springs. This means that when the test masses are properly positioned, in an ideal device, the gravitational force on them is balanced by forces provided by the mechanical cantilever springs, and the currents in the levitation circuits are small. The dc gradiometer uses similar springs, but in an unbiased position, so that when the masses are properly positioned the gravitational forces are compensated for, principally, by magnetic levitation. This difference is not considered to be important to instrument performance. It would reduce any effects due to magnetic creep, at the price of enhancing the effect of any mechanical creep. The temperature dependence of the elastic modulus becomes more important in the biased spring design.

The levitation circuits use current storage methods identical to those used previously in this laboratory. Carbon resistor heat switches are used. Current storage is done under computer control. The circuit topology used here makes balancing the device against sensitivity to external vibration (scale factor balance, described below) relatively simple, at the price of a small decreasing gradient sensitivity. Here, each stored current affects only one test mass. This is not true of more sophisticated designs that, although somewhat less easy to balance, provide lower differential-mode frequencies.

When a persistent current is stored in a circuit and the inductance is varied by the motion of a test mass, the magnetic flux in the circuit remains constant. In order for the magnetic flux to remain constant when the inductance changes, the current must vary. This means that the levitation currents produce a spring constant as well as a force, and thereby increase the CM and DM frequencies.

In this device, the mechanical springs give a zero current differential mode frequency of ~ 20 Hz, and we have an operating (with levitation and sensing currents applied) differential-mode frequency of 26.4 Hz. This is considerably higher than ~ 7 Hz achieved in the three-axis SGG. The transfer function between a gradient signal Γ applied to the gradiometer and the current, I_{SQ} , through the SQUID input coil is

$$\frac{\partial I_{SQ}}{\partial \Gamma} = I_{EX} \frac{l}{\omega_{DM}^2} \frac{\Lambda \zeta}{8 \sqrt{L_{SQ} L_{BR}}}, \quad (3-3)$$

where I_{EX} is the bridge excitation current, ω_{DM} is the differential mode angular frequency and l is the effective separation between the test masses. L_{SQ} is the SQUID input coil inductance and L_{BR} is the inductance of one arm of the bridge. (The arms are assumed here to be perfectly matched.) Here the factor $\zeta \leq 1$ relates to imperfections in the coupling transformer. It is calculated to be 0.72 from the measured transformer characteristics. When a known gradient source is used, we obtain a signal level 68% of that predicted by this equation.

When an acceleration is applied to the gradiometer, it is desirable that this not affect the gradient (DM) output. Because of mismatches in sensing coils, fixed inductors, and gaps, the DM circuit has imperfect rejection of translational accelerations along the sensitive axis of the accelerometers. (Geometrical imperfections in the gradiometer produce additional sensitivities to off-axis translational acceleration and to rotational accelerations.) This on-axis sensitivity can be viewed simply as a discrepancy in the scale factors of the two accelerometers. In the dc gradiometers this can be nicely dealt with by storing different sensing currents for the two different accelerometers. In the present device, scale factor balance is achieved by storing currents in the levitation circuits, thereby varying the spring constants of the two accelerometers. This allows for balance at very low frequencies, well below the CM or DM frequencies. We achieve scale factor balance of a few parts per thousand, which is adequate to reject the ambient seismic noise. At this level of balance other noise sources are dominant, in the laboratory environment.

In addition to bridge balance and scale factor balance, there is quadrature balance. Ideally, a balanced bridge would put zero current into the SQUID. We typically observe a significant out-of-phase (or quadrature) signal. The constant component of the quadrature signal can be canceled at the SQUID input using the nulling transformers. In the recent tests this quadrature balancing has not been necessary since the time-varying in-phase signal from the CM and DM modes is larger than the (approximately constant) quadrature signal. The origin of the quadrature signal is not known; it is not proportional to I_{DR} .

3.3 Mechanical and Electrical Construction

To reduce costs, a single-axis gradiometer operated in 1982 was refurbished with new sensing coils, levitation coils, and electronics. The old test masses and springs were used in the original housing. A new cryostat insert was required. This followed closely a previous design although several details were changed. Production of a new Nb vacuum can and flange was required along with the insert.

Several coils and transformers of various types were constructed and tested. No new technology was required. However, epoxy or varnish impregnation was used on fixed inductors and transformers in order to minimize wire motion. The flat coils in this device have been thermally cycled several times without failure.

The spot welding is one of the most critical and time-consuming parts of the instrument assembly. The techniques used parallel those used previously in this laboratory.

3.3.1 Electronics

One electronics box was built for this device. It contained two circuits which allowed control over the amplitude and phase of a sinusoidal input signal. These were used to send signals to the nulling transformers. It also contained two voltage-to-current converters having low noise characteristics. These provided sensing currents to excite the primary of the drive transformers. An Ithaco 3961B lock-in amplifier is used to demodulate the SQUID output signal and to provide a stable oscillator from which to derive the drive current I_{DR} . This is the current sent to the primary of the drive transformer; the current I_{EX} sent through the bridge is about four times larger.

The SQUIDs used were one BTI RF and one BTI dc SQUID, used for the CM and DM sensing, respectively. Filtering of the signal was done using a dual Krohn-Hite filter.

The automated current storage was done using a PC and a digital interface which this experiment shared with the three-axis SGG. A Keithley DVM and Keithley current source were also part of the current storage system. An SHE current source was used to provide the fine bridge balance control.

The HP Dynamic Signal Analyzer was used to evaluate the power spectral characteristics of the gradiometer output and to evaluate transfer functions.

3.3.2 Software

The software for the current storage did not require much modification for the recent series of tests. Minor alterations were made to be consistent with the redesigned levitation circuits.

3.3.3 Suspension

We operate the SAGG in a vertical orientation, using a pendulum suspension. The upper part of the pendulum shaft is a metal coil spring. The lower part is a G-10 fiber glass shaft. A small permanent magnet at the top of the shaft is situated between a pair of Helmholtz coils just outside the vacuum space. The coils and magnet act as a voice coil actuator to move the SAGG along the vertical axis. The lowest suspension mode is 0.50 Hz. Pendulum modes are at 0.75 Hz (2nd harmonic response), and the vertical mode is at 1.20 Hz. It is expected that a different suspension, one that allows control over the tilt angle, will be needed for a moving base application.

3.4 Noise and Error Sources

There are many noise and error sources for gravity gradiometers. We shall begin by cataloging those effects which are understood. The following section will assess the observed instrument performance and discuss possible further development.

3.4.1 SQUID noise

A BTI dc SQUID was used for the DM circuit, and a BTI RF SQUID for the CM circuit. The CM circuit SQUID performed as per specifications. The intrinsic SQUID noise for the DM SQUID was verified in a storage dewar as $75 \text{ nV/Hz}^{1/2}$ (gain $\times 1$), which should correspond to $1.5 \times 10^{-12} \text{ A/Hz}^{1/2}$. In the dewar insert and attached to the SAGG, with no excitation on the DM bridge, the white noise was degraded by about a factor of 7. Also, the SQUID unlocked frequently (of order once a second) in FAST (high bandwidth) mode. Consequently, data was taken using NORM mode, which has a reduced slew rate.

There are large test mass displacements at the DM and CM resonance frequencies. These displacements, together with the SQUID slew rate limit, restrict operation to $\leq 1 \text{ kHz}$. The presence of incompletely shielded dc magnetic fields from the levitation circuits gives us signals from external accelerations much as for a device using persistent current sensing. To avoid contaminating our modulated signal with this 'microphonic' pickup, we need to drive at frequencies above approximately 200 Hz.

The degraded white noise floor is a significant problem. Calculation indicates that a faulty transformer design is coupling Johnson noise into the sensing circuit. We plan to replace this transformer as soon as possible. Some further improvements on RF shielding are also desirable. The SQUIDs already have RC filters on their inputs. We plan to increase the filtering on the shielded twisted pairs at the low temperature end. It is also

possible to use a Quantum Design dc SQUID which has approximately two times better intrinsic white noise performance in terms of amplitude.

SQUID amplifiers are also known to have $1/f$ noise. This is not a problem with the SAGG because the modulation frequency can easily be chosen to be above the $1/f$ 'knee' in the SQUID noise spectrum.

3.4.2 External vibration

External vibration effects are classified as translational, rotational, and centrifugal. The seismic spectral characteristic is readily identifiable in the first two instances. It is more difficult to identify effects from centrifugal terms because apparent gradient output is the square of the angular velocity, rather than being linearly related to the ambient acceleration spectrum as in the first two cases. For a much more detailed discussion of these effects, see ref. 1.

3.4.3 Bridge unbalance effects

When the bridge is not balanced, there is a non-zero demodulated signal at the lock-in output. This signal is subject to drift for all the reasons dc signals can drift (i.e., op amp offsets and thermoelectric potentials). Additionally, amplitude fluctuations in I_{DR} will produce variations in the demodulated signal which are proportional to the bridge unbalance.

An additional aspect of bridge unbalance is the possibility of saturating the lock-in amplifier or exceeding the slew rate of the SQUID amplifier. The quadrature component is not a problem; the background vibration pickup at frequencies comparable to the DM and CM modes is responsible for the largest signals at the SQUID input.

3.4.4 Drive current back action

The drive current produces forces which act on the test masses. Therefore, fluctuations in the drive current will produce a time-varying force on the test masses. If the fluctuations are a fixed fraction of I_{DR} , then the force noise they produce should scale as I_{DR}^2 , because force is proportional to the square of current. This effect is expected to limit the useful drive currents, and is the main theoretical reason why the sensitivity of the SAGG is not expected to be as good as devices with persistent current sensing. Stable room temperature electronics is important for minimizing this effect.

Another effect of the drive current is to produce an additional spring constant. At sufficiently high sensing currents, this spring constant will decrease the displacement of the test masses caused by a gravity gradient. Thus, in Eq. (3-3), ω_{DM} actually increases with I_{EX} , although this effect is small at the relatively low drive currents we have been using.

Note that the circuit is arranged so that, in an ideally symmetric gradiometer, the forces applied to the two test masses by the sensing circuit would be equal and be entirely common mode. However, matching of coils and fixed inductors is only good to 3%. Detailed analysis shows that in the present SAGG it is not possible to balance the drive current forces and simultaneously achieve bridge balance and scale factor balance, using levitation currents alone. It may be possible to balance drive current forces by feeding a portion of the drive current into a feedback transformer.

3.4.5 Temperature fluctuations

This can be important at low frequencies. In a symmetric gradiometer, penetration depth variation with temperature would appear only in the CM sensing circuit, just as was the case for drive current back action. Therefore, the temperature gradients across the device are more important than the variation in the mean temperature.

3.4.6 Microphonics

The drive current shakes the test masses at twice the drive frequency. It also shakes the internal wiring in the device. In an earlier version of the device, there was considerable higher harmonic content in the SQUID output which we believe to be due to wires carrying bridge excitation currents shaking close to superconducting surfaces. Some low frequency wire motion is also possible if hysteretic frictional forces play a role in the wire motion. For present device, we have tried to minimize the amount of loose wiring. Increasing the value of Λ would reduce the size of any such problems.

3.5 Gradiometer Performance Assessment

We use a turntable with a pair of lead blocks, 180° apart, to obtain an estimate of the gradiometer scale factor. The turntable is placed so that the center of mass of the bricks sweeps out a circle in the horizontal plane that passes through the center of mass of the gradiometer. Figure 42 shows the calculated gradient signal as a function of time (dashed line). The calculation models the source and proof masses only as point masses; effects of higher order mass moments are ignored. The figure also shows a differential mode signal, which represents the average of 65 traces (solid line). Both the calculated and measured signals were digitally filtered with an 8-pole Butterworth filter at 1.2 Hz. Clearly, the form of the data matches well to the calculated signal. The dc offset and scale factor of the measured data were selected to minimize, in the least-squares sense, the difference between the measured and calculated values.

Figure 43 shows the power spectral density of the noise, referred to the SQUID input current, at 0.8 Hz, after demodulation, plotted as a function of drive current. The current noise has been normalized by the drive current, so it represents the noise in the

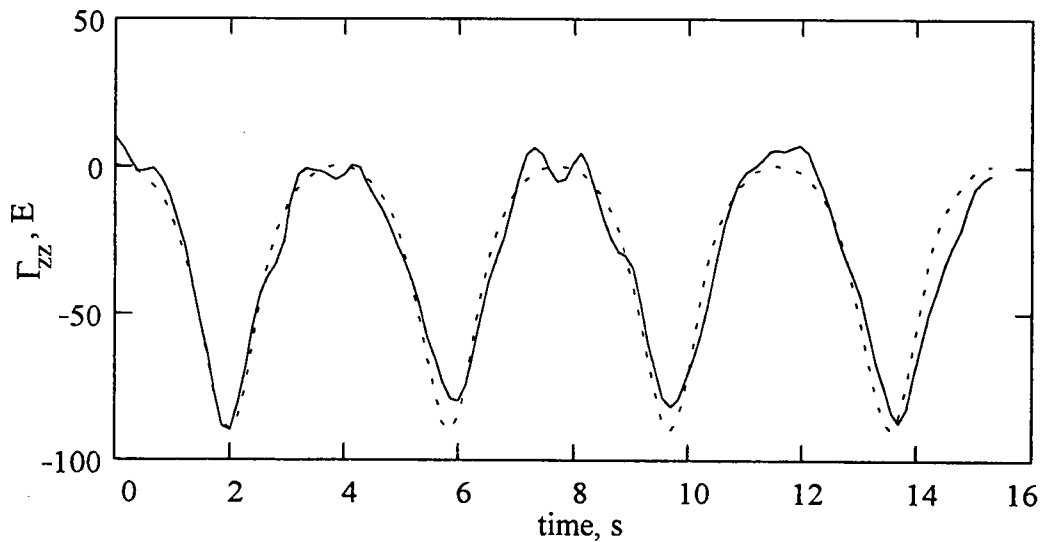


Figure 42. Calculated and measured gradient signal from two lead blocks on a turntable. Dashed line: calculated signal; solid line: measured signal.

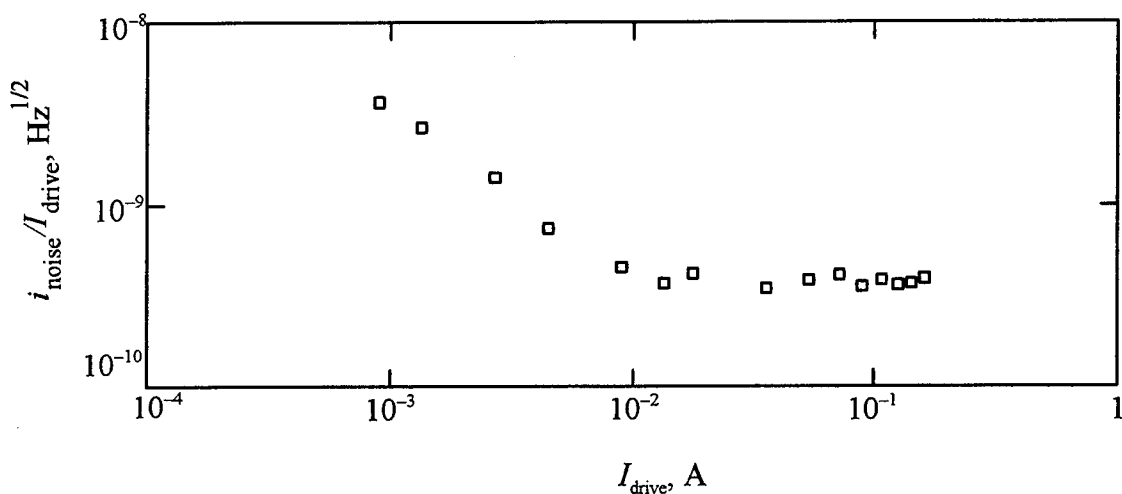


Figure 43. Ratio of current noise at the input of the differential-mode SQUID to the drive current versus drive current.

bridge balance. Below approximately 10 mA, the noise drops as $1/I_{\text{drive}}$, as would be expected for SQUID noise. In this region, i_{noise} is approximately three times the value specified by Quantum Design. Above 10 mA, the ratio $i_{\text{noise}}/I_{\text{drive}}$ is approximately constant. This is equivalent to a gradient noise of approximately $40 \text{ E/Hz}^{1/2}$. The origin of this noise is unknown. It is seen on both the in-phase and quadrature response, and it shows a noise spectrum which increases at low frequencies (below 0.5 Hz). This seems to rule out acceleration or temperature effects and points to an electronics saturation effect or a poorly understood drive current back action effect. The gradient noise at 0.32 Hz is found to be about $30 \text{ E/Hz}^{1/2}$.

An increase in noise level at lower frequencies is apparent. Future development plans are first to improve the RF isolation for the SQUID and eliminate possible Johnson noise sources, such as normal metal transformer cores. The goal here is to achieve the expected level of SQUID noise performance. Second, we would like a better understanding of the noise mechanisms at high current. This problem may be difficult to fix. If it is a drive current back action effect, then improved sensing coil matching and finer pitch

would help. This can be easily done *if* we can acquire or produce lithographically patterned coils. Presently our coils use wire of 0.1 mm (0.004 in) diameter.

Solving the white noise problems, and using a Quantum Design SQUID, would give us approximately $2 \text{ E/Hz}^{1/2}$. At that level of sensitivity we would be ready to seriously examine the effects of large vibrational inputs on the gradiometer. Some type of multi-axis cryogenic accelerometry would be desirable. All of the problems and partial solutions used for the three-axis SGG would be relevant. If a multi-axis gradiometer was constructed using ac sensing, we could use the improved lower frequency springs that are in the three-axis SGG, and thereby improve the basic sensitivity by about a factor of 8.

4. PRECISION TESTS OF GRAVITY

One of the most demanding tests of superconducting inertial instruments is in a precision experiment to search for deviations for the inverse square law of gravity. These deviations, if they exist, cause an additional gravity error and thus limit the precision of inertial guidance. The possibility of such departures from the inverse square law is suggested by recent theories proposed to address certain inconsistencies in quantum mechanics and gravity. Some theories predict the existence of light mass particles that mediate a new fundamental ("fifth") force between massive particles (Adelberger, 1991), (Fischbach and Talmadge, 1992). Such a force would have a limited range, and would appear as a small Yukawa potential perturbation in the equation for the gravitational potential:

$$\phi = -\frac{Gm}{r}(1 + \alpha e^{-r/\lambda}), \quad (4-1)$$

where α and λ represent the strength and the length scale of the new interaction, respectively. Gauss's law for a purely Newtonian field states that $\nabla^2\phi = 0$ outside the source mass. However, the Yukawa term does not vanish. Note that $\nabla^2\phi$ is just the trace of the gradient tensor:

$$\nabla^2\phi = \sum_i \frac{\partial^2\phi}{\partial x_i^2} = \sum_i \Gamma_{ii}. \quad (4-2)$$

Thus, an ideal 3-axis in-line gravity gradiometer, stationary in the inertial frame of reference, will measure no change in the vicinity of a moving source mass if the gravitational force law is purely Newtonian. Any signal will be due to a deviation from this coupling. Note that imperfections in the knowledge of the density distribution and path of the source are irrelevant.

This is the basis for the experiment we recently performed using the 3-axis SGG. Appendices D and E contain papers which describe the experiment in detail, so we will only summarize it here. As described above, a stationary, ideal gradiometer would

measure non-Newtonian coupling directly. In a real device, departures from the ideal generate non-zero signals. The challenge of performing this experiment, then, is to understand these errors and to remove them to the greatest degree possible. There are two basic categories of errors: those due to the non-ideality of the gradiometer itself, and those due to the fact that the gradiometer could not be made completely stationary during the experiment: motion of the source mass caused motion of the gradiometer. The two most important ways in which the SGG differs from an ideal gradiometer are 1) that its output contains random noise, and 2) that it does not make a truly differential measurement; rather, it measures the difference between accelerations at two points separated by a finite baseline. Because of the latter effect, it does couple to higher order gradients of the Newtonian potential of sources that are not very distant compared to its baseline. However, the coupling can be minimized by properly orienting the source with respect to the gradiometer, and, to the degree that relative position of the proof masses and the source mass can be measured, this small error term can be removed.

The source mass used for this experiment, a large (1498 kg) pendulum which moved in the vertical plane passing through the center of the gradiometer, caused the building to move (albeit by a very small amount) as it swung. This motion, which is synchronous with the source, couples to the gradiometer through three important mechanisms. The first is centrifugal acceleration. A gravity gradiometer in a rotating frame of reference measures not just gravity gradient, but gravity plus a component of angular rate squared. Fortunately, this signal appears 90° out of phase with respect to the gradient signal, and so can be removed with phase-sensitive detection. The second coupling mechanism is through angle with respect to local vertical. The component of the Earth's strong (3000 E at vertical) gradient field along the axis of a gradiometer is a sensitive function of the angle with respect to vertical. An optical lever was used to measure the tilt of the gradiometer and so remove this term. Finally, the gradiometer couples to linear and angular acceleration because it relies on the alignment of the sensitive axes of each pair of component accelerometers to cancel common accelerations. Imperfections in this alignment are

stable, so this term can be removed if the accelerations can be measured. The SGG does measure linear accelerations along all 3 axes. Data from the tilt sensor gives the angular acceleration about two horizontal axes. A ring laser gyroscope (loaned by the Phillips Laboratory, Hanscom Air Force Base, Massachusetts) mounted on the dewar platform provided the angular acceleration about the vertical axis.

After removal of all these terms, the measured value for α at $\lambda = 1.5$ m with 2σ error is $(0.9 \pm 4.6) \times 10^{-4}$. Thus, no Yukawa potential is measured within the 2σ error limit. This represents an improvement by more than an order of magnitude over other measurements of α at this distance range (Moody and Paik, 1993). By properly adjusting the distribution of mass as a function of distance along the axis of a cylindrically symmetric shell, one can produce a near-null source. An experiment using such a source could yield a hundredfold improvement in the resolution of α at $\lambda = 0.1 - 1$ m. In addition, the three-axis SGG or the single-axis SAGG could be moved up and down a tower to search for a violation of the inverse square law at larger distances, with greater resolution than possible with the earlier gravimeter-tower experiments (Eckhardt et al., 1988), (Speake et al., 1990).

5. REFERENCES

- E. G. Adelberger, B. R. Heckel, C. W. Stubbs, and W. F. Rogers, "Searches for new macroscopic forces", *Annual Review of Nuclear and Particle Science* **41**, 269–320 (1991).
- B. Bachrach, "Control of a superconducting six-axis accelerometer", Masters thesis, University of Maryland, College Park, Maryland, 1990.
- B. Bachrach, E. R. Canavan, and W. S. Levine, "Diagonalizing controller for a superconducting six-axis accelerometer", *Proceedings of the 29th Conference on Decision and Control*, Honolulu, Hawaii, December, 1990, **5**, 2785–2793.
- H. A. Chan and H. J. Paik, "Superconducting gravity gradiometer for sensitive gravity measurements. I. Theory", *Physical Review D* **35**, 3551–3571 (1987).
- J. C. Doyle and G. Stein, "Multivariable feedback design: Concepts for a classical/modern synthesis", *IEEE Transactions on Automatic Control* **AC-26**, 4–16 (1981).
- D. H. Eckhardt, C. Jekeli, A. R. Lazarewicz, A. J. Romaides, and R. W. Sands, "Tower gravity experiment: Evidence for non-Newtonian gravity", *Physical Review Letters* **60**, 2567–2570 (1988).
- E. Fischbach and C. Talmadge, "Six years of the Fifth Force", *Nature* **356**, 207–215 (1992).
- J. N. Hollenhorst, "Signals and noise in the rf SQUID", PhD Thesis, Stanford University, Stanford, California, 1979.
- J. N. Hollenhorst and R. P. Giffard, "Input noise in the hysteretic SQUID: theory and experiment", *Journal of Applied Physics* **51**, 1719–1725 (1980).
- M. V. Moody and H. J. Paik, "Gauss's law test of gravity at short range", *Physical Review Letters* **70**, 1195–1198 (1993).
- H. J. Paik, J. W. Parke, and E. R. Canavan, *Development of a Superconducting Six-Axis Accelerometer*, Final Report to the Geophysics Laboratory, Report Number GL-TR-89-0181 (1989).
- J. W. Parke, "Null test of the gravitational inverse square law and the development of a superconducting six-axis accelerometer", PhD thesis, University of Maryland, College Park, Maryland, 1990.
- N. A. Robertson, "Vibration isolation for the test masses in interferometric gravitational wave detectors", in *The Detection of Gravitational Waves*, ed. D. G. Blair, pp. 353–368, (Cambridge University Press, 1991).

C. C. Speake, T. M. Niebauer, M. P. McHugh, P. T. Keyser, J. E. Faller, J. Y. Cruz, J. C. Harrison, Jaako Mäkinen, and R. B. Beruff, "Test of the inverse-square law of gravitation using the 300-m tower at Erie, Colorado", *Physical Review Letters* **65**, 1967-1971 (1990).

W. R. Smythe, *Static and Dynamic Electricity*, (Hemisphere Publishing Company, New York, 1989).

6. LIST OF PUBLICATIONS RESULTING FROM THIS CONTRACT

- B. Bachrach, "Control of a superconducting six-axis accelerometer", Master's thesis, University of Maryland, College Park, Maryland, 1990.
- B. Bachrach, E. R. Canavan, and W. S. Levine, "Diagonalizing controller for a superconducting six-axis accelerometer", *Proceedings of the 29th Conference on Decision and Control*, Honolulu, Hawaii, December, 1990, **5**, 2785–2793.
- E. R. Canavan, H. J. Paik, and J. W. Parke, "A superconducting six-axis accelerometer", *IEEE Transactions on Magnetics*, **MAG-27**, 3253–3256 (1991).
- E. R. Canavan and H. J. Paik, "A superconducting six-axis accelerometer for platform control and space applications", *Sixteenth Biennial Guidance Test Symposium*, Holloman AFB, New Mexico, October, 1993, **1**, 19–32.
- M. V. Moody and H. J. Paik, "Gauss's law test of gravity at short range", *Physical Review Letters* **70**, 1195–1198 (1993).
- M. V. Moody and H. J. Paik, "Gauss's law test of gravity at short range", *Perspectives in Neutrinos, Atomic Physics, and Gravitation*, ed. J. Trân Than Vân, T. Damour, E. Hinds, and J. Wilkerson, pp. 403–408, (Editions Frontiers, Gif-sur-Yvette Cedex, France, 1993).
- H. J. Paik and M. V. Moody, "Null test of the inverse-square law of gravity", *Classical and Quantum Gravity* **11**, A145–A152 (1994).
- H. J. Paik, E. R. Canavan, Q. Kong, and M. V. Moody, "Laboratory demonstrations of superconducting gravity and inertial sensors for space and airborne gravity measurements", in *From Mars to Greenland: Charting Gravity with Space and Airborne Instruments*, ed. O. S. Columbo (Springer-Verlag, New York, 1992).
- H. J. Paik, "Superconducting accelerometry: Its principles and applications", *Classical and Quantum Gravity* **11**, A133–A144 (1994).

7. LIST OF RELATED CONTRACTS

Previous Contract

Air Force Contract Number F19628-85-K-0042,
"Development of a superconducting six-axis accelerometer"
(April 1, 1985 – March 31, 1988)

Related Contract

NASA Contract Number NAS8-38137,
"Development of a three-axis superconducting gravity gradiometer for space-borne
gravity survey"
(June 29, 1989 – December 31, 1995)

8. CONTRIBUTING PERSONNEL

H. J. Paik – P. I.

E. R. Canavan – Research Associate

H. J. Hauke – Research Associate

B. Bachrach – Research Assistant

Q. Kong – Engineer

R. Liu – Engineer

R. Eckblad – Faculty Research Assistant

R. Williamson – Technician

9. APPENDICES

Appendix A: A superconducting six-axis accelerometer for platform control and space applications E. R. Canavan and H. J. Paik, <i>Sixteenth Biennial Guidance Test Symposium</i> , Holloman AFB, New Mexico, October, 1993.	126
Appendix B: Diagonalizing controller for a superconducting six-axis accelerometer B. Bachrach, E. R. Canavan, and W. S. Levine, <i>Proceedings of the 29th Conference on Decision and Control</i> , Honolulu, Hawaii, December, 1990.	140
Appendix C: MATLAB simulation parameters.	149
Appendix D: Gauss's law test of gravity at short range M. V. Moody and H. J. Paik, <i>Physical Review Letters</i> (1993).	153
Appendix E: Null test of the inverse-square law of gravity H. J. Paik and M. V. Moody, <i>Classical and Quantum Gravity</i> (1994).	157

Appendix A

A Superconducting Six-Axis Accelerometer for Platform Control and Space Applications

E. R. Canavan and H. J. Paik
*Department of Physics and
Center for Superconductivity Research
University of Maryland
College Park, MD 20742*

Approved for public release; distribution is unlimited.

Introduction and Background

Continued advancement in inertial navigation, platform stabilization and gravity survey depends on the ability to resolve ever smaller accelerations. Further progress in this direction depends on a clear understanding of the basic physical limitations on the resolution of accelerometers. One of the most critical limitations is imposed by the Fluctuation - Dissipation Theorem, which states that any dissipation in a system causes random fluctuations, with amplitude proportional to the square root of temperature, in the variables describing its state (Brownian motion in mechanical systems; Johnson noise in electrical systems).

Physicists working on probably the most challenging motion measurement problem, the detection of gravitational waves, realized a few decades ago that this restriction can be circumvented by cooling instruments to the boiling point of liquid helium (4.2 K). Not only are all fluctuations reduced by a factor of ten from room temperature values, assuming fixed dissipation, but in many cases the dissipation in the system can be made drastically lower. This is particularly true for low frequency electrical subsystems, in which superconducting materials can be used to effectively eliminate dissipation.

Additionally, a new device becomes available: the Superconducting QUantum Interference Device (SQUID), an extremely low-noise magnetic-flux-to-voltage amplifier. The magnetic flux in a superconducting loop is quantized. However, if the loop is broken by two superconductor-insulator-superconductor junctions and a bias current is applied through the junctions, the voltage across the junctions is a periodic function of the number of flux quanta in the loop. The Johnson noise on this voltage is low enough that a very small fraction of one flux quantum may be resolved. In the laboratory, SQUIDs have demonstrated energy resolutions per unit bandwidth approaching the Heisenberg uncertainty limit, $\Delta E \Delta t > h/2\pi$, where h is Planck's constant. Although commercially available SQUIDs are about a thousand times noisier, they are still by far the quietest amplifier, and SQUID manufacturers are making steady progress toward matching the performance achieved by researchers.

How can the unsurpassed magnetic flux sensitivity of the SQUID be exploited for high resolution acceleration measurements? Typically, these devices are operated in closed-loop, or "flux-locked", mode: a room temperature controller feeds current back to a small coil to cancel flux changes in the SQUID loop. A second small coil (the input coil),

inductively coupled to the loop, induces a flux proportional to its current. In this configuration, the system acts as a linear, high gain, extremely low noise current-to-voltage amplifier. Because of the controller, commercial systems have small-signal bandwidths on the order of a few tens of kilohertz and dynamic ranges (the ratio of the maximum input signal to the power spectral density of input referred noise) of $10^8 \text{ Hz}^{1/2}$ below 100 Hz. The input coils are relatively small (typically $2 \mu\text{H}$), so SQUID systems are optimally matched to low impedance devices. The signal source must also have very low resistance to keep Johnson noise small. Thus, SQUIDs are usually used with superconducting transducers.

The Meissner effect, the exclusion of all magnetic field from the interior of superconductors, allows the construction of a very simple superconducting displacement transducer. A superconducting coil connected to the input coil of a SQUID forms a superconducting loop. If the loop carries a large current, it contains a large, fixed number of flux quanta. Now, if a large piece of superconductor in the vicinity of the coil moves toward the coil, it effectively pushes flux quanta out of the coil and into the SQUID input coil, where the change is detected. Transducers of this type used in gravitational wave detectors typically achieve displacement sensitivities (power spectral density of noise referred to displacement) smaller than $10^{-16} \text{ m Hz}^{-1/2}$. By using such a technique to measure the displacement of a relatively compliant mass-spring system, extremely good acceleration sensitivity can be obtained.

Although the prime motivation for using cryogenic devices is the reduction of noise, low temperatures offer another important benefit: greatly enhanced dimensional stability. Coefficients of thermal expansion must go to zero at 0 K. For most materials, the

coefficients at 4.2 K are approximately three orders of magnitude lower than at room temperature. Furthermore, creep is caused primarily by thermally activated processes which are frozen out at these temperatures. Additionally, many internal friction mechanisms are also frozen out, allowing very low loss springs.

Building on the experience of the gravitational wave detection community, the University of Maryland group developed the Superconducting Gravity Gradiometer (SGG), currently the most sensitive gravity gradiometer. However, because of residual sensitivity to platform motion, the most demanding applications of the gradiometer, such as global gravity mapping from orbit, require extremely good platform control in all six rigid-body degrees of freedom. In order to provide a sensitive, compact and cryogenically compatible readout device for such a controller, we invented the Superconducting Six-Axis Accelerometer. To keep the instrument relatively simple and compact, it uses only a single proof mass, which is magnetically levitated to provide good compliance in all degrees of freedom.

Physical Description

Figure 1 shows an exploded view of the sensor. The 144 g proof mass is formed by three intersecting, orthogonal square slabs, 50.2 mm on a side and 2.39 mm thick. The proof mass fits into a cavity formed by mounting the eight cubical coil-forms inside the cubical cavity (50.8 mm (2") on a side) in the housing. Three sides of each coil-form face the proof mass; mounted on each of these sides are two concentric, spiral niobium coils. We use the inner coils for sensing and the outer coils for levitation. When the proof mass is levitated, there is a 0.3 mm (0.012") gap

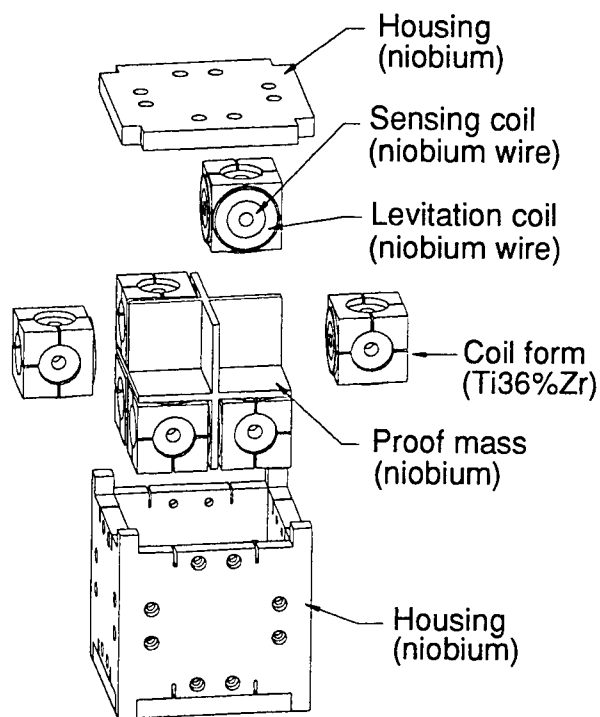


Figure 1. Exploded view of the SSA.

between it and the coils, but small stops on the coils prevent it from moving more than 0.1 mm (0.004"). Although it is not displayed this way on the figure, the SSA is usually mounted in the "umbrella" orientation, that is, with the center of the housing and two diagonally opposed vertices along a vertical line. This makes all circuits symmetric with respect to \mathbf{g}_E , the gravitational field of the earth, thus reducing the maximum magnetic field required for levitating the mass. In this orientation, coils in three planes are "below" the proof mass and coils in the three other planes are "above" it.

Naturally, selection of the proper materials is critical to the performance of the device. The proof mass and all superconducting wires are pure niobium, because niobium has the highest known first critical field, H_{c1} . H_{c1} is the highest field a superconductor can tolerate while completely excluding magnetic flux. (High T_c superconductors all have extremely

low H_{c1} , and thus would not provide the same performance.) When using niobium, particularly for the manufacture of fine wire, it is important to avoid any processing step that might increase the concentration of interstitial impurities, especially oxygen, since these increase the ductile-to-brittle transition temperature. Each junction between superconducting circuit elements must be carefully welded to maintain a high quality superconducting path through the circuit.

The Magnetic Spring

We connect the four coils in each of the three planes below the proof mass to form three translational levitation circuits, which provide linear levitation force along three orthogonal axes. As Figure 2 shows, the four coils are simply connected in series with a transformer. The sets of coils above the proof mass are connected to form rotational levitation circuit, which provides torques about the three axes. Figure 3 shows that the coils on one side of the torque axis and the coils on the other side of axis are connected in parallel with a transformer.

We use the heaters shown in the two figures to trap flux or "store current" in the

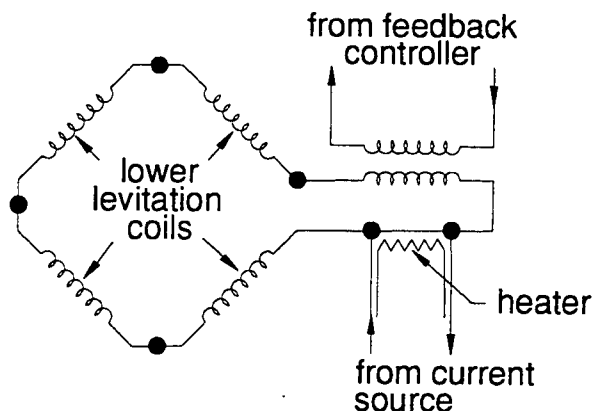


Figure 2. Translational levitation circuit.

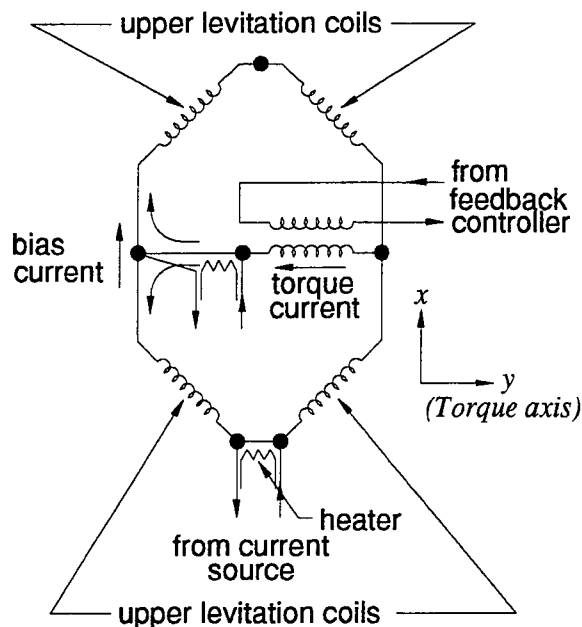


Figure 3. Rotational levitation (torquing) circuit.

circuits. By applying a heat pulse large enough to momentarily raise the temperature of a small section of wire above the critical temperature, we break the superconducting path and force any current passing through the charging leads (labeled "from current source") to pass through and induce a flux in the inductors. When the warm section becomes superconducting again, the flux in these inductors is trapped and remains absolutely constant after the current source is removed.

Storing current in a translational circuit or in the outer loop of the rotational circuit ("bias current") creates a force normal to the plane of the coils. The rotational circuit has an additional heater which allows us to store current through the central branch of the circuit ("torque current"). This current adds to the bias current on one side of the circuit and subtracts from it on the other, creating a torque. Normally, the currents in the rotational circuits are an order of magnitude smaller than those in the translational circuits.

The force between a superconductor and a current-carrying wire comes from the interaction of surface currents on the superconductor and the current in the wire. The superconductor sets up surface currents to cancel any field in its interior. The force between the surface currents on a superconducting plane and the current, I , in a nearby coil is $\Lambda I^2/2$. The force provided by the four translational levitation coils, $2\Lambda I^2$, must cancel the component of the proof mass weight normal to the coils, $mg_E \cdot \hat{n}$ (plus a small force, which we ignore here, due to the bias current in the coils above the proof mass). The current required in each translational circuit to lift the proof mass is then

$$I_{lev} = \sqrt{\frac{mg_E}{2\sqrt{3} \Lambda}} \quad (1)$$

The force coefficient Λ is proportional to the turns density squared. The wire-wound coils of the present SSA have a turn-to-turn spacing of approximately $100 \mu\text{m}$, giving $I_{lev} = 5.5 \text{ A}$. Such currents are rather easily generated and handled. Furthermore, the current is only needed for several brief ($\sim 1 \text{ min}$) periods during the initial setup of the device. In contrast, capacitive levitation schemes generally require thousands of volts to levitate significant masses against the Earth's field. If photolithographic techniques were used to make the coils, a reduction in the line spacing, and hence the required current, by an order of magnitude could easily be achieved.

For a flat spiral coil parallel to a superconducting plane, the force coefficient is a function of the gap, x , but as x becomes small compared to the coil diameter, $\Lambda(x)$ approaches a constant value. In this case, the coil inductance is $L = x \Lambda$. If the coil is connected to a fixed inductor, L_f , then the total flux trapped in the circuit is $(x \Lambda + L_f) I$. Because

of flux quantization, this quantity must remain fixed even if the gap changes by δx :

$$(x\Lambda + L_f)I = [(x + \delta x)\Lambda + L_f](I + \delta I). \quad (2)$$

Thus,

$$\delta I = -I \frac{\Lambda \delta x}{\Lambda x + L_f}, \quad (3)$$

where we have dropped the small quadratic ($\delta x \delta I$) term. Therefore, if $L_f \gg \Lambda x > \Lambda \delta x$, the change in current, and thus the change in force, with a change in gap is very small. In other words, the mass will act as though it is supported by a spring with very small spring constant.

Unfortunately, the gap dependence of $\Lambda(x)$ puts a lower bound on the spring constant. If we approximate $\Lambda(x)$ with a linear function of x ,

$$\Lambda(x + \delta x) = \Lambda(x) - \gamma(x)\delta x, \quad (4)$$

then the force on a superconducting plane displaced by a small amount δx from the equilibrium position is

$$\begin{aligned} \delta F(x + \delta x) &= F + \delta F \\ &= [\Lambda(x) - \gamma(x)\delta x]I^2/2. \end{aligned} \quad (5)$$

Therefore, even if L_f is large enough to make δI negligible, there is still a change in force, $\delta F = -\gamma(x)I^2\delta x/2$, giving an effective spring constant of $\gamma(x)I^2/2$.

This minimum spring constant sets the minimum realizable resonance frequency for the translational modes of the SSA proof mass. Taking the spring constant of a circuit with four such coils and substituting the levitation current given by Eq. (1) yields

$$\omega_{\min} = \sqrt{\frac{k}{m}} = \sqrt{\frac{g_E/\sqrt{3}}{\Lambda(x)/\gamma(x)}}. \quad (6)$$

This is the frequency of a pendulum with length $\Lambda(x)/\gamma(x)$. The quantities $\Lambda(x)$ and $\gamma(x)$ are not calculable in closed form. However, numerical computations show that the length $\Lambda(x)/\gamma(x)$ is a weak function of the gap. It is also a weak function of the coil geometry; for example, a solenoid and a pancake coil with the same maximum diameter and number of turns have values that differ by less than 30%. For the present SSA, $\omega_{\min}/2\pi = 11.3$ Hz.

The derivation of the complete expression for the rotational mode frequencies is rather lengthy [1], but the following heuristic argument provides the proper expression for the dominant term. Consider the coordinate system shown in Figure 4. The coils of the y translational levitation circuit are on the $-y$ side of the x - z plane. To first order, the total inductance of this circuit remains unchanged with a rotation of the proof mass about the x axis, because the inductance of the two coils on the $-z$ side increases by the same amount as the inductance of those on the $+z$ side decreases. The same is true for rotations about the z axis. Since the total flux is fixed, the current does not change with rotation.

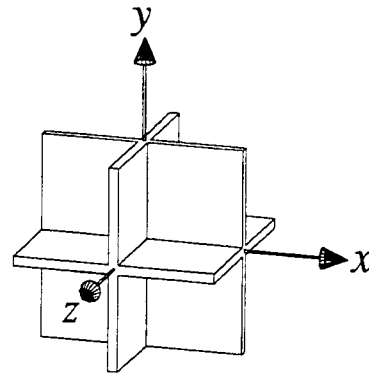


Figure 4. The proof mass coordinate system.

With fixed current, the effective spring constant is $\gamma(x)I^2/2$. If we assume that the force of a coil acts at its center, a distance c from the axis of rotation, and that the displacement at this point due to a rotation by an angle $\delta\theta$ is $c\delta\theta$, then the torque due to the four coils is

$$\delta T = c\delta F = c[4(\gamma I^2/2)(c\delta\theta)]. \quad (7)$$

A rotation about one axis affects coils in two planes. (A rotation about the z axis changes inductances in the y - z and x - z planes.) Therefore, the total angular spring constant is $\tau = 4c^2\gamma I^2$. Again substituting Eq. (1), we obtain

$$\omega_{rot} = \sqrt{\frac{\tau}{J}} = \sqrt{\left(\frac{2mc^2}{J}\right) \frac{g_E}{\Lambda(x)/\gamma(x)}}, \quad (8)$$

where J is the moment of inertia of the proof mass. Using the values for the present SSA, $\omega_{rot}/2\pi = 9.1$ Hz. As mentioned above, this is only an approximation; the actual frequency is approximately 60% higher.

Up to this point, we have considered motion in only one degree of freedom at a time, but the position and orientation of the proof mass with respect to each coil is affected by motion in several degrees of freedom. The force due to the magnetic fields always acts perpendicular to the proof mass surface. This causes the force in one degree of freedom to be proportional to displacements in other degrees of freedom. Thus, the action of the levitation circuits must be described by a spring constant matrix with non-zero off-diagonal terms. A full analysis of the proof mass motion is presented elsewhere [1]; here we present only an intuitive derivation of these cross terms.

Consider small motions of the proof mass with respect to the coordinate system defined by Figure 4. The coils in the y - z plane, the x

translational levitation circuit and the θ_y rotational levitation circuit normally apply a force along the x axis. The total force, $F_{dc} = 2\Lambda(I_{lev}^2 - I_{bias}^2)$, cancels the x component of the proof mass weight. In the umbrella orientation, F_{dc} is the same for all three axes. A small rotation about the z axis, $\delta\theta_z$, will cause a component of this force, $F_{dc} \sin(\delta\theta_z) \approx F_{dc} \delta\theta_z$, to appear in the y direction. Similarly, the same rotation $\delta\theta_z$ will cause a small component, $-F_{dc} \delta\theta_z$, of the force from the coils in the x - z plane to appear in the x direction.

A translation of the proof mass places a torque on an orthogonal axis because of a change in the effective moment arms. Consider the coils in the x - z plane, which produce a force F_{dc} in the y direction. We assume that the force from a coil acts on a single point on the proof mass directly above the center of the coil, a distance c from the z axis. The coils on the $+x$ side generate a torque $cF_{dc}/2$ about the z axis, and those on the $-x$ side generate $-cF_{dc}/2$, so the total is zero. Now, if we displace the proof mass by a small distance δx along the x axis, the coils on the $+x$ side produce a torque $(c - \delta x)F_{dc}/2$ (relative to the center of the proof mass) and those on the $-x$ side produce $-(c + \delta x)F_{dc}/2$, so the total is $-F_{dc}\delta x$. The same displacement δx causes the coils in the x - y plane to generate a torque $F_{dc}\delta x$ about the y axis.

Applying the same reasoning to displacements in all degrees of freedom, we find that the spring constant of the levitation circuits can be represented as

$$\mathbf{k} = \begin{pmatrix} k\mathbf{I} & F_{dc}\mathbf{S}^T \\ F_{dc}\mathbf{S} & \tau\mathbf{I} \end{pmatrix}, \quad (9)$$

where k and τ are the linear and angular spring constants, respectively, \mathbf{I} is a 3×3 identity matrix, and \mathbf{S} is the unit antisymmetric matrix,

$$\mathbf{S} = \begin{pmatrix} 0 & 1 & -1 \\ -1 & 0 & 1 \\ 1 & -1 & 0 \end{pmatrix}. \quad (10)$$

The cross-coupling terms due to these off-diagonal spring constants can be strongly suppressed by applying feedback.

An important property of a precision accelerometers is the stability of its spring constant. The spring constants of the SSA depend solely on purely geometric quantities such as L , $\Lambda(x)$ and $\gamma(x)$. As mentioned in the introduction, creep and thermal contraction are negligible in most materials at liquid helium temperature. However, to this point we have been treating superconducting bodies as perfect diamagnetic objects, with zero field just inside the surface and a large field just outside. In actuality, the field drops exponentially with distance inside the surface. The length scale of the exponential decrease is called the *penetration depth*, λ , and it has a temperature dependence given by

$$\lambda(T) = \frac{\lambda(0)}{\sqrt{1 - (T/T_c)^4}}. \quad (11)$$

where $\lambda(0)$ is the penetration depth at 0 K. For niobium, $\lambda(0) = 47$ nm and $T_c = 9.2$ K.

For the field, the effective gap is the distance between the plane passing through the center of the coil wire and a plane approximately $\lambda(T)$ inside the surface of the proof mass. It is this effective gap that remains fixed, so if $\lambda(T)$ increases, the position of the proof mass drops by an equal distance. Well below the mass-spring resonance frequency, ω_0 , the acceleration a and the displacement x

are related by $a = \omega_0^2 x$. Thus, the temperature coefficient of acceleration is

$$\begin{aligned} \frac{da}{dT} &= \omega_0^2 \frac{d\lambda}{dT} \\ &= \frac{\lambda(0)}{T_c [1 - (T/T_c)^4]^{3/2}} \left(\frac{T}{T_c} \right)^3. \end{aligned} \quad (12)$$

At $T = 4.2$ K, this coefficient is 4×10^{-9} m s⁻² K⁻¹ for the present SSA. This implies that if we require an acceleration sensitivity of 10^{-11} m s⁻², we must keep the temperature noise below 2.5 mK Hz^{-1/2}. Temperature control at this level can be provided by commercially available instruments. If we attain higher acceleration sensitivity, we will need tighter temperature control. Cryogenic devices with temperature noise levels around 1 μ K Hz^{-1/2} are routinely constructed. Furthermore, the temperature coefficient can be lowered by an order of magnitude by reducing the temperature to below the superfluid helium transition temperature (2.17 K), a measure that has additional benefits for temperature control.

Displacement Sensing

We showed in the introduction that a large superconductor, a superconducting coil, and a SQUID can be configured as an extremely sensitive displacement transducer. If the superconducting surface and the coil are flat and separated by a small gap, the change in the current of a closed circuit is directly proportional to the gap, as given by Eq. (3). Since a (flux locked) SQUID is a linear voltage-to-current amplifier, the voltage out of the SQUID controller is linearly proportional to the displacement. This type of sensing circuit is used in the SGG and in gravitational wave antennas. Unfortunately, the closed-loop behavior of the SQUID system gives this

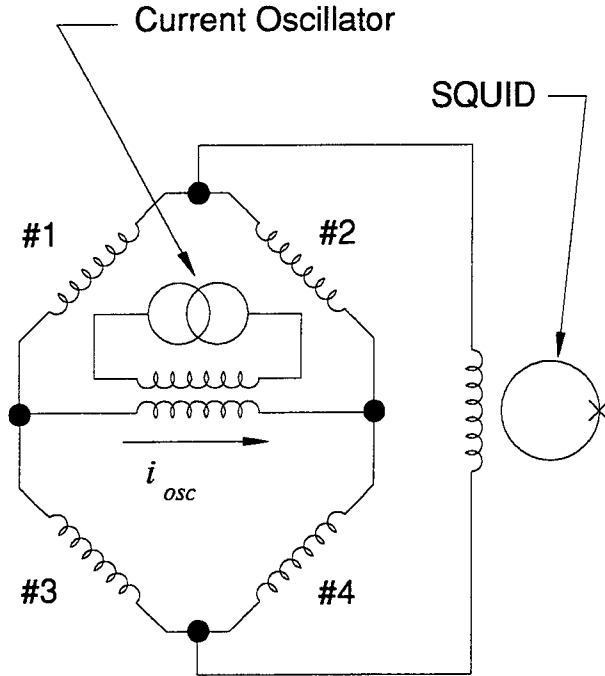


Figure 5. Displacement sensing circuit. For translational sensing, coils #1 and #4 are below the proof mass; #2 and #3 are above.

configuration an undesirable feature. If the signal exceeds the slew rate of the controller, or if rf interference causes a temporary loss of the SQUID voltage, the controller "loses lock." When the system resettles, the output voltage offset by an amount equivalent to an integral number of flux quanta. Even if the dc level is unchanged, the number of flux quanta in the SQUID loop, and thus the dc displacement, may have shifted. This property is especially objectionable when the output is the input of a feedback controller, such as for platform stabilization.

For this reason, the SSA uses an ac inductance bridge, as shown in Figure 5. An oscillator with a current output stage, coupled through a superconducting transformer, provides a sinusoidal current across two vertices of the bridge. In the translational sensing circuit, the coils labeled #1 and #4 are below the proof mass and those labeled #2 and #3 are above it. If the coils are identical, then when

the proof mass is centered between the upper and lower coils, all the inductances are equal and no current flows through the SQUID input coil. An upward or downward displacement unbalances the bridge, forcing current i_{SQ} through the input coil.

More quantitatively, we can represent the variation of inductance with displacement, δx , using a truncated Taylor expansion:

$$L(\delta x) = L_0 + \Lambda_0 \delta x - \frac{\gamma}{2} (\delta x)^2. \quad (12)$$

L_0 , Λ_0 , and γ_0 are the inductance and its first and second derivatives with the proof mass centered. Solving the circuit equations for i_{SQ} and expanding to third order yields

$$i_{SQ} = i_{osc} \frac{\Lambda_0}{L_{SQ} + L_0} \delta x + O[(\delta x)^3], \quad (13)$$

where i_{osc} is the current through the secondary of the transformer. For proper impedance matching, $L_{SQ} = L_0$. Since $L_0 \approx x_0 \Lambda_0$, where x_0 is the gap, Eq. (13) reduces to

$$i_{SQ} \approx i_{osc} \frac{\delta x}{2x_0}. \quad (14)$$

The rotational sensing circuits differ only in the position of the coils. They are arranged so that #1 and #4 increase with rotation about the appropriate axis and #2 and #3 decrease. In this configuration, the SQUID output is proportional only to rotation about the axis, to first order.

Thus, the signal from the SQUID, after demodulation, provides a voltage proportional to displacement of the proof mass from the centered position. This has an important advantage for the SSA: centering the proof mass, first at dc by choosing the proper set of currents to store in the various levitation circuits, then over a wide bandwidth by applying feedback, is simply a matter of minimizing the

SQUID output. The proof mass must be centered as well as possible in order to minimize cross coupling and certain other dynamical errors. Furthermore, any shift in the dc level due to SQUID unlocks appears after demodulation as a pulse, so the feedback controller can set the proof mass back to its proper position following such an event. The scheme has an additional benefit: because it is sensitive only to the difference between the upper and lower gap, it is insensitive to changes in the penetration depth caused by a change in the average temperature of the proof mass. Only changes in temperature gradients, which are small, cause a response.

The frequency f_{osc} of the oscillator that drives the bridge circuit, typically around 1 kHz, is a compromise between bandwidth and dynamic range. Demodulation of a signal in a band around f_{osc} produces a band of equal magnitude around $2f_{osc}$. This must be reduced by filtering before the signal enters the SSA controller. However, filters introduce low frequency poles which limit the bandwidth of the closed loop system. Thus, a modulation frequency at least an order of magnitude above the closed loop bandwidth (~ 100 Hz) is desirable. On the other hand, with the SQUID controller presently in use, the maximum tolerable sine wave amplitude, and thus the dynamic range, decreases with frequency. At 1 kHz, the dynamic range is $\sim 3 \times 10^6 \text{ Hz}^{1/2}$ with a frequency dependence of approximately f^{-1} . This is not an inherent limitation; systems having a constant dynamic range of $2 \times 10^7 \text{ Hz}^{1/2}$ up to 6 kHz have been built [2]. A previous version of the SSA used a single SQUID coupled to all six sensing circuits. In this case, the oscillator frequencies had to be widely spaced in frequency, so some of the axes had a significantly lower dynamic range than others. The present design uses one SQUID for each circuit to avoid this problem.

Acceleration Sensitivity

As we discussed in the introduction, thermally induced mechanical and electrical fluctuations limit the resolution of an accelerometer. In the SSA, the dissipation of the superconducting magnetic springs is low enough that the noise of the SQUID amplifier generally dominates over the Brownian motion noise. The noise of SQUID can be modeled as a simple current noise source across its input coil with a constant power spectral density of P_{isq} . P_{isq} shows $1/f$ frequency dependence below approximately 0.1 Hz, but because the signal is modulated, it is unaffected by this red noise. Well below the mass-spring resonance frequency, we can estimate the equivalent acceleration noise by combining Eq. (14) and the relationship between displacement and acceleration, $\delta x = a/\omega_0^2$. We substitute $2P_{isq}$ for i_{sq} . (Demodulation causes the SQUID noise to contribute twice.) Using Eq. (6) for ω_0 , we obtain an expression for the equivalent acceleration noise:

$$P_a = 4x_0\omega_0^2 \frac{P_{isq}}{i_{osc}} = \frac{4g_E}{\sqrt{3}} \left(\frac{\gamma_0 x_0}{\Lambda_0} \right) \frac{P_{isq}}{i_{osc}} \quad (15)$$

For a given coil diameter, the dimensionless quantity $(\gamma_0 x_0 / \Lambda_0)$ is a weak function of gap and geometry. Thus, for a given SQUID and coil size, minimizing P_a depends primarily on maximizing i_{osc} .

Unfortunately, there is an inherent limitation on i_{osc} . The current through the sensing coils produces a force on the proof mass proportional to i_{osc}^2 at dc (and $2f_{osc}$, but the proof mass does not respond at this frequency). At zero displacement, the net force is zero (assuming perfectly matched coils). When the

proof mass moves up, the impedance of the lower coils increases and that of the upper coils decreases, so more current flows through the upper coils, increasing the downward force. Hence, the sensing circuit provides an additional spring constant which tends to lower the acceleration sensitivity. By including the spring constant due to the sensing circuit in the calculation of P_a , we find that P_a reaches a minimum when i_{osc} is large enough to double the initial spring constant. This optimum i_{osc} is on the order of the levitation currents. With the present SQUIDs (S.H.E. rf SQUIDs), for which $P_{isq} \approx 10^{-11} \text{ A Hz}^{-1/2}$, the optimum i_{osc} would give an acceleration noise of approximately $2 \times 10^{-11} \text{ m s}^{-2} \text{ Hz}^{-1/2}$. For a more modern system, the Quantum Design dc SQUID, $P_{isq} \approx 6 \times 10^{-13} \text{ A Hz}^{-1/2}$, after reflection through an impedance matching transformer. This is equivalent to an acceleration noise of $2 \times 10^{-12} \text{ m s}^{-2} \text{ Hz}^{-1/2}$. The equivalent angular acceleration noise is $2 \times 10^{-10} \text{ rad s}^{-2} \text{ Hz}^{-1/2}$. In a low g background, the acceleration sensitivity is at least an order of magnitude lower.

A practical limitation prevents us from using the optimum current. The coils are not perfectly matched. Because of this, the force on the proof mass is not zero when it is at a position which balances the bridge. This dc force is a problem because it depends on the amplitude of the oscillator. Drift in the oscillator will cause a changing force on the proof mass, and hence a drift in the acceleration output. We can estimate this acceleration by calculating the total force on the proof mass when the parameter Λ for two lower coils differs from that of the two upper ones by $\delta\Lambda$. Simple circuit analysis gives this force as $\delta\Lambda i_{osc}^2$. If i_{osc} changes by a small amount δi , the resulting shift in the acceleration output is $\delta a = 2\delta\Lambda i_{osc} \delta i / m$, or in terms of relative errors,

$$\delta a = 2 \left(\frac{\delta\Lambda}{\Lambda} \right) \left(\frac{\delta i}{i_{osc}} \right) \frac{\Lambda i_{osc}^2}{m}. \quad (16)$$

We want to set i_{osc} low enough so that oscillator noise does not dominate over SQUID noise in the useful bandwidth of the device. Because of the temperature dependence of critical components in the voltage-to-current output stage, even a well designed current oscillator will have significant red noise. The SQUID output, after demodulation, has little excess red noise above the millihertz regime. Thus, the worst oscillator noise is at the lowest frequency that we expect to use, approximately 1 mHz. We estimate that at this frequency, a current source using the best available components should be stable to 10 ppm. The force coefficients Λ are matched to about 1%. Setting Eq. (16) equal to Eq. (15) (times the square root of frequency) gives a limiting i_{osc} of 90 mA. Even with this limitation, performance is quite good. Substituting $i_{osc} = 90 \text{ mA}$ back into Eq. (15) yields an acceleration noise of $8 \times 10^{-10} \text{ m s}^{-2} \text{ Hz}^{-1/2}$ and an angular acceleration noise of $6 \times 10^{-8} \text{ rad s}^{-2} \text{ Hz}^{-1/2}$, using the current SQUIDs. Of course, if the signal frequencies of interest are higher than this, the limitation is relaxed. For frequencies above a few Hertz, the noise of the oscillator is white and low enough not to matter (assuming the present SQUIDs are used).

This limitation on i_{osc} is purely a technological one. The dimensions of the present wire-wound coils cannot be controlled to better about 100 μm . Using standard photolithographic techniques, thin film coils with dimensional tolerances close to 1 μm should be easily manufacturable. In this case, $\delta\ln\Lambda$ would be small enough that this error source will no longer be relevant. Thin film devices of high quality niobium (such as the SQUIDs) are routinely manufactured, although making reliable, high current (hundreds of

milliamps) superconducting junctions between the films and wires will require some development.

The noise levels calculated for the current design are a substantial improvement over those of a previous version of the device. In that model, all six bridge circuits were connected in series directly with the SQUID input coil. Unfortunately, the impedances are not correctly matched in this configuration. Additionally, the secondary of the feedback transformer was not large enough to minimize the resonance frequency of the translational modes; resonance frequencies were typically 21 Hz. Improving the impedance matching and lowering the resonance frequency will reduce the acceleration noise in the current device by approximately one order of magnitude. For example, the measured acceleration noise of first model of the device was $3 \times 10^{-9} \text{ m s}^{-2} \text{ Hz}^{-1/2}$, using $i_{osc} = 0.23 \text{ A}$ in one of its translational sensing circuits. This matches the value calculated from its parameters to within 25%. An angular acceleration noise of $7 \times 10^{-8} \text{ rad s}^{-2} \text{ Hz}^{-1/2}$ was measured on an angular sensing circuit with $i_{osc} = 0.48 \text{ A}$. For the same current, the acceleration noise of the current design should be $3.0 \times 10^{-10} \text{ m s}^{-2} \text{ Hz}^{-1/2}$. The improvement in angular acceleration noise will only be by about a factor of 4, because the dominant term in the angular spring constant depends only on the coil geometry, which is approximately the same.

Controller

Many of the characteristics of the SSA can be improved by using feedback. Because of the low dissipation of the magnetic levitation, the open-loop acceleration-to-voltage transfer function of the SSA has an undesirable

large peak at the resonance frequency. In addition, the levitation force is a nonlinear function of position. Feedback flattens the response and increases the bandwidth from ~ 13 to $\sim 100 \text{ Hz}$. It also reduces displacement, particularly at low frequencies where the controller gain is high, and thus improves linearity and reduces displacement-related dynamical errors. One of the most important dynamical errors is the cross-axis sensitivity introduced by the off-diagonal terms of the spring constant matrix (Eq. (9)). Although ordinary single-input, single-output feedback reduces cross coupling substantially, the SSA controller uses a sophisticated multiple-input, multiple-output (MIMO) design to further suppress these terms [3], [4].

There are several important considerations in the design of the controller. One of the main challenges when designing a room-temperature controller for an extremely low noise cryogenic instrument is making sure that the controller does not eliminate the advantage of using a cryogenic system by introducing noise that greatly exceeds the SQUID noise. Satisfying this criterion requires careful attention to the output stage of the controller, which takes the voltages from the signal conditioning stage and produces a current that is coupled into the levitation circuits to produce the feedback force. Any noise due to this stage appears as an equivalent acceleration noise. By choosing the voltage-to-current conversion ratio to be low enough, the equivalent acceleration noise can be made to match that of the SQUID. However, a low V-to-I ratio implies that the maximum tolerable signal is small. Increasing the ratio increases the maximum signal, but at the cost of greater noise. Equivalently, the controller can displace upward (not increase) the dynamic range of the system.

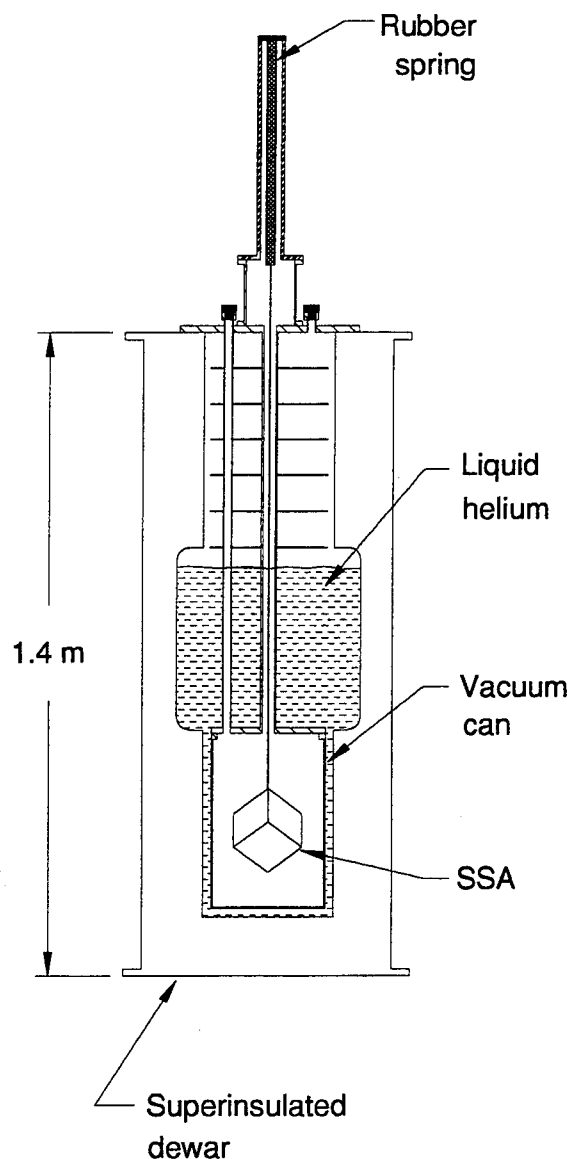


Figure 6. Schematic drawing of the SSA in a typical cryostat used for testing. A shaker, used for applying accelerations, is not shown.

The controller must also not diminish the dynamic range. Because of the relatively large dynamic range of available SQUID controllers (on the order of $10^7 \text{ Hz}^{1/2}$), as well as the sensitivity of the SQUID to rf noise (such as produced by digital systems), we choose to implement the controller with analog circuits. With this type of device we must choose the various gains throughout the system to avoid

saturation in any stage when accelerations are below the design maximum. We have also designed the SSA controller to be stable and robust against changes in the accelerometer parameters.

Ancillary Equipment

Although the proof mass of the SSA is only 5 cm on a side, the overall system, including all electronics and cryogenic hardware, is presently quite large. With modest effort, it can be substantially reduced. Figure 6 schematically portrays the SSA in a cryostat similar to one recently built for a gravity gradiometer. The accelerometer and its superconducting circuitry hang inside a vacuum can from a long rubber spring that provides isolation from high-frequency ($> 2 \text{ Hz}$) seismic noise. For applications in a quiet environment, the device could be mounted with a much stiffer suspension directly to the inside of the vacuum can. The vacuum can fits into a liquid helium dewar. The one shown here is 1.4 m high and 0.4 m in diameter. With careful design, one could reduce the dewar height to less than 1 m.

The extreme sensitivity of SQUIDs to electromagnetic fields that makes them so desirable also makes it necessary to use great care to shield them from undesirable fields. We use several stages of isolation. First, the SSA housing and connection boxes are superconducting, and all critical leads pass through superconducting tubes. We have used a resistive titanium alloy for the coil forms and for the oscillator transformers because these will strongly damp rf signals. The vacuum can is also superconducting. The inner wall of the dewar around the vacuum can and the entire outer wall are of aluminum. In addition, we use two concentric mu-metal shields inside the

dewar's vacuum space to reduce the background magnetic field. Finally, all leads entering the cryostat pass through EMI filters.

Applications

The extremely low noise of the SSA will allow it to extend the state of the art in several important applications. The initial impetus for its development came from the need to meet the extremely demanding platform motion requirements on the proposed Superconducting Gravity Gradiometer Mission [5]. The drag-free satellite contemplated for this mission would contain an SGG that would map the Earth's gravity with unprecedented resolution [6], [7]. Because the SSA is also a cryogenic instrument, it can be mounted directly on the SGG. More importantly, although the SSA can be operated and fully tested in the one-g background field on Earth, in orbit only small levitation currents are needed to provide a bias for the feedback current. Therefore, the effective spring constant, and thus the equivalent acceleration noise level, will be several orders of magnitude lower than on Earth.

Using the SSA, actively controlled terrestrial platforms could offer unprecedented quiet seismic environments. Active quiet platforms are under investigation for a number of uses. The Seismically Stable Platform (SSP) at Holloman Air Force Base is intended for testing of inertial guidance systems. Similar devices could be used in laser interferometer gravitational-wave antennas. The mirrors of the interferometer must be mounted on seismically quiet platforms. Particularly at low frequencies (<100 Hz), the level of allowed platform motion is extremely small. Active control of the SGG platform in the laboratory could reduce several motion-related error

sources, and so improve measurements of the inverse-square law of gravity [8].

Although gravity survey from orbit has the advantage of providing complete global coverage, resolution of features substantially smaller than 50 km is not likely in the foreseeable future. However, at an altitude of 1 km, geological features with a size on the order of 1 km produce gravity gradient signals that even a much less sensitive gradiometer can detect. Unfortunately, an airplane is a hostile environment for sensitive motion detectors. An actively controlled platform can remove angular and high-frequency translational motion. However, control of translational motion at low frequencies is not possible (using existing autopilots), because the displacements needed exceed the dimensions of airplane interiors. An SGG/SSA package could be mounted on a platform controlled by standard instruments, and the SSA could be used to remove errors from low-frequency translational motion and residual angular motion of the platform.

The SSA could also be used alone for airborne gravity survey. In this case, the SSA would be mounted on a simple passive isolation platform along with a GPS receiver. Subtracting the acceleration of the vehicle, obtained using the GPS data, from the acceleration measured by the SSA will give the variation in local gravity. This technique has been successfully tried in airplanes [9] and unmanned balloons [10] using single-degree-of-

freedom gravimeters. Because the SSA provides the motion in all six degrees of freedom, it would allow the local gravity *vector* to be mapped. An SSA to be used in such a seismically noisy environment would have to be optimized to maximize its dynamic range.

Acknowledgements

This work was supported by the Air Force Phillips Laboratory under contract F19628-87-K-0053.

References

- [1] Paik, H.P., Parke, J.W., and Canavan, E.R., "Development of a superconducting six-axis accelerometer", Final Report to the Air Force Geophysics Laboratory, Report No. GL-TR-89-0181 (1989).
- [2] Wellstood, F., Heiden, C., and Clarke, J., "Integrated dc SQUID magnetometer with a high slew rate", *Reviews of Scientific Instruments* **55**(6):952-957 (1984).
- [3] Bachrach, B., *Control of a superconducting six-axis accelerometer*, Master's Thesis, University of Maryland (1990).
- [4] Bachrach, B., Canavan, E.R., and Levine, W.S., "Diagonalizing controller for a superconducting six-axis accelerometer", *Proceedings of the 29th IEEE Conference on Decision and Control*, Honolulu, HI (1990).
- [5] Paik, H.J., et al., "Global gravity survey by an orbiting gravity gradiometer", *EOS* **69**(48): 1601, 1610-1611 (1988).
- [6] Paik, H.J., "Superconducting tensor gravity gradiometer for satellite geodesy and inertial navigation", *Journal of the Astronautical Sciences* **29**(1):1-18 (1981).
- [7] Moody, M.V., Chan, H.A., and Paik, H.J., "Superconducting gravity gradiometer for space and terrestrial applications", *Journal of Applied Physics* **60**(12):4308-4315 (1986).
- [8] Moody, M.V. and Paik, H.J., "Gauss's Law test of gravity at short range", *Physical Review Letters* **70**(9): 1195-1198 (1993).
- [9] Brozena, M. and Peters, M.F., "An airborne gravity survey of eastern North Carolina", *Geophysics* **53**(2): 245-253 (1988).
- [10] Lazarewicz, A., et al., "Balloon-borne high altitude gravimetry: The flight of DUCKY II", Environmental Research Papers, No. 988, Air Force Geophysics Laboratory (1987).

DIAGONALIZING CONTROLLER FOR A SUPERCONDUCTING SIX-AXIS ACCELEROMETER

B. Bachrach†, E. R. Canavan† and W. S. Levine‡
University of Maryland,
College Park, MD 20742

Abstract

A relatively simple MIMO controller which converts an instrument with a non-diagonally dominant transfer function matrix into a strongly diagonally dominant device is developed. The instrument, which uses inductance bridges to sense the position of a magnetically levitated superconducting mass, has very lightly damped resonances and fairly strong cross coupling. By taking advantage of the particular structure of the instrument's transfer function matrix, it is possible to develop a relatively simple controller which achieves the desired decoupling. This controller consists of two parts. The first part cancels the non-diagonal terms of the open loop transfer function matrix, while the second part is simply a set of SISO controllers. The stability of the closed loop system is studied using Rosenbrock's INA technique, which produces a simple set of conditions guaranteeing stability. The robustness of the closed loop system with respect to multiplicative plant perturbations is studied, and bounds on the admissible singular values of the perturbation matrices are found. Simulation of the closed loop system indicates that it should easily achieve its performance goals.

Acknowledgement

This work was supported in part by the Air Force Geophysics Laboratory under contracts F19628-85-K-0062 and F19628-87-K-0053, and by the Systems Research Center at the University of Maryland under National Science Foundation Grant CDR 8803012.

1 Introduction

An extremely sensitive¹ Superconducting Six-Axis Accelerometer (SSA) is under construction at the University of Maryland². This instrument has been designed to monitor the platform motions of a Superconducting Gravity Gradiometer (SGG) which is being developed for space applications [6]. The signals from the accelerometer will be used to control the position and attitude of the gradiometer platform. It is envisioned that the combined SGG/SSA package will be flown in earth orbit to perform global gravity mapping in the late 1990's. A superconducting gravity gradiometer/accelerometer system with such high sensitivity, if successfully developed, will find many important applications in local gravity survey, inertial guidance and fundamental physics.

A six-axis accelerometer measures translational and rotational acceleration in all six degrees of freedom. The desired outputs of the instrument are six signals, each proportional to the acceleration of the device along one of the measured axes, and independent of the accelerations along the other axes. Hence, the instrument should ideally have a diagonal transfer function matrix. However, analysis of the system model reveals that in open loop operation, the SSA

does not have a diagonal transfer function. In fact, due to the weakly damped modes of the SSA, it does not even have a diagonally dominant transfer function. The goal of the control aspect of the project is to design an easily implementable compensator that will provide a diagonal (or almost diagonal) closed loop transfer function matrix, while also improving the linearity and bandwidth of the instrument. By taking advantage of the particular structure of the open loop transfer function, it is possible to develop a relatively simple controller which fulfills these requirements. This controller consists of two parts, one of which cancels the effect of the non-diagonal terms of the open loop transfer function, while the other is simply a set of SISO controllers. Using this approach, we reduce a MIMO design problem to six independent SISO design problems. The stability of the closed loop system is analyzed using Rosenbrock's Inverse Nyquist Array (INA) method [4], and a very simple set of stability conditions is obtained. Also, since it is known that diagonalized systems are not always robust, the robustness of the closed loop system is evaluated by finding bounds on the maximum admissible singular values of multiplicative perturbations³. Finally, the performance of this controller is simulated, and the main results are presented.

The paper is divided into five sections. Section 1 is an introduction to the control problem. In Section 2, a brief description of the SSA as well as its equations of motion are introduced. Based on the linearization of these dynamic equations, a model of the transfer functions of the SSA is derived. Section 3 describes the SSA in closed loop operation and presents the proposed controller. An analysis of the closed loop system stability, together with the means to evaluate its robustness are also included. Section 4 presents the performance achieved by the controller for a simulation based on the open loop model derived in Section 2. Finally, Section 5 summarizes the results of the paper and proposes directions for future study.

2 The SSA in Open Loop Operation

2.1 Description of the SSA

The Superconducting Six-Axis Accelerometer (SSA) consists of a housing within which a superconducting proof mass is magnetically levitated. The magnetic field is created by persistent currents stored in a set of superconducting coils. By monitoring the motion of the proof mass with respect to the housing in all six degrees of freedom, it is possible to determine the accelerations acting on the housing in all six degrees of freedom.

Figure 1a shows a perspective view of the proof mass used in the SSA prototype. The material is niobium (Nb), which becomes superconducting below 9.2 K. Twenty four pairs of coils made of niobium-titanium alloy (NbTi) are mounted on eight titanium alloy (Ti-6Al-4V) coil forms like the one shown in Fig. 1b. Each pair of coils consists of a sensing and a feedback/levitation coil. Fig. 2

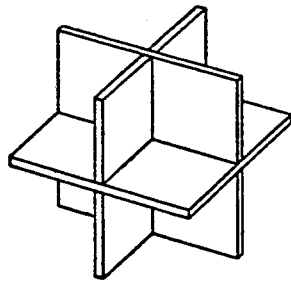
† Department of Physics and Astronomy

‡ Department of Electrical Engineering

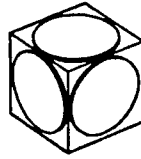
¹ According to [7] the ultimate sensitivity is 10^{-12} gHz^{1/2} for the translational acceleration measurements, and 10^{-3} arcsec sec²Hz^{1/2} for the rotational acceleration measurements.

² Department of Physics and Astronomy, General Relativity Laboratory, directed by Professor H. J. Paik.

³ In this context, the term "admissible" is to be interpreted as not causing instability of the closed loop system.



a) Proof mass perspective



b) Coil form

Figure 1 Proof mass perspective and coil form

shows a cross-sectional view of the proof mass and the sensing and levitation coils of the assembled instrument.

The twenty four levitation/feedback coils are connected to form six circuits, each of which controls the displacement⁴ of the proof mass in one degree of freedom, without coupling to the other degrees of freedom as long as the system has cubic symmetry, and the displacements of the proof mass are kept small.

The twenty four sensing coils are connected to form six bridge circuits, each containing four coils. Each bridge is driven with an AC current source at a unique carrier frequency. Since the inductance of a coil is proportional to the distance between the coil and the superconducting proof mass [5], the circuit can be arranged so that the output of each bridge is an oscillating current proportional in amplitude to the displacement of the proof mass in the corresponding degree of freedom. Each signal will be independent of other displacements as long as the system has cubic symmetry, and the displacements of the proof mass are kept small. The six bridges are connected in series with the input coil of a single SQUID (Superconducting QUantum Interference Device), an extremely high gain, low noise magnetic flux to voltage converter (see [3] or [9]). Because six unique carrier frequencies are used, the SQUID output can be demodulated with the six carrier signals to recover the displacement signals. These displacement signals are to be used as inputs to the feedback controller.

2.2 Dynamic Equations of the SSA

For an accelerometer with a single degree of freedom, the dynamic equations which relate the acceleration of the housing to the position of the proof mass are relatively simple. In the SSA, however, it is necessary to contend with both the translational and rotational degrees of freedom. The rotational degrees of freedom greatly complicate the description of the proof mass motion, making it necessary to use three reference frames: an inertial reference frame, a reference frame attached to the accelerometer housing, and a reference frame attached to the proof mass. The complete derivation of the dynamic equations of the SSA is beyond the scope of this paper. An extensive analysis of the theoretical aspects of the SSA can be found in [7] or [8]. The analysis presented below follows this treatment, but extends the dynamic equations to include the effect of the feedback currents.

Dynamic Equations of the Translational Axes. The equations of translational motion of the proof mass can be written

$$\ddot{\mathbf{r}}_k^p + \frac{\partial V(R^p, \bar{\mathbf{r}}^p)}{m \partial \mathbf{r}_k^p} = \mathbf{a}_k^e, \quad k = x, y, z, \quad (1)$$

⁴ The displacements of the proof mass are defined as the position (translational displacements) and orientation (rotational displacements) of the proof mass in the housing reference frame. Hence, zero displacement corresponds to the position and orientation where the principal axes of the proof mass coincide with the housing reference frame.

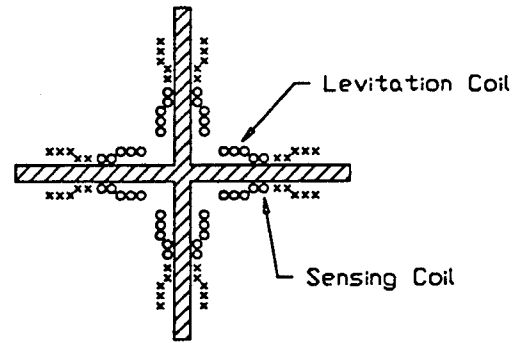


Figure 2 Coils distribution around proof mass

where

\mathbf{r}_k^p = k -th component of the proof mass translational displacement,

R^p = rotation matrix describing the orientation of the proof mass in the housing reference frame,

$V(R^p, \bar{\mathbf{r}}^p)$ = potential energy of proof mass,

m = mass of proof mass.

The effective external translational acceleration applied to the proof mass, $\bar{\mathbf{a}}^e$, is given by

$$\bar{\mathbf{a}}^e = -\ddot{\mathbf{r}}^H - \bar{\mathbf{g}} - 2\bar{\boldsymbol{\omega}}^H \times \dot{\mathbf{r}}^p - \bar{\boldsymbol{\omega}}^H \times (\bar{\boldsymbol{\omega}}^H \times \bar{\mathbf{r}}^p) - \dot{\bar{\boldsymbol{\omega}}}^H \times \bar{\mathbf{r}}^p, \quad (2)$$

where

$\bar{\mathbf{r}}^p$ = proof mass translational displacement vector,

$\bar{\mathbf{r}}^H$ = housing position in inertial reference frame,

$\bar{\boldsymbol{\omega}}^H$ = angular velocity of the housing,

$\bar{\mathbf{g}}$ = gravitational acceleration vector (in the intended use, $\bar{\mathbf{g}}$ is not constant).

The currents in the superconducting coils surrounding the proof mass generate the potential energy $V(R^p, \bar{\mathbf{r}}^p)$. The displacement of the proof mass is controlled by these currents. Ideally, the effective external acceleration sensed by the proof mass ($\bar{\mathbf{a}}^e$), i.e. the measured acceleration, should be equal and opposite to the acceleration of the housing ($\ddot{\mathbf{r}}^H$). From Eqn. (2) we see that, in order to equate the translational acceleration of the housing to the effective translational acceleration of the proof mass, we must keep the displacement of the proof mass $\bar{\mathbf{r}}^p$, and its velocity $\dot{\bar{\mathbf{r}}}^p$, to a minimum.

An expression for $V(R^p, \bar{\mathbf{r}}^p)$ can be found in [7] or [8]. Introducing the feedback currents into this expression, differentiating, substituting in Eqn. (1), and linearizing the resulting expression, we obtain for the r_x degree of freedom (Note that we drop the superscript p for the linearized quantities.):

$$\ddot{r}_x + \omega_{r_x}^2 r_x = \frac{f_{DC}}{m} + \frac{f_{DC}}{m} (\theta_y - \theta_z) + k_{r_x} I_{r_x} + a_x^e,$$

ω_{r_i} = resonance frequency of the i -th translational degree of freedom,

f_{DC} = DC force applied by levitation current (must be equal and opposite to the corresponding component of the proof mass weight),

k_{r_i} = ratio of feedback current to feedback acceleration for the i -th translational degree of freedom,

θ_i = linearized (see Eqns. (3), (4) and (5)) rotation angle of the proof mass about the i -th axis of the housing reference frame,

I_{r_i} = feedback current applied to the i -th translational degree of freedom.

Up to this point, we have assumed that no damping of the motion of the proof mass occurs. Actually, coupling to the strongly damped experimental suspension and viscous damping by the residual gas in the vacuum chamber limit the Q of the resonant modes of the SSA. The damping of the proof mass in the translational degrees of freedom can be modeled by the addition of a velocity-dependent term, $(\omega_{r_x}/Q_{r_x})\dot{r}_x$, to the equations of motion for the SSA, where Q_{r_x} is the quality of the resonance for the translational x -axis. Introducing this term, we obtain the following dynamic equation for r_x :

$$\ddot{r}_x + \frac{\omega_{r_x}}{Q_{r_x}}\dot{r}_x + \omega_{r_x}^2 r_x = \frac{f_{DC}}{m} + \frac{f_{DC}}{m}(\theta_y - \theta_z) + k_{r_x} I_{r_x} + \alpha_x^e.$$

Similarly, the equations of motion for r_y and r_z can be obtained:

$$\ddot{r}_y + \frac{\omega_{r_y}}{Q_{r_y}}\dot{r}_y + \omega_{r_y}^2 r_y = \frac{f_{DC}}{m} + \frac{f_{DC}}{m}(\theta_z - \theta_x) + k_{r_y} I_{r_y} + \alpha_y^e,$$

$$\ddot{r}_z + \frac{\omega_{r_z}}{Q_{r_z}}\dot{r}_z + \omega_{r_z}^2 r_z = \frac{f_{DC}}{m} + \frac{f_{DC}}{m}(\theta_x - \theta_y) + k_{r_z} I_{r_z} + \alpha_z^e.$$

Dynamic Equations of the Rotational Axes. The equation of rotational motion of the proof mass about the x -axis can be written:

$$\ddot{\theta}_x^p + \frac{\partial V(R^p, \bar{r}^p)}{I \partial \theta_x^p} = \alpha_x^e, \quad (3)$$

where

I = moment of inertia of proof mass about principal axes,
 θ_i^p = rotation angle of proof mass about the i -th axis of the housing reference frame,

and the effective external rotational acceleration about the x -axis of the proof mass (α_x^e) is given by

$$\alpha_x^e = -\dot{\omega}_x^H + \frac{1}{2}(\dot{\omega}_z^H \theta_y^p - \dot{\omega}_y^H \theta_z^p) - \omega_z^H \dot{\theta}_y^p + \omega_y^H \dot{\theta}_z^p, \quad (4)$$

where ω_i^H = i -th component of rotational velocity of housing.

As with the translational degrees of freedom, in order to equate the rotational acceleration of the housing ($\dot{\omega}_i^H$) to the effective rotational acceleration sensed by the proof mass (α_i^e), we must keep the rotational displacement of the proof mass θ_i^p and its velocity, $\dot{\theta}_i^p$, to a minimum.

Substituting $V(R^p, \bar{r}^p)$ into Eqn. (3), and proceeding in the same way as with the translational degrees of freedom, we obtain for θ_x (Note that we drop the superscript p for the linearized quantities.):

$$\ddot{\theta}_x + \frac{\omega_{\theta_x}}{Q_{\theta_x}}\dot{\theta}_x + \omega_{\theta_x}^2 \theta_x = \frac{f_{DC}}{I}(r_z - r_y) - k_{\theta_x} I_{\theta_x} + \alpha_x^e, \quad (5)$$

where

ω_{θ_i} = resonance frequency for the i -th rotational degree of freedom of the proof mass,
 Q_{θ_i} = quality of the resonance for the i -th rotational degree of freedom of the proof mass,
 k_{θ_i} = ratio of feedback current to feedback acceleration for the i -th rotational degree of freedom of the proof mass,
 I_{θ_i} = feedback current applied to the i -th rotational degree of freedom of the proof mass.

In an analogous way, we obtain for θ_y and θ_z :

$$\ddot{\theta}_y + \frac{\omega_{\theta_y}}{Q_{\theta_y}}\dot{\theta}_y + \omega_{\theta_y}^2 \theta_y = \frac{f_{DC}}{I}(r_x - r_z) - k_{\theta_y} I_{\theta_y} + \alpha_y^e,$$

$$\ddot{\theta}_z + \frac{\omega_{\theta_z}}{Q_{\theta_z}}\dot{\theta}_z + \omega_{\theta_z}^2 \theta_z = \frac{f_{DC}}{I}(r_y - r_x) - k_{\theta_z} I_{\theta_z} + \alpha_z^e.$$

2.3 Transfer Functions of the SSA

Taking the Laplace transform of the linearized equations of motion derived in the previous section, we can obtain the relations between the proof mass displacements, the external accelerations, and the feedback currents. These relations can be written in matrix form by defining the vectors:

$$\begin{aligned} \bar{a}^E(s) &= [\alpha_x^e + \frac{f_{DC}}{m}s, \alpha_y^e + \frac{f_{DC}}{m}s, \alpha_z^e + \frac{f_{DC}}{m}s, \alpha_x^e, \alpha_y^e, \alpha_z^e]^T, \\ \bar{I}_f(s) &= [I_{r_x}, I_{r_y}, I_{r_z}, I_{\theta_x}, I_{\theta_y}, I_{\theta_z}]^T, \\ \bar{r}(s) &= [r_x, r_y, r_z, \theta_x, \theta_y, \theta_z]^T, \end{aligned}$$

(where dependencies on s have been omitted for brevity) and matrices:

$$\Psi(s) = \begin{bmatrix} T_{r_x}(s) & 0 & 0 & 0 & -f_m & f_m \\ 0 & T_{r_y}(s) & 0 & f_m & 0 & -f_m \\ 0 & 0 & T_{r_z}(s) & -f_m & f_m & 0 \\ 0 & f_I & -f_I & T_{\theta_x}(s) & 0 & 0 \\ -f_I & 0 & f_I & 0 & T_{\theta_y}(s) & 0 \\ f_I & -f_I & 0 & 0 & 0 & T_{\theta_z}(s) \end{bmatrix},$$

$$K = \text{diag}\{k_{r_x}, k_{r_y}, k_{r_z}, -k_{\theta_x}, -k_{\theta_y}, -k_{\theta_z}\}, \quad (6)$$

where

$$\begin{aligned} T_i(s) &= s^2 + \frac{\omega_i}{Q_i}s + \omega_i^2, \quad i = r_x, r_y, r_z, \theta_x, \theta_y, \theta_z, \\ f_I &= \frac{f_{DC}}{I}, \quad f_m = \frac{f_{DC}}{m}. \end{aligned}$$

Substituting the above definitions, we obtain:

$$\Psi(s)\bar{r}(s) = K\bar{I}_f(s) + \bar{a}^E(s). \quad (7)$$

Eqn. (7) expresses the feedback currents and external accelerations as a function of the proof mass displacements. Inverting this relation, we obtain an expression for the position of the proof mass as a function of the external acceleration and feedback currents:

$$\bar{r}(s) = \Psi^{-1}(s)K[\bar{I}_f(s) + K^{-1}\bar{a}^E(s)]. \quad (8)$$

Finally, since the signals available to the controller are the output voltages of the sensing circuits, we need to relate the position of the proof mass to the output voltages. This relation is modeled by:

$$\bar{V}_{out}(s) = \Xi(s)\bar{r}(s),$$

where

$$\begin{aligned} \Xi(s) &= \text{diag}\{\xi_{r_x}(s), \xi_{r_y}(s), \xi_{r_z}(s), \xi_{\theta_x}(s), \xi_{\theta_y}(s), \xi_{\theta_z}(s)\}, \\ \bar{V}_{out}(s) &= [V_{r_x}, V_{r_y}, V_{r_z}, V_{\theta_x}, V_{\theta_y}, V_{\theta_z}]^T, \end{aligned}$$

and

$$\xi_i(s) = \rho_i \frac{\omega_s}{s + \omega_s}, \quad i = r_x, r_y, r_z, \theta_x, \theta_y, \theta_z,$$

where

ρ_i = DC gain of sensing circuit for the i -th degree of freedom,
 $\xi_i(s)$ = transfer function between i -th displacement and corresponding output voltage,
 ω_s = cutoff frequency of low pass filter in the sensing circuit.

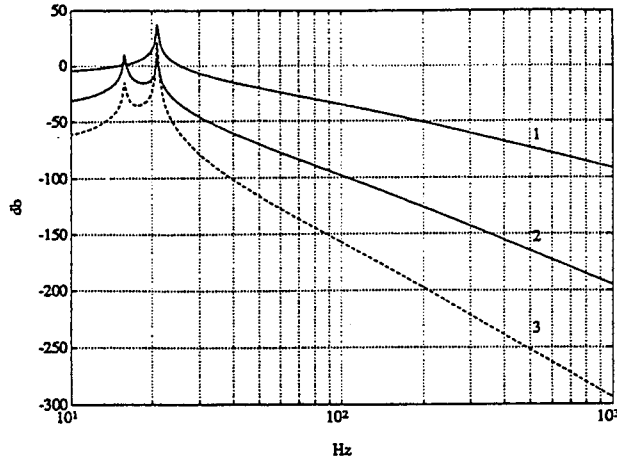


Figure 3 Predicted open loop response: (1) $V_{rx}(s)/a_x^e(s)$; (2) $V_{\theta_y}(s)/a_x^e(s)$ (or $V_{\theta_x}(s)/a_x^e(s)$); (3) $V_{ry}(s)/a_x^e(s)$ (or $V_{rx}(s)/a_x^e(s)$).

The low pass filter in the sensing circuit exists because of the modulation/demodulation required to efficiently sense the displacements. As already mentioned, all six currents are frequency multiplexed through a single SQUID. There are practical advantages to this, but a significant disadvantage is that ω_s is relatively small. Taking into consideration the sensing circuit response, we rewrite Eqn. (8) as follows:

$$\bar{V}_{out}(s) = \underbrace{\Xi(s) \Psi^{-1}(s) K}_{G(s)} [\bar{I}_f(s) + K^{-1} \bar{a}^E] \quad (9)$$

Under the assumption of perfect geometry:

$$T_{r_i}(s) = T_r(s) \text{ and } T_{\theta_i}(s) = T_\theta(s) \text{ for } i = x, y, z,$$

Hence,

$$\Xi(s) = \frac{1}{\begin{bmatrix} T_r(s) T_\theta(s) - 3f_I f_m & 0 & f_m & -f_m \\ \frac{-M(s)}{T_r(s)} & \frac{f_I f_m}{T_r(s)} & \frac{f_I f_m}{T_r(s)} & 0 \\ \frac{f_I f_m}{T_r(s)} & \frac{-M(s)}{T_r(s)} & \frac{f_I f_m}{T_r(s)} & -f_m \\ \frac{f_I f_m}{T_r(s)} & \frac{f_I f_m}{T_r(s)} & \frac{-M(s)}{T_r(s)} & f_m \end{bmatrix} \begin{bmatrix} f_m & -f_m & 0 \\ \frac{M(s)}{T_\theta(s)} & \frac{-f_I f_m}{T_\theta(s)} & \frac{-f_I f_m}{T_\theta(s)} \\ \frac{-f_I f_m}{T_\theta(s)} & \frac{M(s)}{T_\theta(s)} & \frac{-f_I f_m}{T_\theta(s)} \\ \frac{-f_I f_m}{T_\theta(s)} & \frac{-f_I f_m}{T_\theta(s)} & \frac{M(s)}{T_\theta(s)} \end{bmatrix} K,$$

where

$$M(s) = T_r(s) T_\theta(s) - f_I f_m.$$

The transfer functions of the operating device have been measured. The results of two of these measurements are compared with the predicted transfer functions in Appendix A. These results indicate that the model is indeed quite accurate. Fig. 3 shows the predicted transfer functions between a translational acceleration (a_x^e) and the different outputs of the open loop system. An important point revealed by this model is the fact that neither $G(s)$ nor $G^{-1}(s)$ are diagonally dominant matrices on the $j\omega$ axis.

3 Design of a Diagonalizing Controller

3.1 The SSA in Closed Loop Operation

In the previous section, we demonstrated the importance of minimizing the displacements and displacement velocities of the

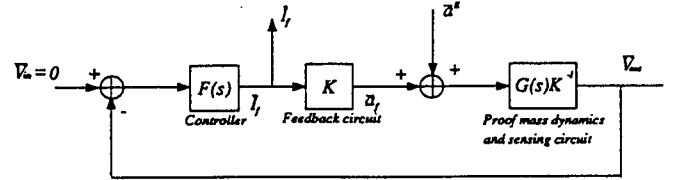


Figure 4 The SSA as a closed loop system

proof mass. This can be achieved by adding a feedback controller, thus operating the instrument as a null detector (Fig. 4). The second important requirement is for the closed loop transfer function matrix to be diagonal, or at least diagonally dominant. Let us first consider the problem of diagonalizing the closed loop transfer function.

From Fig. 4, the transfer function between acceleration input \bar{a}^E and controller output current \bar{I}_f is:

$$\bar{I}_f = [I + F(s) G(s)]^{-1} F(s) G(s) K^{-1} \bar{a}^E$$

or

$$\bar{I}_f = [I + G^{-1}(s) F^{-1}(s)]^{-1} K^{-1} \bar{a}^E. \quad (10)$$

Mathematically, this transfer function could be made perfectly diagonal simply by choosing $F(s) = G^{-1}(s) g(s)$, where $g(s)$ is a scalar transfer function which could be designed to produce any desired closed loop transfer function. This scheme, however, is based on the assumption that one could construct a controller $F(s)$ such that $G^{-1}(s) F^{-1}(s) = I g^{-1}(s)$. In practice, it is very unlikely that such an identity could be made to hold over a wide frequency range mainly because of plant uncertainties. In the SSA, realizing such an $F(s)$ would be especially difficult because the modes of the SSA are very lightly damped (Q_{θ_i} are up to 1500), making the product $G^{-1}(s) F^{-1}(s)$ particularly sensitive to model uncertainties.

Since attaining the perfect diagonalizing controller is not feasible, we could place a weaker assumption on $F(s)$, requiring only that it produces a diagonally dominant $G^{-1}(s) F^{-1}(s)$. The stability of the resulting closed loop system could then be partially analyzed using Rosenbrock's Inverse Nyquist Array (INA) [4] method. For the SSA, however, finding a relatively simple $F(s)$ which would ensure diagonal dominance of $G^{-1}(s) F^{-1}(s)$ proves particularly difficult because of the high values of Q_{r_i} and Q_{θ_i} .

3.2 The Controller

Eqn. (10) does not immediately suggest any other choices of $F(s)$. However, if one takes the output voltage of the sensing circuit as the output of the system, the closed loop transfer function becomes:

$$\bar{V}_{out} = [F(s) + G^{-1}(s)]^{-1} K^{-1} \bar{a}^E. \quad (11)$$

One can see from Eqn. (11) that the closed loop transfer function can be made diagonal by choosing $F(s)$ such that:

$$F(s) = D_0(s) + C(s),$$

where

$$(D_0(s))_{ij} = (\delta_{ij} - 1) (G^{-1}(s))_{ij}; \quad i, j = 1, \dots, 6 \quad (12)$$

and

$$C(s) = \text{diag} \{c_{rx}(s), c_{ry}(s), c_{rz}(s), c_{\theta_x}(s), c_{\theta_y}(s), c_{\theta_z}(s)\}.$$

Thus, $D_0(s)$ cancels the non-diagonal elements of $G^{-1}(s)$. Assuming such cancellation to be possible, the obtained transfer function is diagonal, and the diagonal elements of the closed loop are:

$$h_{ii}(s) = \frac{\xi_i(s)/T_i(s)}{1 + \xi_i(s) k_i(s) c_i(s)/T_i(s)}, \quad i = r_x, r_y, r_z, \theta_x, \theta_y, \theta_z. \quad (13)$$

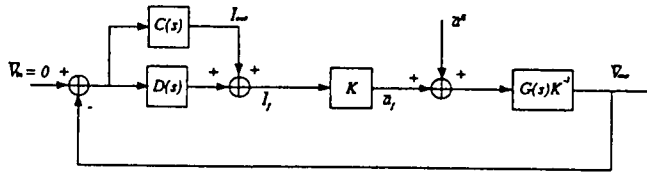


Figure 5 Complete solution with $D(s)$ as a physical realization of $D_0(s)$

This solution is still unsatisfactory. We see that the Eqn. (13) is not a typical SISO transfer function, since the controller $c_i(s)$ does not appear in the numerator. This problem can be solved by dividing the controller in the way shown in Fig. 5, obtaining the closed loop transfer function

$$\bar{I}_{out} = -C(s) [G^{-1}(s) + D_0(s) + C(s)]^{-1} K^{-1} \bar{a} E, \quad (14)$$

with the diagonal elements:

$$h_{ii}(s) = \frac{k_i \xi_i(s) c_i(s) / T_i(s)}{1 + k_i \xi_i(s) c_i(s) / T_i(s)} \left(\frac{1}{k_i} \right), \quad i = r_x, r_y, r_z, \theta_x, \theta_y, \theta_z. \quad (15)$$

So, under the assumption that $D_0(s)$ can be implemented to cancel the non-diagonal elements of $G^{-1}(s)$, $C(s)$ can be designed as six independent SISO controllers, transforming our MIMO design problem into six independent SISO design problems.

In the present case, however, perfect cancellation of the non-diagonal terms of $G^{-1}(s)$ by $D_0(s)$ is impossible because the non-diagonal elements of $G^{-1}(s)$ are not realizable. Thus, a crucial question for the design is: How accurately do the elements of $D(s)$ ($D(s)$ being a realizable approximation of $D_0(s)$) have to approximate the non-diagonal elements of $G^{-1}(s)$? A realizable transfer function can be made to fit well at low frequencies, but it diverges from the desired function at high frequencies, since the non-diagonal terms of $G^{-1}(s)$ are not proper. We will show, based on Rosenbrock's INA method, that the cancellation of the non-diagonal elements need not be perfect; it is sufficient that $G^{-1}(s) + D(s) + C(s)$ be diagonally dominant in order to guarantee the stability of the closed loop system. Fortunately, the diagonal terms of $G^{-1}(s)$ for the SSA are of higher order than the non-diagonal terms, so at high frequencies $G^{-1}(s)$ is naturally diagonally dominant. Thus, $D(s)$ needs to be an accurate approximation of the non-diagonal terms of $G^{-1}(s)$ only over a limited frequency range. For the SSA, a relatively simple implementation of $D(s)$ will ensure this condition.

So far, we have addressed the problem of diagonalizing the closed loop transfer function. The second important consideration for operating the SSA in a closed loop configuration is to minimize the displacements and displacement velocities of the proof mass with respect to the housing. In particular, in order to minimize the steady state error of the proof mass displacements, we include an integrator in each element of $C(s)$. It is thus convenient to write $C(s)$ as $C(s) = \hat{C}(s) \frac{1}{s}$, where $\frac{1}{s}$ is a diagonal matrix of integrators, and $\hat{C}(s)$ is a diagonal matrix whose elements are all asymptotically stable. The convenience of this notation becomes clear in the following section.

3.3 Imperfect Cancellations: Stability and Robustness

In probing the effects of imperfect cancellation, it is useful to write $D(s)$ as $D_0(s) + \Delta D(s)$, where $D_0(s)$ perfectly obeys Eqn. (12) and $\Delta D(s)$ is an error matrix. Substituting into Eqn. (14), we obtain the closed loop transfer function:

$$H(s) = -C(s) [G^{-1}(s) + D_0(s) + \Delta D(s) + C(s)]^{-1} K^{-1}. \quad (16)$$

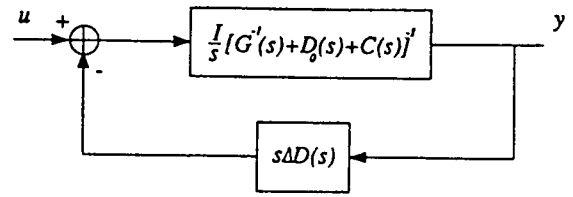


Figure 6 Reduced system

Before proceeding to study the effect of $\Delta D(s)$ in the closed loop transfer function $H(s)$, we note that K is diagonal and constant. Also, $\hat{C}(s)$ is diagonal, and we assume all its elements to be asymptotically stable. Hence, we can limit our analysis of stability to the following transfer function:

$$H_R(s) = \frac{1}{s} [G^{-1}(s) + D_0(s) + \Delta D(s) + C(s)]^{-1}. \quad (17)$$

This transfer function corresponds to the system shown in Fig. 6. We will carry out the investigation of stability and robustness of the SSA on this *reduced* system.

Stability. We study the stability of the reduced system by applying Rosenbrock's Inverse Nyquist Array (INA) stability criterion.

Definition 1. We define the contour C as the contour consisting of the imaginary axis from $s = -rj$ to $s = rj$, together with a closing semicircle of radius r in the right-hand plane, r being large enough to include any right-hand plane poles or zeros of the relevant function.

Theorem 1. (Inverse Nyquist Array stability criteria) Consider the system shown in Fig. 7, where $Q(s)$, and $F(s)$ are $n \times n$ transfer function matrices. Let $N_{Q^{-1}}^i$ and $N_{Q^{-1}+F}^i$, for $1 \leq i \leq n$, denote the number of counter-clockwise encirclements about the origin of the image of contour C under the mappings $[Q^{-1}(s)]_{ii}$ and $[Q^{-1}(s) + F(s)]_{ii}$, respectively. If the following conditions hold:

- C1. $Q^{-1}(s)$ is row (column) diagonally dominant on C ,
- C2. $Q^{-1}(s) + F(s)$ is row (column) diagonally dominant on C ,
- C3. No poles of $[Q^{-1}(s)]_{ii}$ fall on C ,
- C4. No poles of $[Q^{-1}(s) + F(s)]_{ii}$ fall on C ,
- C5. $Q(s)$ is stable,

then, the closed loop system shown in Fig. 7 is stable if and only if:

$$\sum_{i=1}^n N_{Q^{-1}}^i = \sum_{i=1}^n N_{Q^{-1}+F}^i. \quad (18)$$

For the system in Fig. 6, $F(s) = s\Delta D(s)$ and $Q(s) = [sG^{-1}(s) + sD_0(s) + \hat{C}(s)]^{-1}$. Note that, by definition, $\hat{C}(s)$ is diagonal and $sD_0(s)$ cancels the non-diagonal elements of $sG^{-1}(s)$. Note also that since $s\Delta D(s)$ has no diagonal elements,

$$\begin{aligned} [sG^{-1}(s) + sD_0(s) + \hat{C}(s)]_{ii} &= \\ [sG^{-1}(s) + sD_0(s) + \hat{C}(s) + s\Delta D(s)]_{ii}. \end{aligned} \quad (19)$$

In order to translate the conditions C1 – C5 for the reduced system into conditions on $\hat{C}(s)$ and $D(s)$, we make two initial assumptions about $\hat{C}(s)$:

A1.

$$\text{Det} [\hat{C}^{-1}(s)] \neq 0, \quad \forall s | \text{Re}(s) \geq 0.$$

That is, $\hat{C}(s)$ is asymptotically stable.

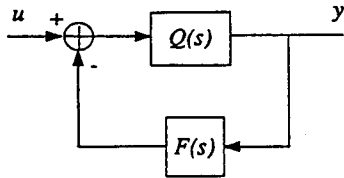


Figure 7 General configuration

A2.

$$\text{Det} [sG^{-1}(s) + sD_0(s) + \hat{C}(s)] \neq 0, \forall s | \text{Re}(s) \geq 0.$$

That is, $\frac{1}{s} [G^{-1}(s) + D_0(s) + C(s)]^{-1}$ is asymptotically stable.

Under these assumptions, we verify conditions C1, C3, C4, C5 and equality (18). By A2, $\text{Det} [sG^{-1}(s) + sD_0(s) + \hat{C}(s)] \neq 0, \forall s \in C$. Thus, since the matrix $[sG^{-1}(s) + sD_0(s) + \hat{C}(s)]$ is diagonal, C1 is satisfied. By A1, $\hat{C}(s)$ is asymptotically stable, so the elements of $\hat{C}(s)$ have no poles on C . Clearly, the diagonal elements of $sG^{-1}(s)$ have no finite poles. Hence, C3 is satisfied. C4 is equivalent to C3 by Eqn. (19). C5 is fulfilled by A2. Equality (18) holds by Eqn. (19). Therefore, under A1 and A2, C2 implies the stability of the closed loop system.

Robustness. Since it is known that diagonalized systems often suffer poor robustness characteristics (see, for example, [1]), for a complete evaluation of any diagonalizing scheme it is important to obtain a measure of the resulting closed loop system robustness. To obtain such a measure, it is common to introduce some kind of perturbation to the nominal plant (i.e. some possible deviation from the analytic model of the plant), and calculate the bounds within which such perturbation must remain so as to guarantee the fulfillment of a given performance criteria. The perturbation to be introduced is chosen so as to reflect the robustness of the closed loop system with respect to the kind of errors we expect the analytical model to make. In our case, the analytical model derived in section 2 has been verified to be accurate in the low frequency region, but no information on its behavior at higher frequencies is available. In the presence of such uncertainty, the use of multiplicative perturbations is appropriate for the evaluation of the closed loop system robustness. In the following analysis, the performance criteria to be fulfilled will be the closed loop systems stability. Let $L_i(s)$ and $L_o(s)$ denote multiplicative input and output perturbation matrices respectively, i.e. of the form:

$$G'(s) = G(s)(I + L_i(s)), \quad L_i(s) = \text{input perturbation matrix,}$$

$$G'(s) = (I + L_o(s))G(s), \quad L_o(s) = \text{output perturbation matrix.}$$

We make two basic assumptions on $L_i(s)$ and $L_o(s)$. First, we assume that $G'(s)$ remains a strictly proper system. Second, we assume that the number of unstable poles of $G'(s)$ is the same as that of $G(s)$. Under these assumptions, it is well known how to obtain bounds on the maximum admissible singular values of $L_i(s)$ and $L_o(s)$. Consider again the system shown in Fig. 7. Using the spectral norm $\|\cdot\|_2$, these bounds are given by the following inequalities (see [1] or [2]):

$$\bar{\sigma}[L_i(j\omega)] < \underline{\sigma}[I + (F(j\omega)Q(j\omega))^{-1}], \quad (20)$$

$$\bar{\sigma}[L_o(j\omega)] < \underline{\sigma}[I + (Q(j\omega)F(j\omega))^{-1}], \quad (21)$$

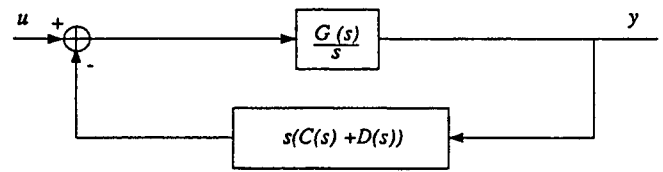


Figure 8 Equivalent representation of the reduced system

where $\bar{\sigma}[M]$ and $\underline{\sigma}[M]$ denote the maximum and minimum singular values of the matrix M , respectively.

Following the same arguments presented in the stability analysis, it is sufficient to analyze the robustness characteristics of the reduced system

$$H_R(s) = \frac{I}{s} [G^{-1}(s) + D(s) + C(s)]^{-1},$$

which can also be represented as shown in Fig. 8. Let us define the functions $\hat{\sigma}[L_i(j\omega)]$ and $\hat{\sigma}[L_o(j\omega)]$ as follows:

$$\hat{\sigma}[L_i(j\omega)] = \underline{\sigma} \left[I + j\omega \left((\hat{C}(j\omega) + j\omega D(j\omega)) G(j\omega) \right)^{-1} \right], \quad (22)$$

$$\hat{\sigma}[L_o(j\omega)] = \underline{\sigma} \left[I + j\omega \left(G(j\omega) (\hat{C}(j\omega) + j\omega D(j\omega)) \right)^{-1} \right].$$

Then, according to Eqns. (20) and (21), it follows that the maximum admissible singular values of $L_i(s)$ and $L_o(s)$ for the reduced system shown in Fig. 8 are given by $\hat{\sigma}[L_i(j\omega)]$ and $\hat{\sigma}[L_o(j\omega)]$ respectively.

4 Simulation

4.1 Design Procedure and Simulation Parameters

Design Procedure The stability conditions obtained in the previous section can be translated into simple design constraints on $C(s)$ and $\Delta D(s)$. First, $\hat{C}(s)$ is designed with asymptotically stable elements (A1), and such that the transfer function of the *ideal* closed loop system ($\Delta D(s) = 0$) has the desired performance. This will automatically fulfill the requirement that $\frac{1}{s} [G^{-1}(s) + D_0(s) + C(s)]^{-1}$ be asymptotically stable (A2). Once $C(s)$ is chosen, $D(s)$ is designed as a realizable approximation of $D_0(s)$, and so that the matrix $[G^{-1}(s) + D_0(s) + C(s) + \Delta D(s)]$ is diagonally dominant (C2). The fulfillment of these conditions ensures the stability of the closed loop system.

The transfer functions of the closed loop system, as well as the singular value plots $\hat{\sigma}[L_i(j\omega)]$ and $\hat{\sigma}[L_o(j\omega)]$ are then simulated. Based in this simulation, both $C(s)$ and $D(s)$ can be adjusted in order to improve the closed loop system performance. By repeating this procedure, it is possible to arrive to a controller design which achieves the desired performance.

Simulation Parameters The following design is based on experimental parameters measured on the actual prototype (see [7] or [8]). These parameters are the resonance frequencies and resonance qualities of each degree of freedom. The resonance frequencies can be measured to great accuracy, and the measured values agree with the predictions of an existing theoretical model of the SSA (see [7] or [8]). It has also been verified that they do not change noticeably over long periods of time. Thus, a fairly accurate knowledge of the resonance frequencies is assumed. The qualities

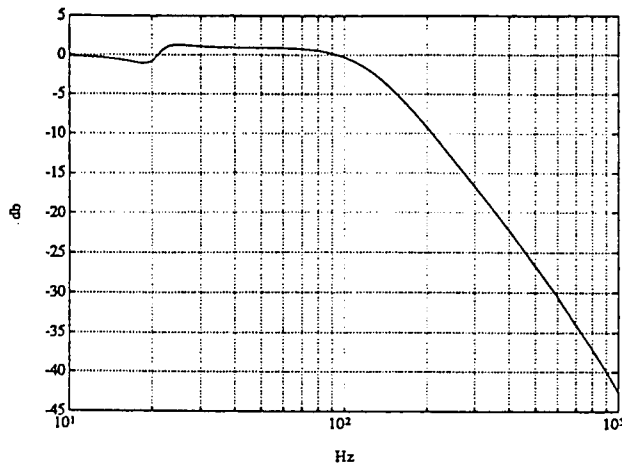


Figure 9 $V_{r_x}(s)/a_x^e(s)$, diagonal element of ideal closed loop transfer function $\Delta D(s) = 0$

of resonance, on the other hand, are not very well characterized. Throughout most of the data taking, the pressure in the vacuum chamber is high enough that the Q_i are determined by viscous damping. Because of a small vacuum leak, the pressure, and thus the different Q_i , varied significantly from day to day, although they always remain high ($Q_r > 100$, $Q_\theta > 1000$).

4.2 Simulation Results

Implementation of $C(s)$. To achieve its goals, $C(s)$ is designed to minimize the displacements of the proof mass, to increase the bandwidth of the instrument (from about 20 Hz. for the translational degrees of freedom and 15 Hz. for the rotational degrees of freedom to about 100 Hz. for both), and to provide adequate damping to the closed loop system. Using standard SISO design tools, and iteratively adjusting $C(s)$ as described above, we obtain the following transfer function for $c_i(s)$:

$$c_i(s) = \frac{0.4 \times 10^6 (s^2 + \hat{\omega}_i s / \hat{Q} + \hat{\omega}_i^2) (s/754 + 1)}{k_i \theta_i \omega_s (s/1068 + 1) (s/6283 + 1) (s/6912 + 1)s},$$

for $i = r_x, r_y, r_z, \theta_x, \theta_y, \theta_z$, where, under the assumption that an accurate estimate of ω_i is known, we take $\hat{\omega}_i \approx \omega_i$, $\hat{Q} \approx 4$. This design fulfills A1 and A2, while providing satisfactory performance to the ideal closed loop transfer function $-C(s) [G^{-1}(s) + D_0(s) + C(s)]^{-1} K^{-1}$. As mentioned in the previous section, an integrator is included in each element of $C(s)$ to minimize the steady state displacement of the proof mass. Fig. 9 shows the closed loop transfer function of the ideal system for the r_x axis. A 100 Hz bandwidth with adequate damping is achieved. The design is robust to changes in Q_i , as long as Q_i is high ($Q_i > 50$). Finally, the resulting open loops have over 12 dB gain margin and 54° phase margin.

Implementation of $D_0(s)$. We now proceed to design $D(s)$ as a realizable version of $D_0(s)$. First, we verify that the matrix $[G^{-1}(s) + C(s)]$ is already diagonally dominant. Thus, even if any or all the connections of $D(s)$ are broken, the closed loop system still remains stable. For $D(s) = 0$, Fig. 10 shows the transfer functions between a translational acceleration (a_x^e) and the different outputs of the closed loop system as predicted by the model derived in section 2. Although the closed loop system is guaranteed to be stable, and the different axis of the instrument are already partially decoupled, it is required for the satisfactory performance

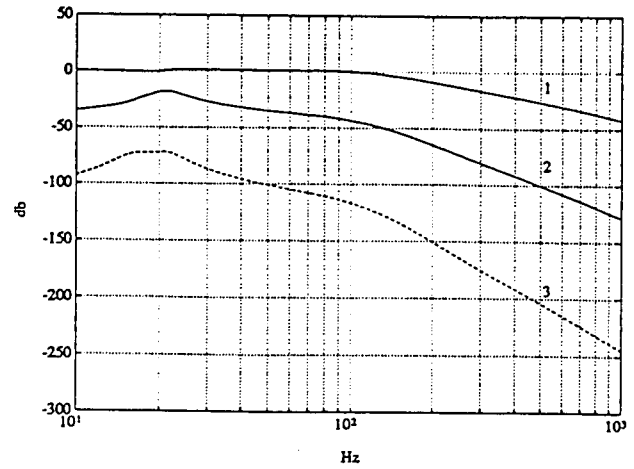


Figure 10 Closed loop response for $D(s)=0$: (1) $V_{r_x}(s)/a_x^e(s)$; (2) $V_{\theta_y}(s)/a_x^e(s)$ (or $V_{\theta_z}(s)/a_x^e(s)$); (3) $V_{r_y}(s)/a_x^e(s)$ (or $V_{r_z}(s)/a_x^e(s)$)

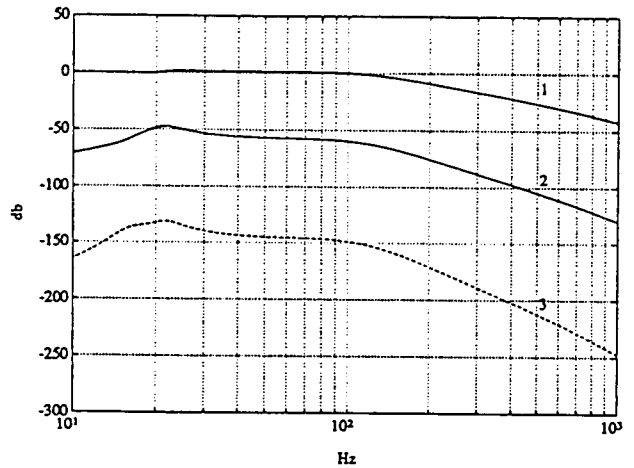


Figure 11 Closed loop response with designed $D(s)$: (1) $V_{r_x}(s)/a_x^e(s)$; (2) $V_{\theta_y}(s)/a_x^e(s)$ (or $V_{\theta_z}(s)/a_x^e(s)$); (3) $V_{r_y}(s)/a_x^e(s)$ (or $V_{r_z}(s)/a_x^e(s)$)

of the instrument to further decouple them. Fig. 11 shows the same transfer functions after the following $D(s)$:

$$\frac{5\omega_s}{(s + 5\omega_s)} K^{-1} \begin{bmatrix} 0 & 0 & 0 & 0 & f_m & -f_m \\ 0 & 0 & 0 & -f_m & 0 & f_m \\ 0 & 0 & 0 & f_m & -f_m & 0 \\ 0 & -f_I & f_I & 0 & 0 & 0 \\ f_I & 0 & -f_I & 0 & 0 & 0 \\ -f_I & f_I & 0 & 0 & 0 & 0 \end{bmatrix} \Xi^{-1}(s)$$

has been added. Clearly, by adding the suggested $D(s)$ we have succeeded in effectively decoupling the different axes of the device, without affecting the performance of the diagonal elements of the closed loop transfer function.

Robustness. In the previous section we emphasized the importance of evaluating the robustness of the proposed diagonalizing scheme. Also, $\hat{\sigma}[L_i(j\omega)]$ and $\hat{\sigma}[L_o(j\omega)]$ were defined as the maximum admissible singular values of $L_i(j\omega)$ and $L_o(j\omega)$. These bounds are plotted in Fig. 12 and Fig. 13. As with other plots in this paper, these plots were obtained assuming the same drive currents in all the sensing circuits. For this choice of parameters, $G(s)$ has a condition number close to one (at almost all frequencies), causing $\hat{\sigma}[L_i(j\omega)]$ and $\hat{\sigma}[L_o(j\omega)]$ to be very similar to each

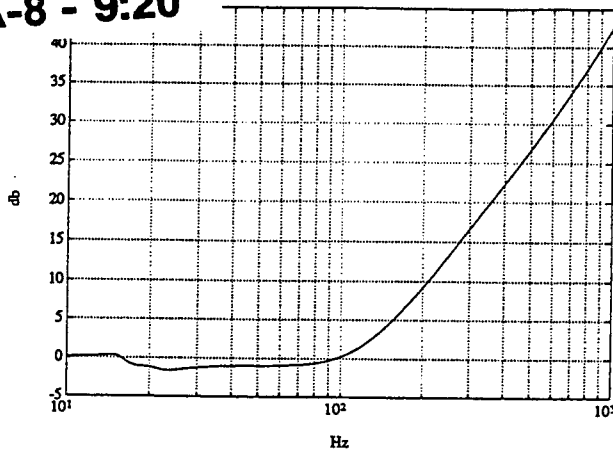


Figure 12 Maximum admissible singular values for input perturbation matrices

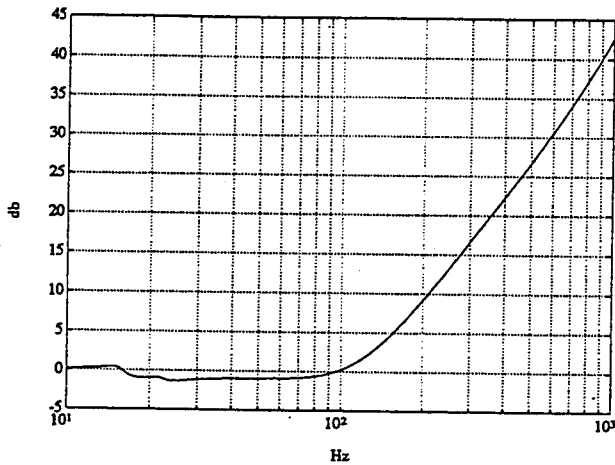


Figure 13 Maximum admissible singular values for output perturbation matrices

other. Hence, unless otherwise mentioned, our conclusions apply equally well to either $L_i(j\omega)$ or $L_o(j\omega)$. It is also important to remark that the bounds we obtain assume that only one kind of perturbation is present at a time, i.e. we assume that $L_i(j\omega) = 0$ when we evaluate the robustness of the system with respect to $L_o(j\omega)$, and vice-versa.

Based on Fig. 12 and Fig. 13, we obtain the following conclusions: first, for frequencies above 100 Hz, the robustness of the system increases rapidly with frequency. This is an essential requirement of the closed loop system robustness, since (as already mentioned) it is expected that the accuracy of the analytic model will decrease as frequency increases. Second, since the design of the proposed controller is based on the assumption that the analytic model is accurate at low frequencies, it is now possible to verify how accurate indeed it needs to be. At its minima, which occurs at $\omega \approx \omega_r$ (for input perturbation matrices), $\hat{\sigma}[L_i(j\omega)]$ can take values as low as -1.66 dB, which roughly means that gain errors ($\hat{\sigma}[L_i(j\omega)]$ automatically considers the worst possible phase errors) in the model of up to $\pm 80\%$ (at the worst possible frequency) will not cause the closed loop system to become unstable. In other words, the stability of the closed loop system is guaranteed if the actual transfer function of the plant is within $\pm 80\%$ (in terms of gain) of our analytic model.

Is this a good margin? From Eqns. (20) and (21), we obtain the following inequalities:

$$\bar{\sigma}[L_i(j\omega)] \leq 1 + \frac{1}{\underline{\sigma}[F(j\omega)Q(j\omega)]},$$

$$\bar{\sigma}[L_o(j\omega)] \leq 1 + \frac{1}{\underline{\sigma}[Q(j\omega)F(j\omega)]}.$$

These inequalities show that for any closed loop system where the output is required to closely "follow" the input (or signal to be measured), the need for high gains over the frequencies of interest will limit the admissible singular values of both input and output perturbations to values close to one. In other words, for a closed loop system to be considered robust, it is necessary to have an accurate knowledge of the plant over the frequency regions where high open loop gains are being applied. In fact, the presence of an integrator in the design of the controller automatically forces the minima of $\hat{\sigma}[L_i(j\omega)]$ and $\hat{\sigma}[L_o(j\omega)]$ to be at most one. Hence, the largest admissible model error must always be smaller than $\pm 100\%$. Considering that this is the most we can hope for, and that the model has been shown to be accurate over the frequencies in question, $\pm 80\%$ is a very reasonable margin.

Lastly, there is another interpretation of $\hat{\sigma}[L_i(j\omega)]$. From Eqn. (22),

$$\hat{\sigma}[L_i(j\omega)] = \frac{1}{\bar{\sigma}[(C(j\omega) + D(j\omega))G(j\omega)(I + (C(j\omega) + D(j\omega))G(j\omega))^{-1}]},$$

and $(C(j\omega) + D(j\omega))G(j\omega)(I + (C(j\omega) + D(j\omega))G(j\omega))^{-1}$ is the transfer function between a signal at the input of the plant and the currents fed by the controller. This transfer function corresponds to the complementary sensitivity of the system. Hence, inverting the plot in Fig. 12, we obtain the norm of the complementary sensitivity. The obtained complementary sensitivity behaves as expected for a system where the output is required to closely follow the input over a certain frequency range. Noise signals at the input of the plant are passed through in the same frequency band as the acceleration signals we desire to measure, and are attenuated outside of this band. This is a well known disadvantage of systems where the output is required to follow the input closely. It should be clear that this is unavoidable, since such noise signals are injected into the system at the same point as the accelerations we are trying to measure (although they may arise from different sources, such as white noise in the controller electronics, etc.), and cannot be attenuated without attenuating the desired signals.

5 Conclusions

We have developed a relatively simple MIMO controller which converts an instrument with fairly strong cross coupling into an almost decoupled system, while also achieving the desired increase in bandwidth and improved damping of resonances for the diagonal terms of the closed loop transfer function matrix. This controller consists of two parts, one of which cancels the effect of the non-diagonal terms of the open loop transfer function, while the other is simply a set of SISO controllers. A straightforward approach is possible because the particular structure of the open loop transfer function allows the cancellation of its non-diagonal terms by a fairly simple element. The development of the rest of the controller then reduces to the problem of designing a set of independent SISO elements. The stability of the system is studied through Rosenbrock's INA stability criteria, and a simple set of conditions which

guarantee stability is obtained. As it is well known that INA based designs can be sensitive to coupled perturbations, the robustness of the system with respect to input and output perturbation matrices is evaluated. The performance of a controller designed according to the suggested diagonalizing scheme is simulated, and the characteristics of the obtained closed loop system are found to be satisfactory.

As for future work, it would be useful to study the possible generalization of the suggested technique to a broader class of MIMO problems. In this respect, it is worth noting that since the matrix $G^{-1}(s)$ is not diagonally dominant, the application of the INA stability criteria would have been impossible without the introduction of the matrices $D_0(s)$ and $\Delta D(s)$ (or some other artifice). Nevertheless, the obtained stability conditions apply also for the case $D(s) = 0$, suggesting possible generalizations of the INA method. Finally, once the technical challenges of implementing the design (in a way that does not worsen the noise level of the SSA) have been overcome, the behavior of the actual system must be compared with the predictions.

Bibliography

- [1] John C. Doyle and Gunter Stein. Multivariable feedback design: Concepts for a classical/modern synthesis. *IEEE Trans. Automat. Contr.*, AC-26:4-16, 1981.
- [2] Alan J. Laub. An inequality and some computations related to the robust stability of linear dynamic systems. *IEEE Trans. Automat. Contr.*, AC-24:318-320, 1979.
- [3] O. V. Lounasmaa. *Principles and Methods Below 1 K*. Academic Press: London and New York, 1974.
- [4] D. H. Owens. *Feedback and Multivariable Systems*. Imprint: Stevenage, Eng.:Peter Peregrinus [for] The Institution of Electrical Engineers, 1978.
- [5] H. J. Paik. *Analysis and Development of a Very Sensitive Low Temperature Gravitational Radiation Detector*. PhD thesis, Stanford University, Stanford, California, 1974. Unpublished.
- [6] H. J. Paik, Jurn-Sun Leung, Samuel H. Morgan, and Joseph Parker. Global gravity survey by an orbiting gravity gradiometer. *EOS Transactions, American Geophysical Union*, Vol. 69:pp. 1601, 1610-1611, 1988.
- [7] H. J. Paik, J. W. Parke, and E. R. Canavan. Development of a superconducting six-axis accelerometer. Final report to the Air Force GL-TR-89-0181, Geophysics Laboratory, Hanscom Air Force Base, Massachusetts, 1989.
- [8] J. W. Parke. *Null Test of the Gravitational Inverse Square Law and the Development of a Superconducting Six-Axis Accelerometer*. PhD thesis, University of Maryland, College Park, Maryland, 1990.
- [9] M. Tinkham. *Introduction to Superconductivity*. New York, McGraw Hill, 1975.

Appendix A. Predicted and Measured Transfer Functions

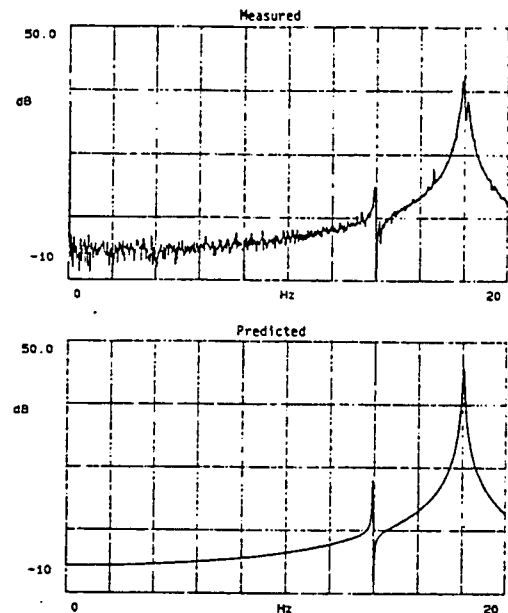


Figure 14 Diagonal transfer function, $V_{r_s}(s)/I_{r_s}(s)$

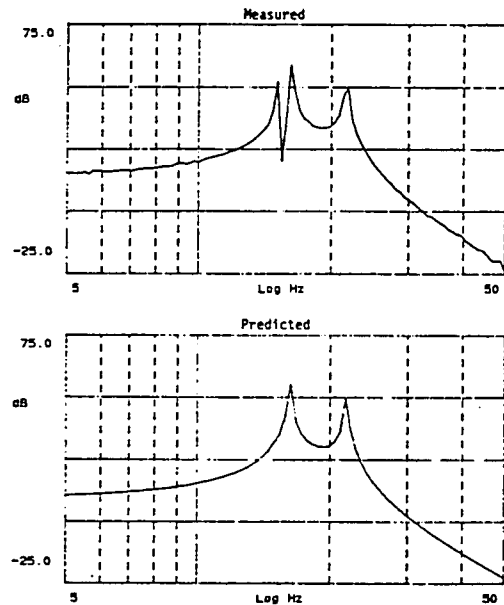


Figure 15 Non-diagonal transfer function, $V_{\theta_s}(s)/I_{r_s}(s)$

We include a comparison of the predicted and the measured transfer functions in two cases. The first transfer function corresponds to a diagonal element of $G(s)$, $V_{r_s}(s)/I_{r_s}(s)$. The second transfer function corresponds to a non-diagonal element of $G(s)$, $V_{\theta_s}(s)/I_{r_s}(s)$. For the second comparison (Fig. 15), the predicted transfer function does not correspond accurately to the measured transfer function near the lower resonance peak. This error can be explained by the fact that the current simulation program assumes the resonant frequencies and resonance qualities of all the rotational degrees of freedom to be the same (similarly for the translational degrees of freedom). Clearly, in the actual system this is not true. A more accurate model which takes into consideration the imperfections of the device is already being tested.

Appendix C

MATLAB simulation parameters

The following parameters were used in the MATLAB simulations used in

- Design of controller, theoretical,
- Design of the controller, implementation,
- Noise analysis.

```
%%%%%%%%%%%%%%%%%%%%%%%%%%%%%%%%%%%%%%%%%%%%%%%%%%%%%%%%%%%%%%%%%%%%%%%%
%% this file includes all the definitions which characterize the %%
%% SSA-Ib.                                                         %%
%%%%%%%%%%%%%%%%%%%%%%%%%%%%%%%%%%%%%%%%%%%%%%%%%%%%%%%%%%%%%%%%%%%%%%%%
```

%Physical parameters:

```
%%%%%%%%%%%%%%%%%%%%%%%%%%%%%%%%%%%%%%%%%%%%%%%%%%%%%%%%%%%%%%%%%%%%%%%%
```

```
g          = 9.8;          %mt/s^2

Mass       = 0.144;        %Kilograms

c          = 1.35E-2;      %mt

d          = 3.05E-4;      %mt

I          = 4.0E-5;        %Moment of Inertia

lambdaLev  = 0.01724;     %H/mt
```

```

lambdaSen      = 0.007856;          %H/mt

GamaLev        = 15.32;              %H/mt^2
BetaLev        = 0;                 %H

LoLev          = 5.704E-6;           %H, Levitation coil inductance in
                                     %   balanced position
LoSen          = 2.6599E-6;          %H, Sensing coil inductance in
                                     %   balanced position

Lsq            = 2E-6;               %H, Squid input coil, reflected to
                                     %   sensing circuit

Lf             = 662E-6;             %H, Secondary inductance of feedback
                                     %   transformer
Mf             = 63.5E-6;            %H, Mutual inductance feed-secondary

Ls            = 2.66E-6;            %H, Secondary inductance of sensing
                                     %   transformer
Ms            = 195E-6;             %H, Mutual inductance sens-secondary

SquidGain      = 1.0E4;             %Volts/Amps (Range 3)

VIConverterRatio = 1.;              %Amps/Volts

Vomax          = 10.0;              %Volts, maximum output voltage

```

```

% Transformations from dimensionless to dimensional units

```

```

%%%%%%%%%%%%%%%%%%%%%%%%%%%%%%%%%%%%%%%%%%%%%%%%%%%%%%%%%%%%%%%%%%%%%%%%

```

```

Eta           = d/c;
PslambdaLev   = lambdaLev*d/(LoLev);
PslambdaSen   = lambdaSen*d/(LoSen);
PsGamaLev     = GamaLev*d^2/(LoLev);
PsBetaLev     = BetaLev*(d/c)^2/(LoLev);

```

```

% Maximum Measurable Accelerations

```

```

%%%%%%%%%%%%%%%%%%%%%%%%%%%%%%%%%%%%%%%%%%%%%%%%%%%%%%%%%%%%%%%%%%%%%%%%

```

```

raccmax = 1E-4;          %Maximum measurable translational acc.
aaccmax = 5E-4;          %maximum measurable rotational acc.

```

```

% Levitation Currents:

```

%%

frac = 0.1;

LxLevitationCurrent = 4.88554; %Amps

AxLevitationCurrent1 = LxLevitationCurrent*frac;

(i.e. we assume approx. .488 A in theta1 circuits)

% Oscillator voltages for sensing circuit:

%%

LxVosc = 100E-3; %Volts rms

AxVosc = 100E-3;

We assume 100mV rms in all channels

%Sensitivity setting in Lock-in amplifiers:

%%

LxSens = 1; %Volts

AxSens = 1;

We assume 1V sensitivity in all channels (gain of
putput stage of lock-in amplifiers = 10)

% Plant parameters

%%

Qrx = 300;

Qax = 1500;

Wrx = 12.95*2*pi;

Wax = 13.07*2*pi;

(resonance frequencies based on mathematica model)

%% Design parameters

%%

%% Diagonalizing element (D(s))

%%

n = 10;

Ws = 125*2*pi;

pole corresponding to stage: $Ws \cdot n$

%% Diagonal controller (C(s))

%%

z1 = 120;

z2,z3 = complex conjugate pair with $W_r = W_r + .5 \text{ Hz}$, $Q = 4$;

p1 = 170;

p2 = 200;

p3 = 1200;

p4 = 0;

%% Definition of Rho (VCCS)

%%

Rhorx = raccmax/(Vomax*Krx);

Rhoax = aaccmax/(Vomax*Kax);

(designed so that at masimum expected acceleration the output voltage
is 10 V)

Gain = 0.28E6; (Carefull how this is interpreted, has to be associated with
corresponding program)

Gauss's Law Test of Gravity at Short Range

M. V. Moody and H. J. Paik

Department of Physics and Center for Superconductivity Research, University of Maryland, College Park, Maryland 20742
(Received 2 October 1992)

A null test of the gravitational inverse-square law can be performed by testing Gauss's law for the field. We have constructed a three-axis superconducting gravity gradiometer and carried out such a test. A lead pendulum weighing 1500 kg was used to produce a time-varying field. This experiment places a new (2σ) limit of $\alpha = (0.9 \pm 4.6) \times 10^{-4}$ at $\lambda = 1.5$ m, where α and λ are parameters for the generalized potential $\phi = -(GM/r)(1 + \alpha e^{-r/\lambda})$.

PACS numbers: 04.90.+c, 04.80.+z

Various types of light-mass bosons have been suggested to answer open questions in particle physics and gravity. The presence of these bosons would give rise to a Yukawa-type potential and thus appear as a violation of the gravitational inverse-square law. Numerous experiments have been performed to search for a composition-dependent as well as a composition-independent violation of the inverse-square law [1]. The experiment reported here is unique in that it employs a new instrument, a superconducting gravity gradiometer (SGG), and is based on a new approach, a test of Gauss's law for gravity. The result is $\alpha = (0.9 \pm 4.6) \times 10^{-4}$ at $\lambda = 1.5$ m, where $\phi = -(GM/r)(1 + \alpha e^{-r/\lambda})$ and the error corresponds to a 2σ level. This represents an improvement of 2 orders of magnitude over our previous result [2] and more than an order of magnitude over the best existing limit [3].

A differential equivalent of the inverse-square force law is Gauss's law for the field, $\nabla \cdot \mathbf{g} = -4\pi G\rho$, where $\mathbf{g} = -\nabla\phi$. By summing the outputs of an in-line gravity gradiometer rotated into three orthogonal directions, one can perform a near null test of the inverse-square law. The advantage of this type of experiment is its reduced sensitivity to the source density and metrology errors [4]. The residual sensitivity to the source errors results from higher moments of the gradiometer which couple to higher-order field gradients.

Each axis of the SGG consists of two spring-mass accelerometers in which the proof masses are confined to motion in a single degree of freedom along a common axis, and are coupled together by superconducting circuits. Platform motions that are common to both accelerometers are canceled by adjusting the ratio of two persistent currents in the sensing circuit. The sensing circuit is connected to a commercial SQUID amplifier to sense changes in the persistent currents generated by differential accelerations, i.e., gravity gradients. A second sensing circuit is used to sense common accelerations. The design and analysis of this gradiometer have been previously published [5].

A three-axis gravity gradiometer is formed by mounting six accelerometers on the faces of a precision cube. The accelerometers on two opposite faces of the cube form one of three in-line gradiometers. Aligning the diagonal of the cube with the vertical equally biases the

three gradiometer axes with respect to the Earth's gravitational acceleration (see Fig. 1). This orientation also permits the cyclic interchange of the gradiometer axes by a 120° rotation about the vertical.

In a perfect gradiometer the platform accelerations could be canceled to the degree to which the persistent currents could be adjusted. In actuality, the sensitive axes of the component accelerometers are not perfectly aligned. This misalignment results in a residual coupling to platform motion. The gradiometer alignment errors can be described in terms of a misalignment between the directions of the sensitive axes, $\delta\hat{n} = \hat{n}_2 - \hat{n}_1$, and a misalignment between the average direction of the sensitive axes and the baseline vector, $\delta\hat{l} = (\hat{n}_1 + \hat{n}_2)/2 - \hat{l}$. The gradiometer couples to translational accelerations and tilt through $\delta\hat{n}$, whereas $\delta\hat{l}$ results in coupling to angular acceleration [6]. The errors in sensitive axes alignment will also result in a misorientation of the gradiometer.

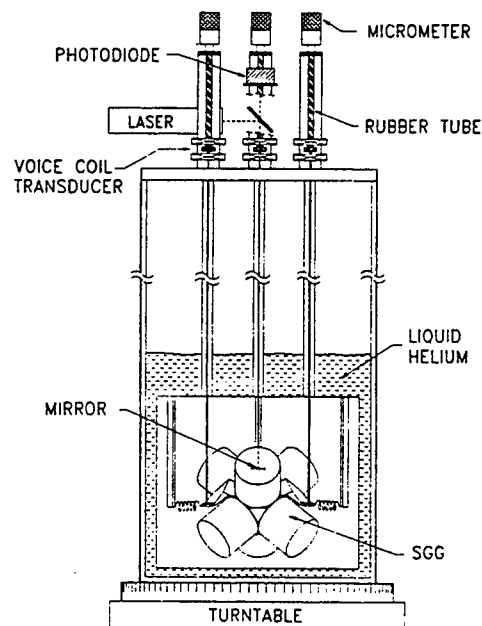


FIG. 1. Schematic side view of the SGG and supporting hardware. The laser beam passes down a center tube (not shown) in the cryostat. The three vertical supports are symmetric relative to the center tube.

ter axes, $\delta\hat{x}$. This error will result in an error in the orthogonality among the three in-line gradiometers and among the cyclic orientations for an individual gradiometer axis.

Even in a perfectly aligned gradiometer, angular motion about an axis other than its own sensitive axis produces centrifugal acceleration errors. If the gradiometer platform is stationary in the Earth's reference frame,

$$\sum_j \Gamma_i^{(j)} = (1 + \epsilon_i) \left\{ 3\sqrt{3}(\hat{z} \cdot \Gamma \cdot \hat{z})(\delta\hat{x}_i \cdot \hat{z}) + 2\Omega^2 - \frac{\sqrt{3}}{2} [3(\Omega \cdot \hat{z})^2 - \Omega^2] (2\delta\hat{x}_i \cdot \hat{z} + \delta\hat{l}_i \cdot \hat{z}) - 3(\hat{n} \cdot \hat{z})[(\delta\hat{l}_i \times \hat{n}) \cdot \hat{z}] - \frac{3}{l}(\ddot{\mathbf{r}} + \mathbf{g}) \cdot \hat{z}(\delta\hat{n}_i \cdot \hat{z} + \delta h_i/\sqrt{3}) \right\}. \quad (1)$$

Here, ϵ is the error in the gradiometer scale factor, Γ is the gravity gradient tensor, $\Omega = \Omega_E + \delta\Omega_p$, $\ddot{\mathbf{r}}$ represents the acceleration of the platform, \mathbf{g} represents the gravitational acceleration, l is the gradiometer baseline, and δh is the persistent current misbalance. This result indicates that, after summing over the three orthogonal orientations, only the vertical components of the error terms are significant.

Figure 1 shows a schematic of the apparatus. The SGG is composed of six cylindrical accelerometers, 10.2 cm in diameter and 8.9 cm long, mounted on a cube, 10.2 cm on a side. It is cooled inside an Al vacuum can with liquid helium contained in a vapor-cooled cryostat. Magnetic isolation consists of the SGG niobium (Nb) accelerometer housings, two layers of superconducting Pb shield, and a double wall Mumetal shield at room temperature. The vibration isolation of the SGG is passive and consists of three vertical suspension legs, and three springs located in the horizontal plane passing through the SGG center of mass. These springs increase the horizontal and torsional resonance frequencies of the SGG isolation to well above the signal frequency. The primary purpose of the vibration isolation is to reduce SGG platform motions at frequencies where the seismic noise can cause overloading of the SQUID amplifiers. Voice-coil type transducers are incorporated into each leg of the suspension. By varying the magnitude and phase of the currents through the coils, vertical motion or tilt (in any direction) may be applied to the SGG. The tilt motion is sensed with a two-dimensional optical lever consisting of a laser, a beam splitter, an x-y photodiode at room temperature, and a flat mirror mounted on the SGG cube (perpendicular to the diagonal). The cryostat and Mumetal shields rest upon a turntable driven by a stepper motor. The rotational accuracy of the turntable was determined to be better than 10^{-4} rad.

Since we are approximating the gradient by subtracting acceleration over a finite (nonzero) baseline l , 0.1905 ± 0.0003 m, there is a residual Newtonian term that must be removed to obtain $\nabla \cdot \mathbf{g}$. Errors in the source metrology limit the accuracy to which this term can be removed. The source used in this experiment is a 1498 ± 3 kg pendulum confined to a single plane of

the centrifugal acceleration error is given by $2[(\hat{n} \cdot \Omega_E) \times (\hat{n} \cdot \delta\Omega_p) + \Omega_E \cdot \delta\Omega_p]$, where Ω_E is the angular velocity of the Earth and $\delta\Omega_p$ is the angular jitter of the platform [6].

To perform the experiment, the gradiometer is rotated twice by 120° about the vertical to obtain a measurement of $\nabla \cdot \mathbf{g}$ with each gradiometer axis. The sum of the three cyclic orientations j of gradiometer axis i is given [7] by

motion by an Al tube and bearings at the pivot. The pendulum mass is a 0.324 m diam, 0.0064 m thick spherical Al shell with a Pb core. The eccentricity of this mass is less than 0.01. The distance between the pendulum pivot and the center of the sphere is 3.300 ± 0.005 m. The position of the pendulum is obtained using a 13 bit optical shaft encoder attached to one end of the pivot shaft. The amplitude of the pendulum is maintained to within ± 0.0004 rad (± 0.5 bit) per cycle by a pneumatic drive attached to the other end of the pivot shaft. The vertical and horizontal positions of the pendulum pivot relative to the SGG center were 4.583 ± 0.003 and 4.235 ± 0.003 m, respectively. The turntable, SGG mirror, and pendulum pivot were leveled to better than 0.0002 rad. The pendulum's plane of motion was aligned with the center of the turntable to better than 0.0002 rad. A numerical model of the experiment, in which the SGG accelerometers were modeled as point masses confined to a single degree of freedom, and the source was modeled as a simple pendulum, gives $(-4.04 \pm 0.11) \times 10^{-3}$ E ($1 \text{ E} \equiv 10^{-9} \text{ s}^{-2}$) for the residual term due to the finite baseline.

When the gradiometer axes are permuted by rotating the turntable, a displacement of the center of mass of the SGG, δr , leads to an error in the measurement of $\nabla \cdot \mathbf{g}$. The SGG was centered on the turntable rotation axis by observing the SGG mirror with a transit as the turntable was rotated through 360° . The resolution of this measurement, ± 0.0004 m, places an upper bound on δr . The numerical model indicates the error due to δr is minimized when the initial turntable orientation ϕ_i is such that the sensitive axis of one gradiometer is in the pendulum's plane of motion pointing away from the pendulum. This orientation (denoted as 0°) was chosen for the experiment resulting in an upper bound of 1.34×10^{-4} E for this displacement induced error.

The model was also used to investigate and minimize the SGG nonorthogonality error. Equation (1) indicates that this is accomplished by minimizing Γ_{zz} . If, as in the present experiment, the analysis is limited to measurements at the pendulum frequency f_p of 0.2681 ± 0.0001 Hz, then only the fundamental component of Γ_{zz} contributes to the error. The vertical gradient, Γ_{zz} , of the

source as a function of SGG polar angle has a zero at 54.74° . By positioning the pendulum so that at its maximum amplitude of 34.06° the mass is at a polar angle of 54.23° , we were able to reduce the fundamental component of Γ_{zz} to 0.009 E.

Equation (1) shows that the torsional acceleration of the platform, $\dot{\Omega} \cdot \hat{z}$, couples to the measurement of $\nabla \cdot \mathbf{g}$ through the z component of $\delta \hat{l} \times \hat{n}$. To make an accurate determination of this component, the torsional mode of the SGG platform was excited using the turntable. This motion results in a peak in the power spectrum at the torsional frequency, f_t , due to $(\delta \hat{l} \times \hat{n})_z$, and a second peak at $2f_t$ due to centrifugal acceleration. The magnitude of the $2f_t$ peak gives a measure of the torsional motion amplitude. Combining this with the magnitude of the f_t peak, we obtain $(\delta \hat{l} \times \hat{n})_z = (2.72 \pm 0.03) \times 10^{-4}$, $(0.59 \pm 0.03) \times 10^{-4}$, and $(-0.77 \pm 0.03) \times 10^{-4}$ for axes 1, 2, and 3, respectively. To measure $\dot{\Omega} \cdot \hat{z}$, a ring laser gyro (RLG) was mounted to the turntable with its sensitive axis vertical. Since the SGG platform modes are much higher than the source frequency, this measurement of the torsional motion of the turntable should translate directly to the SGG platform. The RLG data were recorded and analyzed in the same manner as the SGG data discussed below. Calibration of the RLG was achieved using the Earth's rotation. A total of 130 sets of 254 records was recorded over a span of 14 days. Analysis of these data gave a torsional motion amplitude of $(3.22 \pm 0.09) \times 10^{-9}$ rad at f_p in phase with the source. The quoted error is 2 standard deviations of the 130 sets.

In order that the gradiometer noise not be limited by seismic noise, sensitivity to acceleration must be minimized. Sensitivity to vertical acceleration is minimized by shaking the SGG vertically and adjusting the ratio of the persistent currents in the differential-mode sensing loops to null the outputs. To extend this balance to three dimensions, the SGG is tilted with amplitude θ in 2 degrees of freedom at a frequency f [$\ll (2\pi)^{-1}(g_E/l)^{1/2} \approx 1$ Hz] so that the translational acceleration error ($\propto \theta g_E/l$) dominates the angular acceleration error [$\propto \theta(2\pi f)^2$]. This permits determination of the components of the $\delta \hat{n}$'s. A three-dimensional balance against acceleration is then achieved by combining each gradiometer output, Γ_i , with the acceleration outputs, G_j , according to $\Gamma_i' + \sum_j s_{ij} G_j$, where the coefficients s_{ij} are determined from the $\delta \hat{n}$'s. After performing this balance, the noise performance of the SGG was approximately $0.07 \text{ EHz}^{-1/2}$ at f_p . The tilt measurements also permit absolute calibration of the accelerometer outputs.

For the experiment, the three gradient and three acceleration outputs from the SGG were recorded along with the pendulum position for 33 nights. The turntable was automatically rotated 120° twice each night. After acquisition, the data were time averaged, using the pendulum position as a reference, with a record length of six pendulum cycles. Approximately 710 records were ob-

tained per orientation per night. The dominant analog filter was a 1.6 Hz, low pass, 8 pole butterworth. During the averaging, unlocks in the SQUID amplifiers were detected, and the record in which the unlock occurred was rejected. To minimize effects of people in the laboratory, all records with a gradient fast Fourier transform value at f_p more than 5 standard deviations from the mean were also rejected. These two rejection criteria resulted in a loss of about 0.2% of the data.

The SGG acceleration data reveal the motion of the SGG platform induced by the source. A power spectrum of these data shows that, upon summation of the three cyclic orientations, the platform acceleration is below the random noise level at the fundamental signal frequency. This result indicates that translational acceleration effects generated by the pendulum at f_p contain no significant vertical component.

Figure 2 shows that gradiometer output of axis 1 over six cycles of the pendulum for each of the three orientations and their sum. The remaining structure in the sum is primarily in the second and fourth harmonics, and is due to residual coupling to the vertical motion of the laboratory induced by the pendulum at these frequencies. The standard deviations of the three gradiometer outputs (after summing over the three cyclic orientations) for the 33 nights of data were 1.81×10^{-4} , 7.15×10^{-4} , and $1.70 \times 10^{-4} \text{ E}$ for axes 1, 2, and 3, respectively. For axes 1 and 3, the 33 data sets exhibited a Gaussian distribution and the standard deviations compared favorably with the short term power spectral density noise value of $0.07 \text{ EHz}^{-1/2}$. The data from axis 2 exhibited a drift of 2.9σ over the 33 data sets. The drift for axes 1 and 3 was 1.4σ and 0.9σ , respectively. Large changes in the current balance were observed for axis 2, requiring that it be rebal-

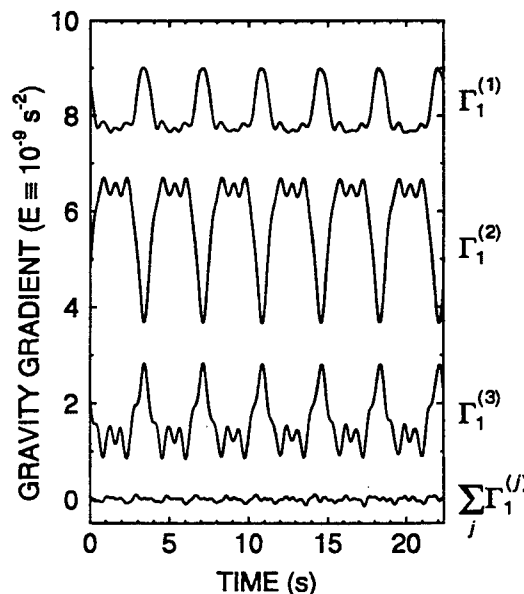


FIG. 2. The output of the differential mode sensing circuit of axis 1 for each of the three orientations and their sum. The time axis covers six cycles of the pendulum. The dc level is arbitrary.

TABLE I. Dominant errors.

Error source	2σ level (rms) (E)
Random	2.48×10^{-4}
Gradiometer rotation axis	$\leq 0.95 \times 10^{-4}$
Gradiometer axis nonorthogonality	$\leq 0.40 \times 10^{-4}$
Residual torsional acceleration	1.12×10^{-4}
Source metrology	1.08×10^{-4}
Magnetic coupling	$\leq 10^{-7}$
Total	3.1×10^{-4}

anced several times over the course of the experiment. No such problem was observed for axes 1 and 3. There is some evidence of a systematic effect arising from the large dc current induced in the loop containing the SQUID input coil, which would result from a leakage of the magnetic flux out of a sensing circuit loop. Consequently, we feel the data from this axis are substantially less reliable than that from axes 1 and 3, and our final result is given using only the two stable axes.

In addition to 33 nights of data in the 0° , 120° , and 240° orientations, 3 nights of data were recorded in the 60° , 180° , and 300° orientations. Summing the data at the 0° and 180° orientations for each axis eliminates residual coupling to horizontal and tilt motion of the floor, the dominant measurement error. Comparing the result with the value predicted by the model allows calibration of the SGG to better than 0.5%. Taking into account the torsional motion error would improve the calibration accuracy; however, the near null nature of this experiment makes further improvement unnecessary.

After time averaging the 33 data sets, the data are Fourier transformed, using a Hanning window, and separated into components in-phase (real) and out-of-phase (imaginary) with the source. These results are $(3.59 - 1.31i) \times 10^{-3}$, $(-1.88 - 2.26i) \times 10^{-3}$, and $(-6.22 - 1.18i) \times 10^{-3}$ E for axes 1, 2, and 3, respectively. As previously discussed, a quadrature component will arise from centrifugal acceleration due to angular motion of the platform mixing with the Earth's rotation. Thus the out-of-phase component should agree for the different axes, and it is within 1 standard deviation for the two stable axes, 1 and 3.

After subtracting the term due to torsional motion of the floor, the sum of the gradients in the three orientations is $(-3.87 \pm 0.45) \times 10^{-3}$ E for axis 1 and $(-4.10 \pm 0.37) \times 10^{-3}$ E for axis 3. Thus the two axes agree. Taking a simple average of these two axes reduces the relative contribution of the δr and $\delta \hat{r}$ errors, and gives, after subtracting the finite baseline term, our final result of $(0.58 \pm 3.10) \times 10^{-4}$ E.

The error budget for this result is given in Table I. The random noise comes from the scatter of the $\Sigma \Gamma_i$ data. The gradiometer rotation axis error represents an upper limit corresponding to the worst case in the direction and magnitude of δr . The axis nonorthogonality er-

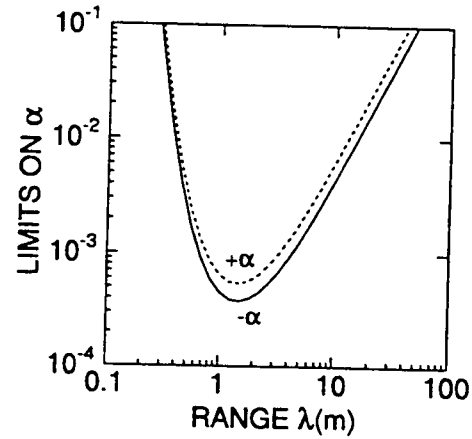


FIG. 3. 2σ limits on the Yukawa coupling constant set by this experiment.

ror is computed from the model using the maximum error in the polar angle, 0.001 rad. The residual torsional acceleration error comes from the scatter of the RLG data. The source metrology error arises from the uncertainties in the geometric parameters that are used in the numerical model. The magnetic coupling error has been obtained by combining a null response of the gradiometer to an applied, time-varying field with the estimated residual magnetic contamination of the pendulum mass.

Figure 3 shows the 2σ limits on a positive and negative α vs λ . The strictest limits are obtained at $\lambda = 1.5$ m and are $\alpha = (0.9 \pm 4.6) \times 10^{-4}$. Table I shows that the total error could be reduced by a factor of 3 by improving the random noise of the gradiometer and the gyro. A much more substantial improvement on the result can be achieved with the construction of an improved source. We are in the process of designing a near null source that does not shake the building.

This work was supported in part by the National Aeronautics and Space Administration under Contract No. NAS 8-38137, and by the U.S. Air Force under Contract No. F19628-87-K-0053. We are indebted to Lieutenant Colonel Gerry Shaw of Phillips Laboratory and Fred Nadeau of Wright Laboratories for providing the RLG and to Randell Jaffe of Rockwell International for assisting us in its operation. We gratefully acknowledge important contributions from Qin Kong, Joel Parke, Ed Canavan, Hans Haucke, and Ruozeng Liu.

- [1] For a review, see E. G. Adelberger *et al.*, Annu. Rev. Nucl. Part. Sci. **41**, 269 (1991), or E. Fischbach and C. Talmadge, Nature (London) **356**, 207 (1992).
- [2] H. A. Chan, M. V. Moody, and H. J. Paik, Phys. Rev. Lett. **49**, 1745 (1982).
- [3] J. K. Hoskins *et al.*, Phys. Rev. D **32**, 3084 (1985).
- [4] H. J. Paik, Phys. Rev. D **19**, 2320 (1979).
- [5] M. V. Moody, H. A. Chan, and H. J. Paik, J. Appl. Phys. **60**, 4308 (1986).
- [6] H. A. Chan and H. J. Paik, Phys. Rev. D **35**, 3551 (1987).
- [7] J. W. Parke, Ph.D. thesis, University of Maryland, College Park, Maryland, 1990 (unpublished).

Null test of the inverse-square law of gravity

H.J. Paik and M.V. Moody

Department of Physics and Center for Superconductivity Research
University of Maryland, College Park, Maryland 20742, USA

ABSTRACT: A differential equivalent of the inverse-square force law is Gauss's law for the field, $\nabla \cdot \mathbf{g} = -4\pi G\rho$, where $\mathbf{g} \equiv -\nabla\phi$. Thus, by summing the outputs of an in-line gravity gradiometer rotated into three orthogonal directions, one can perform a near-null test of the inverse-square law. The primary advantage of this type of experiment is its reduced sensitivity to the density and metrology errors of the source. We have developed a three-axis superconducting gravity gradiometer and carried out such a test using a 1500 kg lead (Pb) pendulum to produce a time-varying field. This experiment places a new (2σ) limit of $\alpha = (0.9 \pm 4.6) \times 10^{-4}$ at $\lambda = 1.5$ m, where α and λ are parameters of the generalized potential $\phi = -GM/r (1 + \alpha e^{-r/\lambda})$. This result represents an improvement of an order of magnitude over the best existing limit at $\lambda = 1.5$ m. To achieve further improvement in the resolution of α with the present instrument, a near-null source is needed. We plan to carry out an improved test of the inverse-square law using a long cylindrical shell as the source. Looking farther into the future, we hope to be able to conduct a geological-scale null experiment by moving the gradiometer up and down on a tower above a plain.

1. INTRODUCTION

Various light-mass bosons have been proposed to explain inconsistencies in particle physics and gravity. The existence of these bosons, which may represent a "fifth force", would give rise to a Yukawa-type potential and appear as a violation of the inverse-square law. The total potential would have the form:

$$\phi(r) = -GM/r [1 + \alpha \exp(-r/\lambda)] \quad (1)$$

where α and λ are the dimensionless coupling constant and the range of the Yukawa potential.

Numerous experiments have been performed to search for such a violation (Adelberger et al. 1992, Fischbach and Talmadge 1992). Most of these experiments have involved searches for non-Newtonian gravitational acceleration from near-null sources by employing torsion

balances, beam balances, or commercial gravimeters as detectors. Our experiment is unique in that it employs a new instrument, a three-axis superconducting gravity gradiometer (SGG), and is based on a new approach, a test of Gauss's law for gravity.

Gauss's law for the Newtonian field,

$$\nabla \cdot \mathbf{g} = -4\pi G\rho \quad (2)$$

is a differential equivalent of the inverse-square force law. Here $\mathbf{g} \equiv -\nabla\phi$ and ρ is the local mass density. Outside a source ($\rho = 0$), $\nabla \cdot \mathbf{g}$ must vanish regardless of the source geometry and density homogeneity. Therefore, summing the outputs of an in-line gravity gradiometer rotated into three orthogonal directions produces a null test of the inverse-square law. The primary advantage of this experiment is its relative insensitivity to the source density and metrology errors (Paik 1979).

We have performed a laboratory test of the inverse-square law and improved the limit in the resolution of α by a factor of 10 at the range of 1.5 m. The full advantage of the new approach will be realized in a geological-scale experiment, which usually involves a natural source whose density and shape are irregular. The experiment reported here is a stepping stone toward more advanced laboratory and geological-scale experiments with the SGG.

2. DESCRIPTION OF THE EXPERIMENT

The source used in this experiment was a 1498 kg lead (Pb) pendulum confined to a single plane of motion by a shaft and bearings at the pivot. The length of the pendulum is 3.300 ± 0.005 m. Figure 1 shows a schematic of the experiment.

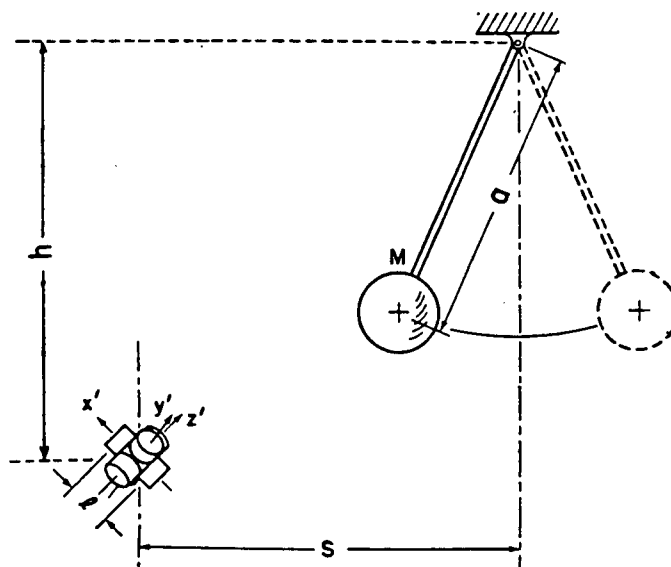


Figure 1. The source-detector configuration in the experiment. Here s is 4.234 m, h is 4.583 m, and the gradiometer baseline, l , is 0.1905 m.

Each axis of the SGG consists of two spring-mass accelerometers in which the proof masses are confined to motion in a single degree of freedom along a common axis, and are coupled together by superconducting circuits (see Figure 2). Platform motions appear as common-mode accelerations and are canceled by adjusting the ratio of two persistent currents (I_{d1} and I_{d2}) in the sensing circuit. The sensing circuit is connected to a commercial SQUID amplifier to sense changes in the persistent currents generated by differential accelerations, i.e., gravity gradients. The design and analysis of this gradiometer have been published (Moody et al. 1986, Paik 1993).

A three-axis gradiometer is formed by mounting six accelerometers on the faces of a precision cube. The accelerometers on any two opposite faces of the cube form one of three in-line gradiometers. Aligning the diagonal of the cube with the vertical equally biases the three gradiometer axes with respect to the Earth's gravitational acceleration. This "umbrella orientation" also permits the cyclic interchange of the gradiometer axes by a 120° rotation about the vertical.

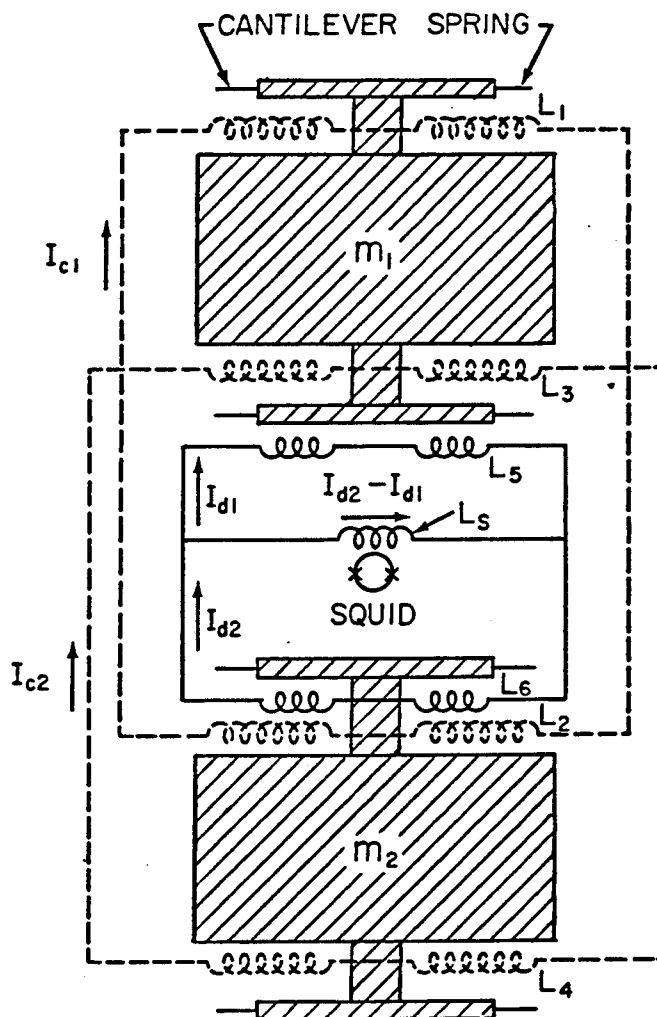


Figure 2. Schematic circuit diagram of one axis of the SGG.

The three-axis SGG is cooled to 4.2 K inside a liquid helium cryostat. The cryostat sits on an automated turntable, which rotates the gradiometer axes about the vertical. Voice-coil shakers for vertical acceleration and tilt as well as optical tilt sensors are provided in the cryostat to balance common-mode accelerations and measure various dynamic error coefficients.

To increase the resolution of the inverse-square law test in the laboratory, the source should be brought close to the gradiometer. However, as the ratio of the gradiometer baseline to the source-detector separation increases, the finite baseline effect, which results from higher moments of the gradiometer coupling to higher-order field gradients (Chan and Paik 1987), becomes significant, and metrological errors become more important. This effect, along with the error in the source metrology, establishes a lower limit on the source-detector separation.

3. DISCUSSION OF ERRORS IN THE NULL EXPERIMENT

An ideal gradiometer does not couple to acceleration; however, in reality, misalignment of the sensitive axes of the component accelerometers results in residual coupling to platform motion. A misalignment in the parallelism of the accelerometer sensitive axes couples to translational acceleration, and a misalignment in the concentricity of the sensitive axes couples to angular acceleration (Chan and Paik 1987). The errors in sensitive axes alignment also cause a misorientation of the gradiometer axes. This misorientation gives rise to an error in orthogonality among the three in-line gradiometers and among the cyclic orientations for an individual gradiometer axis. The orthogonality error results in coupling to cross-component gravity gradients.

One can show that, after summing over the three cyclic orientations, only the vertical components of these error terms remain (Parke 1990):

$$\sum_j \Gamma_i^{(j)} = (1 + \epsilon_i) \{ 3\sqrt{3}(\hat{\mathbf{z}} \cdot \mathbf{r} \cdot \hat{\mathbf{z}})(\delta \hat{\mathbf{x}}_i \cdot \hat{\mathbf{z}}) + 2\Omega^2 - \frac{\sqrt{3}}{2}[3(\Omega \cdot \hat{\mathbf{z}})^2 - \Omega^2](2\delta \hat{\mathbf{x}}_i \cdot \hat{\mathbf{z}} + \delta \hat{\mathbf{l}}_i \cdot \hat{\mathbf{z}}) - 3(\dot{\Omega} \cdot \hat{\mathbf{z}})[(\delta \hat{\mathbf{l}}_i \times \hat{\mathbf{n}}_i) \cdot \hat{\mathbf{z}}] - \frac{3}{l}(\bar{\mathbf{r}} + \mathbf{g}) \cdot \hat{\mathbf{z}}(\delta \hat{\mathbf{n}}_i \cdot \hat{\mathbf{z}} + \delta h_i / \sqrt{3}) \} \quad (3)$$

where $\Gamma \equiv -\nabla \nabla \phi$ is the gravity gradient tensor; \mathbf{r} and Ω are the linear position and angular velocity vectors of the platform; $\hat{\mathbf{n}}_i$ is the sensitive axis of the i -th gradiometer; $\delta \hat{\mathbf{n}}_i$, $\delta \hat{\mathbf{l}}_i$, and $\delta \hat{\mathbf{x}}_i$ are misalignment vectors from parallelism, concentricity, and proper umbrella angle; $\hat{\mathbf{z}}$ is the unit vector in the vertical direction; δh_i is the scale factor mismatch; respectively. In particular, the orthogonality error, $\delta \hat{\mathbf{x}}_i$, couples to the vertical component of the gravity gradient, Γ_{zz} . For the pendulum source, the fundamental component of Γ_{zz} was made to vanish by choosing the source-detector orientation shown in Figure 1.

By confining the data analysis to the fundamental of the pendulum frequency, the error due to direct coupling of the gradiometer to the source-generated linear acceleration of the building was also eliminated. This error removal was possible because the vertical component of this acceleration is limited to the second and other even harmonics. For the fundamental and odd harmonics, the acceleration of the building, which is in the horizontal plane, canceled upon summation over the three cyclic orientations.

The pendulum produces a vertical as well as horizontal components of angular acceleration of the floor at its fundamental frequency. To remove the angular acceleration error, the vertical component of angular acceleration and the corresponding error coefficient must be measured. A ring laser gyro (RLG), mounted directly to the turntable with its sensitive axis aligned with the vertical, was used for the acceleration measurement. The error coefficient was measured by shaking the SGG about the vertical axis.

An error in the experiment also arises from a displacement of the center of mass of the SGG upon the 120° rotations, $\delta \mathbf{r}$. This error can be minimized by choosing an optimum value for the initial SGG azimuthal angle. This error and the error due to an uncertainty in the

azimuthal angle of the gradiometer can be reduced to second order effects by summing the signals of the three gradiometer axes, i.e., by averaging over three concurrent measurements of $\nabla \cdot \mathbf{g}$ (Parke 1990). This was not possible in the present experiment due to malfunctioning of one axis, causing a first-order error in δr .

The final error we need to discuss is centrifugal acceleration. The SGG, like all other gravity gradiometers, is inherently sensitive to this error. However, the centrifugal acceleration generates a velocity term, which is in quadrature with the acceleration terms. This error term is rejected by phase-sensitive detection.

4. EXPERIMENTAL RESULTS

For the experiment, the three gradient and three acceleration outputs from the SGG were recorded along with the pendulum position for 33 nights. The turntable was automatically rotated 120° twice each night. After time-averaging the 33 data sets, the data is Fourier-transformed to identify the fundamental component. Because of a faulty superconducting joint in the circuit of one axis, the analysis of the data was limited to the other two axes.

Figure 3 shows the output of axis 1 for each of the three orientations and their sum. The time axis covers six cycles of the pendulum. The contamination of $\sum_j \Gamma_1^{(j)}$ is mainly in even harmonics, as expected from the source-induced vertical acceleration of the floor. In addition, the induced torsional motion of the floor caused an error term at the fundamental signal frequency. Subtracting the term due to the torsional angular acceleration and the finite baseline term gives our final result of $(0.58 \pm 3.10) \times 10^{-4} E$, a null result, where $1 E \equiv 10^{-9} \text{ s}^{-2}$ and the uncertainty represents a 2σ error.

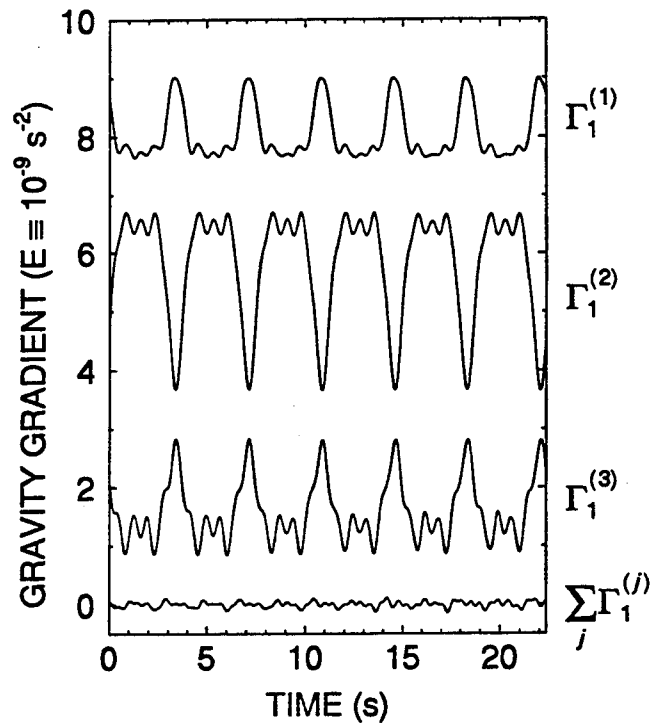


Figure 3. The output of axis 1 of the SGG for each of the three orientations and their sum. The dc level is arbitrary.

The error budget for this result is given in Table I. The random noise comes from the scatter of the $\sum \Gamma_i$ data. The main contributors to this random noise are the SQUID noise and the residual angular acceleration, which couples to the gradiometer through a misalignment of the sensitive axes. The gradiometer rotation axis error represents an upper limit corresponding to the worst case in the direction and magnitude of δr . The axis non-orthogonality error is calculated by assuming the maximum error in the polar angle, 0.001 rad. The residual

Error Source	2 σ Level
Random	2.48×10^{-4} E
Gradiometer Rotation Axis	$\leq 0.95 \times 10^{-4}$ E
Gradiometer Axis Non-orthogonality	$\leq 0.40 \times 10^{-4}$ E
Residual Torsional Acceleration	1.12×10^{-4} E
Source Metrology	1.08×10^{-4} E
Magnetic Coupling	$\leq 10^{-7}$ E
Total	3.1×10^{-4} E

Table 1. DOMINANT ERRORS

torsional acceleration error comes from the scatter of the RLG data. The source metrology error arises from the uncertainties in the geometric parameters of the experiment.

The strictest limits on the Yukawa coupling constant are $\alpha = (0.9 \pm 4.6) \times 10^{-4}$ at $\lambda = 1.5$ m, where the uncertainty represents a 2σ error. This represents an improvement of more than two orders of magnitude over our previous result (Chan et al. 1982) and an order of magnitude over the best existing limit at $\lambda \approx 1$ m (Hoskins et al. 1985, Muller et al. 1989).

Figure 4 shows the 1σ limit on α versus λ set by our experiment (solid line), in contrast to the limits obtained by previous experiments (shaded area). The expected resolution of a future SGG experiment with a laboratory null source, which will be discussed in the next section, is shown by a dotted line.

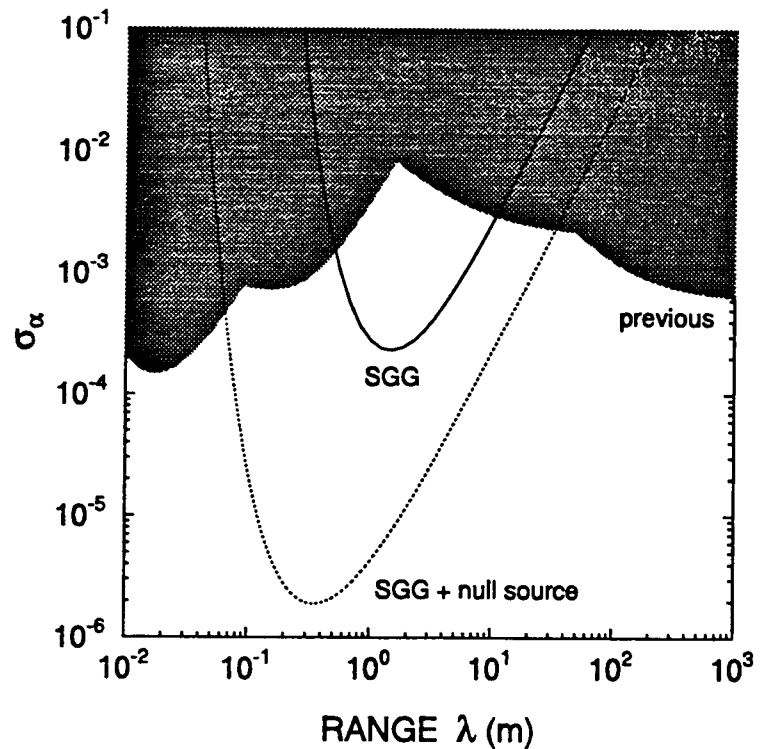


Figure 4. 1σ limit on the Yukawa coupling constant set by this experiment in contrast to the limits obtained by other experiments.

5. FUTURE EXPERIMENTS

Substantial improvement in the resolution of α on the sub-meter distance scale will require significant advancements in the SGG or in the source. Incorporating an approximately null gravity source into the experiment would reduce the errors which couple to gravity itself and allow the source to be brought much closer to the detector.

Unlike the pendulum experiment in which the data was recorded continuously and Fourier analyzed, the null source experiment would require that the data be recorded only when the detector is in the null regions of the source. Hence, any signal, or error, would appear as a square wave. Since the data is only recorded when the source is stationary, dynamic coupling is eliminated. However, such an experiment must be done at frequencies sufficiently low as to be in the red noise region of the SGG (< 0.05 Hz). We are currently making improvements to the SGG in an effort to suppress the low-frequency noise.

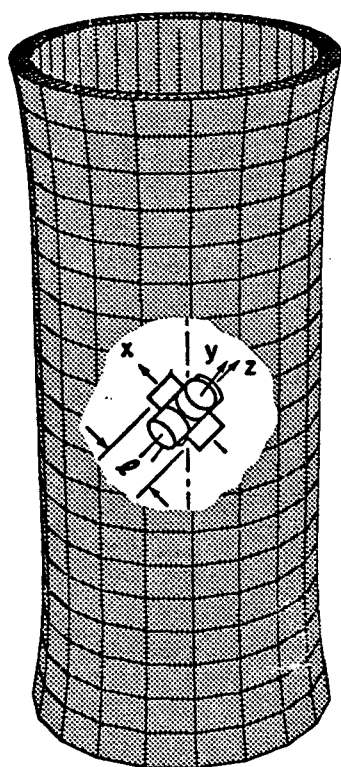


Figure 5. A preliminary design of a null gravity source.

An infinite cylindrical shell is a well-known null source for a $1/r$ potential. By making the mass distribution a function of the axial coordinate, while maintaining cylindrical symmetry, a near-null source of moderate dimensions can be designed. Initial calculations have shown that a cylinder with a sufficiently null region about its center can be made using a height-to-diameter ratio of 2 (see Figure 5). However, such a source would have to be more than 5 diameters away from the detector at the far position for its Newtonian field to become sufficiently weak. The dimensions of our laboratory disallow such an experiment given the present detector dimensions. Consequently, we are in the process of designing a cylindrical source with additional null regions near its ends. By modulating between these three regions, we expect to achieve a resolution of 10^{-6} in α at $\lambda \approx 0.2$ m.

Improving the resolution in α at larger ranges will require a geological-scale source. Such an experiment could be realized by mounting the SGG on a large turntable in the vicinity of a cliff, or in an SGG tower experiment. These experiments have the potential to improve the resolution in α to 10^{-5} around $\lambda \approx 100$ m. Such experiments require the detector to be on a moving platform and be able to suffer the dynamics of this platform. This is a significant step from the present experiment where the SGG is stationary in the laboratory.

In addition to the improved laboratory test of the inverse-square law, we are developing a program to test the SGG on an aircraft in preparation for airborne gravity survey. For such moving-base application, additional compensation needs to be provided for the gradiometer

errors arising from coupling to the linear and angular accelerations of the platform. Once the SGG is flight-qualified, it could be used as a detector in a cliff or a tower experiment.

The Yukawa signal at a height z above a plain can be shown (Chan and Paik 1984) to be

$$\nabla \cdot \mathbf{g} = -2\pi G \rho \alpha \exp(-z/\lambda) \quad (4)$$

for λ small compared to the radius of the Earth, where ρ is the mass density of the Earth near the surface. If z is modulated from 0 to at least 2λ , the peak-to-peak signal is about 1000α E. A resolution of $\alpha = 10^{-5}$ would then be achieved by an SGG with a noise level of $0.5 \text{ E Hz}^{-1/2}$, the initial goal for the airborne SGG, in an integration time of 10^4 s .

6. CONCLUSIONS

A Gauss's law test for gravity has been designed and carried out (Moody and Paik 1993). The experiment employs a new instrument, a three-axis superconducting gravity gradiometer. The result represents an improvement of an order of magnitude over the best existing limit at $\lambda = 1.5 \text{ m}$. Table I shows that the total error with the pendulum source could be reduced by a factor of 3 by improving the random noise of the gradiometer and the gyroscope used to remove the residual torsional motion error. A much more substantial improvement on the result can be achieved with the construction of an improved source. A laboratory experiment with a near-null source and a geological-scale experiment on a tower are planned.

ACKNOWLEDGEMENTS

This work was supported in part by NASA under contract NAS 8-38137, and by the U.S. Air Force under contract F19628-87-K-0053. We are indebted to the entire staff of the SGG laboratory for their technical assistance and valuable discussions.

REFERENCES

- Adelberger E G et al. 1991, *Ann. Rev. Nucl. Part. Sci.* **41**, 269.
- Chan H A, Moody M V, and Paik H J 1982, *Phys. Rev. Lett.* **49**, 1745.
- Chan H A and Paik H J 1984, **Precision Measurement and Fundamental Constants II**, B N Taylor and W D Phillips, Eds., Natl. Bur. Stand. (U.S.), Spec. Publ. 617, pp. 601-606.
- Chan H A and Paik H J 1987, *Phys. Rev. D* **35**, 3551.
- Fischbach E and Talmadge C 1992, *Nature* **356**, 207.
- Hoskins J K et al. 1985, *Phys. Rev. D* **32**, 3084.
- Moody M V, Chan H A, and Paik H J 1986, *J. Appl. Phys.* **60**, 4308.
- Moody M V and Paik H J 1993, *Phys. Rev. Lett.* **70**, 1195.
- Muller G et al. 1989, *Phys. Rev. Lett.* **63**, 2621.
- Paik H J 1979, *Phys. Rev. D* **19**, 2320.
- Paik H J 1993, in this volume.
- Parke J W 1990, Ph.D. thesis, University of Maryland, College Park, Maryland.